ELASTOHYDRODYNAMICS OF ACTUATED SLENDER BODIES IN STOKES FLOWS: METHODS, TOOLS, AND SIMULATIONS OF MICROSCALE MOTILITY

by

ATTICUS L. HALL-McNAIR

A thesis submitted to
The University of Birmingham
for the degree of
DOCTOR OF PHILOSOPHY

School of Mathematics
College of Engineering and Physical Sciences
The University of Birmingham
May 2022

Abstract

Countless microorganisms use slender elastic filaments to affect and traverse their surroundings. From the metachronal synchronisation of tracheal cilia to transport mucus, to the propulsive undulatory motion of sperm flagella, cells of all shapes and sizes use filament-like structures in a variety of fluid environments. The key physics in such environments arise from the interactions between slender-body filament-like elastic structures comprising the organism and surrounding viscous fluid. Understanding the coupled elastohydrodynamics of microscale propulsive mechanisms can provide insights into cell ultrastructure and rheology, paving the way for experimental studies and data interpretation, and suggesting novel diagnostics useful to researchers and clinicians alike.

In this thesis, we present two mathematical models for describing the dynamics of elastohydrodynamic filaments, in particular for simulating the motion of human spermatozoa. Both methods are accompanied by bespoke implementations in open source MATLAB® code. The methods, dubbed the EIF and SPX methods, differ principally in dependent variables, which is the angle made between the filament centreline and a fixed axis in the EIF, and nonplanar centreline position, tension, and twist curvature in the SPX model. Key considerations in both approaches are (a) accuracy, improving upon many de-facto standard approaches by considering nonlocal hydrodynamic interactions and nonlinear geometries, (b) generalisability, so that the proposed methods can be applied to a variety of problems in a straightforward manner, and (c) efficiency, to reduce the formidable computational requirements that have historically stood as barriers to entry for rapid and reliable simulation studies. The methods developed derive from exploiting the slenderness property of the propulsive structures (i.e. cilia and flagella); auxiliary structures such as cell bodies or heads are not required to be slender provided the overall cell length is much longer than the width.

The EIF method is formulated and applied to simulate groups of planar active and passive filaments in quiescent fluid, shear flows, and sedimenting due to gravity. By using novel discretisation techniques and exploitation of optimised MATLAB® built-in algorithms, the resulting numerical implementation enables rapid simulations on even modest readily-available computer hardware.

Expanding upon the EIF, the SPX method provides a model for simulating filaments and monoflagellate cells moving in three dimensions. Maintaining accuracy and nonlocal interactions in the fluid dynamics through the method of regularised stokeslets, the elasticity model is generalised to account for arbitrary bend and twist deformations. The presented tools and methodology are applied to simulate human spermatozoa locomoting through a rhythmic twist and bend motion. Results indicate that the

rate of axial rolling exhibited by nonplanar swimmers is reduced in the presence of a plane wall, with the rate of reduction dependent on the angle of approach towards the boundary and a dimensionless parameter characterising the relative ratio of twist drag to viscous drag in the system.

Acknowledgements

The work in this thesis was supported by an EPSRC Doctoral Training Award.

I would like to thank first my PhD supervisors, Prof. Dave Smith and Dr Meurig Gallagher, for their expertise, insight, and more than anything else, their patience. Further thanks go to Dr Tom Montenegro-Johnson and Dr Jackson Kirkman-Brown, who, alongside sharing their expansive knowledge, have both provided valuable career and personal advice throughout my years of postgraduate study. I feel extremely thankful to have been surrounded by such accomplished scientists over the past four years, who have all supported me continuously throughout this journey. Thank you.

Thanks to my parents, who never once doubted my ability even when I myself was unsure. To the countless friends I made the University of Birmingham, with particular love to Eoin, Norman, Euan, Arthur, Martin, Jennifer, and John. Last, and by no means least, my thanks to Cara, who has always been there to discuss mathematical intricacies, share in my successes, and help me through my tribulations. I do not think it an exaggeration to say this thesis would not exist without her friendship and support.

For Grandad.

List of publications

Efficient implementation of Elastohydrodynamics via Integral Operators. Atticus L. Hall-McNair, Thomas D. Montenegro-Johnson, Hermes Gadêlha, David J. Smith, and Meurig T. Gallagher. *Physical Review Fluids*, 4(11):113101, 2019. This work forms the basis of chaper 2, presented here in additional detail, incorporating previously supplemental material such as convergence properties in sections 2.4.1, 2.4.2 and 2.4.3.

Doing more with less: The flagellar end piece enhances the propulsive effectiveness of human spermatozoa. Cara V. Neal, Atticus L. Hall-McNair, Jackson Kirkman-Brown, David J. Smith, and Meurig T. Gallagher. *Physical Review Fluids*, 5(7):073101, 2020. The extensions this work provides over the aforementioned EIF is summarised in section 2.5, and the resulting numerical method is used in simulations in chapter 3.

Twist and bend beating of human sperm. Atticus L. Hall-McNair, Meurig T. Gallagher, David J. Smith. *Unpublished.* The contents of chapter 4, introducing the SPX method and applying it to simulate human sperm swimming through a combined active twist and bend beat, is intended for publication after the submission of this thesis.

Statement of collaborative work

Over the duration of my research, Cara Neal and myself have worked together closely, engaging in detailed discussions on our research and providing feedback and fostering ideas throughout. For clarity, the EIF formulation in chapter 2 for modelling elastic filaments was developed by Hall-McNair. Extension to include a rigid body head was joint work by both Neal and Hall-McNair. Neal developed the varying stiffness and passive end piece additions to the model. Consideration of different head morphologies (chapter 3) was original work by Hall-McNair. The SPX method discussed in chapter 4 was wholly developed by Hall-McNair.

Contents

List of Figures

List of Tables

Chapter 1

Introduction

1.1 Sperm structure and swimming behaviour

Flexible filaments are ubiquitous in the natural world. Consequently, an intimate understanding of the mechanics and physics governing their motion is of great interest in many microbiological problems. Countless numbers of organisms utilise mechanically-driven flagella to propel themselves through their fluid environment, be it monoflagellate spermatozoa swimming through the female reproductive tract, or multiflagellated *Escerichia coli* travelling with their erratic 'run-and-tumble' gait. Sheets of motile cilia lining the human trachea, bronchi, and bronchioles work together in synchronous wavy (or *metachronal*) motion to transport mucus and dirt away from the lungs, and in the uterus, generate macroscale cyclical flows that shape the early embryo (Montenegro-Johnson *et al.*, 2012). Elsewhere, long elastic polymer chains tangle and twist to form complex fluids such as cervical mucus, through which many microorganisms themselves must navigate. The intricate connections between geometry, elasticity, and fluid mechanics in these scenarios is known as *elastohydrodynamics*.

Properties crucial to a complete physical understanding of microscale filaments,

such as torque and drag profiles, are often difficult to determine due to a combination of highly nonlinear geometry and structural complexity. Experimental imaging and data collection can be a lengthy and expensive process, routinely requiring specialist equipment, compounding these technical hurdles.

There is no better example of the barriers to scientific progress these issues create than that of fertility research. Recent data suggests that within developed countries around the world, around 1 in 6 couples will suffer difficulty in conceiving due to factors of fertility. Around half of these cases involve a male factor (Human Fertilisation and Embryology Authority, 2014). Estimates for sperm count and motility, important metrics for fertility, require trained experts to manually categorise cells through a microscope by eye (World Health Organisation, 2010) – a costly and inefficient process, alleviated only by recent developments in CASA techniques and flagellar tracking (Gallagher *et al.*, 2018, 2019). Mathematical modelling and numerical simulations of swimming cells, especially in the vicinity of plane boundaries, could assist in the development of novel microchannel designs for use in sperm selection for Assistive Reproductive Techniques (ARTs), including IVF and ICSI. For example, understanding the trajectory of cells over and around microchannel features such as steps or pillars could lead to improved maze-like constructions, designed to isolate cells based on their motility or shape.

Sperm are quintessential examples of monoflagellate cells, with their ellipsoidal heads pushed through fluid by a single, long elastic flagellum. In the next section, we consider the structure of human sperm, before reviewing the underlying fluid mechanics and elasticity essential to understanding this rich problem in greater detail.

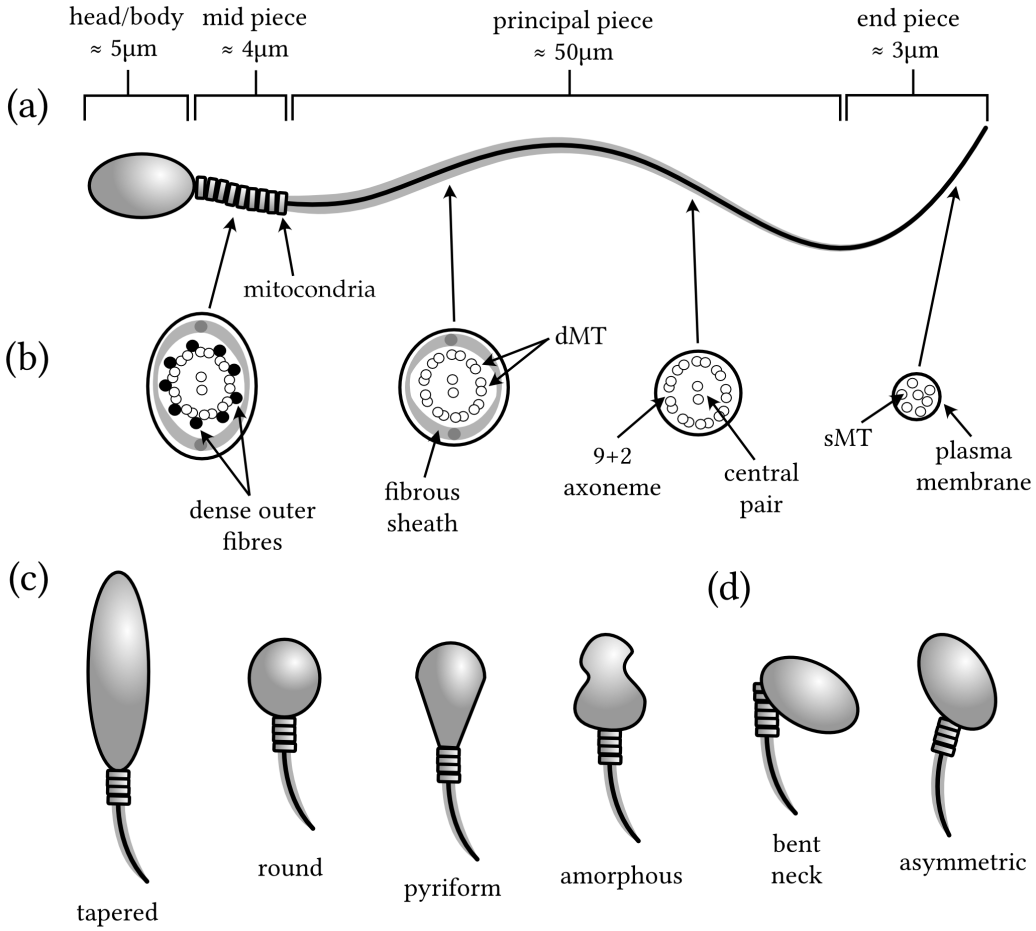

Figure 1.1: Overview of the macro- and microscale structures of human sperm. (a) Schematic of a typical idealised human spermatozoa. (b) Cross sections along the flagellum showing the internal ultrastructure, indicating singlet microtubules (sMT) and doublet microtubules (dMT). Sketches redrawn from Neal *et al.* (2020), deriving from figures in Zabeo *et al.* (2019). (c) and (d) Examples of defective head morphologies and head-neck junction abnormalities, redrawn from World Health Organisation (2010).

1.1.1 Ultrastructure of human sperm

Broadly, human sperm comprise four main elements, that are (i) the cell head (or body – we use these terms interchangeably), an approximately prolate ellipsoidal structure containing packaged DNA for delivery to the ovum; (ii) the midpiece, a stiff construct

a few microns in length containing ATP-generating mitochondria which fuel the cell; (iii) the flagellum, typically 40–60μm in length, generating periodic travelling waves in the bending moment along the flagellum length in order to propel the cell through viscous fluid, and (iv) the end piece, a region of reduced thickness a few microns in length where the ordered structure present elsewhere in the flagellum degrades Neal *et al.* (2020). While differing in size and relative length, the overall cellular structure and presence of these features is remarkably consistent across many mammalian species (Cummins & Woodall, 1985). A schematic of an idealised human sperm cell is given in figure 1.1a, redrawn from Zabeo *et al.* (2019).

Prototypical human sperm heads exhibit little variation in volume due to the approximately homogeneous DNA payload across cells (World Health Organisation, 2010). For cells with prescribed flagellar beat patterns, alterations to head geometry have been shown to be highly influential in cell swimming dynamics, particularly upon approaching and swimming along surfaces (Katz & Phillips, 1986; Woolley, 2003). Smith *et al.* (2009a) showed that cells with larger heads exhibited stabilised swimming trajectories, and studies by Gillies *et al.* (2009) indicate that cells with elongated heads swam faster over equal-volume alternatives; a result of decreased yawing rather than reduced viscous drag. Deviations from conventional head dimensions can have severe consequences for the viability of cells to fertilise, through both reduced swimming efficiency decreasing the likelihood of a successful sperm-egg rendezvous, and increased potential for DNA damage (World Health Organisation, 2010). For instance, spherical heads characteristic of the pathology *globozoospermia* are often symptomatic of sterility in human sperm cells (Dam *et al.*, 2007). Examples of abnormal body geometries, as well as examples of body-flagellum joint defects, are displayed in figures 1.1c and 1.1d, redrawn from World Health Organisation (2010).

Very early flagellar imaging by Ballowitz (1888) suggested that flagella contain an organised collection of approximately 9–11 microtubules spanning their length. This hypothesis was confirmed when, much later, studies using electron microscopy revealed the *axoneme*, an internal structure comprising 9 inextensible outer microtubule doublets, connected via passive linking elements (Manton & Clarke, 1952; Fawcett, 1954; Afzelius, 1959; Gibbons, 1981). Human sperm exhibit an additional *central pair* running along the core of the flagellum, motivating the so-called "9+2" axoneme. Asymmetry of the ultrastructure leads to preferential bending in the direction normal to the plane of the central pair (Lindemann, 2004; Gaffney *et al.*, 2011). The mid piece, reinforced by outer dense fibres and a mitochondrial sheath, in combination with the tapering fibrous sheath encasing the principal region, mean the effective stiffness of the entire flagellar structure varies along its length. Cross-sectional sketches of the flagellum ultrastructure, redrawn from Neal *et al.* (2020), are displayed in figure 1.1b.

The presence of a distal flagellum region with diminished structure was first hypothesised by Omoto & Brokaw (1982). Recent experimental findings indeed indicate that the end piece comprises an unorganised collection of single microtubules only (Zabeo *et al.*, 2019). Without the axonemal structure common to the rest of the flagellum, Neal *et al.* (2020) hypothesise that this region is incapable of active bending, with important consequences on the propulsive speed and efficiency of the swimming cell.

1.1.2 Modelling flagellar actuation

The fundamental interaction between fluid and the bending flagellum that results in cell propulsion was first derived by Gray & Hancock (1955). Their *resistive force theory* (RFT) postulates that the hydrodynamic drag of a *slender body* (i.e. a body whereby the

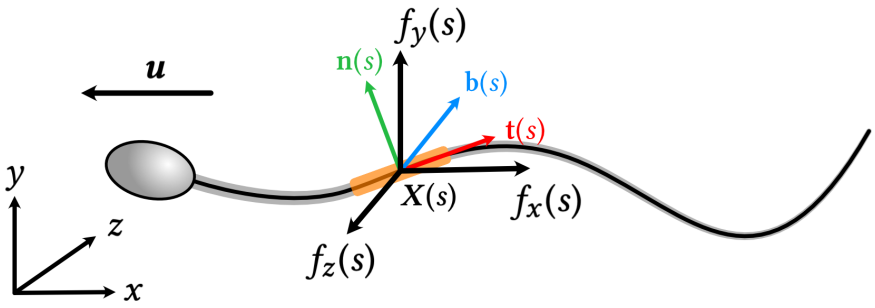

Figure 1.2: A linear section of flagellum, indicated in orange, is orientated in Cartesian space according to the unit vectors **t**, **n**, and **b**, the tangent, normal and binormal respectively. With resistive force theory, the force components $\boldsymbol{f}$ can be written in terms of the resultant velocity $\boldsymbol{u}$, proportional to coefficients $c_\parallel$, $c_\perp$.

length L is much larger than its radius a) can be decomposed into contributions acting normal- and tangential to the body, so that

$$\boldsymbol{f} = c_\parallel(\boldsymbol{u}\cdot\mathbf{t})\mathbf{t} + c_\perp(\boldsymbol{u}\cdot\mathbf{n})\mathbf{n} + c_\perp(\boldsymbol{u}\cdot\mathbf{b})\mathbf{b}, \tag{1.1}$$

where $\boldsymbol{f}$ is the force per unit length the body exerts on the fluid, $\boldsymbol{u}$ is the body velocity, and **t**, **n**, and **b** are unit vectors tangential, normal and binormal to the body respectively. The dependent variable of each quantity (omitted for clarity) is the material arclength, varying along the flagellum length $0 \leqslant s \leqslant L$. A schematic is provided in figure 1.2. The coefficients $c_\perp$ and $c_\parallel$ are *resistance coefficients*, derived from analytic approximations of the full slender body equations (to be discussed in section 1.2). Gray & Hancock (1955) determined the tangential coefficient and the ratio of coefficients suitable for a swimming slender body as

$$c_\parallel = \frac{2\pi\mu}{\ln(2\lambda/a) - 1/2}, \qquad \frac{c_\perp}{c_\parallel} \approx 2, \tag{1.2}$$

where λ is the wavelength of the flagellar beat and a is the filament radius. The values of these coefficients were later improved by Lighthill (1976), who derived

$$c_{\parallel} = \frac{2\pi\mu}{\ln(2q/a)}, \qquad c_{\perp} = \frac{4\pi\mu}{1/2 + \ln(2q/a)}, \tag{1.3}$$

where $q = 0.09\Lambda$, with Λ the beat wavelength measured along the flagellum centre-line. Importantly for the discussions in this thesis, resistive force theory neglects the long-range hydrodynamic interactions between the body and itself, other bodies, and boundaries. Nonetheless, following a suitable adjustment to the resistance coefficient ratio $c_{\perp}/c_{\parallel}$, RFT has been shown repeatedly to provide accurate results for isolated headless cells in the absence of boundary walls (Johnson & Brokaw, 1979; Dresdner & Katz, 1981; Friedrich *et al.*, 2010), and corrected theories can provide accurate results for cells swimming above walls, provided the plane of beating is parallel to the surface (Katz *et al.*, 1975; Walker *et al.*, 2019). By adding to the local approximation (equation (1.1)) nonlocal integral terms, Gueron & Liron (1992) developed the so-called *Lighthill-Gueron-Liron (LGL) theory*, with resistance coefficients derived from a modification of the Lighthill coefficients given as

$$c_{\parallel} = \frac{8\pi\mu}{-2 + 4\ln(2q/a)}, \qquad c_{\perp} = \frac{8\pi\mu}{1 + 2\ln(2q/a)}. \tag{1.4}$$

LGL theory has been used to model elastica (Gueron & Levit-Gurevich, 2001a), multiciliary interactions (Gueron & Liron, 1992; Gueron & Levit-Gurevich, 2001b), and human sperm near boundaries (Montenegro-Johnson *et al.*, 2015). Detailed reviews of other hydrodynamic models not considered in this thesis for sperm and cilia are given in Fauci & Dillon (2006) and Simons & Olson (2018).

Generally, RFT is inaccurate for cells with large cell bodies (Johnson & Brokaw, 1979), and when nonlinear flagellum geometry means that self-interaction effects become large, such as for hyperactivated sperm swimming in highly viscous or non-Newtonian fluids (Smith *et al.*, 2009b). Despite these shortcomings, resistive force theory remains a popular choice of hydrodynamic interaction model, owing to its conceptual simplicity and ease of implementation. In such approaches, the relationship between viscosity and elasticity is accounted for through the *sperm number*, denoted Sp, a dimensionless parameter arising from the underlying differential equations, that is dependant on the choice of resistance coefficient. The sperm number characterises progressively more effectively elastic slender bodies as its value increases.

An early study by Machin (1958) established that sperm, cilia, and other eukaryotes generate bending throughout the length of their flagellum, as opposed to arising from a single biomechanical motor, such as in bacteria. Subsequent experimental observations of cilia revealed that travelling waves are generated through a combination of microtubule sliding, elasticity and cross-linking within the axoneme (Satir, 1965, 1968). Crucially, the microtubules are inextensible, in that they do not extend or contract, so that motion arises from the relative motion of one filament over another. Coined *sliding filament theory*, this model has formed the basis of many mathematical studies in the intervening decades. Describing the elastic flagellum using classical Euler–Bernoulli theory, Brokaw (1970) investigated the relations between the bending moment for a headless swimming cell, observing that the work done by restorative elastic forces is not constant along the arclength – a potential consequence of the distributive effects arising from a sliding filament mechanism. A schematic of the internal sliding filament mechanism, recreated from Camalet & Jülicher (2000), is provided in figure 1.3.

Since the shearing force is generated internally within the axoneme, its form de-

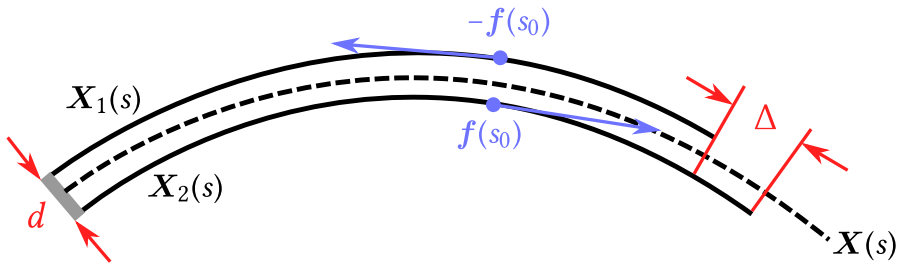

Figure 1.3: Illustration of the sliding filament model of flagellar actuation, as described in and recreated from Camalet & Jülicher (2000). An active shear force $f(s_0)$ with $s_0 \in [0, L]$ acts in opposite directions on two filaments X_1 and X_2 lying above and below the filament centreline X at a fixed distance d, producing the centreline displacement Δ resulting in the generation of a travelling wave.

pends on the biological mechanisms that control the rates of detachment and reattachment of dynein molecular motors connecting microtubules comprising the flagellar structure. However, the control mechanism relating the sliding filament apparatus and the dynein switching rates is not yet fully understood. In the following, we briefly cover three popular hypotheses.

In a formidable body of work spanning nearly five decades, Brokaw developed the so-called *curvature control* hypothesis, whereby the size of the shear force in the flagellum produced by the active sliding filament mechanism is informed by the local curvature of the flagellum, that is

$$f(s, t) \propto \kappa(s, t - t_0), \tag{1.5}$$

where $f(s, t)$ is the actuating force, $\kappa(s, t)$ is the local curvature, and the value of t_0 describes the delay in switching on the dynein arms. Equation (1.5) describes motion under the assumption that instantaneous changes in flagellum curvature, caused by the attachment and detachment of dynein arms along the central pair, initiates bending

forces along the length of the flagellum. This model naturally is specific to the very-low Reynolds number fluid environment typical to the slender-body organisms considered in this thesis.

Modelling the central pair as two filaments connected through internal links along their arclength, Brokaw (1971) showed that the feedback loop arising from the curvature control mechanism is indeed able to generate propulsive travelling waves propagating along the flagellar arclength. Subsequent simulation studies (Brokaw, 1972, 1984, 1985, 1991, 1994, 1999, 2001, 2002, 2009) progressively highlighted the increasing potential of numerical approaches in delivering important insight into the internal dynamics of sperm flagella.

The curvature control model has been adopted in multitudinous works since its initial proposal by Brokaw. The works of Hines & Blum (1978, 1983) expanded upon the simple travelling wave model used in Brokaw (1971, 1972), coupling equations for planar elasticity with Gray & Hancock (1955) RFT to account for local hydrodynamic interactions. In the latter paper, Hines & Blum (1983) generalise to consider an elastic filament bending and twisting in three dimensions, concluding that the sliding filament model cannot produce twist without additional external forces causing bending out of the plane of alignment of the central pair. Recent work by Olson & Leiderman (2015) simulates sperm swimming in a viscous Brinkman fluid, with cells actuated through a preferred curvature condition on the flagellar waveform. Through simulations in conjunction with experiments, Sartori *et al.* (2016b) determined that the curvature control mechanism best approximates the bending dynamics of *Chlamydomonas* flagella. Other investigations into the intricate mechanical mechanisms within flagella and their effects on beat propagation indicate the complexities of bend generation at the body-flagellum join in sea urchin sperm (Brokaw, 1991), and the effects of dynein

arm removal on waveform (Brokaw, 1999). Other approaches modelling the discrete dynamics of individual dynein arms have proven effective in simulating cilia and sperm in fluids of varying viscosity (Dillon & Fauci, 2000; Dillon *et al.*, 2003, 2007).

An alternative *sliding velocity control* hypothesis, proposed in Camalet *et al.* (1999), forms the basis of a number of studies investigating sperm flagellum dynamics. Here, the rate of dynein detachment is proportional to the load on the arms. Increases in the velocity of the sliding filament mechanism decrease load, yielding a decrease in the dynein detachment rate, and leading to an increase in the shear force generated (Riedel-Kruse *et al.*, 2007). Deformations to the filament are resisted by the inherent elastic bending properties of the flagellum, producing a positive feedback loop and generating waveforms capable of propulsion (Camalet *et al.*, 1999). The approach was later generalised to other internally driven filaments (Camalet & Jülicher, 2000), and used to model symmetric and asymmetric motor-filament pairs, finding that such systems can undergo a Hopf bifurcation for a critical choice of control parameter.

A third hypothesis relating the sliding filament model to dynein detachment rates is the *geometric clutch* model, proposed initially in Lindemann (1994a) and developed extensively over the following fifteen years (Lindemann, 1994b, 1996, 2002, 2004, 2009). In this approach, dynein attachment dynamics are governed by changes in spacing between doublet pairs. The relative sliding of neighbouring doublets causes the connective nexin links to stretch, generating an elastic tensile force causing the spacing between the doublets to decrease. The clutch hypothesis itself then postulates that increasing proximity promotes dynein switching, increasing the shear force and actively bending the flagellum. As in the other hypotheses, motion is resisted by the internal elastic properties of the flagellum, leading to a positive feedback loop which forms the basis of the wave generation process for cell propulsion. A detailed analysis

of the stable and unstable periodic modes of flagella motion arising from each of the aforementioned actuation hypotheses is given in Bayly & Wilson (2015).

Other studies have sought to increase understanding by considering additional aspects and components of the flagellar model, and in particular through the interplay between elasticity, geometry, and the sliding filament model. Instead of employing a local bend control hypothesis, Gadêlha *et al.* (2010) prescribes the internal actuating shear force as a travelling wave of the form

$$f(s,t) = f_0 \cos(ks - \omega t), \tag{1.6}$$

where f_0 is the shear amplitude, k is the wave number, and ω is the beat angular frequency. Departing from the hitherto commonly used geometrically linear beam theory[1], and building upon position formulation methods developed by Tornberg & Shelley (2004) for passive fibres, Gadêlha *et al.* (2010) note the importance of nonlinear elastodynamic modelling on swimming cell beat pattern and trajectory. Describing the cell flagellum as two cross-linked filaments, Gadêlha *et al.* (2013), and more recently Coy & Gadêlha (2017), consider the *counterbend phenomenon*, whereby curvature in one region of the fibre is countermatched elsewhere. Notably, the authors find that counterbending dynamics induce a bimodal length dependent material response departing from the classical Euler-Bernoulli theory of elasticity, with potential implications on the prevailing understanding of flagellar wave propagation. Maxian *et al.* (2021) examine a similar problem, extended to include nonlocal hydrodynamic interactions using slender body theory. Recent developments by Olson and coauthors have sought to examine the effects of calcium concentrations on flagellar hyperactuation (Olson *et al.*,

[1]We refer here to models in terms of centreline position, noting the geometrically nonlinear theories in terms of tangent angle developed in the late 1970s by Hines & Blum (1978).

2011; Carichino & Olson, 2019). By coupling a preferred curvature elastohydrodynamic model with a calcium concentration response, planar swimming speed and trajectory nonlinearity are found to both increase when accounting for the presence calcium.

1.1.3 Dynamics of sperm at surfaces

In their anticipated physiological environment, sperm must swim not only through a variety of viscous fluids, but also navigate varied and complex geometries comprising the female reproductive system in search of the ovum. In a lab environment, advances in the fabrication of intricate microchannel devices have promoted novel cell selection techniques through exploiting the behaviour of sperm as they swim near and alongside flat and curved boundaries. To this end, understanding the dynamics of sperm near surfaces is paramount in designing microchannel designs for use in clinical ARTs.

Historically, insights into the dynamics of sperm cells close to surfaces have been gleaned through experimentation, or, more recently, through simulation approaches with prescribed flagellar waveforms. Regarding the latter approach, the focus in these models has been largely directed towards hydrodynamic modelling of the cell, the boundary, and their interactions through the fluid environment, neglecting elasticity by necessity and/or in the interests of simplicity.

Various studies have sought to understand the hydrodynamic 'trapping' effect experienced by some cells as they approach rigid surfaces. Experimental studies by Woolley (2003) investigated single-cell dynamics upon approaching a plane wall, considering sperm driven by planar beats as well as helical beats. Cells exhibiting a helical beat tend to roll and spin about their long axis, producing a nonlinear trajectory that prevents hydrodynamic capture and adherence to the surface. Cells with hyperacti-

vated flagellar beats more readily detach than those with symmetric waveforms, shown through simulation studies in both 2D (Simons *et al.*, 2014) and 3D (Simons *et al.*, 2015). Whether through suppression of a global moment (that reduces cell rolling) or increased viscosity, waveforms of cells approaching surfaces have been shown to adopt approximately planar beats (Woolley, 2003; Nosrati *et al.*, 2015). If the plane of beating is perpendicular to the surface, hydrodynamic interactions between the wall and flagellum can have a marked effect on cell trajectory (Montenegro-Johnson *et al.*, 2015; Walker *et al.*, 2019). The angle of approach and geometry of the cell head have also been shown to determine how a cell is hydrodynamically trapped near a surface in prescribed waveform simulation studies (Fauci & McDonald, 1995; Smith *et al.*, 2009a). Additionally, cells with small heads but long flagella are inclined to rotate as they approach a wall, increasing their angle of approach (Spagnolie & Lauga, 2012).

A typical ejaculate can contain many millions of spermatozoa, jostling together as they collectively traverse the reproductive tract. Rothschild (1963) was the first to quantitatively assess gathering behaviour of sperm at a fluid-solid boundary, noting the accumulation of bull sperm cells upon each surface of a microchamber formed between two glass slides. Groups of cells also have a tendency to align with one another, aiding in rheotaxis through synchronisation of their flagellar beats. This finding was first theorised following experiments by Walton (1952), and since verified in a variety of computational models (Yang *et al.*, 2008; Olson & Fauci, 2015) as resulting from hydrodynamic interactions within neighbourhoods of proximal cells. For cells in a shear flow, accumulation at low-shear regions near a no-slip boundary have been theorised to promote collective cell motion (Ishimoto & Gaffney, 2015). Indeed, fluid flows within the reproductive tract have been shown to be important in the successful navigation of cells in both mice and humans (Miki & Clapham, 2013; Kantsler *et al.*, 2014).

With increased access to and availability of powerful computational equipment, researchers have been able to design and solve mathematical models for cells near boundaries of ever increasing complexity. Crucially, elastohydrodynamic models such as those of Gueron & Levit-Gurevich (2001b); Tornberg & Shelley (2004); Gadêlha *et al.* (2010) and others (reviewed in detailed in section 1.4) allow for increased physical accuracy in simulations by accounting for the complex interplay between viscous fluid drag and elastic deformations of the cell flagellum. Considering a scenario where the plane of beating is perpendicular to the surface, Montenegro-Johnson *et al.* (2015) illustrated the scattering behaviour of cells as they pass over a microchannel backstep feature, with the angle of deflection related to the value of the sperm number. In chapter 4 of this thesis, we expand upon the nonlinear centreline model proposed by Montenegro-Johnson *et al.* by allowing for genuinely nonplanar flagellum geometry arising from both bending and twisting elastic deformations, and nonlocal fluid interactions. In particular, in section 4.4.2, we build on the aforementioned studies by examining the dynamics of cells swimming with a nonplanar beat arising from active bending and twisting as they approach an infinite plane wall.

1.2 Inertialess hydrodynamics: fundamental solutions and methods

In this section, we discuss the fundamental aspects of the hydrodynamic modelling underpinning this thesis. Section 1.11a introduces the Stokes flow equations, forming the basis of the fluid mechanical modelling considered throughout. The Stokes flow equations and their fundamental solutions, in particular the *stokeslet*, are discussed in sections 1.2.1 and 1.2.2 respectively. In sections 1.2.3 and 1.2.4, we derive the boundary integral formulation for Stokes flow. Alterations to the solutions when considering flow near a wall through the method of images are detailed in section 1.2.5. In sections 1.2.6–1.2.9, we consider regularised forms of the fundamental solutions, discussing the *regularised stokeslet* and *regularised blakelet*, which enable efficient numerical methods for solving Stokes flow problems. In this thesis, we consider only studies and models within Newtonian fluids. Comprehensive reviews of non-Newtonian swimming are given in works by Morozov & van Saarloos (2007); Gaffney *et al.* (2011); Elfring & Lauga (2015); Goyal (2016).

1.2.1 Stokes flow and the Reynolds number

The Navier-Stokes equations for an incompressible fluid are

$$\rho\left(\boldsymbol{u}^*_{t^*} + (\boldsymbol{u}^* \cdot \nabla^*)\boldsymbol{u}^*\right) = -\nabla^* p^* + \mu\nabla^{*2}\boldsymbol{u}^* + \rho\boldsymbol{F}^*, \tag{1.7a}$$

$$\nabla \cdot \boldsymbol{u}^* = 0, \tag{1.7b}$$

where $\boldsymbol{u}^* := \boldsymbol{u}^*(\mathbf{x}^*, t^*)$ is the fluid velocity, $p^* := p^*(\mathbf{x}^*, t^*)$ is the pressure, t^* is time, and $\boldsymbol{F}^* := \boldsymbol{F}^*(\mathbf{x}^*, t^*)$ is a force acting on the fluid. Here, and in what follows, asterisks

denote dimensional variables. The first argument of velocity, pressure and force ($\mathbf{x}^*$) is a material point within the domain of the fluid. The dependence of variables on space and time is suppressed for clarity, but assumed throughout. The parameters μ and ρ are the fluid dynamic viscosity and density respectively, assumed here to be constant throughout the fluid. Scaling variables as,

$$\boldsymbol{u} = U\boldsymbol{u}^*, \quad \boldsymbol{F} = G\boldsymbol{F}^*, \quad p = (G/L^3)p^*, \tag{1.8}$$

where L is a characteristic length scale, U is the local flow velocity, and G is the local force scaling. Here and throughout, we refer by *local* to the region of fluid close to the point under consideration. Conversely, far-off regions of fluid are described as being *nonlocal* to the point. With these scalings, we recover the dimensionless Navier-Stokes equations for an incompressible fluid as

$$\mathrm{Re}\big(\boldsymbol{u}_t + (\boldsymbol{u}\cdot\nabla)\boldsymbol{u}\big) = -\nabla p + \nabla^2\boldsymbol{u} + \frac{\mathrm{Re}}{\mathrm{Fr}^2}\boldsymbol{F}, \tag{1.9a}$$

$$\nabla\cdot\boldsymbol{u} = 0, \tag{1.9b}$$

where the parameter groups

$$\mathrm{Re} = \frac{\rho LU}{\mu}, \qquad \mathrm{Fr} = \frac{U}{\sqrt{GL}}, \tag{1.10}$$

are the *Reynolds number* and *Froude number* respectively, which characterise the fluid properties. The Reynolds number describes the ratio of inertial forces to viscous forces in the system, and the Froude number defines the ratio of inertial forces to other body forces. Typical values of the Reynolds number for various self-propelled organisms

	Re
A large whale swimming at $10\,\mathrm{m\,s^{-1}}$	3×10^{8}
A tuna swimming at $10\,\mathrm{m\,s^{-1}}$	3×10^{7}
A duck flying at $20\,\mathrm{m\,s^{-1}}$	3×10^{5}
Flapping wings of a small insect	30
Invertebrate larvae, 0.3mm long moving at $1\,\mathrm{mm\,s^{-1}}$	3×10^{-1}
A sea urchin sperm swimming at $0.2\,\mathrm{mm\,s^{-1}}$	3×10^{-2}
A human sperm swimming in saline at $0.2\,\mathrm{mm\,s^{-1}}$	1×10^{-2}
A bacterium swimming at $0.01\,\mathrm{mm\,s^{-1}}$	1×10^{-5}

Table 1.1: Values of the Reynolds number characteristic to some example biological systems. Recreated from Vogel (2020).

are given in table 1.1. When the fluid viscosity is very large, inertial effects are negligible, yielding $\mathrm{Re} \ll 1$. By choosing the force scaling as $G = \mu U/(\rho L^2)$, we obtain the dimensionless *Stokes flow* equations

$$-\nabla p + \nabla^2 \boldsymbol{u} + \boldsymbol{F} = \boldsymbol{0}, \tag{1.11a}$$

$$\nabla \cdot \boldsymbol{u} = 0, \tag{1.11b}$$

where $p := p(\mathbf{x}, t)$, $\boldsymbol{u} := \boldsymbol{u}(\mathbf{x}, t)$, and $\boldsymbol{F} := \boldsymbol{F}(\mathbf{x}, t)$ are the dimensionless fluid pressure, fluid velocity and force acting at a material point $\mathbf{x} \in \mathbb{R}^3$. The Stokes equations (1.11a,1.11b) form the basis of the hydrodynamical regime considered in this thesis.

1.2.2 Fundamental solutions to the Stokes flow equations

An important property of the Stokes flow equations is their linearity. That is, if $(\boldsymbol{u}_1, p_1)$ and $(\boldsymbol{u}_2, p_2)$ are both solutions, then

$$\mu\nabla^2(\boldsymbol{u}_1 + \boldsymbol{u}_2) - \nabla(p_1 + p_2) + \boldsymbol{F} = (\mu\nabla^2\boldsymbol{u}_1 - \nabla p_1) + (\mu\nabla^2\boldsymbol{u}_2 - \nabla p_2) + \boldsymbol{F} = \boldsymbol{0} \tag{1.12a}$$

$$\nabla \cdot (\boldsymbol{u}_1 + \boldsymbol{u}_2) = \nabla \cdot \boldsymbol{u}_1 + \nabla \cdot \boldsymbol{u}_2 = 0 \tag{1.12b}$$

and thus $(\boldsymbol{u}_1 + \boldsymbol{u}_2, p_1 + p_2)$ satisfied the Stokes equations; indeed any finite sum, line or surface integral of solutions is also a solution. Exploiting linearity enables complex flows to be considered by combining solutions of the Stokes flow equations (1.11a,1.11b).

We continue by outlining the derivation for key fundamental solutions to the stokes flow equations given in (1.11a,1.11b). We consider the fluid flow at a material point $\mathbf{x} = (x_1, x_2, x_3)$, with $\mathbf{x} \in \mathbb{R}^3$ driven by a force per unit volume $\boldsymbol{F}$ acting at an arbitrary point $\mathbf{y} = (y_1, y_2, y_3)$ also in the domain. Letting be $\boldsymbol{g}$ be a finite but infinitely-constrained force, the driving force can be written as

$$\boldsymbol{F} = \boldsymbol{g}\delta(\mathbf{x} - \mathbf{y}), \tag{1.13}$$

so that the (three dimensional) Dirac-δ has dimensions of inverse volume. Taking the divergence of equation (1.11a) and using the incompressibility condition (1.11b) allows an equation for the fluid pressure to be derived as

$$\nabla^2 p = \nabla^2\big(\boldsymbol{g} \cdot \nabla G(\mathbf{x}, \mathbf{y})\big), \tag{1.14a}$$

$$\implies p = \boldsymbol{g} \cdot \nabla G(\mathbf{x}, \mathbf{y}) = \frac{1}{4\pi}\left(\boldsymbol{g} \cdot \frac{\boldsymbol{r}}{r^3}\right). \tag{1.14b}$$

The Green's function is $G(\mathbf{x}, \mathbf{y}) = -1/(4\pi r)$, where $\boldsymbol{r} = \mathbf{x} - \mathbf{y}$ and $r = \sqrt{r_i r_i}$, with index summation notation used to simplify the product. By this definition, $G(\mathbf{x}, \mathbf{y})$ is singular at $\mathbf{x} = \mathbf{y}$. Combining the specific expressions for pressure (1.14b) and force (1.13) yields component solutions as

$$u_i(\mathbf{x}) = \frac{1}{8\pi} S_{ij}(\mathbf{x}, \mathbf{y}) g_j(\mathbf{y}), \qquad p(\mathbf{x}) = \frac{1}{8\pi} P_i(\mathbf{x}, \mathbf{y}) g_j(\mathbf{y}). \tag{1.15}$$

The Green's function G becomes S, and is specified as the *stokeslet*, defined

$$S_{ij}(\mathbf{x}, \mathbf{y}) = \frac{\delta_{ij}}{r} + \frac{r_i r_j}{r^3}, \qquad P_i(\mathbf{x}, \mathbf{y}) = \frac{2 r_i}{r^3}, \tag{1.16}$$

alongside the pressure tensor P_i. Crucially, like the Green's function before it, the stokeslet is singular, diverging like $1/r$ as $r \longrightarrow 0$. If the forces are concentrated on a two dimensional surface in $\mathbb{R}^3$, the stokeslet solution in equation (1.15) is integrable and the singularity may be avoided, with the flow bounded on the surfaces. Conversely, if forces are concentrated along curves in $\mathbb{R}^3$, the solution is singular, a result of great importance in the modelling of slender bodies, which will be discussed more fully in section 1.2.6. The stress field associated with the flow is

$$\sigma_{ik}(\mathbf{x}) = \frac{1}{8\pi} T_{ijk}(\mathbf{x}, \mathbf{y}) g_j(\mathbf{y}), \tag{1.17}$$

where the associated stress tensor is defined

$$T_{ijk}(\mathbf{x}, \mathbf{y}) = -\delta_{ik} P_j(\mathbf{x}, \mathbf{y}) + \frac{\partial S_{ij}(\mathbf{x}, \mathbf{y})}{\partial x_k} + \frac{\partial S_{jk}}{\partial x_i}(\mathbf{x}, \mathbf{y}) = -6 \frac{r_i r_j r_k}{r^5}, \tag{1.18}$$

with simplifications possible through substituting in the expressions in equation (1.16).

1.2.3 Boundary integral formulation

The microbiological scenarios considered within this thesis consist wholly of moving surfaces within Stokesian fluids. To this end, we formulate the Stokes flow problem to consider the flow around a dynamic boundary, following the derivation provided by Pozrikidis (1992).

We begin by recalling the Lorentz reciprocal identity, which states that for any two nonsingular flows with velocities $\boldsymbol{u}$, $\boldsymbol{u}'$ with corresponding stress tensors $\boldsymbol{\sigma}$, $\boldsymbol{\sigma}'$, evaluated at a material point $\mathbf{x} = (x_1, x_2, x_3)$, we have that

$$\frac{\partial}{\partial x_k}\left(u_i'\sigma_{ik} - u_i\sigma_{ik}'\right) = 0. \tag{1.19}$$

If the flow with velocity $\boldsymbol{u}'$ is arising from a point force with vector strength $\boldsymbol{g}$ located at $\mathbf{x}_0$, we can write

$$u_i'(\mathbf{x}) = \frac{1}{8\pi}G_{ij}(\mathbf{x}, \mathbf{x}_0)g_j(\mathbf{x}_0), \qquad \sigma_{ik}' = \frac{1}{8\pi}T_{ijk}(\mathbf{x}, \mathbf{x}_0)g_j(\mathbf{x}_0), \tag{1.20}$$

where $\boldsymbol{G}(\mathbf{x}, \mathbf{x}_0)$ is the Green's function (or fundamental solution) for the flow and $\boldsymbol{T}$ the corresponding stress tensor. The reciprocal identity thus yields, after dividing out the force strength $\boldsymbol{g}$,

$$\frac{\partial}{\partial x_k}\left(G_{ij}(\mathbf{x}, \mathbf{x}_0)\sigma_{ik} - u_i(\mathbf{x})T_{ijk}(\mathbf{x}, \mathbf{x}_0)\right) = 0. \tag{1.21}$$

We consider a control volume V bounded by the closed surface ∂V comprising fluid surfaces, fluid interfaces, or solid boundaries. By choosing $\mathbf{x}_0 \notin V$, the argument of the derivative in equation (1.21) is nonsingular. Thus, integrating over V and applying the

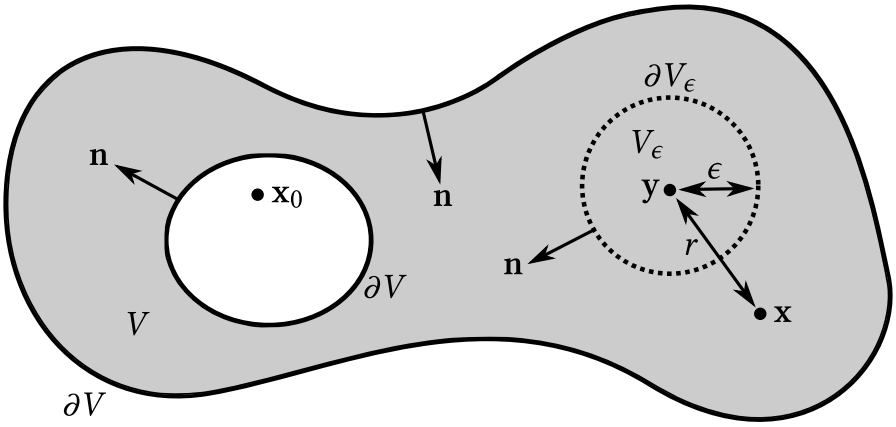

Figure 1.4: Schematic of the boundary integral problem derivation, indicating the control volume V and its boundary ∂V, and the reduced volume V_ϵ with boundary ∂V_ϵ. The unit normals $\mathbf{n}$ point into V.

divergence theorem to obtain an expression over the boundary ∂V yields

$$\iiint_V \frac{\partial}{\partial x_k}\Big(G_{ij}(\mathbf{x},\mathbf{x}_0)\sigma_{ik} - u_i(\mathbf{x})T_{ijk}(\mathbf{x},\mathbf{x}_0)\Big)\,dV_{\mathbf{x}} = \iint_{\partial V}\Big(G_{ij}(\mathbf{x},\mathbf{x}_0)\sigma_{ik} - u_i(\mathbf{x})T_{ijk}(\mathbf{x},\mathbf{x}_0)\Big)n_k(\mathbf{x})\,dS_{\mathbf{x}} = 0. \quad (1.22)$$

where $\mathbf{n} = (n_1, n_2, n_3)$ is the unit normal vector pointing into the control volume. A schematic of the problem is provided in figure 1.4.

Selecting a new source point $\mathbf{y} \in V$, we define by V_ϵ the spherical volume of radius ϵ centred about $\mathbf{y}$, enclosed by the surface ∂V_ϵ. The argument of the derivative in equation (1.21) remains regular in the reduced domain $V - V_\epsilon$; integrating over this domain and applying the divergence theorem we obtain

$$\iint_{\partial V \cup \partial V_\epsilon}\Big(G_{ij}(\mathbf{x},\mathbf{y})\sigma_{ik}(\mathbf{x}) - u_i(\mathbf{x})T_{ijk}(\mathbf{x},\mathbf{y})\Big)n_k(\mathbf{x})\,dS_{\mathbf{x}} = 0. \quad (1.23)$$

On the surface ∂V_ϵ, we have that $\mathbf{n} = (\mathbf{x} - \mathbf{y})/\epsilon = \boldsymbol{r}/\epsilon$ and $dS = \epsilon^2 d\Omega$, where $d\Omega$ is

the differential solid angle. The scaling by ϵ in the construction of $\mathbf{n}$ facilitates later simplifications in the integral arguments. Substituting these expressions into equation (1.23), splitting the integral over the union, and rearranging yields

$$\iint_{\partial V} \left(G_{ij}(\mathbf{x},\mathbf{y}')\sigma_{ik} - u_i(\mathbf{x})T_{ijk}(\mathbf{x},\mathbf{y}')\right) n_k(\mathbf{x})\, dS_{\mathbf{x}} = -\iint_{\partial V_\epsilon} \left[\left(\delta_{ij} + \frac{r_i r_j}{\epsilon^2}\right)\sigma_{ik}(\mathbf{x}) + 6u_i(\mathbf{x})\frac{r_i r_j r_k}{\epsilon^4}\right] r_k\, d\Omega. \quad (1.24)$$

As $\epsilon \longrightarrow 0$, the Green's function $\boldsymbol{G}$ and stress tensor $\boldsymbol{T}$ become through definition the stokeslet and associated stress tensor defined in equations (1.16) and (1.18) respectively. Additionally, since $\mathbf{x}$ decreases linearly with respect to the sphere radius ϵ, the contribution from the stress terms in the right hand side of equation (1.24) decay $\mathcal{O}(\epsilon)$. Similarly, the contribution from the velocity terms decay $\mathcal{O}(1)$. Thus, in the limit as $\epsilon \longrightarrow 0$, we have that

$$\iint_{\partial V} \left(S_{ij}(\mathbf{x},\mathbf{y})\sigma_{ik}(\mathbf{x}) - u_i(\mathbf{x})T_{ijk}(\mathbf{x},\mathbf{y})\right) n_k(\mathbf{x})\, dS_{\mathbf{x}} \approx -6u_i(\mathbf{y}) \iint_{\partial V_\epsilon} \frac{r_i r_j r_k^2}{\epsilon^4}\, d\Omega = -8\pi u_j(\mathbf{y}), \quad (1.25)$$

with the integral on the right hand side being analytically integrated following an application of the divergence theorem. Rearranging, and letting $f_i = -\sigma_{ik} n_k$ be the force exerted by the surface ∂V onto the fluid, we arrive at the boundary integral equation

$$u_j(\mathbf{y}) = \frac{1}{8\pi} \iint_{\partial V} S_{ij}(\mathbf{x},\mathbf{y}) f_i(\mathbf{x})\, dS_{\mathbf{x}} + \frac{1}{8\pi} \iint_{\partial V} u_i(\mathbf{x}) T_{ijk}(\mathbf{x},\mathbf{y}) n_k(\mathbf{x})\, dS_{\mathbf{x}}, \quad (1.26)$$

valid for $\mathbf{y} \notin \partial V$. If $\mathbf{y} \in \partial V$, the left hand side of equation (1.26) is replaced by $(1/2)u_j(\mathbf{y})$,

provided the boundary is smooth. In particular, we can write

$$S_{ij}(\mathbf{x}, \mathbf{y}) = S_{ji}(\mathbf{y}, \mathbf{x}) = S_{ji}(\mathbf{x}, \mathbf{y}), \tag{1.27}$$

with the first equation as a consequence of symmetric property of Green's functions, and the second equality due to the choice of an infinite fluid domain. The contribution to the velocity from the stokeslet integral term can be thus written as

$$u_i^S(\mathbf{x}) = \frac{1}{8\pi} \iint_{\partial V} S_{ij}(\mathbf{x}, \mathbf{y}) f_j(\mathbf{y}) \, dS_{\mathrm{y}}, \tag{1.28}$$

a form which will be used later on. The contribution to the velocity from the stress term is

$$u_i^D(\mathbf{x}) = \frac{1}{8\pi} \iint_{\partial V} u_j(\mathbf{y}) T_{jik}(\mathbf{y}, \mathbf{x}) n_k(\mathbf{y}) \, dS_{\mathrm{y}}. \tag{1.29}$$

In what follows, we refer to the stokeslet integral contribution to the velocity in the boundary integral equation (1.26) as the *single-layer potential* (SLP, equation (1.28)) and the stress tensor contribution as the *double-layer potential* (DLP, equation (1.29)), terminology analogous to their use in electric potential theory. Similarly, the velocity in (1.28) is the *SLP velocity*, and (1.29) is the *DLP velocity*.

Further simplifications to the boundary integral equation (1.26) are afforded by considering only problems involving an infinite, or partially-infinite fluid domain, such as cells swimming over an infinite plane boundary. In these problems, we choose the control volume with boundary ∂D, and a large spherical volume extending to infinity with boundary ∂D_∞. If the very-far field flow is quiescent i.e. $\boldsymbol{u}_\infty = \mathbf{0}$ (as is the case in the above formulation), then the velocity decays $\mathcal{O}(1/r)$ and the stress and pressure decay $\mathcal{O}(1/r^2)$, where r is the distance between $\mathbf{x}$ and ∂D (Pozrikidis, 1992). The Green's

function thus decays $\mathcal{O}(1/r)$ and the stress tensor decays $\mathcal{O}(1/r^2)$, so that as the radius of the spherical domain extends to infinity, the contributions to the fluid flow from both the SLP and DLP vanish. Thus, we can let $\partial V = \partial D$ and work with the reduced problem.

1.2.4 Neglecting the double layer potential

The problems considered in this thesis all feature dynamic slender bodies in Stokes flows, which conserve volume as they interact with the fluid. In this section we illustrate how this property allows the double layer potential in the boundary integral equation (1.26) to be neglected, simplifying the modelling problem.

Consider a dynamic body with fixed and conserved volume V in a Stokes flow. By *dynamic*, we refer here to objects which are permitted to change shape but not volume, such as a flexible swimming cells or inextensible cilia. The slip velocity normal to the surface ∂V is

$$\iint_{\partial V} u_i(\mathbf{x}) n_i(\mathbf{x})\, dS_{\mathbf{x}} = 0, \tag{1.30}$$

a condition which implies the existence of a unique solution to the flow in the interior region of V. We label the solution as having velocity $u_i'(\mathbf{x})$ and stress tensor $\sigma_{ik}'(\mathbf{x})$, satisfying $u_i'(\mathbf{y}) = u_i(\mathbf{y})\, \forall \mathbf{y} \in V$. This "fictitious solution" exists in the interior of V and thus does not actually lie within the fluid domain. Nonetheless, the solution satisfies the Lorentz reciprocal identity and so

$$\frac{\partial}{\partial x_k}\left(S_{ij}(\mathbf{x},\mathbf{y})\sigma_{ik}'(\mathbf{x}) - u_i'(\mathbf{x}) T_{ijk}(\mathbf{x},\mathbf{y})\right) = 0. \tag{1.31}$$

As in section 1.15, integration over the volume and applying the divergence theorem

yields

$$\iint_{\partial V} S_{ij}(\mathbf{x},\mathbf{y})\sigma'_{ij}n_k(\mathbf{x})\,dS_{\mathbf{x}} - \iint_{\partial V} u'_i(\mathbf{x})T_{ijk}(\mathbf{x},\mathbf{y})n_k(\mathbf{x})\,dS_{\mathbf{x}} = 0, \tag{1.32a}$$

$$\implies -\iint_{\partial V} S_{ij}(\mathbf{x},\mathbf{y})g'_i(\mathbf{x})\,dS_{\mathbf{x}} - \iint_{\partial V} u_i(\mathbf{x})T_{ijk}(\mathbf{x},\mathbf{y})n_k(\mathbf{x})\,dS_{\mathbf{x}} = 0, \tag{1.32b}$$

where we define $g'_i := -\sigma'_{ik}n_k$ and note that $u_i = u'_i$. Adding equations (1.32b) and (1.26) cancels the integral contribution from the stress tensor, leaving

$$u_j(\mathbf{y}) = \frac{1}{8\pi}\iint_{\partial V} S_{ij}(\mathbf{x},\mathbf{y})\big(g_i(\mathbf{x}) - g'_i(\mathbf{x})\big)\,dS_{\mathbf{x}} = \frac{1}{8\pi}\iint_{\partial V} S_{ij}(\mathbf{x},\mathbf{y})f_i(\mathbf{x})\,dS_{\mathbf{x}}, \tag{1.33}$$

where $f_i = g_i - g'_i$. As in section (1.15), equation (1.33) can be rearranged exploiting the symmetry of the stokeslet yielding

$$u_i(\mathbf{x}) = \frac{1}{8\pi}\iint_{\partial V} S_{ij}(\mathbf{x},\mathbf{y})f_j(\mathbf{y})\,dS_{\mathbf{y}}, \tag{1.34}$$

which is the form of the boundary integral equation which will be used throughout the remainder of this thesis.

1.2.5 Stokes flow near a boundary and the blakelet

In the previous sections, we considered the fluid flow arising from the presence of a slender body in an infinite fluid. Upon approaching a rigid boundary, the fluid flow will change in a way that is not captured by the stokeslet solution, and a new fundamental solution must be derived. Wall effects are not just confined to regions near the wall; hydrodynamic interactions between the boundary influence the far-field flow, limiting further the accuracy of the stokeslet solution whenever rigid surfaces are present.

In the most basic case, the boundary can be modelled as infinite plane. For microbiological problems involving small cells near boundaries, such as sperm in the female reproductive tract or cilia protruding from a ciliated surface, the length scale of the bodies is much less than the radius of curvature of the boundary and so this infinite plane approximation is appropriate. In what follows, we assume both no-slip ($\boldsymbol{u} = \mathbf{0}$) and no-penetration ($\boldsymbol{u} \cdot \mathbf{n} = 0$) conditions on the surface of the wall and the cell boundary.

Motivated by modelling cilia protruding from a wall, Blake (1971) developed a flow solution using the method of images. For a singularity located at $\mathbf{y} = (y_1, y_2, w + h)$, a perpendicular distance of h above the plane $x_3 = w$, a virtual "image" is supposed to exist outside of the flow below the plane at $\mathbf{y}^* = (y_1, y_2, w - h)$. If the force at the singularity is $\boldsymbol{f}$, the force associated with the image will be $-\boldsymbol{f}$. Using equation (1.16), the contribution to the solution from the image will be

$$S^*_{ij}(\mathbf{x}, \mathbf{y}^*) = \frac{\delta_{ij}}{R} + \frac{R_i R_j}{R^3} + \alpha_{ij}, \qquad R_i = x_i - y^*_i, \qquad R = \sqrt{R_i R_i}, \tag{1.35}$$

where $\mathbf{x} = (x_1, x_2, x_3)$ is a point in the domain and where α_{ij} are terms to be determined. The fundamental flow solution at $\mathbf{x}$ due to force $\boldsymbol{f}(\mathbf{y})$ is thus the combination of the stokeslet solution (1.16) and the stokeslet image (1.35). Requiring a no-slip condition on the surface of the boundary yields $S^*_{ij}(\mathbf{x}_w, \mathbf{y}^*) = -S_{ij}(\mathbf{x}_w, \mathbf{y})$ where $\mathbf{x}_w$ is a point lying in the plane of the boundary. The unknowns α_{ij} can be determined (see Pozrikidis

(1992) for details) to obtain the *blakelet*, denoted $B_{ij}(\mathbf{x}, \mathbf{y})$, as

$$B_{ij}(\mathbf{x}, \mathbf{y}) = S_{ij}(\mathbf{x}, \mathbf{y}) - S^*_{ij}(\mathbf{x}, \mathbf{y}^*) + 2h^2 G^D_{ij}(\mathbf{x}, \mathbf{y}^*) - 2h G^{SD}_{ij}(\mathbf{x}, \mathbf{y}^*), \tag{1.36a}$$

$$G^D_{ij}(\mathbf{x}, \mathbf{y}^*) = \pm \left(\frac{\delta_{ij}}{R^3} - 3\frac{R_i R_j}{R^5} \right), \tag{1.36b}$$

$$G^{SD}_{ij}(\mathbf{x}, \mathbf{y}^*) = R_3 G^D_{ij} \pm \frac{\delta_{j3} R_i - \delta_{i3} R_j}{R^3}, \tag{1.36c}$$

where G^D and G^{SD} are a potential dipole and a stokeslet doublet respectively. The signs in equations (1.36a–1.36c) are positive for $j = 1, 2$ and negative for $j = 3$. The stokeslet term in equation (1.36a) is as defined in (1.16).

The fluid flow induced by a point force orientated perpendicular to the boundary decays as $\mathcal{O}(1/r^3)$, whereas the flow arising from a point force parallel but far away to the wall decays as $\mathcal{O}(1/r^2)$. This discrepancy is crucial, for example in the case of ciliated microorganisms, suggesting that motion parallel to the creatures surface contributes far more to the resulting fluid motion than motion normal to its surface (Blake & Chwang, 1974). Additionally, the motion of the cilium most distant to the wall produces more flow than motion close to the wall.

1.2.6 The method of regularised stokeslets

Flagella, cilia, and other slender bodies are driven by moments acting along and throughout their length. It is convenient to describe the three dimensional geometry of the filament through coordinates along its centreline, parametrised by arclength. A force distribution arises naturally from the interaction of the internally-driven slender body with surrounding viscous fluid. Thus, following the arguments discussed in section 1.2.2, evaluating the flow on or near the body produces singular or near-singular

stokeslet solutions.

The singularity issue is present in many Stokes flow problems. By smearing the driving force over a sphere of arbitrary radius, concentrated at the centre and decaying rapidly away from it, Cortez and coauthors demonstrated that the singularity in the stokeslet may be smoothed over and thereby regularised, first in two dimensions (Cortez, 2001) and then in three dimensions (Cortez *et al.*, 2005). Crucially, the regularisation procedure leads to solutions that are exact roots of the Stokes flow equations but driven by a smoothed force, so that the flow remains incompressible (i.e. the continuity equation continues to be satisfied). The body force density is altered by replacing the Dirac-δ distribution with a radially symmetric *blob function* $\phi_\varepsilon(\mathbf{x})$ so that $\boldsymbol{F}(\mathbf{x}) = \boldsymbol{f}\,\phi_\varepsilon(\mathbf{x}-\mathbf{y})$. Crucially, the property

$$\iiint_{\mathbb{R}^3} \phi_\varepsilon(\mathbf{x})d\mathbf{x} = 1 \tag{1.37}$$

is satisfied, which acts to remove the force singularity. The *regularisation parameter* $0 < \varepsilon < 1$ controls the spatial spread of the force, and works to limit the volume about $\mathbf{x}$ to which its influence extends. As discussed in sections 1.2.1–1.2.4, a classical result of Stokes flow in a smooth bounded domain $D \in \mathbb{R}^3$ is that the Stokes flow equations (1.11a) can be written as an integral over the boundary of the domain ∂D, and in terms of the velocities and forces acting on ∂D. With the regularised choice of $\boldsymbol{F}$, Cortez *et al.* derived the dimensionless regularised stokeslet boundary integral equation

$$\iiint_D u_i(\mathbf{x})\phi_\varepsilon(\mathbf{x}-\mathbf{y})\,dV_{\mathbf{x}} = \frac{1}{8\pi}\iint_{\partial D} S_{ij}^{\varepsilon}(\mathbf{x},\mathbf{y})f_j(\mathbf{y})\,dS_{\mathbf{x}}, \tag{1.38}$$

which can be numerically implemented using a chosen quadrature rule (discussed fur-

ther in section 1.2.7). For the specific choice of blob function

$$\phi_\varepsilon(\mathbf{x}-\mathbf{y}) = \frac{15\varepsilon^4}{8\pi r_\varepsilon^7} \tag{1.39}$$

the kernel of the integral on the right hand side of equation (1.38) is the *regularised stokeslet*, defined

$$S_{ij}^\varepsilon(\mathbf{x},\mathbf{y}) = \delta_{ij}\frac{r^2+2\varepsilon^2}{r_\varepsilon^3} + \frac{r_i r_j}{r_\varepsilon^3}, \qquad r_\varepsilon = \sqrt{r^2+\varepsilon^2}, \quad r^2 = r_i r_i, \tag{1.40}$$

where δ_{ij} is the Kronecker-δ tensor. The resulting *method of regularised stokeslets* approximates the fluid velocity at a point $\mathbf{x}$ via

$$u_i(\mathbf{x}) = \frac{1}{8\pi}\iint_{\partial D} S_{ij}^\varepsilon(\mathbf{x},\mathbf{y}) f_j(\mathbf{y})\, dS_\mathbf{y} + \mathcal{O}(\varepsilon^p), \tag{1.41}$$

where $\boldsymbol{f}$ is the force density (that is, per unit length or per unit area) exerted by the body onto the fluid. The error term arises from the regularisation of the force, analytically a Dirac-δ distribution in the classical theory, to a smoothed blob of radius ε. For the choice in equation (1.39), the error is $\mathcal{O}(\varepsilon^2)$ for $r > \sqrt{5\varepsilon/2}$ (i.e. in the near-field) and $\mathcal{O}(\varepsilon)$ in the far-field (Cortez *et al.*, 2005; Smith, 2018). The varying, but rapidly decaying, nature of the force across the blob allows the regularised stokeslet to be used in any situation in which forces drive motion.

Research into improving the accuracy and efficiency of regularised stokeslet methods continues through both computational and analytical avenues. By constructing blob functions with specific far-field error properties, Nguyen & Cortez (2014) illustrate how the near-field regularisation error can be reduced by isolating and removing the leading error term. Approaches for reducing the far-field regularisation error are

provided by Zhao *et al.* (2019), who consider alternative power-law and compactly-supported blobs. In particular, the authors find that asymmetric blobs induce force dipole flows proportional to ε in the far field, linearly approaching the singular flow solution as $\varepsilon \longrightarrow 0$. A quadratic rate of convergence to the true flow solution is derived for blob functions with three symmetry planes.

For the case of a point force in the presence of a plane boundary, a regularised form of the blakelet (1.36a) can be derived (Ainley *et al.*, 2008) as

$$B_{ij}^{\varepsilon}(\mathbf{x},\mathbf{y}) = \frac{\delta_{ij}(r^2+2\varepsilon^2)+r_i r_j}{r_\varepsilon^3} - \frac{\delta_{ij}(R^2+2\varepsilon^2)+R_i R_j}{R_\varepsilon^3} + 2h\Delta_{jk}\left(\frac{\partial}{\partial R_k}\left\{\frac{hR_i}{R_\varepsilon^3} - \frac{\delta_{i3}(R^2+2\varepsilon^2)+R_i R_3}{R_\varepsilon^3}\right\} - 4\pi h\delta_{ik}\varphi_\varepsilon(R)\right) - \frac{6h\varepsilon^2}{R_\varepsilon^5}(\delta_{i3}R_j - \delta_{ij}R_3), \quad (1.42)$$

where $r_\varepsilon = \sqrt{r^2+\varepsilon^2}$, $R_\varepsilon = \sqrt{R^2+\varepsilon^2}$ and

$$\Delta_{jk} = \begin{cases} +1 & j=k=1,2, \\ -1 & j=k=3, \\ 0 & \text{otherwise} \end{cases}. \quad (1.43)$$

The blob function in (1.39), desirable for the regularised stokeslet, is complemented with a 'companion' blob function $\varphi_\varepsilon(R) := 3\varepsilon^2/(4\pi R_\varepsilon^5)$ for the source dipole, which decays more slowly to account for the far-field hydrodynamic effects caused by the presence of the boundary, and provides convenient analytic cancellations (Ainley *et al.*, 2008). Choosing a blob function for the regularised blakelet distinct to the regularised stokeslet necessitates the final term, which accounts for this difference. Cortez

& Varela (2015) generalised the method of Ainley *et al.* (2008), developing a systematic way to derive the companion blob and resulting image system for any given blob function, and considering exponential and Gaussian blob pairings in addition to the established algebraic choices. The ability to use general blob functions allows the regularised stokeslet method to be used in problems where, for example, specific decay properties are required.

1.2.7 Numerical discretisation of the boundary integral equation

The linearity of Stokes flow enables solutions to geometrically complicated problems to be found by combining stokeslet solutions arising from point forces in the domain. Moreover, the regularised stokeslet method provides a way of avoiding singular solutions by assuming the point forces are instead spread over small (spherical) blobs. With this in mind, we next consider the steps to spatially discretise the regularised stokeslet boundary integral equation (1.41) for implementation as code for simulations.

Consider a body with surface ∂B immersed in viscous fluid described by the Stokes flow equations. Forces, measured at *source points* $\{\mathbf{y}[1], \dots, \mathbf{y}[M]\}$, drive the fluid flow at *field points* $\{\mathbf{x}[1], \dots, \mathbf{x}[N]\}$. These sets of points comprise two general discretisations of the surface ∂B. Assuming a no-slip condition, by placing field points across the surface so as to adequately approximate the body geometry, the fluid velocity on the surface of the body is given by

$$u_i(\mathbf{x}[n]) = \frac{1}{8\pi} \sum_{m=1}^{M} S_{ij}^{\epsilon}(\mathbf{x}[n], \mathbf{y}[m]) f_j(\mathbf{y}[m])\, dS(\mathbf{y}[m]), \qquad n = 1, \dots, N, \tag{1.44}$$

where $\boldsymbol{f}(\mathbf{y}[m])$ is the force density exerted by the body onto the fluid at the point

$\mathbf{y}[m]$ over the surface area $dS(\mathbf{y}[m])$. In this way, equation (1.44) approximates the boundary integral equation (1.34) with a quadrature rule, with the source points being the abscissae and corresponding weights given by the surface area associated with each point. The particular discretisation where field and source points coincide (and $N = M$) is referred to in this thesis as *Nyström discretisation*, arising from an application of the classical method of Nyström (1930). In this case, equation (1.44) can be written

$$u_i(\mathbf{x}[n]) = \mathbf{x}_t[n] = \frac{1}{8\pi} \sum_{m=1}^{N} S_{ij}^{\epsilon}(\mathbf{x}[n], \mathbf{x}[m]) f_j[m]\, dS[m], \qquad n = 1, \dots, N, \tag{1.45}$$

where $\boldsymbol{f}[n] := \boldsymbol{f}(\mathbf{x}[n])$ and $dS[n] := dS(\mathbf{x}[n])$. The discrete equation (1.45) can be expressed as a linear matrix system of the form

$$A\boldsymbol{z} = \boldsymbol{b}, \tag{1.46}$$

where the $3N \times 1$ vectors are

$$\boldsymbol{z} = \left(F_1[1], \dots, F_1[N], F_2[1], \dots, F_2[N], F_3[1] \dots, F_3[N]\right)^T, \tag{1.47a}$$

$$\boldsymbol{b} = \left(\mathrm{x}_{1,t}[1], \dots, \mathrm{x}_{1,t}[N], \mathrm{x}_{2,t}[1], \dots, \mathrm{x}_{2,t}[N], \mathrm{x}_{3,t}[1], \dots, \mathrm{x}_{3,t}[N]\right)^T, \tag{1.47b}$$

and with $F_i[n] = f_i[n] dS[n]$ denoting the force at each node. The $3N \times 3N$ *stokeslet matrix* has block form

$$A = \begin{pmatrix} A_{11} & A_{12} & A_{13} \\ A_{21} & A_{22} & A_{23} \\ A_{31} & A_{32} & A_{33} \end{pmatrix}, \tag{1.48}$$

where

$$A_{ij}\{m,n\} = \frac{1}{8\pi}\sum_{q=1}^{N} S_{ij}^{\epsilon}(\mathbf{x}[m],\mathbf{x}[q]), \qquad m,n = 1,\dots,N. \tag{1.49}$$

The unknowns of the matrix system (either position or force) are dependent on the problem under consideration. Situations in which the body motion is prescribed, with forces being unknown, are referred to as *resistance problems*. Conversely, if the total force and moment are known, the velocity and stokeslet distribution are unknown and the problem is referred to as a *mobility problem* (Smith, 2018). In general, mobility problems will require additional equations for, say, elasticity and kinematics. Applying appropriate boundary and initial conditions yields a linear system to be solved as desired.

The Nyström discretisation of the stokeslet boundary integral is widely used due to its simplicity and ease of implementation. The Nyström method is $\mathcal{O}(h^2/\epsilon)$ accurate; halving ϵ to reduce the regularisation error thus necessitates reducing the grid spacing h by $\sqrt{2}$ to maintain the same level of quadrature error in the numerical integration. The number of nodes N requires to cover the domain thus increases by $\sqrt{2}$. The assembly cost scales with N^2, thus doubling the memory requirement for storing the integrand values at all nodes, and quadrupling the direct solver cost. Plainly, increasing the accuracy of the Nyström approach rapidly necessitates increases in computational resources.

Numerical optimisations by Gallagher & Smith (2020) reveal the computational speed up obtainable when exploiting dedicated GPUs to build and store mobility matrices. By formulating the assembly and solution of the linear system solely in terms of matrix operations, GPU-enabled basic linear algebra subroutines can be automatically exploited. This *passive parallelisation* technique allows problems with very large

degrees of freedom to be considered and simulated in reasonable real world time. Alternatively, recent developments by Gallagher & Smith (2021) employ a Richardson extrapolation of the regularisation error to allow for larger choices of ϵ without a loss in accuracy, allowing coarser discretisations to appropriately cover a surface leading to smaller linear system sizes.

1.2.8 The nearest-neighbour discretisation of the regularised stokeslet method

As discussed in section 1.2.2, the stokeslet itself decays quickly $\mathcal{O}(1/r)$ away from the source. Capturing this rapidly-varying nature can require very fine discretisations (i.e. a large number of points) to accurately resolve the integral using equation (1.45), increasing computational expense – a trade off for the simplicity of implementation offered by the Nyström approach.

Since the value of the regularisation parameter ε determines the variation of the stokeslet kernel, by choosing ε smaller than the length scales characterising the geometry, the variation in the forces on the body will be comparatively slowly varying. Smith (2018) exploited this property by considering two distinct discretisations of the body surface, decoupling the stokeslet quadratures from the force discretisation. The rapidly-varying kernel is treatable with a suitably high discretisation, retaining numerical accuracy, whilst the slowly-varying force is captured using a much coarser discretisation, requiring significantly reduced computational resources than the Nyström discretised problem. Moreover, one does not need to compute a mesh of the body surface, which can add significantly to computational cost.

We denote by $\{\mathbf{x}[1], \dots, \mathbf{x}[N]\}$ and $\{\mathbf{y}[1], \dots, \mathbf{y}[Q]\}$ the discretisations for the force

and stokeslet respectively, with $N \leqslant Q$. These collections will be referred to as the *traction* and *quadrature* discretisations respectively. Following Smith (2018), the nearest-neighbour mapping from the quadrature to the traction discretisations is

$$\mathcal{N} : \{1, \dots, Q\} \longrightarrow \{1, \dots, N\}, \qquad \mathcal{N}(q) = \underset{n=1,\dots,N}{\arg\min} |\mathbf{x}[n] - \mathbf{y}[q]|, \tag{1.50}$$

for each quadrature node i.e. $\mathcal{N}(q)$ is the index of the nearest traction point to the quadrature point $\mathbf{y}[q]$. The nearest neighbour operator is expressible as a $Q \times N$ matrix through

$$v[q, n] = \begin{cases} 1 & \text{for } n = \underset{m=1,\dots,N}{\arg\min} |\mathbf{x}[m] - \mathbf{y}[q]|, \\ 0 & \text{otherwise.} \end{cases} \tag{1.51}$$

The components of the force density associated with each quadrature node can thus be written (Gallagher & Smith, 2018) as

$$f_i(\mathbf{y}[q]) dS(\mathbf{y}[q]) \approx f_i(\mathbf{x}[\mathcal{N}(q)]) dS(\mathbf{x}[\mathcal{N}(q)]) \approx -\sum_{n=1}^{N} v[q, n] g_i[n] dS(\mathbf{x}[n]), \tag{1.52}$$

where $g_i[n] := -f_i(\mathbf{x}[n])$. Applying this interpolation to the regularised stokeslet boundary integral equation (1.38) yields

$$u_i(\mathbf{x}[n]) = -\frac{1}{8\pi} \sum_{m=1}^{N} g_j[m] dS(\mathbf{x}[m]) \sum_{q=1}^{Q} S_{ij}^{\varepsilon}(\mathbf{x}[n], \mathbf{y}[q]) v[q, m], \qquad n = 1, \dots, N. \tag{1.53}$$

Practically there is no need to distinguish between the force densities $\boldsymbol{g}[n]$ and their associated weights $dS(\mathbf{x}[n])$, and so we write

$$u_i(\mathbf{x}[n]) = -\frac{1}{8\pi} \sum_{m=1}^{N} \phi_j[m] \sum_{q=1}^{Q} S_{ij}^{\varepsilon}(\mathbf{x}[n], \mathbf{y}[q]) v[q, m], \qquad n = 1, \dots, N, \tag{1.54}$$

where $\boldsymbol{\phi}[n] := \boldsymbol{g}[n]dS(\mathbf{x}[n])$ for each n.

To demonstrate the advantages of the nearest-neighbour discretisation over the Nyström approach, we briefly examine a simple test problem. Consider a spherical body translating with velocity $\boldsymbol{U}$ and rotating with angular velocity $\boldsymbol{\Omega}$ in a stationary Stokes flow. The geometric simplicity of the body enables an analytic solution to be found (Acheson, 1991). For the elementary case where $\boldsymbol{U} = \mathbf{e}_i$ and $\boldsymbol{\Omega} = \mathbf{e}_i$, Stokes' law provides the dimensionless force and moment that the body exerts on the surrounding fluid as

$$\boldsymbol{F} = 6\pi\mu a\mathbf{e}_i, \qquad \boldsymbol{M} = 8\pi\mu a^3\mathbf{e}_i, \tag{1.55}$$

where a is the radius of the sphere and the collection $\{\mathbf{e}_1, \mathbf{e}_2, \mathbf{e}_3\}$ form an orthonormal three dimensional basis spanning the domain. In this section it is assumed that the fluid viscosity is $\mu = 1$ for simplicity. The force and moment may be numerically approximated and subsequently compared to the analytical solutions by solving the resulting resistance problem.

To begin, we require a suitable discretisation of the surface of the sphere. With no requirement for equispaced nodes, a straightforward way to obtain such a collection is to enclose the sphere by a cube and project nodes from each of its faces onto the surface. The resulting cloud of coordinates can be transformed through scalar multiplication and rotations to obtain discretisations of prolate or oblate spheroids. High resolution discretisations can be obtained by increasing the number of nodes on each face of the enclosing cube. A diagram of this discretisation technique, referred to in this thesis as *cubic projection*, is given in figure 1.5. We define by H_t and H_q the number of nodes along an edge of the enclosing cube to produce the traction/force and quadrature/kernel spherical discretisations respectively. Each cubic face will have $H_t \times H_t$ or

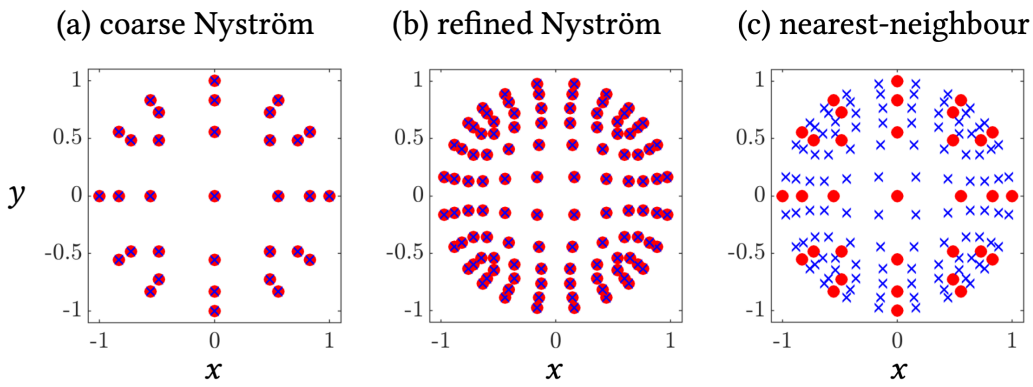

Figure 1.5: Distribution of nodes across the surface of a unit sphere, viewed from the xy-axis. In all panels, red circles represent traction nodes and blue crosses quadrature/kernel nodes. Plots indicate (a) a coarse Nyström discretisation, where force and quadrature nodes coincide, generated from a cubic projection with 3×3 nodes per face; (b) a refined Nyström discretisation, generated from a cubic projection with 6×6 nodes per face; and (c) a nearest-neighbour discretisation, combining a coarse discretisation for the slowly-varying force and a refined discretisation for the rapidly-varying kernel.

$H_q \times H_q$ nodes, leading to $N_t = 6H_t^2$ and $N_q = 6H_q^2$ points distributed across the spherical surface, for each case.

The accuracy afforded by using the nearest neighbour discretisation is indicated in figure 1.6, which compares the relative error between the computed total force and total moment, and the exact Stokes law solutions for a translating unit sphere resistance problem. For even relatively coarse traction discretisations of the sphere, choosing a quadrature discretisation so that $H_q = 2H_t$ yields relative errors of $< 5\%$ for both quantities. At low N_t choices, the relative error is minimal when using $H_q = 2H_t$, as opposed to $H_q = 3H_t$, a counterintuitive erroneous result likely caused by inadequate coverage of the sphere's surface, yielding a coincidentally more accurate result. When surface coverage is improved, the expected behaviour is observed and larger N_q choices yield improved accuracy (aside from the anomalous result recorded in figure 1.6b).

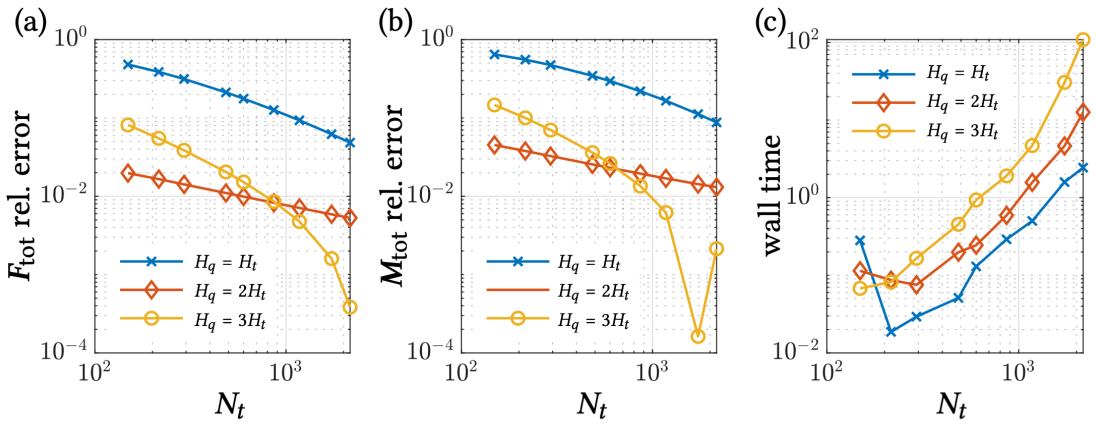

Figure 1.6: Error in computing (a) the total force and (b) total moment, relative to the analytic Stokes' law solutions (1.55) on a unit sphere translating with $\boldsymbol{U} = (1, 0, 0)^T$. In (c), the walltime (in seconds) for each simulation. The sphere is discretised using a cubic projection mapping, with H_t the number of nodes per face of the cube used to obtain the traction discretisation, and H_q the similarly defined variable to obtain the quadrature discretisation; N_t is the resulting number of traction/force nodes.

The times (measured in seconds) for the resistance problem to be constructed (excluding discretisation generation) and solved for each simulation are given in 1.6c. In general, increasing the number of nodes comprising the quadrature discretisation for a fixed level of force discretisation increases the computational cost of the method, evidenced by the cleanly separated lines in figure 1.6c (excluding the first erroneous point for the $H_q = H_t$ line). Reading across figures 1.6, to achieve a level of relative error $\lessapprox$ 5% in the force and moment, the Nyström method requires $N_t = N_q > 2100$ and takes $\approx$ 2.5 seconds to solve. The same level of relative error can be achieved with a nearest-neighbour discretisation with $N_t = 216$, $N_q = 3N_t$, and solves in $\approx$ 0.8 seconds; a nearly 3 times speed increase. For detailed benchmarking, refer to Smith (2018).

1.2.9 Regularised stokeslet segments

In the section 1.2.8, we examined how nearest-neighbour discretisations of regularised stokeslet integral equations of the form

$$\boldsymbol{u}(\mathbf{x}) = \frac{1}{8\pi} \iint_{\partial D} \boldsymbol{S}^{\epsilon}(\mathbf{x}, \mathbf{y}) \cdot \boldsymbol{g}(\mathbf{y}) \, dS_{\mathrm{y}} \tag{1.56}$$

provide solutions with improved accuracy for fewer degrees of freedom compared to classical Nyström discretisations. For notational simplicity, in this section we will work with the vectorised boundary integral equation (1.56) rather than its component form in (1.41). When modelling slender bodies, it is convenient to describe their hydrodynamics by line integrals of stokeslets along their centreline as opposed to surface integrals, negating the need for complex surface meshes when using 'meshless' approaches such as regularised stokeslet methods. Consider the regularised stokeslet line integral

$$\boldsymbol{u}(\mathbf{x}) = \frac{1}{8\pi} \int_0^L \boldsymbol{S}^{\epsilon}\big(\mathbf{x}, \boldsymbol{X}(s)\big) \cdot \boldsymbol{f}(s) \, ds, \tag{1.57}$$

where $\boldsymbol{X}(s)$ are material points along the centreline of a filament parametrised by arclength $s \in [0, L]$. Whilst a Nyström or nearest-neighbour discretisation could be employed in order to numerically solve equation (1.57), to do so would require generation of a refined discretisation, either for the force and kernel for the Nyström approach, or for the kernel using a nearest-neighbour method. Due to the dynamic nature of the elastic filament, interpolating a coarse force discretisation to obtain a refined kernel discretisation whilst preserving geometry requires care – for example, a piecewise linear interpolation may inadequately describe the curve.

An alternate approach is to discretise the filament into $Q \in \mathbb{R}$ straight line seg-

ments. The *regularised stokeslet segments* method as described in this thesis derives from Smith (2009), with recent formalisations by Cortez (2018), though a similar approach for singular stokeslets was used by Higdon (1979a,b). Adopting a piecewise linear geometric approximation, the line integrals become

$$\int_0^L \boldsymbol{S}^\varepsilon\big(\mathbf{x}, \boldsymbol{X}(s)\big)\cdot\boldsymbol{f}(s)\,ds \approx \sum_{n=1}^{Q}\int_{s[n]-\delta s}^{s[n+1]+\delta s} \boldsymbol{S}^\varepsilon\big(\mathbf{x}, (\tilde{s}[n]-\xi)\tilde{\boldsymbol{X}}_s[n]+\tilde{\boldsymbol{X}}[n]\big)\cdot\boldsymbol{f}(\xi)\,d\xi, \quad (1.58)$$

where variables with tildes are measured at the segment midpoints. To simplify the analysis, we consider integration across a single segment $\xi \in [s-\delta s, s+\delta s]$ so that the segment midpoint is $\boldsymbol{X}(s)$. The tangent to this segment is $\boldsymbol{X}_s(s)$, so that the straight line segment is $\boldsymbol{X}(\xi) \approx \boldsymbol{X}(s) + (\xi - s)\boldsymbol{X}_s(s)$. By assuming a constant hydrodynamic force per unit length $\boldsymbol{f}$ on the segment, the regularised stokeslet integral can thus be approximated as

$$\begin{aligned}
\int_{s-\delta s}^{s+\delta s} \boldsymbol{S}^\varepsilon\big(\boldsymbol{X}(s),\boldsymbol{X}(\xi)\big)\cdot\boldsymbol{f}(\xi)\,d\xi &\approx \int_{s-\delta s}^{s+\delta s} \boldsymbol{S}^\varepsilon\big(\boldsymbol{X}(s),\boldsymbol{X}(\xi)\big)\,d\xi\cdot\boldsymbol{f}(s), && (1.59a)\\
&\approx \int_{s-\delta s}^{s+\delta s} \boldsymbol{S}^\varepsilon\big(\boldsymbol{X}(s),\boldsymbol{X}(s)+(\xi-s)\boldsymbol{X}_s(s)\big)\,d\xi\cdot\boldsymbol{f}(s), && (1.59b)\\
&=: \boldsymbol{D}(\boldsymbol{X},s)\cdot\boldsymbol{f}, && (1.59c)
\end{aligned}$$

where δs is the half length of integration. Higher order force discretisations are considered in Cortez (2018); Walker *et al.* (2019). Denoting by $\{\mathbf{e}_1, \mathbf{e}_2, \mathbf{e}_3\}$ the basis local to the straight line segment, the rotation matrix transforming into the local frame is given by the sum of dyadic products through $\boldsymbol{\Theta} = \mathbf{d}_i \otimes \mathbf{e}_i$, where $\{\mathbf{d}_1, \mathbf{d}_2, \mathbf{d}_3\}$ is the orthonormal frame describing the orientation of the segment in the fixed Euclidean frame. After performing the coordinate transformation $x_i^L = \Theta_{ij}(x_j - X_j(s))$, the integrals can be

expressed in local coordinates as

$$\boldsymbol{D}^L(\boldsymbol{X}^L, \xi) = \int_{-\delta s}^{\delta s} \boldsymbol{S}^\varepsilon\left(\boldsymbol{X}^L, \xi \mathbf{e}_1\right) d\xi \tag{1.60}$$

Note that this coordinate transformation does not change $\boldsymbol{D}$ as the regularised stokeslets $\boldsymbol{S}^\varepsilon$ are not functions of $\boldsymbol{X}(s)$ and $\boldsymbol{X}(\xi)$ directly, but of their difference $\boldsymbol{r} = \boldsymbol{X}(s) - \boldsymbol{X}(\xi)$ (see definition (1.40)). The integral expressed in the lab frame coordinates is obtainable through the rank-2 tensor transformation

$$D_{ij}(\boldsymbol{X}, \xi) = \Theta_{ki}\, D^L_{kl}(\boldsymbol{X}^L, \xi)\, \Theta_{lj}. \tag{1.61}$$

The diagonal entries of the integrals provide the dominant contribution of the stokeslet in the calculation of the force per unit length. Letting ε be a proxy for the cross sectional radius of the segment and $\varepsilon \ll q \ll L$, we define the indefinite integrals as

$$\boldsymbol{I}^L(\boldsymbol{X}^L, \xi) = \int \boldsymbol{S}^\varepsilon(\boldsymbol{X}^L, \xi \mathbf{e}_1)\, d\xi. \tag{1.62}$$

The diagonal entries of $\boldsymbol{I}^L$ are

$$I^L_{11} = -\left(\frac{x-s}{r_\varepsilon}\right)\left(\frac{\varepsilon^2}{y^2+z^2+\varepsilon^2} - 1\right) + 2\log(s - x + r_\varepsilon), \tag{1.63a}$$

$$I^L_{22} = -\left(\frac{x-s}{r_\varepsilon}\right)\left(\frac{\varepsilon^2+y^2}{y^2+z^2+\varepsilon^2}\right) + \log(s - x + r_\varepsilon), \tag{1.63b}$$

$$I^L_{33} = -\left(\frac{x-s}{r_\varepsilon}\right)\left(\frac{\varepsilon^2+z^2}{y^2+z^2+\varepsilon^2}\right) + \log(s - x + r_\varepsilon), \tag{1.63c}$$

where $(x, y, z) := (X^L_1, X^L_2, X^L_3)$ is a convenient shorthand, and $r^2_\varepsilon = (x-s)^2 + y^2 + z^2 + \varepsilon^2$.

The off-diagonal entries are more easily computable through symmetry relations as

$$I_{12}^L = I_{21}^L = \frac{y}{r_\varepsilon}, \tag{1.64a}$$

$$I_{13}^L = I_{31}^L = \frac{z}{r_\varepsilon}, \tag{1.64b}$$

$$I_{23}^L = I_{32}^L = -\left(\frac{x-s}{r_\varepsilon}\right)\left(\frac{yz}{y^2+z^2+\varepsilon^2}\right). \tag{1.64c}$$

The definite integrals are calculable through $\boldsymbol{D}^L\left(\boldsymbol{X}^L, \xi\right) = \left[\boldsymbol{I}^L(\boldsymbol{X}^L, \xi)\right]_{-\delta s}^{\delta s}$. The diagonal entries D_{11}, D_{22}, D_{33} are expressible directly in terms of q and ε. In these cases, $\boldsymbol{x} = \boldsymbol{0}$, and so after applying the limits of integration only the logarithmic terms remain. Considering the first diagonal term, one can compute

$$D_{11}^L = 2\log\left(\frac{\delta s + \sqrt{\delta s^2+\varepsilon^2}}{-\delta s + \sqrt{\delta s^2+\varepsilon^2}}\right), \tag{1.65a}$$

$$= 2\log\left(\frac{\delta s + \varepsilon\sqrt{\delta s^2/\varepsilon^2+1}}{-\delta s + \varepsilon\sqrt{\delta s^2/\epsilon^2+1}}\right), \tag{1.65b}$$

$$= 2\log\left(\frac{\delta s\left(1+(\varepsilon/\delta s)\sqrt{\delta s^2/\varepsilon^2+1}\right)}{-\delta s\left(1-(\varepsilon/\delta s)\sqrt{\delta s^2/\varepsilon^2+1}\right)}\right), \tag{1.65c}$$

$$= 2\log\left((1)\left(-\frac{1+(\varepsilon/\delta s)\sqrt{\delta s^2/\varepsilon^2+1}}{1-(\varepsilon/\delta s)\sqrt{\delta s^2/\varepsilon^2+1}}\right)\right), \tag{1.65d}$$

$$= -2\log\left(\frac{1+(\varepsilon/\delta s)\sqrt{\delta s^2/\varepsilon^2+1}}{1-(\varepsilon/\delta s)\sqrt{\delta s^2/\varepsilon^2+1}}\right), \tag{1.65e}$$

$$= -4\,\mathrm{arctanh}\left(\frac{\varepsilon}{\delta s}\sqrt{\frac{\delta s^2}{\varepsilon^2}+1}\right), \tag{1.65f}$$

$$= -4\,\mathrm{arctanh}\left(\sqrt{1+\left(\frac{\varepsilon}{\delta s}\right)^2}\right), \tag{1.65g}$$

where we employ the inverse hyperbolic tangent identity to simplify the quotient. The remaining diagonal entries of the local integrals can be computed in a similar fashion,

and are

$$D^L_{22} = D^L_{33} = 2\left(\sqrt{1+\left(\frac{\varepsilon}{\delta s}\right)^2}\right)^{-1} - 2\,\mathrm{arctanh}\left(\sqrt{1+\left(\frac{\varepsilon}{\delta s}\right)^2}\right). \tag{1.66}$$

Scaled appropriately, the values D^L_{11}, $D^L_{22} = D^L_{33}$ are analogous to the normal and tangent drag coefficients $c_\perp$ and $c_\parallel$ of Gray & Hancock (1955) resistive force theory, describing the fluid drag resistance of the segment upon translation about each of its principal axes. By modelling a continuous filament as a connected sequence of such rods, the line integral of stokeslets is analytically approximated, providing benefits in both accuracy and numerical efficiency, as discussed further in chapter 2 section 2.3.

1.3 Elasticity of slender bodies

In the following section, we review the fundamentals underpinning nonlinear geometric descriptions and elasticity of slender bodies deforming in three dimensions. Throughout this thesis, the slender object under consideration may be referred to interchangeably as a fibre, rod, or filament, and when considering a filament attached to a rigid body (as in chapters 3–5), it will also be referred to as a flagellum or tail.

Generalised descriptions of nonlinear filament geometry are introduced in section 1.3.1. Simplifications for the reduced problem of planar bending are described in section 1.3.2, forming the basis of the EIF method introduced in chapter 2 and the extended EIF method for human sperm used in chapter 3. Equations of motion for a filament deforming in three dimensions are derived in section 1.3.3, arriving finally at the general Kirchhoff equations, which form the core of the SPX method introduced in chapter 4.

1.3.1 Geometry of a bending, twisting filament

To describe elastic deformations of a filament, we first require a geometric description of the body that enables the tracking of its position and rotation in space and time. The approach to geometry presented here is an expansion of the ideas of Euler and Bernouilli (a summary of *Euler-Bernoulli beam theory* can be found in Timoshenko (1983)), and later Kirchhoff and Cosserat. Indeed, the ultimate goal of this section is to derive the *Kirchhoff rod model*, named after the mid-19$^{\text{th}}$ century German physicist Gustav Kirchhoff, who was instrumental in formalising many of the modern ideas and notions surrounding the elasticity of rods. The derivation here follows that of Landau & Lifshitz (1965), which was described in detail by Gueron & Levit-Gurevich (2001a,b); Wolgemuth *et al.* (2004). We adopt some of the more modern notation used

in contemporary presentations by Bower (2009); Audoly & Pomeau (2010). Similar representations have been used to model geometry for both open and closed rings, active filaments, and swimming cells in elastohydrodynamic studies by Lim *et al.* (2008); Lim (2010); Olson *et al.* (2013); Simons *et al.* (2015) (discussed further in section 1.4).

Consider a cylindrical filament, that at rest forms a straight rod. At each material point $\boldsymbol{X}(s)$ along the filament centreline, parametrised by the arclength $s \in [0, L]$, we define an orthonormal basis $\{\mathbf{d}_1(s), \mathbf{d}_2(s), \mathbf{d}_3(s)\}$. In the rest configuration, this frame is parallel at every point. The vectors $\mathbf{d}_3(s)$ point along the rod axis, and $\mathbf{d}_1(s)$ points to an imaginary line traced along the surface of the filament. The triad is completed by taking $\mathbf{d}_2(s) = \mathbf{d}_3(s) \times \mathbf{d}_1(s)$. This orthonormal basis will be referred to as the *director basis* or *material frame* of the filament. In this work, we constrain the axial director by

$$\mathbf{d}_3(s) := \mathbf{T}(s) = \boldsymbol{X}_s(s), \tag{1.67}$$

where $\mathbf{T}$ is the tangent to the filament centreline, and the subscript denotes partial differentiation with respect to s, though in general this constraint is not required (Lim, 2010; Olson *et al.*, 2013). The time dependence of all variables is suppressed for clarity. A sketch of a filament described in this way is presented in figure 1.7. Integrating equation (1.67) over the proximal curve allows the centreline to be computed through

$$\boldsymbol{X}(s) = \boldsymbol{X}_0 + \int_0^s \mathbf{d}_3(\xi)\, d\xi, \tag{1.68}$$

where $\boldsymbol{X}_0 := \boldsymbol{X}(0)$ is the coordinate of the leading point of the filament. The derivative of an arbitrary vector $\mathbf{x}$ can be expressed as (Hines & Blum, 1983)

$$\mathbf{x}_s = (\mathbf{x}_s)_b + \boldsymbol{\kappa} \times \mathbf{x}, \tag{1.69}$$

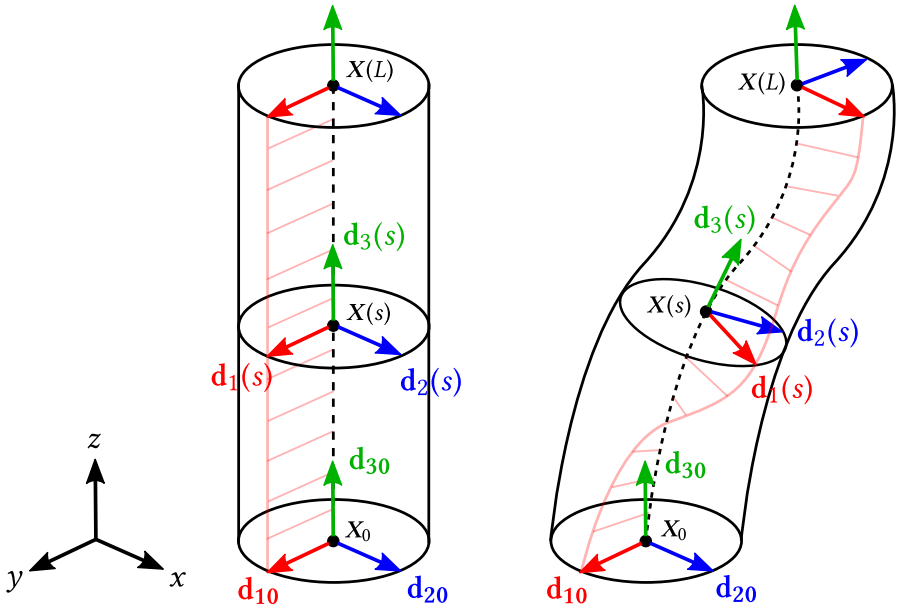

Figure 1.7: Geometric description of a cylindrical slender body via the director frame. At rest (left), the filament is a line with $\boldsymbol{\kappa}(s) = \mathbf{0}$ with the frames at each point parallel. The vector $\mathbf{d}_1$ points to an imaginary line drawn on the surface of the filament, drawn here in pink. After deformation (right), the frame rotates according to the mechanical bending and twisting undergone by the filament.

where $()_b$ denotes the representation of the vector $\mathbf{x}$ in body coordinates i.e. described by basis vectors aligned with the body. Since $\mathbf{d}_{i,b} = \delta_{ij}\mathbf{e}_j \implies (\mathbf{d}_{i,s})_b = \mathbf{0}$, equation (1.69) gives the rate of change of the triad along the length of the filament as

$$\mathbf{d}_{i,s} = \boldsymbol{\kappa} \times \mathbf{d}_i \implies \begin{cases} \mathbf{d}_{1,s} = \kappa_3 \mathbf{d}_2 - \kappa_2 \mathbf{d}_3, \\ \mathbf{d}_{2,s} = -\kappa_3 \mathbf{d}_1 + \kappa_1 \mathbf{d}_3, \\ \mathbf{d}_{3,s} = \kappa_2 \mathbf{d}_1 - \kappa_1 \mathbf{d}_2, \end{cases} \tag{1.70}$$

where the vector $\boldsymbol{\kappa} := \boldsymbol{\kappa}(s) = \kappa_i(s)\mathbf{d}_i(s)$ is referred to in this thesis as the *curvature vector*. The entries κ_1 and κ_2 are *bending curvatures* describing the rotation of the frame about the $\mathbf{d}_1$ and $\mathbf{d}_2$ axes respectively along the filament, and κ_3 is the *twist curvature*

similarly describing the rotation of the frame about the centreline tangent $\mathbf{d}_3$.

By taking the scalar product of the first equation in (1.70) with $\mathbf{d}_2$, the second with $\mathbf{d}_3$, and the third with $\mathbf{d}_1$, the curvature components can be expressed in terms of the basis vectors as

$$\kappa_1 = \mathbf{d}_{2,s} \cdot \mathbf{d}_3, \qquad \kappa_2 = \mathbf{d}_{3,s} \cdot \mathbf{d}_1, \qquad \kappa_3 = \mathbf{d}_{1,s} \cdot \mathbf{d}_2, \tag{1.71a}$$

$$\implies \boldsymbol{\kappa} = (\mathbf{d}_{2,s} \cdot \mathbf{d}_3)\mathbf{d}_1 + (\mathbf{d}_{3,s} \cdot \mathbf{d}_1)\mathbf{d}_2 + (\mathbf{d}_{1,s} \cdot \mathbf{d}_2)\mathbf{d}_3 \tag{1.71b}$$

recalling that by orthonormality $\mathbf{d}_i \cdot \mathbf{d}_j = \delta_{ij}$. The time evolution of the director frame, similar to equation (1.70), can be expressed in terms of the vector formed by the angular velocities about each of the basis vectors, written $\boldsymbol{\Omega} = \Omega_i \mathbf{d}_i$, as

$$\mathbf{d}_{i,t} = \boldsymbol{\Omega} \times \mathbf{d}_i \implies \begin{cases} \mathbf{d}_{1,t} = \Omega_3 \mathbf{d}_2 - \Omega_2 \mathbf{d}_3, \\ \mathbf{d}_{2,t} = -\Omega_3 \mathbf{d}_1 + \Omega_1 \mathbf{d}_3, \\ \mathbf{d}_{3,t} = \Omega_2 \mathbf{d}_1 - \Omega_1 \mathbf{d}_2, \end{cases} \tag{1.72}$$

with the angular velocity components expressible in terms of the basis vectors following a similar procedure as in equation (1.71a), yielding

$$\Omega_1 = \mathbf{d}_{2,t} \cdot \mathbf{d}_3, \qquad \Omega_2 = \mathbf{d}_{3,t} \cdot \mathbf{d}_1, \qquad \Omega_3 = \mathbf{d}_{1,t} \cdot \mathbf{d}_2, \tag{1.73a}$$

$$\implies \boldsymbol{\Omega} = (\mathbf{d}_{2,t} \cdot \mathbf{d}_3)\mathbf{d}_1 + (\mathbf{d}_{3,t} \cdot \mathbf{d}_1)\mathbf{d}_2 + (\mathbf{d}_{1,t} \cdot \mathbf{d}_2)\mathbf{d}_3. \tag{1.73b}$$

The geometric description is closed by formulating the compatibility relations between rates of rotation of the frame in space (by $\boldsymbol{\kappa}$) and rotations in time (by $\boldsymbol{\Omega}$). The condi-

tions relating the components of curvature and angular velocity are

$$\kappa_{1,t} = \Omega_3 \kappa_2 - \mathbf{d}_2 \cdot \boldsymbol{X}_{sst}, \tag{1.74a}$$

$$\kappa_{2,t} = -\Omega_3 \kappa_1 + \mathbf{d}_1 \cdot \boldsymbol{X}_{sst}, \tag{1.74b}$$

$$\kappa_{3,t} = \Omega_{3,s} + (\boldsymbol{X}_s \times \boldsymbol{X}_{ss}) \cdot \boldsymbol{X}_{st}. \tag{1.74c}$$

The derivation of the compatibility conditions is detailed in appendix A. Equations (1.70), (1.72) and (1.74a–1.74c), with appropriate boundary and initial conditions, completely describe the kinematics of the director frame aligned with a filament bending and twisting in three dimensions.

An alternative geometric description, widely used in the literature (Camalet *et al.*, 1999; Camalet & Jülicher, 2000; Gueron & Levit-Gurevich, 2001b; Gadêlha *et al.*, 2010; Pozrikidis, 2011), is the so-called *Frenet-Serret (F-S) frame*, which describes the orientation of the curve through an orthonormal basis $\{\mathbf{T}(s), \mathbf{N}(s), \mathbf{B}(s)\}$, where $\mathbf{T} = \boldsymbol{X}_s$ is the tangent to the curve, $\mathbf{N}$ is a unit normal and $\mathbf{B} = \mathbf{T} \times \mathbf{N}$ is a binormal. The frame rotates along the arclength following the Frenet-Serret formulas,

$$\begin{cases} \mathbf{T}_s = k\mathbf{N}, \\ \mathbf{N}_s = -k\mathbf{T} + \tau\mathbf{B}, \\ \mathbf{B}_s = -\tau\mathbf{N}, \end{cases} \tag{1.75}$$

where $k := k(s)$ is the geodesic curvature and $\tau := \tau(s)$ is the torsion characterising the nonplanar deviation of the curve. In this context, the *Darboux vector* can be defined as $\boldsymbol{\kappa}_D = \tau\mathbf{T} + k\mathbf{B}$ (Audoly & Pomeau, 2010; Oprea, 2019), though we avoid its use here to avoid confusion with the curvature vector $\boldsymbol{\kappa}$ introduced previously. The Frenet-Serret

frame, defined through only two parameters (k, τ), contains no notion of mechanical twist; as such the F-S frame is concerned purely with centreline dynamics, and does not encode anything about the material twist of a slender but finite thickness filament.

The director curvature $\boldsymbol{\kappa}$ and the Frenet-Serret curvature k are distinct but related quantities, with both the geodesic curvature and torsion expressible in terms of the director curvatures as

$$k = \sqrt{\kappa_1^2 + \kappa_2^2}, \tag{1.76a}$$

$$\tau = -\kappa_3 - \frac{\kappa_1 \kappa_{2,s} - \kappa_{1,s} \kappa_2}{k^2}. \tag{1.76b}$$

The torsion equation (1.76b) highlights an important caveat of the Frenet-Serret formulas: the frame is undefined anywhere that $k = 0$. For now, we assume that $k \neq 0$.

By their identical construction, $\mathbf{T} = \mathbf{d}_3$. The Frenet-Serret normal and binormal can be written in terms of the director basis vectors as

$$\mathbf{N} = \frac{\kappa_2}{k}\mathbf{d}_1 - \frac{\kappa_1}{k}\mathbf{d}_2, \tag{1.77a}$$

$$\mathbf{B} = \frac{\kappa_1}{k}\mathbf{d}_1 + \frac{\kappa_2}{k}\mathbf{d}_2. \tag{1.77b}$$

Inspection of the first Frenet-Serret equations (1.75) yields the additional relation – since $|\mathbf{T}| = |\mathbf{N}| = 1$, we have that $k = |\mathbf{T}_s| = |\boldsymbol{X}_{ss}|$ and so the geodesic curvature can be written in terms of the material points defining the curve.

To qualitatively appreciate the difference between the director and Frenet-Serret frames, we consider the curve and frames generated by prescribing

$$\kappa_1(s) = a\cos(4\pi s), \qquad \kappa_2(s) = a\sin(4\pi s), \qquad \kappa_3(s) = 0, \tag{1.78}$$

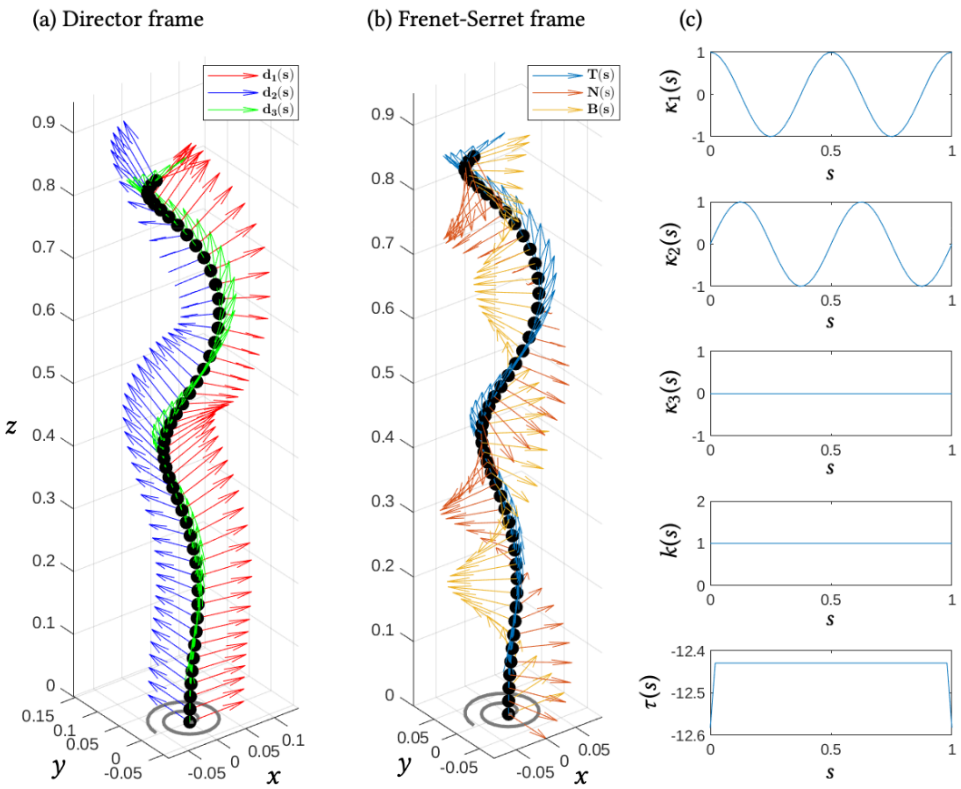

Figure 1.8: For prescribed director curvatures $(\kappa_1(s), \kappa_2(s), \kappa_3(s))$, the resulting (a) director frame, and (b) Frenet-Serret frame offer markedly different descriptions for the three dimensional curve. Here, choosing $\kappa_1(s) = a\cos(4\pi s)$, $\kappa_2(s) = a\sin(4\pi s)$, and $\kappa_3(s) = 0$ for $a \in \mathbb{R}$ produces an expanding spiral curve. The projection of the the curve onto the xy-axis is indicated by the grey line at $z = 0$.

for $s \in [0, 1]$, where $a \in \mathbb{R}$, and choose the proximal directors $\mathbf{d}_i(0) = \mathbf{e}_i$. The director frame is computed through solving the system of equations in (1.70), and the corresponding Frenet-Serret frame is computed using equations (1.76a)–(1.77b). The frames are plotted in figure 1.8. The Frenet-Serret normal (figure 1.8b) always points towards the centre of curvature, thereby rotating the frame along the arclength despite the lack of mechanical twist information in the frame formulas. This potential misunderstanding highlights the need for caution when identifying and using ambiguous terms such

as ‘normal’ and ‘binormal’ without proper specification of the frame by which they are defined.

1.3.2 Planar geometry

As will be discussed in chapter 2, in many situations and species, flagella and cilia exhibit approximately planar beats, making full knowledge of the director frame unnecessary. Of course, in two dimensions twist cannot be modelled, as nonplanar fibre shapes which can arise from twisting are not permitted. However, for an isotropic filament, no twisting arises from bending deformations, and so as long as no external twisting moment is applied, a cylindrical filament bending will not undergo spontaneous twisting deformations (Landau & Lifshitz, 1965). External nonplanar forces are similarly not permitted if they promote nonplanar bending.

With the reduction in dimension, the number of independent variables needed to describe the geometry of the filament also reduces. In the director frame representation, choosing $\mathbf{d}_1$ to lie in the plane of bending allows the curve to be completely described by $\kappa_2(s)$, with $\kappa_1(s) = \kappa_3(s) = 0$, $\forall s$. Using equations (1.76a)–(1.77b), the Frenet-Serret frame similarly reduces, with the torsion $\tau(s) = 0$ and the frame described by only the geodesic curvature $k(s)$.

The relation between k and κ_2 warrants a careful eye. Recalling equation (1.76a), the F-S curvature $k > 0$ is strictly positive whereas $\kappa_2 \in \mathbb{R}$. The Frenet-Serret frame for a planar curve is thus $(\mathbf{T}, \mathbf{N}, \mathbf{e}_z)$ if $k > 0$ and $(\mathbf{T}, -\mathbf{N}, -\mathbf{e}_z)$ if $k < 0$, where $\mathbf{T}$ and $\mathbf{N}$ are restricted to the plane of bending. As in the 3D case, the Frenet-Serret frame is undefined when $k = 0$. A sinusoidal curve produced by $\kappa_2(s) = a\sin(4\pi s)$ (reminiscent of a beating flagellum) will have a smoothly-varying director frame, but the correspond-

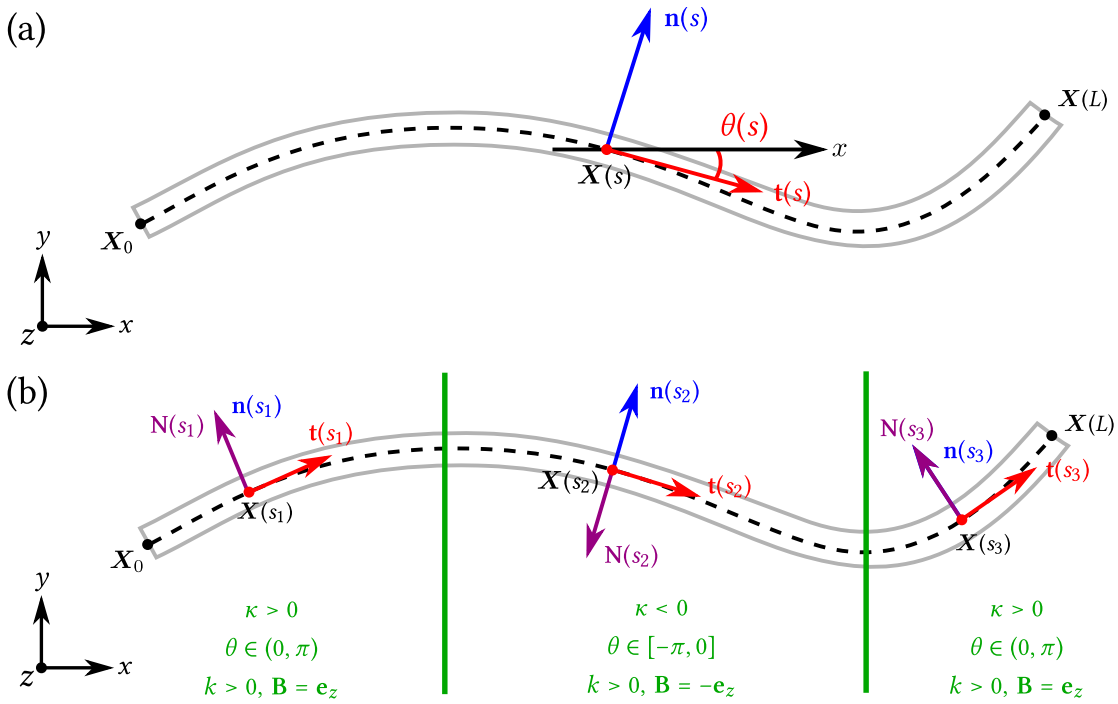

Figure 1.9: Geometric descriptions for a planar curve. (a) The centreline can be described using the tangent angle $\theta(s)$ between the tangent $\mathbf{t}(s)$ and the fixed Cartesian x-axis. (b) Nonnegativity of the geodesic curvature $k(s)$ requires the Frenet-Serret normal $\mathbf{N}(s)$ and binormal $\mathbf{B}(s)$ to 'flip' at each local extrema of the curve, unlike the director normal $\mathbf{n}(s)$, which is smoothly varying.

ing Frenet-Serret frame will 'flip' at each local extrema of the curve. This behaviour is illustrated figure 1.9b.

Planar curves are conveniently describable in terms of the tangent angle $\theta(s)$ formed between the tangent $\mathbf{t}(s)$ to the curve and a Cartesian basis vector lying in the plane of the filament. Consider an xy-planar filament; the tangent to the curve, by simple trigonometry, is

$$\mathbf{t}(s) = \boldsymbol{X}_s(s) = \cos\theta(s)\mathbf{e}_x + \sin\theta(s)\mathbf{e}_y, \tag{1.79}$$

where $\mathbf{e}_x$ and $\mathbf{e}_y$ are unit basis vectors pointing in the positive x- and y-axis directions

respectively. The curve centreline is thus expressible in terms of a single variable $\theta(s)$ using equation (1.68) as

$$\boldsymbol{X}(s) = \boldsymbol{X}_0 + \int_0^s \big(\cos\theta(\xi),\ \sin\theta(\xi),\ 0\big)^T d\xi. \tag{1.80}$$

A sketch of a planar curve described through this *angle formulation* is displayed in figure 1.9a.

The rate of change of the tangent angle along the curve (i.e $\theta_s(s)$) will determine the rotation of the tangent and normal, and thus the change in the corresponding geometric frame about the out-of-plane axis (which in this case is $\mathbf{e}_z$). This logic motivates the definition of the *signed curvature*,

$$\kappa(s) = \theta_s(s), \tag{1.81}$$

with restrictions on θ chosen so as to be suitable for a given problem. For example, the curve in figure 1.9b moves above and below the equilibrium (linear) state, and so taking $\theta(s) \in [-\pi, \pi)$ is sensible. The unit tangent and normal to the curve are

$$\mathbf{t}_s(s) = \theta_s(s)\mathbf{n}(s), \qquad \mathbf{n}_s(s) = -\theta_s(s)\mathbf{t}(s), \tag{1.82}$$

noting that $\mathbf{t} \equiv \mathbf{T} \equiv \mathbf{d}_3$, and $\mathbf{n} \equiv \mathbf{d}_1$ but $\mathbf{n} \equiv \mathbf{N}$ is not guaranteed due to the additional directionality the signed curvature has here over the Frenet-Serret curvature.

The three geometric descriptions of a planar filament considered here (that is, the planar director frame, the planar Frenet-Serret frame, and the angle formulation) are equivalent up to a change in sign. A schematic highlighting the similarities and differences of these frame models for a planar filament is given in figure 1.9b.

1.3.3 Equations of equilibrium

Armed with an understanding of how to best describe the geometry of a two or three dimensional flexible filament, in this section we consider the elastic properties of the filament to derive equations describing the force and moment resulting from deformation.

Consider a continuous filament suspended in a Stokes fluid. The filament may be *passive*, meaning that the filament has no means of self-actuation and so any dynamics are either purely due to elasticity or external effects. Alternatively, the filament may be *active*, impelled to dynamically bend or twist through an internal torque per unit length $\boldsymbol{m}$. Here we consider the (general) latter case.

Imagine an infinitesimal segment of arclength δs of filament from the interior of the filament (the boundary cases will be considered later on). The segment experiences contact forces $\boldsymbol{F}_{\text{int}}$ and moments $\boldsymbol{M}_{\text{int}}$ at each of its ends where it connects to adjacent segments. Specifically, $\boldsymbol{F}_{\text{int}}$ and $\boldsymbol{M}_{\text{int}}$ are the force and moment exerted by the distal segment $[s, L]$ onto the proximal section $[0, s]$. Since the rod is at equilibrium, they must act in opposite directions. An external viscous force per unit length $-\boldsymbol{f}$ acts on the entire segment, so that the force per unit length the filament exerts onto the fluid is $\boldsymbol{f}$. A schematic of the infinitesimal segment is given in figure 1.10. The balance of forces across the segment $[s, s + \delta s]$ is

$$\boldsymbol{F}_{\text{int}}(s + \delta s) - \boldsymbol{F}_{\text{int}}(s) - \delta s \boldsymbol{f}(s + \delta s/2) = \boldsymbol{0}, \tag{1.83}$$

where $\boldsymbol{F}_{\text{int}} = F_i \mathbf{d}_i$ is the elastic contact force exerted on the segment and $\boldsymbol{f} = f_i \mathbf{d}_i$ is the viscous force per unit length the segment exerts onto its surroundings. The axial component of the force F_3 can be understood as the internal elastic tension of the rod.

Dividing by δs, and taking the limit as $\delta s \longrightarrow 0$, we obtain the *force equilibrium equation*

$$\boldsymbol{F}_{\text{int},s}(s) - \boldsymbol{f}(s) = \mathbf{0}. \tag{1.84}$$

The balance of moments about the segment reads as

$$\begin{aligned}\boldsymbol{M}_{\text{int}}(s+\delta s) - \boldsymbol{M}_{\text{int}}(s) + \delta s\, \mathbf{d}_3(s) \times \boldsymbol{F}_{\text{int}}(s+\delta s) \\ - \delta s^2\, \mathbf{d}_3(s) \times \boldsymbol{f}(s+\delta s/2) + \delta s\, \boldsymbol{m}(s+\delta s/2) = \mathbf{0},\end{aligned} \tag{1.85}$$

where $\mathbf{d}_3 \equiv \mathbf{t}$ is the tangent to the rod, $\boldsymbol{M}_{\text{int}} = M_i \mathbf{d}_i$ is the internal elastic moment, and $\boldsymbol{m} = m_i \mathbf{d}_i$ is the internal active moment per unit length. Dividing by δs, in the $\delta s \longrightarrow 0$ limit, the higher order moment arising from to the viscous force per unit length $\boldsymbol{f}$ vanishes yielding the *moment equilibrium equation*

$$\boldsymbol{M}_{\text{int},s}(s) + \mathbf{d}_3(s) \times \boldsymbol{F}_{\text{int}}(s) + \boldsymbol{m}(s) = \mathbf{0}. \tag{1.86}$$

Equations (1.84) and (1.86), complemented by suitable boundary conditions, are referred to in this thesis as the *equilibrium equations*, and are the most general equations of motion for an elastic filament deforming in three dimensions. The elastic models developed in both chapters 2 and 4 derive from these equations.

The elastic moment may be written in terms of the director curvatures $\kappa_1(s)$, $\kappa_2(s)$ and $\kappa_3(s)$ through the constitutive equations for linear elasticity (Landau & Lifshitz, 1965; Audoly & Pomeau, 2010),

$$\boldsymbol{M}_{\text{int}}(s) = M_i(s)\mathbf{d}_i(s) = E\Big(\kappa_1(s)\mathbf{d}_1(s) + \kappa_2(s)\mathbf{d}_2(s)\Big) + C\kappa_3(s)\mathbf{d}_3(s), \tag{1.87}$$

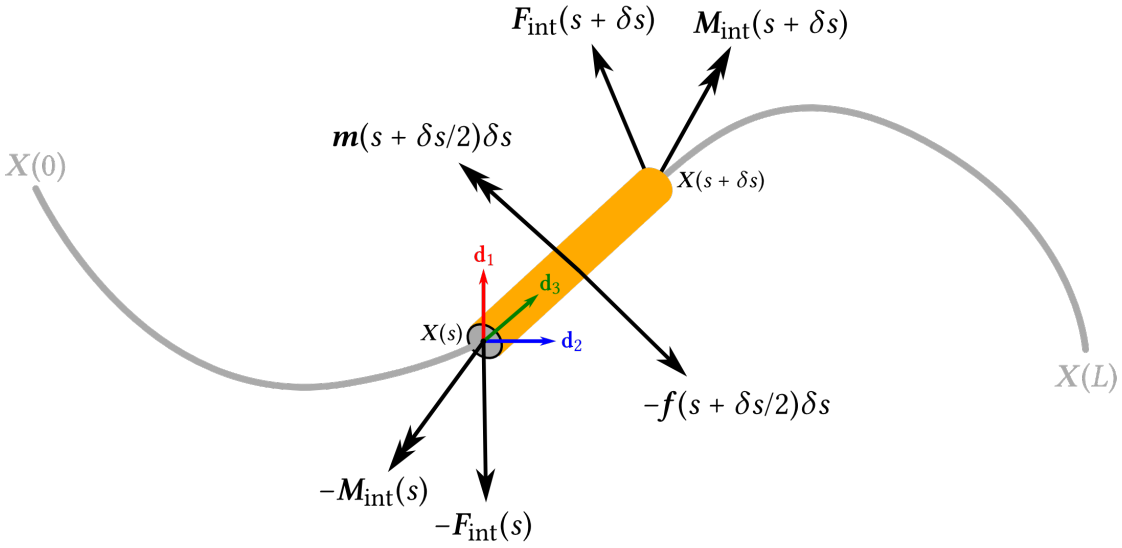

Figure 1.10: Schematic of the the balance of forces and moments acting on an infinitesimal segment of a passive filament. The orientation of the segment is defined by the orthonormal director triad $\{\mathbf{d}_1, \mathbf{d}_2, \mathbf{d}_3\}$. Single-headed arrows indicate forces, and double-headed arrows indicate moments.

where E is the *flexural rigidity* characterising the filaments resistance to bending, and C is the *twisting modulus* with a similar interpretation but for twist deformations. Here, we assume that E is invariant along the arclength; in sections 2.5 and 4.2.3 we consider the effect of spatially varying E. Despite the complex structure of the flagellum axoneme, the linear elasticity model (1.87) has been shown to be accurate for moderate levels of deformation (Hines & Blum, 1983); recent studies using nonlinear elasticity models have been used to recover the counterbend phenomenon discussed in section 1.1.2 (Gadelha, 2018).

Noting that $\kappa_1\mathbf{d}_1 + \kappa_2\mathbf{d}_2 = \mathbf{t}\times\mathbf{t}_s$, equation (1.87) can be rewritten in terms of the rod centreline position $\boldsymbol{X}(s)$ as

$$\boldsymbol{M}_{\text{int}}(s) = E\boldsymbol{X}_s(s)\times\boldsymbol{X}_{ss}(s) + C\kappa_3(s)\boldsymbol{X}_s(s). \tag{1.88}$$

The formula in equation (1.88) is only valid for isotropic rods, whereas the axoneme is decidedly nonhomogenous due to the presence of the central pair (see figure 1.1). Thus E is the effective bending stiffness when (1.88) is applied to model flagella. The twisting rigidity is a combination $C = \nu J$, where ν is the shear modulus and J is the twist rigidity. For a rod with circular cross section, $J = (\pi/2)a^4$ with a the radius (Audoly & Pomeau, 2010).

In summary, the three dimensional bending and twisting of an elastic filament is completely described by

$$\boldsymbol{M}_{\text{int}} = E(\kappa_1 \mathbf{d}_1 + \kappa_2 \mathbf{d}_2) + C\kappa_3 \mathbf{d}_3 = E\boldsymbol{X}_s \times \boldsymbol{X}_{ss} + C\kappa_3 \boldsymbol{X}_s, \tag{1.89a}$$

$$\boldsymbol{M}_{\text{int},s} + \mathbf{d}_3 \times \boldsymbol{F}_{\text{int}} + \boldsymbol{m} = \mathbf{0}, \tag{1.89b}$$

$$\boldsymbol{F}_{\text{int},s} - \boldsymbol{f} = \mathbf{0}, \tag{1.89c}$$

$$\mathbf{d}_{i,s} = \boldsymbol{\kappa} \times \mathbf{d}_i, \qquad i = 1, 2, 3, \tag{1.89d}$$

$$\mathbf{d}_{i,t} = \boldsymbol{\Omega} \times \mathbf{d}_i, \qquad i = 1, 2, 3. \tag{1.89e}$$

The collection comprising the constitutive elasticity law (1.89a), equilibrium equations (1.89b–1.89c), and director frame kinematic relations (1.89d–1.89e) is referred to as the *Kirchhoff equations*.

For a free filament in Stokes flow, inertialess dynamics means that the force and moment at each end will be zero, thus providing the required boundary conditions as $\boldsymbol{F}_{\text{int}}(0) = \boldsymbol{F}_{\text{int}}(L) = \mathbf{0}$ and $\boldsymbol{M}_{\text{int}}(0) = \boldsymbol{M}_{\text{int}}(L) = \mathbf{0}$. Alternatively, the filament could be *clamped* at a material domain point, or to a surface. Rotation and movement about the point of attachment is not allowed, and so both position and tangent vector are invariant in time, yielding the proximal boundary conditions $\boldsymbol{X}_t(0) = \boldsymbol{X}_{st}(0) = \mathbf{0}$. Fix-

ing the connection point, but allowing for rotations leads to the *pivot* problem, with boundary conditions $\boldsymbol{X}_t(0) = \boldsymbol{M}_{\text{int}}(0) = \mathbf{0}$. Other boundary conditions, accounting for the presence of a connected cell body, are discussed later in chapters 2 and 4.

1.4 Models for two and three dimensional elastohydrodynamics

For the past twenty years, there has been a sustained and continuous desire within the biomathematical community to develop elastohydrodynamic models for cilia and flagella (Gueron & Levit-Gurevich, 2001b; Wolgemuth *et al.*, 2004; Tornberg & Shelley, 2004; Gadêlha *et al.*, 2010; Jayaraman *et al.*, 2012; Olson & Fauci, 2015; Montenegro-Johnson *et al.*, 2015; Schoeller *et al.*, 2021; Hall-McNair *et al.*, 2019; Walker *et al.*, 2019). Interdisciplinary research into microbiological problems, particularly those involving motile microorganisms and organelles, has led to increased interest in understanding the fundamental interactions between fluids and elastic cellular structures. Greater availability and access to ever-increasingly computationally-powerful consumer electronics has enabled traditionally "heavy" problems (such as those involving complex fluid interactions and very large collections of fibres (Delmotte *et al.*, 2015b; Schoeller *et al.*, 2021)) to be tackled without the need of high performance computing (HPC) clusters (Hall-McNair *et al.*, 2019; Walker *et al.*, 2019; Neal *et al.*, 2020).

Elastohydrodynamic models for microscale filaments consider the interaction between the elastic physics of the body and surrounding fluid dynamics. Developments towards improving accuracy and applicability of such methods include advances in the elasticity model, fluid flow approximation, and numerical methods allowing for efficient simulations. In the following section, we examine the recent literature, discussing the rich variety of modelling approaches for elastohydrodynamic filaments, within the context of microscale motion.

In what follows, we refer to a mathematical model as being *local* if it employs a reduced hydrodynamic model incapable of accounting for the hydrodynamic influence

of other surrounding objects or structures. Conversely, models capturing these effects are labelled *nonlocal*. Moreover, models which account only for two dimensional dynamics of filaments or flagella are referred to as *planar*. Approaches accounting for three dimensional geometries and elasticity are called *nonplanar* or *3D*. Note that a particular hydrodynamic model does not necessitate a certain geometric description – equations of motion that describe nonplanar nonlocal hydrodynamics whilst assuming only planar elastic deformations are perfectly valid for certain problems, and vice versa. A summary of key models discussed within this literature review is presented in table 1.2.

1.4.1 Lagrange multipliers for tension

A key feature of the microbiological problems considered within this thesis is the requirement of inextensibility, so that the slender body does not stretch or shrink over time. Approaches to enforcing this geometric constraint are a significant differentiating feature between previously developed elastohydrodynamic models. One frequently adopted method introduces Lagrange multipliers working to enforce $\boldsymbol{X}_{st} \cdot \boldsymbol{X}_s = 1$ (or equivalent expressions), where $\boldsymbol{X}$ are material points lying on the centreline parametrised by dimensionless arclength $s \in [0, 1]$. Such approaches result in additional unknown tensile force terms appearing in the model equations, which act along the axis of the filament.

We begin with a Lagrangian description of the physical problem following classical principles, outlined in detail by Goldstein & Langer (1995). The filament is parametrised by its arclength $s \in [0, L]$ so that $\boldsymbol{X}$ and $\boldsymbol{X}_t$ are material centreline points

and their velocities respectively. Lagrange's equations describe the motion through

$$\frac{d}{dt}\left\{\frac{\partial \mathcal{L}}{\partial \boldsymbol{X}_t}\right\} - \frac{\partial \mathcal{L}}{\partial \boldsymbol{X}} = -\frac{\partial \mathcal{R}}{\partial \boldsymbol{X}_t} = \boldsymbol{f}_{\text{vis}}, \tag{1.90}$$

where $\mathcal{L}$ is the Lagrangian and $\mathcal{R}$ is the Rayleigh function describing the energy dissipation due to viscous forces $\boldsymbol{f}_{\text{vis}}$ acting on the filament. The mechanical energy in the system corresponding to the Lagrangian is

$$\mathcal{E} = \int_0^L \boldsymbol{X}_t \cdot \frac{\partial \mathcal{L}}{\partial \boldsymbol{X}_t}\, ds - \mathcal{L}. \tag{1.91}$$

At very low Reynolds number, inertial effects are negligible and thus $\mathcal{L} = -\mathcal{E}$. Equation (1.90) becomes

$$\boldsymbol{f}_{\text{vis}} = -\boldsymbol{f}_{\text{int}} = \frac{\partial \mathcal{E}}{\partial \boldsymbol{X}}, \tag{1.92}$$

noting that the hydrodynamic drag density and elastic force per unit length $\boldsymbol{f}_{\text{int}}$ must balance in the inertialess dynamics regime. Continuing, Goldstein & Langer (1995) enforce arclength conservation by imposing a Lagrange multiplier function $\Lambda(s)$ so that

$$\mathcal{E} = \mathcal{E}^e - \int_0^L \sqrt{g}\Lambda\, ds, \tag{1.93}$$

where $g(s) = \boldsymbol{X}_s(s) \cdot \boldsymbol{X}_s(s)$ is the metric for inextensibility, and $\mathcal{E}^e$ is the elastic energy of the filament due to deformations. The Lagrange multiplier $\Lambda(s)$ acts to resist extension or compression, and is related to the physical tension within the filament. The original paper concludes by completing the model formulation, assuming a local hydrodynamic model, and applying it to model the folding dynamics of closed filaments.

The energy argument outlined in equations (1.90–1.93) forms the basis of many

elastohydrodynamic models in the literature (Camalet *et al.*, 1999; Camalet & Jülicher, 2000; Wolgemuth *et al.*, 2004; Lim *et al.*, 2008; Lim, 2010; Olson & Fauci, 2015). Indeed, subsequent work in Goldstein *et al.* (1998) builds upon their initial model, simplifying the model equations by using a complex curvature parametrisation rather than one in terms of Euclidean position. Their approach is applied to the modelling of twisting filaments, observing the interplay between twisting and writhing dynamics. The complex curvature formulation is further employed in Wiggins & Goldstein (1998), forming the basis for an analytical study into the importance of elastohydrodynamics in low Reynolds number propulsion. A related approach to reducing the complexity of the equations of motion is taken by Coq *et al.* (2009)[1], who use a spatial Fourier transform to solve the nonlinear elastics problem coupled with resistive force theory to investigate modes of helical wave propagation.

The generalised 3D complex curvature model, proposed by Goldstein *et al.* (1998), was expanded by Wolgemuth *et al.* (2000) to account for nonlocal hydrodynamic interactions using slender body theory. Filaments are actuated through a 'crankshaft' motion; the fibre is pinned in space at one end, and rotated about its centreline tangent at the point through a twist injection, in a motion akin to a drive shaft in an engine. Simulations of filaments driven in this way revealed that twist/writhe buckling regimes follow a Hopf bifurcation due to the competing forces from the active twisting (turning the filament at its base), twist diffusion, and writhing.

Versatility of the energy functional argument, and in particular its description of the equations of motion in terms of positions, promotes it as a natural modelling choice for reduced planar problems. In a pair of papers from the mid 2000s, Zhu & Peskin

[1]Whilst the elastohydrodynamic method considered in Coq *et al.* (2009) features no inextensibility constraint, we mention it here for its novel method for reducing the complexity of the model equations.

depart from much of the literature by simulating the planar dynamics of filaments in an incompressible two dimensional Navier-Stokes fluid, solved using the immersed boundary integral method, considering first flapping in soap films (Zhu & Peskin, 2002) and later fibres in shear (Zhu & Peskin, 2007), noting the effects of filament length and flexibility on beat shape and drag.

Numerical instabilities in solving for the tension equation can propagate, leading to unwanted errors and potential violation of the inextensibility condition. By instead enforcing inextensibility through the numerical approximation

$$\frac{1}{2}(\boldsymbol{X}_s \cdot \boldsymbol{X}_s)_t = \boldsymbol{X}_s \cdot \boldsymbol{X}_{ts} = \lambda(1 - \boldsymbol{X}_s \cdot \boldsymbol{X}_s), \tag{1.94}$$

errors in length are removed, with λ a constant defining the strength of the damping (Tornberg & Shelley, 2004). Large values for λ will punish even small deviations in the flagellum length (given by $\boldsymbol{X}_s \cdot \boldsymbol{X}_s$) from the desired unit value. The form in equation (1.94) can be physically interpreted as arising from a linear spring, with stiffness linearly proportional to λ, acting instantaneously at each material point of the filament and working to preserve arclength. Coupling nonlocal hydrodynamics via slender body theory with equations for 3D bending, Tornberg & Shelley (2004) simulate large arrays of passive filaments in shear and examine the buckling arising therein, in a setup analogous to the macroscale structure of viscoelastic fluids comprising long, thin, elastic fibres. Similar studies into filaments in shear have been performed by Pozrikidis (2011); Bouzarth *et al.* (2011).

Gadêlha *et al.* (2010) highlights the differences in cell shape and trajectory obtained when modelling the flagellum using either geometrically linear or nonlinear beam theory. In many biophysical scenarios, such as sperm swimming in cervical mucus, flag-

ellum curvature is high, yielding linear beam theory inappropriate. With this in mind, the authors derive the *sperm equation*,

$$\mathrm{Sp}^4 \boldsymbol{X}_t = -\boldsymbol{X}_{ssss} - (\gamma - 1)(\boldsymbol{X}_s \cdot \boldsymbol{X}_{ssss})\boldsymbol{X}_s + T\boldsymbol{X}_{ss} + \gamma T_s \boldsymbol{X}_s + f_s \mathbf{n} + \gamma f \mathbf{n}_s, \tag{1.95}$$

a geometrically nonlinear equation for the flagellum centreline $\boldsymbol{X}(s, t)$, where $\gamma = c_\perp / c_\parallel$ describes the ratio of normal to tangential viscous drag, T is the Lagrange multiplier of tension, and f is a prescribed function controlling the active shear of the flagellum. The sperm number, which indicates the relative dominance of viscous effects to elasticity, is defined

$$\mathrm{Sp} = L \left(\frac{c_\perp \omega}{E} \right)^{1/4}, \tag{1.96}$$

and derives from nondimensionalisation of the underlying linear partial differential equations. Similar parameters, though not labelled as such, are used in early modern studies by Wiggins & Goldstein (1998) and Camalet *et al.* (1999). Gadêlha *et al.* (2010) couple a planar elastohydrodynamic filament to a rigid three dimensional ellipsoid approximating the sperm head, with fluid interactions approximated using resistive force theory. The model predicts the spontaneous emergence of buckling modes altering the direction of swimming when using the nonlinear geometric model. This behaviour is observed across a range of governing actuation and viscoelastic parameters, concluding that shape nonlinearity is essential in the rheology of motile sperm and cilia. The model was later adopted by Montenegro-Johnson *et al.* (2015), extended to include nonlocal hydrodynamics through a combination of L.G.L. theory (Gueron & Liron, 1992), regularised stokeslets, and the standard boundary element method. Sperm cells swimming over a microchannel backstep are deflected in relation to the viscous and elastic parameters of the fluid and flagellum, with important applications in microchannel

fabrication for assisted reproduction techniques.

1.4.2 Bead models

Alongside continuum models for geometry, extensive research continues into direct discrete models for geometrically nonlinear filaments. Such models often describe the fibre as a sequence of connected discs (in two dimensions) or spheres (in three dimensions), and so are thus referred to here as *bead models*. As a result of their versatility and relative ease of implementation, researchers from a wide range of scientific disciplines have used bead models, with particularly extensive use in polymer physics (Yamakawa, 1970; Meunier, 1994; Jian *et al.*, 1997; Jendrejack *et al.*, 2000, 2002; Schroeder *et al.*, 2004; Schlagberger & Netz, 2005; Bailey *et al.*, 2008; Yamanoi *et al.*, 2010; Gao *et al.*, 2012). Here, we consider only their applications in the mechanics of biofluids.

A continuous elastic filament is discretised through beads placed along its length. For a particular bead model, one must consider three key effects: elasticity between beads, hydrodynamics of individual and connected beads, and kinematic constraints enforcing, for example, fixed bead spacing or macroscale inextensibility. Bead models generally fall into one of three variants, which address primarily the elastic and constraint problems in different ways. Hydrodynamic considerations can be considered separately provided the formulation is consistent. Following the terminology of Delmotte *et al.* (2015a), these categories are spring models (SM), joint models (JM), and gears models (GM). A diagram illustrating these constructions (redrawn from Delmotte *et al.* (2015a)) is given in figure 1.11. In what follows, we consider examples across the literature of all three model types.

An early and comprehensive study by Yamamoto & Matsuoka (1993) used a bead

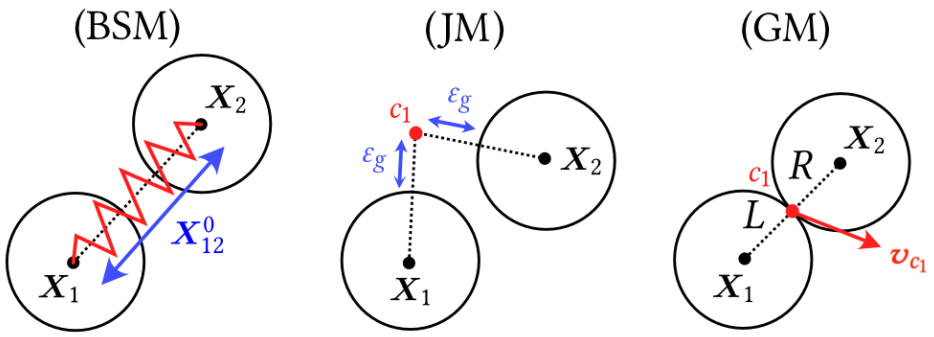

Figure 1.11: Schematic comparing different bead models. In the bead and spring model (BSM), a linear spring works to preserve the inter particle distance. The joint model (JM) assumes bending occurs about connection points c_i exterior to beads. Choosing the outer spacing ε_g too small leads to overlapping upon bending. Gears models (GM) enforce a no slip condition between beads, so that the velocity of the connection point c_i is $\boldsymbol{v}_{c_i}$ between each pair. Figure redrawn from Delmotte *et al.* (2015a).

model for three dimensional elasticity, accounting for bending, stretching, and twisting. Inextensibility is enforced through a spring model, with elastic deformations included by considering the torque generated following rotations between successive beads, constrained by elasticity constants describing the material properties of the filament. Modelling fluid dynamic interactions through local Stokes drag laws for the force and moment, simulations of filaments in shear flow produced results in good agreement with the analytic results of Jeffery (1922) (for rigid fibres) and experimental observations of flexible fibres (Yamamoto & Matsuoka, 1993). Lowe (2003) improves the accuracy of the local hydrodynamic model when applied to moderately slender rods, numerically precomputing resistance coefficients based on those for a filament of infinite length (derived much earlier by Cox (1970)). By comparing their model to experimental results at the time, Lowe highlights a disagreement in results theorised to derive from underestimating the flagellum stiffness.

Schlagberger & Netz (2005) employed a BSM to describe the elastohydrodynamic

behaviour of filaments moving through gravitational and electrical fields, with simulation results matching observations of buckling in anomalous electric birefringence experiments on viral particles. A similar approach by Jayaraman *et al.* (2012) couples a nonlocal singular stokeslet hydrodynamic model to the BSM elastics to model the buckling of an inextensible fibre in an extensional flow. In particular, Jayaraman *et al.* include a Lennard-Jones potential to prevent filament self-intersections. To model inextensible filaments, spring models necessitate large values for the spring constants, contributing greatly to the numerical stiffness of the problem and thus limiting their use for flagellar modelling. Linear spring models can be prone to spurious oscillations leading to potential instabilities (Delmotte *et al.*, 2015b); nonlinear springs have proven to be effective in avoiding this issue (Jendrejack *et al.*, 2000, 2002) but have thus far been used primarily only in polymer simulations as opposed to flagella modelling. Nonetheless, bead models remain a popular choice for modelling elastohydrodynamic filaments, with recent work by Zuk *et al.* (2021) coupling the spring model for elasticity with a general Rotne-Prager-Yamaka (RPY) tensor and multipole expansion with lubrication corrections,x to further probe the buckling phenomenon of elastica in shear. In the RPY approach, hydrodynamic velocities $\boldsymbol{u}_n$ and angular velocities $\boldsymbol{\omega}_n$ of $n = 1, \dots, N$ beads are approximated by

$$\begin{pmatrix} \boldsymbol{u}_n \\ \boldsymbol{\omega}_n \end{pmatrix} = \sum_{n=1}^{N} \begin{pmatrix} \boldsymbol{M}_{nm}^{\mathrm{tt}} & \boldsymbol{M}_{nm}^{\mathrm{tr}} \\ \boldsymbol{M}_{nm}^{\mathrm{rt}} & \boldsymbol{M}_{nm}^{\mathrm{rr}} \end{pmatrix} \begin{pmatrix} \boldsymbol{F}_m \\ \boldsymbol{M}_m \end{pmatrix}, \tag{1.97}$$

where $\boldsymbol{F}_m$ and $\boldsymbol{M}_m$ are the force and moment exerted by the bead onto the fluid. In an

infinite fluid, the component subtensors are defined

$$\boldsymbol{M}^{\mathrm{tt}}_{nm} = \frac{\delta_{nm}}{6\pi\mu a}\boldsymbol{I} + \frac{1-\delta_{nm}}{8\pi\mu r_{nm}}\left(\left(1+\frac{2a^2}{3r^2_{nm}}\right)\boldsymbol{I} + \left(1-\frac{2a^2}{r^2_{nm}}\hat{\boldsymbol{r}}_{nm}\hat{\boldsymbol{r}}_{nm}\right)\right), \tag{1.98a}$$

$$\boldsymbol{M}^{\mathrm{rr}}_{nm} = \frac{\delta_{nm}}{8\pi\mu a^3}\boldsymbol{I} + \frac{1-\delta_{nm}}{16\pi\mu r^3_{nm}}(3\hat{\boldsymbol{r}}_{ij}\hat{\boldsymbol{r}}_{nm} - \boldsymbol{I}), \tag{1.98b}$$

$$\boldsymbol{M}^{\mathrm{tr}}_{nm} = \boldsymbol{M}^{\mathrm{rt}}_{nm} = \frac{1-\delta_{nm}}{8\pi\mu r^2_{nm}}\boldsymbol{\epsilon}\cdot\hat{\boldsymbol{r}}_{nm}, \tag{1.98c}$$

where $\boldsymbol{I}$ is the three dimensional identity matrix, $\boldsymbol{\epsilon}$ is the Levi-Civita tensor, a is the bead radius, μ is the fluid dynamic viscosity, and $\hat{\boldsymbol{r}}_{nm} = \boldsymbol{r}_{nm}/\|\boldsymbol{r}_{nm}\|$, where $\boldsymbol{r}_{nm}$ is the vector separating the n^{th} and m^{th} beads (Schoeller *et al.*, 2021).

An alternative approach is that of a joint model (JM), which assumes that adjacent beads connect at exterior contact points c_i off or close to the surface of the beads (see figure 1.11). These approaches have been used for simulating fibre flocculation (Schmid *et al.*, 2000) and filament suspensions (Qi, 2006). Joint models, whilst alleviating stiffness caused by spring stiffness, feature an additional constraint on the allowable curvature of the macroscale filament before beads overlap, expressible in terms of the bead radius a and joint distance ε_g as

$$\kappa_{\max} = \frac{1}{a}\sqrt{1-\left(\frac{a}{a+\varepsilon_g}\right)^2}. \tag{1.99}$$

With this in mind, problems with, or producing, highly nonlinear geometric filament shapes warrant larger values of ε_g, leading to potential violation of the nonholonomic requirement, making joint models undesirable for modelling, for example, hyperactivated sperm cells.

Delmotte *et al.* (2015a) proposes the gears model (GM), geared to address the short-

comings of other types of bead model through assumption of a no-slip nonholonomic condition between connected beads. Kinematic constraints are enforced through an Euler-Lagrange formalism, with elasticity in the model described through the familiar constitutive bending laws discussed in section 1.3.3 (Landau & Lifshitz, 1965). Nonlocal hydrodynamics are included through use of the RPY tensor (see equation (1.97)), including modifications by Wajnryb *et al.* (2013) to include shear effects. The resulting model is applied to a number of dynamic 2D and 3D problems, with the authors noting improved stability and increased applicability of their approach opposed to spring- and joint-type bead models.

1.4.3 Kirchhoff rod models

Increases in computational power over the past two decades have allowed increasingly complex descriptions of nonlinear geometry, elasticity, and nonlocal hydrodynamics to be coupled and solved to comprehensively simulate problems in elastohydrodynamics. As a result, methods directly coupling the Kirchhoff equations (derived in section 1.3.3) for slender body elastodynamics with hydrodynamics have become increasingly popular. We refer to such models as *Kirchhoff rod models*. Whilst deriving from similar continuum principles, Kirchhoff rod formulations contrast to models deriving from an energy-derived formulation in explicitly including variables describing the three dimensional orientation of the filament at each material point, a detail treated implicitly in other approaches.

A number of early studies considered three dimensional elastic filaments in the absence of hydrodynamics. Developments in the mid-1990s by Klapper & Tabor (1994) derived model equations for general elastic deformations through a similar but distinct

'ribbon' description for twisting fibres. Later improvements in Klapper (1996) used a modified Frenet-Serret orthonormal frame to avoid singularities for cases of zero curvature. A study by Bishop *et al.* (2004) considering purely elastodynamics provided analytical solutions to many simple problems, afforded by the reduced complexity of the isolated setup.

Coupling with a local hydrodynamic force model, Goriely & Tabor (2000) probed the stability of twisted rings and rods, enforcing inextensibility in the latter using a novel perturbation scheme. Wolgemuth *et al.* (2004) considered the dynamics of growing elastic filaments in fluid, formulating equations with a time-varying extensibility constraint. The authors show, through both numerical simulation and linear stability analysis, two dynamic regimes, with small amounts of twist leading to Euler beam-like buckling, and large amounts of twist producing writhing, plectonemic windings comparable to common polymer configurations.

A distinct but heuristically similar model following classical arguments from Landau & Lifshitz (1965) was presented in Gueron & Levit-Gurevich (2001a,b), building upon previous works examining the dynamics of cilia and multicilia interactions (Gueron & Liron, 1992, 1993; Gueron & Levit-Gurevich, 1998). The equations of motion for the filament are given as functions of the curvatures, and coupled with a bespoke nonlocal hydrodynamic scheme accounting for fluid interactions with nearby objects and boundaries. The resulting framework is extremely versatile for elastohydrodynamic modelling of slender bodies. A detailed study of ciliary motion demonstrates metachronal coordination arising from nonlocal hydrodynamics (Gueron & Levit-Gurevich, 2001b).

In a pair of publications, Lim and coauthors employed Kirchhoff models to simulate elastica coupled with the incompressible Navier-Stokes equations. Considering

first closed hoop shapes, Lim *et al.* (2008) provides insight on the buckling and sensitivity of bending and twisting closed fibres to perturbations in their initial condition. The formulation was then applied to investigate the buckling of open filaments (Lim, 2010). Defining fibres with a nonzero intrinsic curvature leads to a distinction between buckled helix-like shapes and stable helices.

Contemporary studies by Olson *et al.* (2013) incorporate the method of regularised stokeslets to further improve the accuracy of coupled hydrodynamic interactions. Applying their framework to a range of elastohydrodynamic problems, Olson and coauthors note the substantial reduction in computational cost a Kirchhoff rod model with meshless hydrodynamics boasts over general boundary integral methods. This model forms the base of Huang *et al.* (2018), extending the hydrodynamic model to include wall interactions. Considering a variety of parameter-driven planar, helical, and quasi-planar beats, they find that helical beats are less propulsive than planar waveforms. Recent work in Carichino & Olson (2019) further extends the framework introduced in Olson *et al.* (2013) by incorporating a calcium-curvature coupling to generate propulsive waveforms through control of a calcium gradient, providing insights into the interplay between microscale mechanosensing of sperm and macroscale elastohydrodynamic effects.

A recent comprehensive modelling framework, proposed by Schoeller *et al.* (2021), avoids singularities in curvature and stiff partial differential equations by recasting the problem using quaternions to track rotations of the director frames. For example, using the notation of the paper, the constitutive moment equation (equivalent to equation (1.87))

$$\boldsymbol{M} = K_B\left[\hat{\boldsymbol{\mu}}(\hat{\boldsymbol{t}}\cdot\hat{\boldsymbol{\nu}}_s - \kappa_\mu) + \hat{\boldsymbol{\nu}}(\hat{\boldsymbol{\mu}}\cdot\hat{\boldsymbol{t}}_s - \kappa_\nu)\right] + K_T\hat{\boldsymbol{t}}\left[\hat{\boldsymbol{\nu}}\cdot\hat{\boldsymbol{\mu}}_s - \gamma_0\right], \tag{1.100}$$

(where $\{\hat{\boldsymbol{t}}, \hat{\boldsymbol{\mu}}, \hat{\boldsymbol{\nu}}\}$ form an orthonormal basis, κ_μ, κ_ν and γ_0 are intrinsic curvatures, and K_B and K_T are bending and twisting moduli) can be rewritten in the compact form

$$\boldsymbol{M} = \mathbf{R}(\mathbf{q})\,\mathbf{D}\Big([2\mathbf{q}^* \bullet \mathbf{q}_s]_{\mathbb{R}^3} - (\gamma_0, \kappa_\mu, \kappa_\nu)^T\Big), \tag{1.101}$$

where $\mathbf{q}$ is a unit quaternion, $\mathbf{R}(\mathbf{q}) = (\hat{\boldsymbol{t}}, \hat{\boldsymbol{\mu}}, \hat{\boldsymbol{\nu}})$ and $\mathbf{D} = \mathrm{diag}(K_T, K_B, K_B)$. Other model equations are similarly rewritten. Using quaternions provides the additional benefit of reducing algorithmic memory requirements compared to storing rotation matrices, which can be very large, depending on the resolution and number of filaments considered. Modelling nonlocal hydrodynamics using the force coupling method, extremely large suspensions of both active and passive filaments can be modelled, allowing for simulations of complex experiments previously confined to a laboratory setting.

1.4.4 Angle formulations

Despite the generality and versatility of many of the approaches considered in this review, in many cases, the resulting model equations are collections of highly-nonlinear, highly-coupled partial differential equations. Such systems require careful discretisation and often yield tight restrictions on allowable time step sizes, with simulations (even those exploiting modern parallelisation techniques) measuring on the order of hours, if not days, of CPU time.

There has been a surge of recent interest in alternative approaches in modelling and numerical implementation to alleviate this cost. Moreau *et al.* (2018) demonstrated that by defining nonlinear planar filament geometry through the evolving tangent angle, elastohydrodynamic problems could be described with reduced degrees of freedom with great accuracy. Employing a *method of lines* description of the filament, equa-

tion (1.80) can be discretised as

$$\tilde{\boldsymbol{X}}[m] = \boldsymbol{X}_0 + \sum_{n=1}^{N-1} \Delta s\big(\cos\theta[n],\ \sin\theta[n],\ 0\big)^T, \qquad m = 1, \dots, N-1, \tag{1.102}$$

with fixed segment length Δs, conservation of arclength is guaranteed, negating the need for computationally-costly Lagrange multipliers of tension or stiff restorative springs. Coupling with a local hydrodynamic model, Moreau *et al.* (2018) show the versatility of this approach by simulating crosslinked filament bundles, fibre buckling, and magnetically actuated swimmers.

The angle formulation method was extended to included nonlocal hydrodynamic interactions using regularised stokeslets in Hall-McNair *et al.* (2019), employing additional numerical techniques such as regularised stokeslet segments (Smith, 2009; Cortez, 2018) (see section 1.2.9 for details) to retain accuracy in coarsely-discretised problems. This original work is discussed in detail within chapter 2 of this thesis.

Subsequent work in Walker *et al.* (2019); Walker & Gaffney (2021b) improves the force approximation on segments from piecewise constant to piecewise linear, addressing potential hydrodynamic errors at the filament ends, and using regularised blakelets to simulate elastohydrodynamics swimming close to surfaces. Simulating swimmers perpendicular to the surface, the authors note the inaccuracy of constant-coefficient local hydrodynamic methods over nonlocal models. Walker & Gaffney (2021a) extended their formulation to model nonplanar filaments with bend and twist, using a novel basis transformation technique to avoid singularities in the Euler angle description of the piecewise linear filament. The increase in complexity arising from consideration of 3D deformations is balanced by a reduction in the hydrodynamic model, returning to resistive force theory for ease of implementation.

Authors & Year	**Elasticity**	**Hydrodynamics**
Brokaw (1971)	2D	Local; RFT
Hines & Blum (1978)	2D	Local; RFT
Gueron & Liron (1992)	2D	Nonlocal; LGL
Yamamoto & Matsuoka (1993)	3D-B	Local; Stokes law
Goldstein & Langer (1995)	3D-BT	Local; RFT
Camalet & Jülicher (2000)	2D	Local; RFT
Goriely & Tabor (2000)	3D-BT	Local; RFT
Wolgemuth *et al.* (2000)	3D-BT	Nonlocal; SBT
Gueron & Levit-Gurevich (2001b)	3D-BT	Nonlocal; LGL
Tornberg & Shelley (2004)	3D-B	Nonlocal; SBT
Gadêlha *et al.* (2010)	3D-B	Local; RFT
Pozrikidis (2011)	3D-B	Nonlocal; SBT
Bouzarth *et al.* (2011)	2D	Nonlocal; RSM
Olson *et al.* (2013)	3D-BT	Nonlocal; RSM
Simons *et al.* (2015)	2D	Nonlocal; RBM
Delmotte *et al.* (2015a)	2D	Nonlocal; RPY
Montenegro-Johnson *et al.* (2015)	3D-B	Nonlocal; LGL, RSM
Huang *et al.* (2018)	3D-BT	Nonlocal; RBM
Hall-McNair *et al.* (2019)	2D	Nonlocal; RSM

Table 1.2: Summary of the key modelling features for a selection of approaches discussed within this review. Elasticity models are divided into three categories (a) 2D, for models only allowing two dimensional bending, (b) 3D-B, for models allowing three dimensional geometry but only bending deformations, and (c) 3D-BT, for models accounting for both bending and twisting deformations. Abbreviations are as follows: RFT: Gray & Hancock (1955) resistive force theory; SBT: slender body theory; LGL: Lighthill–Gueron–Liron theory (Gueron & Liron, 1992); RPY: Rotne–Prager–Yamakawa tensor method; RSM: regularised stokeslet method (Cortez, 2001; Cortez *et al.*, 2005); RBM: regularised blakelet method (Ainley *et al.*, 2008).

Building upon Hall-McNair *et al.* (2019), Neal *et al.* (2020) applied the nonlocal angle formulation approach to human sperm cells, extending the model equations for an isotropic filament to account for many physiological features of the spermatozoon flagellum. Systematic simulations over a wide range of possible types of actuation reveal that the presence of a mechanically inactive end piece (that is, a region of flagellum not generating active bending) increases propulsive speed and swimming efficiency. The importance of the end piece was postulated by Omoto & Brokaw (1982), who was unable to verify his claim, suggesting that verification would come from future numerical simulations.

1.5 Overview of this thesis

The rest of this thesis is structured as follows: in chapter 2, we present an angle formulation model for simulating planar elastic filaments in Stokes flows, accounting for nonlocal hydrodynamic interactions using the method of regularised stokeslets. The formulation, referred to as the *EIF*, is benchmarked against a similar angle formulation using a local hydrodynamic drag law, and a nonlocal bead and spring model employing the regularised stokeslet method. We then demonstrate the applicability and performance of the method by simulating single and multiple filaments in shear flow, sedimenting due to gravity, and swimming via a prescribed active moment per unit length.

Chapter 3 investigates the effect of human sperm body morphology on cell swimming speed and efficiency, modelled using the EIF method augmented to model human sperm following extensions by Neal *et al.* (2020). We consider three dimensional bodies of varying axes length but fixed volume, and fixed length ratios with varying volume, assessing the swimming speed and efficiency of swimmers compared to a cell with an average-shaped body.

In chapter 4, we introduce a newly-developed framework for modelling sperm cells in three dimensions. We refer to this method throughout as the *Sperm-X* or *SPX* method. The derivation and numerical implementation are detailed, with the method verified through comparisons to both the EIF (chapter 2) and other contemporary models. The framework is then used to investigate the dynamics of sperm swimming with nonplanar beats in an infinite fluid and upon approaching a rigid plane wall.

A summary of the methodology and key findings from across this thesis are provided in chapter 5, alongside ideas for further study. Appendices and references follow.

Chapter 2

Integral equation formulations for planar elastohydrodynamic filaments via tangent angle

In this chapter, we begin by introducing the elastohydrodynamic integral equation formulation, referred to throughout as the *EIF method*. The EIF is an efficient modelling framework for simulating planar elastic filaments in Stokes flow, which accounts for nonlocal hydrodynamic interactions, and is applicable to a multitude of problems. In section 2.3, the EIF is benchmarked for accuracy and computational cost against a highly refined bead and link method, as well as against two alternative modelling frameworks utilising a local drag force approximation. With the model validity established, it is applied to systems of single and multiple filaments in shear flow, sedimenting under gravity, and driven by an active moment travelling wave. Results and findings from these simulations are presented as they are discussed in sections 2.4.1, 2.4.2, and 2.4.3 respectively. Finally, in section 2.5, we discuss the applicability of the EIF to modelling sperm-like cells.

2.1 Methods for modelling the dynamics of elastic filaments

Models for simulating the dynamics of elastic slender bodies, whilst plentiful, have historically been mathematically complex and numerically expensive, with even simple computational experiments taking the order of hours or even days to solve – for detailed benchmarking refer to Moreau *et al.* (2018). This computational cost often arises from the need to satisfy filament inextensibility, a property common to slender microbiological structures such as flagella and cilia.

Numerous methods have been proposed that tackle microscale filament problems. Jayaraman *et al.* (2012) used a bead and spring method to model nonlocal buckling dynamics of a planar filament in extensional flow, a construction which forms the base of the bead and link model introduced in section 2.3. Inextensibility in these approaches is enforced by the prescription of large spring constants between each bead, contributing to the numerical stiffness of the systems. In modelling the continuous filament as a series of discrete spheres, the bead and spring framework is similar to the gears model used by Delmotte *et al.* (2015a), which satisfies inextensibility by imposing a nonholonomic constraint to ensure nonpenetrability between adjacent beads rather than through stiff connecting springs between each node. As a result, the gears model necessitates large numbers of points to appropriately describe the geometry of a single filament. In a recent landmark study of group sperm dynamics, Delmotte *et al.* (2015b) modelled large arrays of fibres, accounting for nonlocal effects by employing a force coupling method, involving the computation of Lagrange multipliers of tension to ensure filament inextensibility. This Lagrangian approach is also employed in methods by Wolgemuth *et al.* (2000); Camalet & Jülicher (2000); Lim *et al.* (2008); Gadêlha *et al.*

(2010); Lim (2010); Montenegro-Johnson *et al.* (2015).

A recent promising development via Moreau *et al.* (2018), referred to as *coarse graining*, is based on reformulating the elastohydrodynamic problem as an integral equation with the filament tangent angle as the dependent variable. In describing planar filaments through the tangent angle, filament extensibility is guaranteed, but nonplanar bending and twist deformations cannot be modelled (see section 1.3.2 on the geometry of 2d filaments). For applicable problems, the coarse-graining approach, initially developed using a local hydrodynamic drag law, provides an efficient framework for simulating noninteracting filament dynamics. The method builds upon the early studies of Brokaw (1971, 1972) and Hines & Blum (1978) (discussed in section 1.1.2), and contrasts with Cartesian formulations such as those of Tornberg & Shelley (2004); Gadêlha *et al.* (2010); Montenegro-Johnson *et al.* (2015).

Key to the actuation model used within the presented approach is the control mechanism presented by Brokaw (1971) based upon the sliding filament model (refer to section 1.1.2 for more details). Coupling with resistive force theory (Gray & Hancock, 1955) to model local fluid dynamics, analytical solutions to the equations for a filament of infinite length indicate how bending waves can be generated through an active bending moment formulated simply in terms of the local curvature and moment per unit length magnitude at a given material point along the arclength. Describing the flagellum shape through straight line segments and the curvature at each joint, an early computer model by Brokaw (1972) illustrates a range of physiologically realistic waveforms arising from the aforementioned active moment control mechanism. Subsequent work by Hines & Blum (1978) introduced the integral equations relating the filament centreline and tangent angle, later employed by Moreau *et al.* (2018) and the presented formulation, laying the key foundations in the planar elasticity and geometry in terms

of angle upon which this work is based. The focus on local interactions in Hines & Blum (1978) allows for the numerical implementation (using a Crank-Nicolson-type scheme) to provide fast (for the time) and accurate solutions, indicating the potential for efficient solution methods for elastohydrodynamic problems as early as the late 1970s.

In this chapter, we build upon this work by incorporating nonlocal hydrodynamic interactions into the recent Moreau *et al.* (2018) model. Fibres may be passive or active, and in ambient or dynamic flows, all the while interfacing through the fluid with themselves, others, and surrounding structures. This extension to the model is enabled through use of the method of regularised stokeslets (Cortez, 2001; Cortez *et al.*, 2005), allowing for efficient and accurate simulations of multiple interacting dynamic filaments. Details of the hydrodynamic model are given in section 1.2.6. Methods utilising regularised stokeslets have proven to be effective in modelling the hydrodynamics in various single and multiple-filament scenarios (Gallagher & Smith, 2020; Walker & Gaffney, 2021a). The framework is implemented in a numerically efficient manner, retaining the computational economy and low hardware requirements inherited from the angle formulation.

The MATLAB® code for the methods described in within this chapter are provided in an associated GitLab repository, freely accessible via Hall-McNair (2019).

2.2 Integral equations for planar elasticity

In the following section the equations comprising the proposed EIF model are derived. In section 2.2.1, the model equations describing the dynamics of a single passive filament are formulated, continuing from the discussions of planar filament geometry and elasticity in section 1.3.2. In this thesis, we refer to filaments (and later, cells) as being *passive* if they are not internally actuated. Conversely, filaments which are self-propulsive, due to internal mechanisms or otherwise, are referred to as being *active* or *nonpassive*. The dynamics of passive filaments are dependent on their instantaneous shape, with elastic properties acting to restore an equilibrium configuration, assumed throughout this thesis to be a straight line. External effects, such as surrounding flows or global forces, also contribute to deform the filament. Equations for nonpassive filaments are considered later in section 2.4. Section 2.2.2 details the nondimensionalisation of the model, and in section 2.2.3, we describe the semidiscretised model (that is, the model equations discretised in space but not in time), providing additional details on the efficient numerical implementation as MATLAB® code. Extensions to the method to simulate multiple interacting filaments are detailed in section 2.2.4.

2.2.1 The continuous nonlinear problem

The equations comprising the EIF are derived from consideration of a planar elastic filament, with its dynamics modelled by constructing integral operator formulations for the governing fluid and elastodynamic equations. In this chapter, by *continuous* we refer to the nondiscretised model equations, written in terms of material variables and integrals (rather than discrete sums). The filament is assumed to lie in the Cartesian xy-plane, and described using an angle formulation method as discussed in section 1.3.2.

The filament, parametrised by its centreline arclength $s \in [0, L]$, can be constructed via

$$\boldsymbol{X}(s,t) = \boldsymbol{X}_0(t) + \int_0^s \big(\cos\theta(\xi,t), \sin\theta(\xi,t), 0\big)^T d\xi, \tag{2.1}$$

with $\boldsymbol{X}_0(t) := \boldsymbol{X}(0,t)$ referred to here as the *leading point* at a given time. The tangent angle $\theta(s,t) \in [-\pi, \pi)$ is measured between the vector tangent to the curve $\mathbf{t}(s,t) := \boldsymbol{X}_s(s,t)$ and the fixed Cartesian basis vector $\mathbf{e}_x$. Here and throughout, we use the subscript notation for differentiation i.e. $\boldsymbol{X}_s(s,t) := \partial \boldsymbol{X}(s,t)/\partial s$. The velocity of a point on the filament centreline is given by differentiating (2.1) with respect to time t, yielding

$$\boldsymbol{X}_t(s,t) = \boldsymbol{X}_{0,t}(t) + \int_0^s \theta_t(\xi,t)\big(-\sin\theta(\xi,t), \cos\theta(\xi,t), 0\big)^T d\xi, \tag{2.2}$$

where $\boldsymbol{X}_{0,t}(t) := \boldsymbol{X}_t(0,t)$. Writing the unit tangent and unit normal in terms of θ as

$$\mathbf{t}(s,t) = \big(\cos\theta(s,t),\ \sin\theta(s,t), 0\big)^T, \qquad \mathbf{n}(s,t) = \big(-\sin\theta(s,t),\ \cos\theta(s,t), 0\big)^T, \tag{2.3}$$

equations (2.1) and (2.2) can be written in the more condensed form as

$$\boldsymbol{X}(s,t) = \boldsymbol{X}_0(t) + \int_0^s \mathbf{t}(\xi,t)\, d\xi, \qquad \boldsymbol{X}_t(s,t) = \boldsymbol{X}_{0,t}(t) + \int_0^s \theta_t(\xi,t)\mathbf{n}(\xi,t)\, d\xi, \tag{2.4}$$

with $s \in [0, L]$ and for $t \geqslant 0$.

Equations for the elastic behaviour of the filament are given by the equilibrium equations discussed in section 1.3.3. For a planar filament, the orthonormal basis along the centreline will rotate only about the out of plane axis i.e. for a fibre confined to the xy-plane, the frame $(\mathbf{t}(s), \mathbf{n}(s))$ will rotate only about $\mathbf{e}_z$, a unit vector pointing along the z-axis. Referencing the director frame notation from section 1.3.1, we deduce that

$\kappa_1(s,t) = \kappa_3(s,t) = 0$ and the constitutive moment equation thus reduces to

$$\boldsymbol{M}(s,t) = E\kappa_2(s,t)\mathbf{d}_2(s,t) = E\kappa_2(s,t)\mathbf{e}_z = E\theta_s(s,t)\mathbf{e}_z =: M(s,t)\mathbf{e}_z. \tag{2.5}$$

Letting $\boldsymbol{f}(s,t)$ denote the hydrodynamic force per unit length exerted by the filament on the fluid, we have that the equilibrium equations for the planar filament are

$$\boldsymbol{F}_s(s,t) = \boldsymbol{f}(s,t), \qquad M_s(s,t) + \mathbf{e}_z \cdot \boldsymbol{X}_s(s,t) \wedge \boldsymbol{F}(s,t) = 0, \tag{2.6}$$

where we recall that $\mathbf{d}_3 = \mathbf{t} := \boldsymbol{X}_s$ to replace the director vector in the moment equilibrium equation with the unit tangent in terms of centreline position. Here and throughout, we denote $\boldsymbol{f}(s,t) := \boldsymbol{f}(\boldsymbol{X}(s,t),t)$ (and similarly for other variables). Integrating the equation for the moment over the distal filament $[s,L]$,

$$\int_s^L M_s(\xi,t)\,d\xi = M(L,t) - M(s,t) = -M(s,t) = -\int_s^L \mathbf{e}_z \cdot \boldsymbol{X}_\xi(\xi,t) \wedge \boldsymbol{F}(\xi,t)\,d\xi, \tag{2.7}$$

as $\boldsymbol{M}(L,t) = \mathbf{0} \implies M(L,t) = 0$ at the free end. Noting that $\boldsymbol{X}(\xi,t) - \boldsymbol{X}(s,t)$ is an antiderivative of $\boldsymbol{X}_\xi(\xi,t)$, the right hand side of (2.7) can be integrated by parts to obtain

$$\begin{aligned} -\int_s^L \mathbf{e}_z \cdot \boldsymbol{X}_\xi(\xi,t) \wedge \boldsymbol{F}(\xi,t)\,d\xi = -\mathbf{e}_z \cdot \Big[\big(\boldsymbol{X}(\xi,t) - \boldsymbol{X}(s,t)\big) \wedge \boldsymbol{F}(s,t)\Big]_s^L \\ + \mathbf{e}_z \cdot \int_s^L \big(\boldsymbol{X}(\xi,t) - \boldsymbol{X}(s,t)\big) \wedge \boldsymbol{F}_s(\xi,t)\,d\xi. \end{aligned} \tag{2.8}$$

Applying the force-free distal boundary conditions $\boldsymbol{F}(L,t) = \mathbf{0}$ and using the force

equilibrium equation from (2.6) yields

$$-\int_s^L \mathbf{e}_z \cdot \boldsymbol{X}_\xi(\xi,t) \wedge \boldsymbol{F}(\xi,t)\, d\xi = \mathbf{e}_z \cdot \int_s^L \big(\boldsymbol{X}(\xi,t) - \boldsymbol{X}(s,t)\big) \wedge \boldsymbol{f}(\xi,t)\, d\xi, \tag{2.9}$$

which combined with the constitutive moment equation for planar bending (2.5) results in the elastodynamic equation

$$E\theta_s(s,t) + \mathbf{e}_z \cdot \int_s^L \big(\boldsymbol{X}(\xi,t) - \boldsymbol{X}(s,t)\big) \wedge \boldsymbol{f}(\xi,t)\, d\xi = 0, \tag{2.10}$$

where $0 \leqslant s \leqslant L$ and $t \geqslant 0$.

To model the hydrodynamic interactions between the filament and the fluid we employ the method of regularised stokeslets as introduced in 1.2.6. Consequently, interactions between the filament and itself, as well as with other surrounding bodies and structures are modelled. The filament, exerting a force per unit length $\boldsymbol{f}(s,t)$ on the surrounding fluid, moves with velocity

$$\boldsymbol{u}(\boldsymbol{X}(s,t),t) = \frac{1}{8\pi\mu}\int_0^L \boldsymbol{S}^\varepsilon\big(\boldsymbol{X}(s,t),\boldsymbol{X}(\xi,t)\big)\cdot\boldsymbol{f}(\xi,t)\, d\xi, \qquad 0 \leqslant s \leqslant L,\ \ t \geqslant 0. \tag{2.11}$$

where the rank-2 tensor in the integrand $\boldsymbol{S}^\varepsilon$ is the regularised stokeslet, as defined in section 1.2.6 equation (1.40). The constant ε is the *regularisation parameter*. In using the method of regularised stokeslets, 'blob' forces are assumed to act along the filament centreline, and in this sense ε is given physical meaning as a proxy for the flagellar radius. Further details of the regularised stokeslet method are given in section 1.2.6. Assuming a no-slip condition $\boldsymbol{u}(\boldsymbol{X}(s,t),t) = \boldsymbol{X}_t(s,t)$ on the surface of the filament, we

can write the hydrodynamic velocity in terms of position as

$$\boldsymbol{X}_t(s,t) = \frac{1}{8\pi\mu}\int_0^L \boldsymbol{S}^{\varepsilon}\big(\boldsymbol{X}(s,t),\boldsymbol{X}(\xi,t)\big)\cdot\boldsymbol{f}(\xi,t)\,d\xi, \qquad 0\leqslant s\leqslant L,\ \ t\geqslant 0. \tag{2.12}$$

Inertialess dynamics requires that the filament is force and moment free at each instant, giving the total force and total moment balance equations

$$\int_0^L \boldsymbol{f}(s,t)\,ds = \boldsymbol{0}, \tag{2.13a}$$

$$\int_0^L \boldsymbol{X}(s,t)\wedge\boldsymbol{f}(s,t)\,ds = \boldsymbol{0}. \tag{2.13b}$$

Taking the geometric and kinematic equations (2.1, 2.2) along with the hydrodynamics equations (2.12, 2.13a, 2.13b) and elastics equation (2.10) forms the dimensional elastohydrodynamic integral formulation (abbreviated throughout to EIF) method for simulating a passive elastic filament.

2.2.2 Nondimensionalisation of the EIF for a passive filament

The model is scaled spatially by the filament length L and temporally by τ. Scalings for other variables in the model follow as

$$s = L\hat{s}, \quad \boldsymbol{X} = L\hat{\boldsymbol{X}}, \quad t = \tau\hat{t}, \quad \boldsymbol{f} = \frac{\mu L}{\tau}\hat{\boldsymbol{f}}, \quad \varepsilon = L\hat{\varepsilon} \tag{2.14}$$

where the use of a hat $\hat{\cdot}$ indicates a dimensionless variable. For the case of a passively relaxing filament in a stationary flow, there is no natural timescale inherent to the problem; τ is thus a yet-to-be-determined scaling whose form will be chosen to simplify the dimensionless model. The geometry and kinematic velocity of the filament are given

by the expressions in equation (2.4) but with $\hat{s} \in [0,1]$ now being the dimensionless arclength, so that

$$\hat{\boldsymbol{X}}(\hat{s},\hat{t}) = \hat{\boldsymbol{X}}_0(\hat{t}) + \int_0^{\hat{s}} \mathbf{t}(\xi,\hat{t})\,d\xi, \qquad \hat{\boldsymbol{X}}_{\hat{t}}(\hat{s},\hat{t}) = \hat{\boldsymbol{X}}_{0,\hat{t}}(\hat{t}) + \int_0^{\hat{s}} \theta_{\hat{t}}(\xi,\hat{t})\mathbf{n}(\xi,\hat{t})\,d\xi. \tag{2.15}$$

Substituting the expressions for the scaled variables from (2.14) into the regularised stokeslet integral equation yields

$$\hat{\boldsymbol{X}}_{\hat{t}}(\hat{s},\hat{t}) = \frac{1}{8\pi}\int_0^1 \hat{\boldsymbol{S}}^{\hat{\varepsilon}}\big(\hat{\boldsymbol{X}}(\hat{s},\hat{t}),\hat{\boldsymbol{X}}(\xi,\hat{t})\big)\cdot\hat{\boldsymbol{f}}(\hat{s},\hat{t})\,d\xi, \tag{2.16}$$

noting that the regularised stokeslet scales as

$$S_{ij}^{\varepsilon}\big(\mathbf{x},\mathbf{y}\big) = \delta_{ij}\frac{L^2(\hat{r}^2+2\hat{\varepsilon}^2)}{L^3\hat{r}_{\hat{\varepsilon}}^3} + \frac{L^2\hat{r}_i\hat{r}_j}{L^3\hat{r}_{\hat{\varepsilon}}^3} = \frac{1}{L}\hat{S}_{ij}^{\hat{\varepsilon}}(\hat{\mathbf{x}},\hat{\mathbf{y}}), \tag{2.17a}$$

$$\text{where } \mathbf{x} = L\hat{\mathbf{x}}, \quad \mathbf{y} = L\hat{\mathbf{y}}, \quad r = L(\hat{\mathbf{x}}-\hat{\mathbf{y}}) = L\hat{r}. \tag{2.17b}$$

The total force and total moment balance equations scale as

$$\int_0^1 \hat{\boldsymbol{f}}(\xi,\hat{t})\,d\xi = \mathbf{0}, \tag{2.18a}$$

$$\int_0^1 \hat{\boldsymbol{X}}(\xi,\hat{t})\wedge\hat{\boldsymbol{f}}(\xi,\hat{t})\,d\xi = \mathbf{0}. \tag{2.18b}$$

Similarly, the elastics equation (2.10) nondimensionalises as

$$\theta_{\hat{s}}(\hat{s},\hat{t}) + \mathbf{e}_z\cdot\frac{\mu L^4}{E\tau}\int_s^1 \big(\hat{\boldsymbol{X}}(\xi,\hat{t})-\hat{\boldsymbol{X}}(\hat{s},\hat{t})\big)\wedge\hat{\boldsymbol{f}}(\xi,\hat{t})\,d\xi = 0. \tag{2.19}$$

The time scaling $\tau = \mu L^4/E$ is chosen to remove the coefficient of the integral on the right hand side. Combining the above nondimensional equations with the nondimen-

sionalised kinematic velocity equation, we obtain the dimensionless elastohydrodynamic integral formulation for the evolution of a passive xy-planar filament in stationary Stokes flow. Removing the hats for clarity, the system of equations is

$$\boldsymbol{X}_t(s,t) = \frac{1}{8\pi}\int_0^1 \boldsymbol{S}^{\epsilon}\big(\boldsymbol{X}(s,t),\boldsymbol{X}(\xi,t)\big)\cdot\boldsymbol{f}(s,t)\,d\xi, \tag{2.20a}$$

$$\mathbf{0} = \int_0^1 \boldsymbol{f}(s,t)\,ds, \tag{2.20b}$$

$$\mathbf{0} = \int_0^1 \boldsymbol{X}(s,t)\wedge\boldsymbol{f}(s,t)\,ds, \tag{2.20c}$$

$$\theta_s(s,t) = -\mathbf{e}_z\cdot\int_s^1 \big(\boldsymbol{X}(\xi,t)-\boldsymbol{X}(s,t)\big)\wedge\boldsymbol{f}(\xi,t)\,d\xi, \qquad s\in[0,1], \tag{2.20d}$$

$$\text{where } \boldsymbol{X}(s,t) = \boldsymbol{X}_0(t) + \int_0^s \mathbf{t}(\xi,t)\,d\xi, \qquad s\in[0,1], \tag{2.20e}$$

$$\text{and } \boldsymbol{X}_t(s,t) = \boldsymbol{X}_{0,t}(t) + \int_0^s \theta_t(\xi,t)\mathbf{n}(\xi,t)\,d\xi, \qquad s\in[0,1], \tag{2.20f}$$

with unknowns $\boldsymbol{X}_0(t)$, $\theta(s,t)$ and $\boldsymbol{f}(s,t)$. Solving the EIF requires specification of the initial leading point position $\boldsymbol{X}_0(0)$ and filament shape through $\theta(s,0)$, $s\in[0,1]$.

2.2.3 Spatial semidiscretisation of the EIF

To solve the EIF, we spatially discretise the filament to obtain a set of numerically approximated ordinary differential equations which can be computationally evaluated. In this section we consider the so-called *semidiscrete* problem, discretising spatially but leaving variables continuous in time. Dividing the centreline arclength into $N-1$ segments of length $\Delta s = 1/(N-1)$, the positions of the resulting segment endpoints (or *joints* of the piecewise linear filament) are denoted as

$$\boldsymbol{X}[n](t) := \boldsymbol{X}\big((n-1)\Delta s, t\big), \qquad n = 1,\dots,N, \quad t\geqslant 0. \tag{2.21}$$

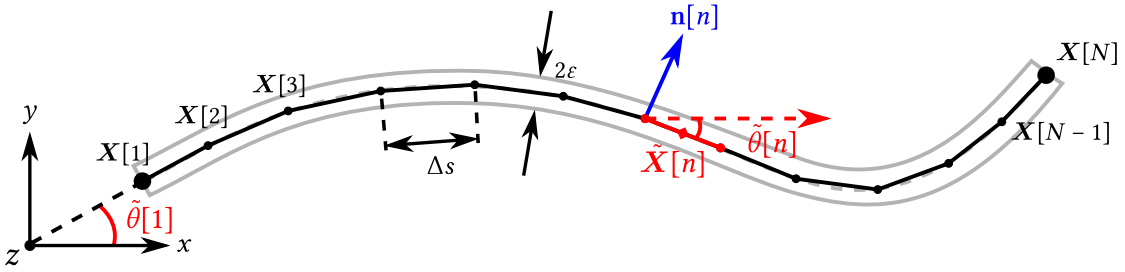

Figure 2.1: Schematic of the geometric discretisation of a continuous filament used in the EIF. The centreline arclength is split into $N-1$ segments of equal length Δs which comprise a piecewise linear approximation to the curve. The tangent angles, measured at the midpoint of each segment, are $\tilde{\theta}[n]$ for $n = 1, \dots, N-1$, define the filament shape at each instant.

The tangent angle to the curve at the midpoint between each pair of consecutive nodes approximates $\theta(s,t)$ and is denoted $\tilde{\theta}[n](t)$ for each segment $n = 1, \dots, N-1$. The positions of the joints are given in terms of the leading point ($\boldsymbol{X}[1](t) = \boldsymbol{X}_0(t)$) and discretised tangent angle by applying the midpoint rule to equation (2.20e) to obtain

$$\boldsymbol{X}[n+1](t) = \boldsymbol{X}[1](t) + \sum_{m=1}^{n} \Delta s \big(\cos\tilde{\theta}[m](t),\ \sin\tilde{\theta}[m](t),\ 0 \big)^T, \tag{2.22}$$

for $n = 1, \dots, N-1$. In what follows, it will be useful to express the segment midpoints $\tilde{\boldsymbol{X}}[m](t) := \big(\boldsymbol{X}[m](t) + \boldsymbol{X}[m+1](t)\big)/2$ in terms of the discretised tangent angles, and so we write

$$\tilde{\boldsymbol{X}}[n](t) = \boldsymbol{X}[1](t) + \sum_{m=1}^{n-1} \Delta s \big(\cos\tilde{\theta}[m](t), \sin\tilde{\theta}[m](t), 0 \big)^T + \frac{\Delta s}{2} \big(\cos\tilde{\theta}[n](t), \sin\tilde{\theta}[n](t), 0 \big)^T, \tag{2.23}$$

for each $n = 1, \dots, N-1$. A schematic of the discretisation described here is presented in figure 2.1. Differentiating the above with respect to t yields a kinematic equation

for the midpoint velocities as

$$\tilde{\boldsymbol{X}}_t[n](t) = \boldsymbol{X}_t[1](t) + \sum_{m=1}^{n-1} \Delta s \tilde{\theta}_t[m](t)\big(-\sin\tilde{\theta}[m](t), \cos\tilde{\theta}[m](t), 0\big)^T + \frac{\Delta s}{2}\tilde{\theta}_t[n](t)\big(-\sin\tilde{\theta}[n](t), \cos\tilde{\theta}[n](t), 0\big)^T \quad (2.24)$$

For the fluid dynamics (equation (2.20a)), rather than using a conventional (and potentially computationally expensive) quadrature rule to evaluate the rapidly-varying regularised stokeslet kernel, we employ the method of Smith *et al.* (2009b) as discussed in section 1.2.9. By approximating the force density in equation (2.20a) as piecewise constant along each segment, the kernel can be analytically integrated, reducing the level of quadrature needed to evaluate the comparatively slowly-varying force density (for higher order force discretisations see Cortez (2018); Walker & Gaffney (2021a)). The arclength at the midpoint of each discrete segment is denoted

$$\tilde{s}[m] = \frac{1}{2}\left(s[m] + s[m+1]\right), \qquad m = 1, \ldots, N-1. \quad (2.25)$$

The force per unit length is then discretised based upon the value at the segment midpoint, so that

$$\boldsymbol{f}(s,t) \approx \boldsymbol{f}(\tilde{s}[m], t) := \tilde{\boldsymbol{f}}[m](t), \qquad \text{for } (m-1)\Delta s \leqslant s < m\Delta s. \quad (2.26)$$

Combined with a piecewise linear discretisation of the filament

$$\boldsymbol{X}(s,t) \approx \tilde{\boldsymbol{X}}[m](t) + (s - \tilde{s}[m])\tilde{\mathbf{t}}[m](t), \quad (2.27a)$$

$$= \tilde{\boldsymbol{X}}[m](t) + (s - \tilde{s}[m])\big(\cos\tilde{\theta}[m](t), \sin\tilde{\theta}[m](t), 0\big)^T, \quad (2.27b)$$

for each $m = 1, \dots, N-1$, we obtain the spatially discrete equation

$$\tilde{\boldsymbol{X}}_t[n](t) = \frac{1}{8\pi} \sum_{m=1}^{N-1} \tilde{\boldsymbol{f}}[m](t) \cdot \int_{(m-1)\Delta s}^{m\Delta s} \boldsymbol{S}^{\varepsilon}\Big(\tilde{\boldsymbol{X}}[n], \tilde{\boldsymbol{X}}[m] + (\xi - \tilde{s}[m])\big(\cos\tilde{\theta}[m](t), \sin\tilde{\theta}[m](t), 0\big)^T \Big) d\xi. \quad (2.28)$$

for $n = 1, \dots, N-1$. The integral on the right hand side of (2.28) can be calculated exactly by transforming to a local coordinate system in which one axis is aligned with the segment tangent (details in 1.2.9). For brevity, this integral is denoted $\boldsymbol{I}^{\varepsilon}[n, m](t; \Delta s)$, allowing the regularised stokeslet integral equation 2.20a to be written as

$$\tilde{\boldsymbol{X}}_t[n](t) = \frac{1}{8\pi} \sum_{m=1}^{N-1} \boldsymbol{I}^{\varepsilon}[n, m](t; \Delta s) \cdot \tilde{\boldsymbol{f}}[m](t), \qquad n = 1, \dots, N-1. \quad (2.29)$$

The total force and total moment balance equations are discretised by employing the midpoint rule as

$$\sum_{m=1}^{N-1} \Delta s\, \tilde{\boldsymbol{f}}[m](t) = \boldsymbol{0}, \quad (2.30a)$$

$$\sum_{m=1}^{N-1} \Delta s\, \tilde{\boldsymbol{X}}[m](t) \wedge \tilde{\boldsymbol{f}}[m](t) = \boldsymbol{0}. \quad (2.30b)$$

Since moments only act out of the plane of bending, the total moment balance equation reduces to

$$\mathbf{e}_z \cdot \sum_{m=1}^{N-1} \Delta s\, \tilde{\boldsymbol{X}}[m](t) \wedge \tilde{\boldsymbol{f}}[m](t) = 0. \quad (2.31)$$

The elastics equations (2.20d) discretise in a similar manner, with the derivative $\theta_s(s)$ approximated through a backwards finite difference. The semidiscrete form of the EIF

is then

$$\tilde{\boldsymbol{X}}_t[n](t) = \frac{1}{8\pi}\sum_{m=1}^{N-1} \boldsymbol{I}^{\varepsilon}[n,m](t;\,\Delta s)\cdot\tilde{\boldsymbol{f}}[m](t), \tag{2.32a}$$

$$\mathbf{0} = \sum_{m=1}^{N-1} \Delta s\tilde{\boldsymbol{f}}[m](t), \tag{2.32b}$$

$$0 = \mathbf{e}_z \cdot \sum_{m=1}^{N-1} \Delta s\tilde{\boldsymbol{X}}[m](t)\wedge\tilde{\boldsymbol{f}}[m](t), \tag{2.32c}$$

$$\frac{\tilde{\theta}[n+1](t)-\tilde{\theta}[n](t)}{\Delta s} = -\mathbf{e}_z\cdot\sum_{m=n}^{N-2}\Delta s\big(\tilde{\boldsymbol{X}}[m+1](t)-\boldsymbol{X}[n+1](t)\big)\wedge\tilde{\boldsymbol{f}}[m+1] \tag{2.32d}$$

$$\text{where } \boldsymbol{X}[n](t) = \boldsymbol{X}[1](t) + \sum_{m=1}^{N-1}\Delta s\big(\cos\tilde{\theta}[m](t), \sin\tilde{\theta}[m](t), 0\big)^T, \tag{2.32e}$$

$$\tilde{\boldsymbol{X}}[n](t) = \boldsymbol{X}[n](t) + \frac{\Delta s}{2}\big(\cos\tilde{\theta}[n](t), \sin\tilde{\theta}[n](t), 0\big)^T, \tag{2.32f}$$

$$\text{and } \tilde{\boldsymbol{X}}_t[n](t) = \boldsymbol{X}_t[1](t) + \sum_{m=1}^{n-1}\Delta s\tilde{\theta}_t[m](t)\,\tilde{\mathbf{n}}[m](t) + \frac{\Delta s}{2}\tilde{\theta}_t[n](t)\,\tilde{\mathbf{n}}[n](t), \tag{2.32g}$$

$$\text{with } \tilde{\mathbf{n}}[n](t) = \big(-\sin\tilde{\theta}[n](t), \cos\tilde{\theta}[n](t), 0\big)^T, \tag{2.32h}$$

where $n = 1,\dots,N-1$ in equations (2.32a, 2.32f, 2.32g, 2.32h), $n = 1,\dots,N-2$ in (2.32d) and $n = 2,\dots,N$ in (2.32e). By using equations (2.32f) and (2.32g), the variables $\tilde{\boldsymbol{X}}[1](t),\dots,\tilde{\boldsymbol{X}}[N](t)$ and $\boldsymbol{X}[2](t),\dots,\boldsymbol{X}[N-1](t)$ can be eliminated from equations (2.32a, 2.32c, 2.32d). The resulting system is then linear in the shape unknowns $\boldsymbol{X}_t[1](t), \tilde{\theta}_t[1](t)\dots,\tilde{\theta}_t[N-1](t)$ and force density unknowns $\tilde{\boldsymbol{f}}[1](t),\dots,\tilde{\boldsymbol{f}}[N-1](t)$. Hence, given the discrete configuration $\boldsymbol{X}[1](t), \tilde{\theta}[1](t),\dots,\tilde{\theta}[N-1](t)$, the rate of change of position and angle can be found by solving a dense $(3(N-1)+2)\times(3(N-1)+2)$ system of linear equations. The semidiscrete system can be expressed concisely as a nonlinear initial value problem

$$Z_t = \mathcal{F}(Z), \quad Z(0) = Z_0, \tag{2.33}$$

where

$$\boldsymbol{Z}(t) := \left(\boldsymbol{X}[1](t), \tilde{\theta}[1](t), \dots, \tilde{\theta}[N-1](t)\right)^T, \tag{2.34}$$

and $\boldsymbol{Z}_0$ is determined by the problem under consideration. By augmenting the problem with the unknown forces per unit length, this can be written as the matrix system

$$A \begin{pmatrix} \dot{\boldsymbol{Z}} \\ \tilde{\boldsymbol{f}} \end{pmatrix} = \boldsymbol{b}, \tag{2.35}$$

where $\dot{\boldsymbol{Z}} := \boldsymbol{Z}_t$ and with

$$A = \begin{pmatrix} 0 & A_E \\ A_K & A_H \end{pmatrix}, \tag{2.36a}$$

$$\boldsymbol{b} = \left(0, \frac{\tilde{\theta}[2](t) - \tilde{\theta}[1](t)}{\Delta s}, \dots, \frac{\tilde{\theta}[N-1](t) - \tilde{\theta}[N-2](t)}{\Delta s}, 0, \dots, 0\right)^T, \tag{2.36b}$$

$$\tilde{\boldsymbol{f}} = \left(\tilde{f}_x[1], \dots, \tilde{f}_x[N-1], \tilde{f}_y[1], \dots, \tilde{f}_y[N-1]\right)^T, \tag{2.36c}$$

where A is a $(3(N-1)+2) \times (3(N-1)+2)$ block matrix, $\boldsymbol{b}$ is a $3(N-1)+2$ column vector, and $\tilde{\boldsymbol{f}}$ is a $2(N-1)$ column vector so that the concatenation $(\dot{\boldsymbol{Z}}, \tilde{\boldsymbol{f}})^T$ is a $3(N-1)+2$ column vector. The nonzero matrix blocks of A, A_E, A_K and A_H encode the elastodynamic, kinematic, and hydrodynamic equations given by equations (2.32d,2.32g,2.32a) respectively. In the vector $\boldsymbol{b}$, the first entry corresponds to the moment balance on the whole filament (via equation (2.32c)); the subsequent $N-1$ rows are the moment balance about each interior joint via equation (2.32d). The next two rows correspond to the total force balance from equation (2.32b), noting that the out-of-plane z-component will be zeros and thus not included in the formation of the linear system. The remaining

zero entries correspond to the equivalence between the hydrodynamic and kinematic velocities in equations (2.32a) and (2.32g). In the special case of a passive (unactuated) filament, the linear system (2.33) is autonomous.

The matrix system (2.35) is solved at each time step using the MATLAB® `mldivide` command for $\dot{\boldsymbol{Z}}$ and $\tilde{\boldsymbol{f}}$. The resulting rates vector $\dot{\boldsymbol{Z}}$ is integrated using the built-in variable step, variable order ODE solver `ode15s` (Shampine & Reichelt, 1997) to obtain the leading point $\boldsymbol{X}[1](t)$ and tangent angles $\tilde{\theta}[1](t), \ldots, \tilde{\theta}[N-1](t)$, from which the filament shape can be obtained via equation (2.32e). Settings for `ode15s` are kept at the MATLAB® defaults; in particular, the absolute and relative error tolerances are 10^{-6} and 10^{-3} respectively. In using many of the built-in functions MATLAB® provides, we ensure that the code scales across different hardware configurations without any additional work from the user. Moreover, the framework benefits from the robust and optimised algorithms the MATLAB® functions offer.

While this IVP exhibits some stiffness, it is less stiff than the systems produced by other methods, as the integral formulation avoids the need of additional Lagrange multipliers of tension to ensure filament inextensibility. Such methods require increasing the degrees of freedom leading to methods that are computationally costly, with additional precautions necessary to minimise numerical errors, such as damping (Tornberg & Shelley, 2004; Montenegro-Johnson *et al.*, 2015). For example, the position formulation method by Montenegro-Johnson *et al.* (2015) requires $N = 160$ nodes per flagellum to ensure convergence of the nonlinear solver and enforce inextensibility, thus yielding at minimum a $3N \times 3N = 480 \times 480$ sized linear system for the geometry alone; as we will see in section 2.3.1, the EIF requires as little as $N = 21$ (i.e. 20 segments) for converged results, requiring only N equations to describe fibre shape. By discretising the filament into segments of equal and fixed length, and by describing the curve

centreline through the tangent angles of these segments (via equation (2.32e)), inextensibility of the fibre is guaranteed by construction. The benefits of this are explored in more detail in the following section 2.3.1.

The right hand side vector $\boldsymbol{b}$ of (2.35) is zero in every entry aside from those containing curvature values, which is computed through a finite difference of the tangent angles about the joints of the discrete model. As a result, when the filament is exactly straight, $\boldsymbol{b} = \boldsymbol{0}$ and the linear system is singular. For dynamic problems, this is rarely a concern as the likelihood of the filament becoming exactly straight is very low. For those problems where a linear configuration is expected (such as the relaxing filament problems in section 2.3.1) or desired (as the initial condition for the sedimentation problems in section 2.4.2), issues can be avoided by ending the simulation upon approaching a singular system (for the first example) or by presolving the problem with reduced degrees of freedom. In the latter case, we simulate for a short amount of small fraction (<1%) of the total time with a coarser fibre representation, then interpolate (using a cubic interpolating spline using the MATLAB® `csaps` function) to obtain a new initial condition with the required level of discretisation for the problem. This new initial condition then satisfies the model equations but will be sufficiently curved so as to not yield a singular system. Both approaches are discussed further in sections 2.3.1 and 2.4.2 respectively.

2.2.4 Arrays of multiple filaments

The EIF can be used to simulate the dynamics of large groups of filaments, accounting for the nonlocal hydrodynamic interactions between them. For each of the problems presented in sections (2.4.1,2.4.2,2.4.3), the kinematic and elastodynamic equations ap-

ply to each filament in the system individually. The hydrodynamic equations are extended so that the interactions between all filaments are considered. For a collection of M passively relaxing planar (though not necessarily coplanar) filaments, this equation reads

$$\boldsymbol{X}^{(\alpha)}(s,t) = \frac{1}{8\pi}\sum_{\beta=1}^{M}\int_0^{L^{(\beta)}} \boldsymbol{S}^{\varepsilon}\left(\boldsymbol{X}^{(\alpha)}(s,t), \boldsymbol{X}^{(\beta)}(\xi,t)\right)\cdot \boldsymbol{f}^{(\beta)}(\xi,t)\, d\xi, \quad \beta = 1,\dots,M, \tag{2.37}$$

where the superscript (α) in this continuous equation refers to the arbitrarily identified α^{th} filament in the array. Whilst three dimensional hydrodynamic effects are computed, the kinematics and elasticity of the multiple filament problem remains two dimensional, ensuring the planarity assumption is not violated.

Modification of equation (2.37) to consider external flows, body forces, or actuation follows from the single filament derivations presented in sections (2.4.1, 2.4.2, 2.4.3). Nondimensionalisation in each case will yield the same governing dimensionless groups for the each problem respectively. Discretisation is similarly performed, producing a linear system comparable in overall structure to that for a single filament problem.

For the (simplest) passively relaxing filament problem, the rates of change of leading points $\tilde{\boldsymbol{X}}_t^{(1)}[1](t),\dots,\tilde{\boldsymbol{X}}_t^{(1)}[M](t)$ and rates of change of tangent angles $\tilde{\theta}_t^{(1)}[1](t),\dots,\tilde{\theta}_t^{(1)}[M](t)$ for each filament are obtained by solving the dense $(3M(N-1)+2M)\times(3M(N-1)+2M)$ system of linear equations. At each time step the matrix system is

$$A\begin{pmatrix}\dot{\boldsymbol{Z}}\\ \tilde{\boldsymbol{F}}\end{pmatrix} = \boldsymbol{b}, \tag{2.38}$$

where

$$A = \left[\begin{array}{ccc|ccccc} & & & (\mathrm{A}_E)_x^{(1)} & & 0 & (\mathrm{A}_E)_y^{(1)} & & 0 \\ & 0 & & & \ddots & & & \ddots & \\ & & & 0 & & (\mathrm{A}_E)_x^{(M)} & 0 & & (\mathrm{A}_E)_y^{(M)} \\ \hline (\mathrm{A}_K)_x^{(1)} & & 0 & & & & & & \\ & \ddots & & & (\mathrm{A}_H)_{xx} & & & (\mathrm{A}_H)_{xy} & \\ 0 & & (\mathrm{A}_K)_x^{(M)} & & & & & & \\ (\mathrm{A}_K)_y^{(1)} & & 0 & & & & & & \\ & \ddots & & & (\mathrm{A}_H)_{yx} & & & (\mathrm{A}_H)_{yy} & \\ 0 & & (\mathrm{A}_K)_y^{(M)} & & & & & & \end{array}\right], \tag{2.39}$$

and the vectors $\dot{\boldsymbol{Z}}$, $\tilde{\boldsymbol{F}}$, and $\boldsymbol{b}$ are, letting $Q = N - 1$, written

$$\dot{\boldsymbol{Z}} = \Big(\boldsymbol{X}_{0,t}^{(1)}(t), \tilde{\theta}_t^{(1)}[1](t), \dots, \tilde{\theta}_t^{(1)}[Q](t), \dots, \boldsymbol{X}_{0,t}^{(M)}(t), \tilde{\theta}_t^{(M)}[1](t), \dots, \tilde{\theta}_t^{(M)}[Q](t) \Big)^T, \tag{2.40a}$$

$$\tilde{\boldsymbol{F}} = \Big(\tilde{f}_x^{(1)}[1], \dots, \tilde{f}_x^{(1)}[Q], \dots, \tilde{f}_x^{(M)}[1], \dots, \tilde{f}_x^{(M)}[Q], \tilde{f}_y^{(1)}[1], \dots, \tilde{f}_y^{(1)}[Q], \dots, \tilde{f}_y^{(M)}[1], \dots, \tilde{f}_y^{(M)}[Q] \Big)^T, \tag{2.40b}$$

$$\boldsymbol{b} = \Big(0, \frac{\tilde{\theta}^{(1)}[2](t) - \tilde{\theta}^{(1)}[1](t)}{\Delta s}, \dots, \frac{\tilde{\theta}^{(1)}[Q](t) - \tilde{\theta}^{(1)}[N-2](t)}{\Delta s}, 0, 0, \dots, 0, \frac{\tilde{\theta}^{(M)}[2](t) - \tilde{\theta}^{(M)}[1](t)}{\Delta s}, \dots, \frac{\tilde{\theta}^{(M)}[Q](t) - \tilde{\theta}^{(M)}[N-2](t)}{\Delta s}, 0, 0, 0, \dots, 0 \Big)^T, \tag{2.40c}$$

where $\dot{\boldsymbol{Z}}$ and $\tilde{\boldsymbol{F}}$ are $M(N+1)$ and $2M(N-1)$ column vectors respectively. The system (2.38) is solved in the same manner as described in section 2.2.3.

2.3 Comparisons to similar EHD models

In the following section we examine the accuracy and efficacy of the proposed EIF method. In section 2.3.1, we compare results of a passively relaxing filament simulation from the EIF against those from a high resolution bead and spring model and the Moreau *et al.* (2018) method. In section 2.3.2, we provide additional comparisons between the EIF and the Schoeller *et al.* (2021) method in simulating a passively sedimenting filament. Spatial convergence properties of the EIF are discussed on a per scenario basis throughout.

2.3.1 Passive relaxation of a deformed filament

To assess the accuracy and efficacy of the EIF, we compare simulated results of a single planarly relaxing filament from the proposed method and from a high resolution bead and spring model. Based upon the work of Jayaraman *et al.* (2012), the bead and spring model (abbreviated here to BSM) accounts for nonlocal hydrodynamic interactions through use of the method of regularised stokeslets, and when highly resolved, provides accurate solutions (see appendix B for details).

The EIF model is tested as follows: consider an xy-planar filament, bent into a parabola, with initial condition $\boldsymbol{Z}_0$ constructed by sampling symmetrically from the curve $y = 0.5x^2$. Unit arclength is ensured (and verified) through use of MATLAB®'s `csaps` function to spline a high-resolution representation of the parabola at fixed-distance arclength values. The filament is then allowed to relax with no external forcing. Motion of the filament in this scenario is solely due to the constitutive bending moments along the arclength given in equation (2.20d).

The experiment is simulated using each of four methods:

- *EIF-RSM*: the proposed EIF method, which uses regularised stokeslets to account for nonlocal hydrodynamic interactions, and an angle geometric formulation to guarantee inextensibility,

- *EIF-RFT*: the EIF method, but with resistive force theory used in place of the method of regularised stokeslets to model only local hydrodynamic interactions (details in appendix D). The geometric model is unchanged from EIF-RSM.

- *MGG*: the original angle formulation method by Moreau *et al.* (2018), which uses resistive force theory to model local hydrodynamic interactions

- *BSM*: the bead and spring model, which accounts for nonlocal hydrodynamic interactions via regularised stokeslets. Inextensibility is enforced through appropriately chosen spring stiffness constants.

The EIF-RFT formulation is included to check the theoretical equivalence of the EIF with that of Moreau *et al.* under the reduction to a local hydrodynamic model. In all simulations in the following chapter, the regularisation parameter used in the method of regularised stokeslets is chosen as $\varepsilon = 0.01$.

The geometric configuration of the relaxing filament is simulated over $t = [0, 0.02]$, using both a high resolution ($N = 201$) BSM formulation and the EIF-RSM with $N = 101$. The initial and final filament shapes from each simulation are displayed in figure 2.2a. Quantitative comparison is given in figure 2.2b, plotting the root mean squared difference (RMSD) in coordinates $\boldsymbol{X}$ between the final filament shape via methods (1)–(3) and the BSM result. Here, excellent convergence is evident, with RMSD small for even coarse discretisations (RMSD $< 3 \times 10^{-3}$ for $Q = N - 1 > 10$). The somewhat counterintuitive initial larger difference with increased N exhibited by the

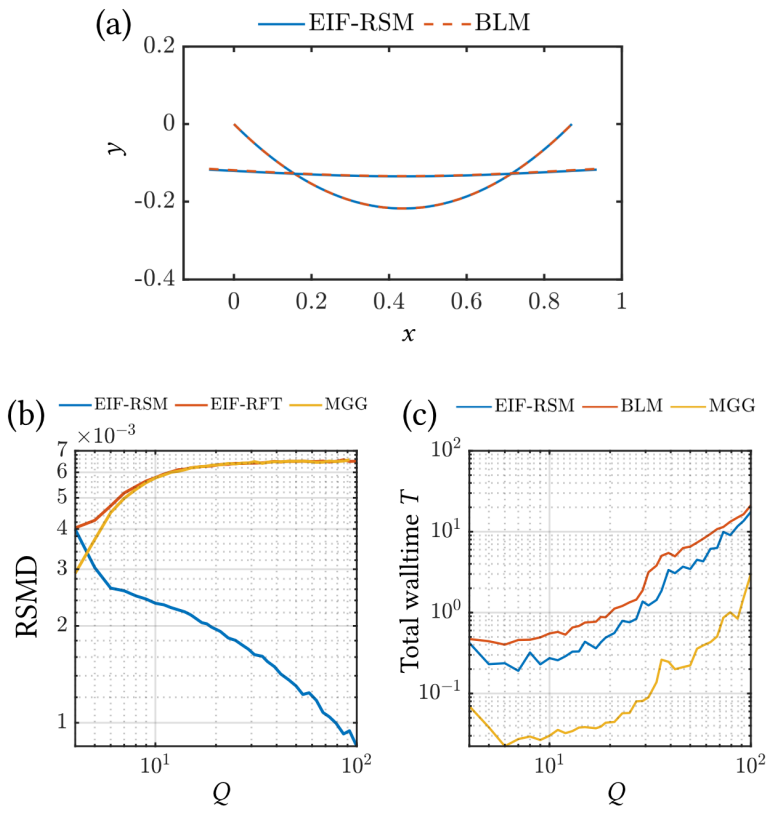

Figure 2.2: Error convergence and benchmarking of the three EIF methods against a high resolution (N=201) bead and spring model. Note $Q = N - 1$ is the number of segments comprising the discrete fibre. (a) Comparison of the filament shape at $t = 0$ and $t = 0.02$, where N=101 for EIF-RSM. (b) RMSD between the Cartesian solution data in the final configuration of (1) EIF-RSM, (2) EIF-RFT and (3) MGG against the highly-resolved BSM result. (c) Total wall time T against the level of discretisation $Q = N - 1$ for the EIF-RSM, MGG and BSM methods.

local hydrodynamic models is due to the drift in the centre of mass that the nonlocal methods correctly capture. Increasing N in the local methods resolves the filament shape leading to convergence of this error. These comparisons highlight the change in dynamics when considering the inclusion of nonlocal hydrodynamics for even single filament problems.

Moreau *et al.* (2018) demonstrated the significant reduction in computational cost

achieved when formulating elastohydrodynamic problems as integro-differential equations. Despite the added complexity of the nonlocal hydrodynamic model, EIF-RSM still performs very well. Simulations are performed on a laptop equipped with an Intel i7-8750H processor with 16GB RAM. Logarithmic comparisons of the simulation runtime for the EIF-RSM, MGG and BLM formulations are given in figure 2.2c. Here, the wall time recorded is the total computational time for the simulation to complete, including setup time. For the tangent angle formulation methods, the majority of this time is accounted for by the linear solve at each time step, with the linear systems being comparatively quick to construct.

It is unsurprising that the local hydrodynamic formulation (MGG) outperforms (with respect to wall time) the methods with nonlocal interactions due to the reduced complexity of the problem. The nonlocal methods (EIF-RSM and BSM) perform on par with each other as N increases. However, the bead and spring model requires large numbers of beads to accurately capture the filament geometry , whereas the EIF-RSM achieves similar accuracy with fewer than half the degrees of freedom required by the BLM, a benefit reinforced by the resulting reduction in wall time obtained by decreasing the level of discretisation of the filament. Moreover, since the BSM uses a position representation for the filament geometry, fibre shape requires at least a $3N \times 3N$-sized system, compared to the $Q + 2 = N + 1$ square matrix required for the EIF approaches, reducing the memory requirements for formulating the elastohydrodynamic problem. This enables code implementing the method to be run on even modest consumer-grade computational hardware, such as personal laptops with only a few gigabytes of RAM. When run on more powerful machines, the memory saved in construction and storage can be used instead to expand the scope of the modelling, for example, by accounting for multiple interacting filaments (as in section 2.2.4).

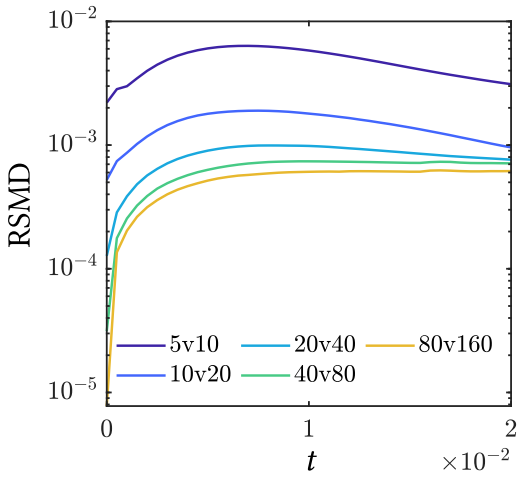

Figure 2.3: Spatial convergence in the numerical simulation of a passively relaxing filament, measured using the root mean squared error between time-evolving coordinate positions with successively-doubled discretisation parameter Q.

Next, the spatial convergence of the EIF method is addressed. We will not report on the temporal convergence of the method, since we use the commercial-standard and robust MATLAB® solver `ode15s` for time stepping. The passively relaxing filament problem is repeated multiple times, each time successively doubling the discretisation parameter $Q = N - 1$. Convergence is assessed by calculated the root mean squared difference (RMSD) at points common to each 'pair' of simulation results as

$$\text{RMSD} = \sqrt{\frac{1}{N_c}\sum_{m=1}^{N_c}\left(\boldsymbol{X}_Q[m] - \boldsymbol{X}_{2Q}[m]\right)^2}, \tag{2.41}$$

where N_c is the number of common points, $\boldsymbol{X}_Q$ are the position vectors for the discretisation with Q segments, and $\boldsymbol{X}_{2Q}$ are the position vectors for the doubly-refined discretisation with the $2Q$ segments, both sampled at matching arclength values. The filament initial condition is chosen the same as in section 2.2.

In using the method of regularised stokeslets, the fluid flow approximation suffers an $\mathcal{O}(\varepsilon)$ regularisation on the surface of the slender body, reducing to $\mathcal{O}(\varepsilon^2)$ in the far field (as discussed in 1.2.6). Consistent with $\varepsilon = 0.01$, we regard convergence as satisfactory if RMSD $\leqslant 10^{-2}$. As shown in figure 2.3, the difference converges to less than 10^{-3} for $Q \geqslant 20$. This result informs the choice of discretisation parameter to be used for simulations throughout the rest of this chapter. More geometrically dynamic problems (i.e. those in which the flagellum forms more nonlinear shapes) necessitate require finer discretisations to adequately capture increased nonlinearity in filament geometry.

2.3.2 Deflection of a sedimenting filament

In the following section we compare the EIF to an alternative filament modelling approach incorporating nonlocal hydrodynamics by Schoeller *et al.* (2021). In their formulation (referred to here as the *STWK method*), Schoeller and coauthors combine the constitutive bending and conservation laws outlined in section 1.3.1 with a direct pairwise evaluation of the Rotne-Prager-Yamakawa (RPY) tensor (Wajnryb *et al.*, 2013) to model the dynamics of a filament sedimenting under gravity. Details of the RPY approach are given in section 1.4.2.

A sedimenting filament is simulated until it has reached a steady state shape, at which time the relative deflection A/L is calculated, where A is the y-height of the final configuration and L is the filament length. The onset and shape of the steady

state shape is determined by the choice of elastogravitational parameter[1]

$$\mathcal{G} = \frac{\rho g L^2}{E}, \tag{2.42}$$

where ρ, L and E are the filament density, length, and bending rigidity respectively, and g is the strength of the gravitational field. Details on how this parameter arises are discussed later in section 2.4.2. Schoeller *et al.* (2021) demonstrated that their model closely agrees with many other formulations for modelling this experiment, such as the gears model of Delmotte *et al.* (2015a) (which also employs the RPY tensor to model nonlocal hydrodynamics), the joint model (proposed by Skjetne *et al.* (1997) and expanded upon by Delmotte *et al.* (2015a)), and experimental results (Marchetti *et al.*, 2018). In the STWK method (recomputed via repository code associated with Schoeller *et al.* (2021)), the filament radius is a and the filament length is $L = \Delta L(N-1)a$. Filament radius in the dimensionless EIF model is approximated by the regularisation parameter $a = \varepsilon = 0.01$, with $L = 1$ the dimensionless filament length. To ensure that the simulated filaments have the same aspect ratio, for simulations with $N = 51$ nodes, we choose $\Delta L = 2$.

In the STWK method, the filament is initialised precisely flat with $\theta = 0$ at each segment. Such a configuration in the EIF yields a singular system, as described in section 2.32. To tackle this, we initialise by symmetrically sampling from a very-low amplitude parabola $y = 10^{-7}x^2$ to closely resemble a linear filament.

The relative deflection is calculated for choices of the elastogravitational parameter $\mathcal{G}$ in the range $\mathcal{G} \in [10^0, 10^4]$. A close general agreement is observed between the EIF and STWK methods, shown in figure 2.4. Comparatively larger ($\mathcal{O}(10^{-1})$) differences

[1]Note that this parameter is identically defined but labelled B in the Schoeller *et al.* (2021) manuscript.

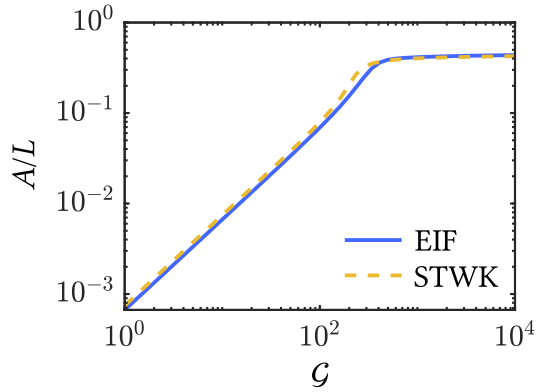

Figure 2.4: Relative deflection of a filament sedimenting under gravity for varying $\mathcal{G}$, modelled using the EIF method and the method of Schoeller *et al.* (2021), labelled here as STWK.

are observed for $10^2 \lesssim \mathcal{G} \lesssim 10^3$, likely due to the differences in the nonlocal hydrodynamic approximations between the formulations. Additionally, numerical stability is key in determining the dynamics of sedimenting planar filaments. For large values of $\mathcal{G} > 3000$, the fibre undergoes a shape change from an unstable 'W'-shape to a stable horseshoe; the onset of this transition depends on the stability of the numerical method and as such differences in the code implementation between the EIF and SWTK methods will likely yield small differences in results. The shapes and stability of sedimenting fibres are examined in more detail in section 2.4.2. In terms of performance, the EIF completes the sedimenting filament simulation $\approx$ 35% faster, taking on average $\approx$ 7.6 seconds to solve opposed to $\approx$ 11.9 seconds for the equivalent STWK simulation.

2.4 Single and multiple filament problems

In the following section, we apply the EIF modelling framework described in section 2.2 to problems involving single and multiple filaments in shear flows (section 2.4.1), in the presence of body forces (section 2.4.2), and undergoing self-powered propulsion (section 2.4.3). Any additional modelling considerations are detailed, including alterations to the 'core' system of equations (2.32a-h) derived in section 2.2.

For each problem we present results from numerical simulations with accompanying discussion. In all cases, the regularisation parameter is $\varepsilon = 0.01$. Motivated by the convergence results in section 2.3, we choose $N = 41$ unless stated otherwise.

Evidenced by the walltime results in section 2.3.1 and figure 2.2c, the EIF is a relatively computationally inexpensive method as a result of the angle formulation model, low degrees of freedom requirement for accurate results, and efficient numerical implementation. To emphasise this, in what follows most simulations are performed on modest, consumer-level computer hardware – in particular, a laptop equipped with an Intel i7-8750H processor and 16GB RAM. Select simulations involving multiple filaments benefit from increased RAM, and are thus performed on the University of Birmingham BlueBEAR cluster, which provides a high performance compute service to the University's research community (University of Birmingham, 2021).

2.4.1 Filaments in shear flow

Consider a single passive filament in a linear shear flow, orientated so as to lie in the plane of the flow. Assuming the shear moves in the xy-plane, the dimensional fluid velocity is

$$\boldsymbol{u}^*(\mathbf{x}^*, t^*) = \dot{\gamma} \mathrm{x}_2^* \mathbf{e}_x, \qquad \mathbf{x}^* = (\mathrm{x}_1^*, \mathrm{x}_2^*, \mathrm{x}_3^*)^T, \tag{2.43}$$

where $\dot{\gamma}$ is the dimensional shear rate with unit s^{-1}, and $\mathbf{e}_x$ is a unit vector in the Cartesian x-direction. Here, and in the following sections, we use asterisks in the superscript to indicate a dimensional variable. Including a shear flow in the hydrodynamic model necessitates the addition of a velocity term on the right hand side of the regularised stokeslet integral equation, which, following nondimensionalisation using the scalings

$$s^* = Ls, \quad \boldsymbol{X}^* = L\boldsymbol{X}, \quad t^* = \dot{\gamma}^{-1}t, \quad \boldsymbol{f}^* = \mu\dot{\gamma}L\boldsymbol{f}, \tag{2.44}$$

yields an equation for the dimensionless hydrodynamic filament velocity

$$\boldsymbol{X}_t(s,t) = \frac{1}{8\pi}\int_0^1 \boldsymbol{S}^{\varepsilon}\big(\boldsymbol{X}(s,t),\boldsymbol{X}(\xi,t)\big)\cdot\boldsymbol{f}(\xi,t)\,d\xi + X_2(s,t)\mathbf{e}_x. \tag{2.45}$$

Use of (2.44) additionally alters the nondimensionalisation of equation (2.10), yielding a modified dimensionless elastodynamic integral equation as

$$\theta_s(s,t) + \mathbf{e}_z\cdot\mathcal{V}\int_s^1 \big(\boldsymbol{X}(\xi,t)-\boldsymbol{X}(s,t)\big)\wedge\boldsymbol{f}(\xi,t)d\xi = 0, \tag{2.46}$$

where the dimensionless viscous-elastic parameter group

$$\mathcal{V} = \frac{\mu\dot{\gamma}L^2}{E} = \frac{\text{shear viscous forces}}{\text{elastic forces}}, \tag{2.47}$$

quantifies the ratio of viscous to elastic forces on a shear timescale, with E denoting the bending rigidity of the filament. The apparent flexibility of the filament is completely characterised by $\mathcal{V}$, with large values describing 'floppy' fibres and small values 'stiff' fibres.

The elasticity equation for the filament in shear (2.46) discretises in a similar man-

ner to that seen previously, but for the inclusion of the dimensionless parameter $\mathcal{V}$. The hydrodynamic shear flow equation (2.45) is semidiscretised following the steps in section 2.2.2 to obtain

$$\tilde{\boldsymbol{X}}[n](t) = \frac{1}{8\pi}\sum_{m=1}^{N-1} \boldsymbol{I}^{\epsilon}[n,m](t;\,\Delta s)\cdot\tilde{\boldsymbol{f}}[m](t) + \tilde{X}_2[n](t)\mathbf{e}_x, \qquad n = 1,\dots,N-1, \tag{2.48}$$

where $\tilde{X}_2[n](t)$ is the y-component of the segment midpoint $\tilde{\boldsymbol{X}}[n](t)$. The additional terms arising from the inclusion of shear will appear on the right hand side of the resulting system. The linear system of equations for a single passive filament in shear flow is thus given as

$$A\begin{pmatrix}\dot{\boldsymbol{Z}}\\ \tilde{\boldsymbol{f}}\end{pmatrix} = \boldsymbol{b}, \tag{2.49}$$

where

$$A = \begin{pmatrix} 0 & \mathcal{V}A_E \\ A_K & A_H \end{pmatrix}, \tag{2.50a}$$

$$\boldsymbol{b} = \left(0, \frac{\tilde{\theta}[2](t)-\tilde{\theta}[1](t)}{\Delta s}, \dots, \frac{\tilde{\theta}[N-1](t)-\tilde{\theta}[N-2](t)}{\Delta s}, 0, 0, \tilde{X}_2[1](t), \dots, \tilde{X}_2[N-1](t), 0, \dots, 0\right)^T, \tag{2.50b}$$

with the terms in the vector of unknowns $(\dot{\boldsymbol{Z}}, \tilde{\boldsymbol{f}})^T$ unchanged from equations (2.34,2.36c). Dynamics of a filament in shear flow are thus simulated by solving equation (2.35) with A and $\boldsymbol{b}$ given by equations (2.50a,2.50b) respectively.

A precisely straight filament lying in the plane of shear will rotate through a Jeffery orbit, with an analytical solution presented in Kim & Karrila (2013). It is well known

that for critical values of the characteristic parameter $\mathcal{V}$ a filament in shear flow exhibits shape buckling due to a stress difference across the fibre whilst under compression by the moving fluid (Tornberg & Shelley, 2004; Liu *et al.*, 2018). As discussed by Tornberg & Shelley (2004), prescribing even minor perturbations in the tangent angle of the straight filament can drastically change the dynamics and produce striking buckling phenomena. We choose an initial condition following Young (2009), writing the discrete angle configuration as

$$\tilde{\theta}[n](0) = \theta_0 + \Delta\theta_0 \left(\frac{\tilde{s}[n]^3}{3} - \frac{\tilde{s}[n]^4}{2} + \frac{\tilde{s}[n]^5}{5} \right), \tag{2.51}$$

where θ_0 is the initial tangent angle and $\Delta\theta_0 \ll 1$ is the perturbation parameter. This initial condition arises from integrating the curvature initial condition $k(s) = \theta_s(s) = \Delta\theta_0(s - s^2)^2$, and sampling at discrete segment midpoints $\tilde{s}[m]$, $m = 1, \ldots, N-1$. Choosing the initial condition in this way seeds a small but significant perturbation in the filament shape which will promote the development of buckling modes.

Figure 2.5 demonstrates how changes in the value of $\mathcal{V}$ affect the amount of buckling a filament experiences as it rotates in shear flow. The fibre is initialised with $\theta_0 = 0.9\pi$ and $\Delta\theta_0 = 0.1$. As the filament rotates, buckling modes form, which are directly linked to the size of $\mathcal{V}$ and the choice of perturbation (2.51). Large values of $\mathcal{V}$ ($\geqslant 3 \times 10^4$) produce high order buckling modes, as evidenced in figure 2.5c,d. Conversely, comparatively small values produce negligible buckling and the filament rotates following a standard Jeffrey orbit. For $\mathcal{V} = 5 \times 10^3$, a first-order buckling mode begins to form (see 2.5a). The amplitude of the buckling increases commensurate with $\mathcal{V}$ until higher order modes are induced. Tornberg & Shelley (2004) examined buckling

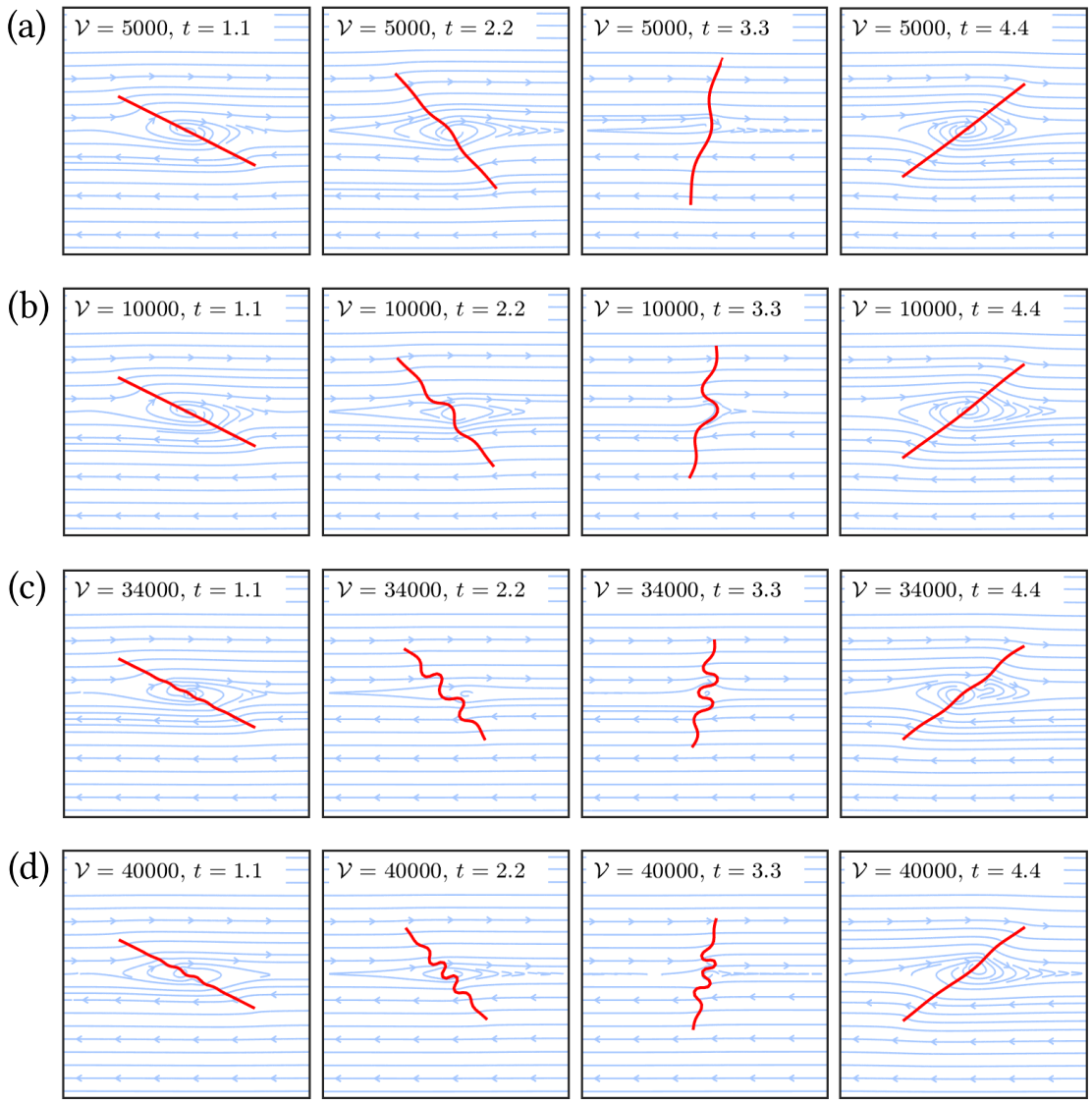

Figure 2.5: Dynamics of a single filament in shear flow. Each row displays the evolving geometric configuration of the filament, characterised by different values of $\mathcal{V}$. Arrows on blue lines indicate the direction of fluid flow. In all cases, the filament is modelled with $N = 41$ and with initial shape parameters $\theta_0 = 0.9\pi$ and $\Delta\theta_0 = 0.1$. For a fixed initial condition, the size of $\mathcal{V}$ completely determines the level of buckling exhibited. For large values (as in (c) and (d)), high order buckling modes appear.

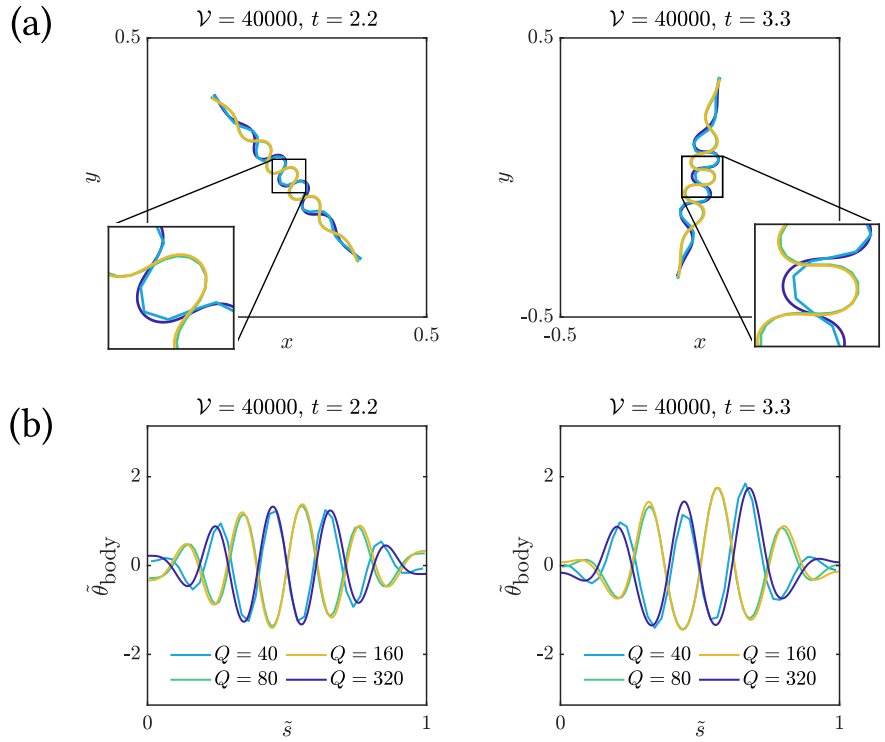

Figure 2.6: Effect of numerical discretisation parameter on (a) filament shapes and (b) body-frame tangent angles $\tilde{\theta}_{\text{body}}$ when $\mathcal{V} = 4\times10^4$. One of two resolved configurations develop depending on the choice of $Q = N - 1$, improving as Q increases.

governed by an effective viscosity parameter $\bar{\mu} = 8\pi\mathcal{V}$, producing filament shapes with a single observable buckling mode similar to those in figure 2.5b.

The buckling problem for an elastic filament in shear can have multiple solutions (Becker & Shelley, 2001; Liu *et al.*, 2018). As noted by Tornberg & Shelley (2004), the choice of initial perturbation to the filament shape can preferentially lead to one of the solutions. For example, changing the sign of the perturbation in (2.51) produces a reflected, but not symmetric, filament shape. When the initial condition does not uniquely determine a specific solution branch (as for this problem with large $\mathcal{V}$), the buckled solution becomes sensitive to the choice of discretisation. When $\mathcal{V} \leqslant 1.6\times10^4$,

the filament exhibits a single buckling mode and a spatially converged result is produced for $N \geqslant 41$. Increasing to $\mathcal{V} = 4\times10^4$ induces higher-order modes, and the shape approximates one of two solutions depending on the value of $Q = N - 1$, the number of segments comprising the discretised filament. This supercritical pitchfork bifurcation of a fibre in shear flow has been reported previously by Becker & Shelley (2001); Liu *et al.* (2018). The nonlinear geometry in these cases requires finer discretisations ($N \geqslant 161$) to resolve accurately, as indicated by figure 2.6

The perturbation to the filament shape due to buckling can be investigated by considering the evolving body-frame tangent angles

$$\tilde{\theta}_{\text{body}}[n](t) = \tilde{\theta}[n](t) - \bar{\theta}(t), \qquad \text{where } \bar{\theta}(t) = \frac{1}{N-1}\sum_{n=1}^{N-1}\tilde{\theta}[n](t), \tag{2.52}$$

for $n = 1, \ldots, N-1$. Using the `chebfun` open-source package (Driscoll *et al.*, 2014), Chebyshev polynomials are fitted to the body-frame tangent angles at each instant, taking sufficiently many modes to reduce interpolation error below 5%. From this, we assess the evolution of both the order of Chebyshev polynomials required and their associated magnitude. In figures 2.8a,b we show the results of this fitting process for two choices of $\mathcal{V}$. An increase in $\mathcal{V}$ requires a commensurate increase in the polynomial order required, illustrated by examining the Chebyshev coefficients in figure 2.8c,d. The ability to accurately describe the nonlinear filament geometry using Chebyshev polynomials suggests that spectral integration techniques, such as those of Muldowney & Higdon (1995), may be integrated into the EIF allowing for increased quadrature accuracy with potentially fewer degrees of freedom.

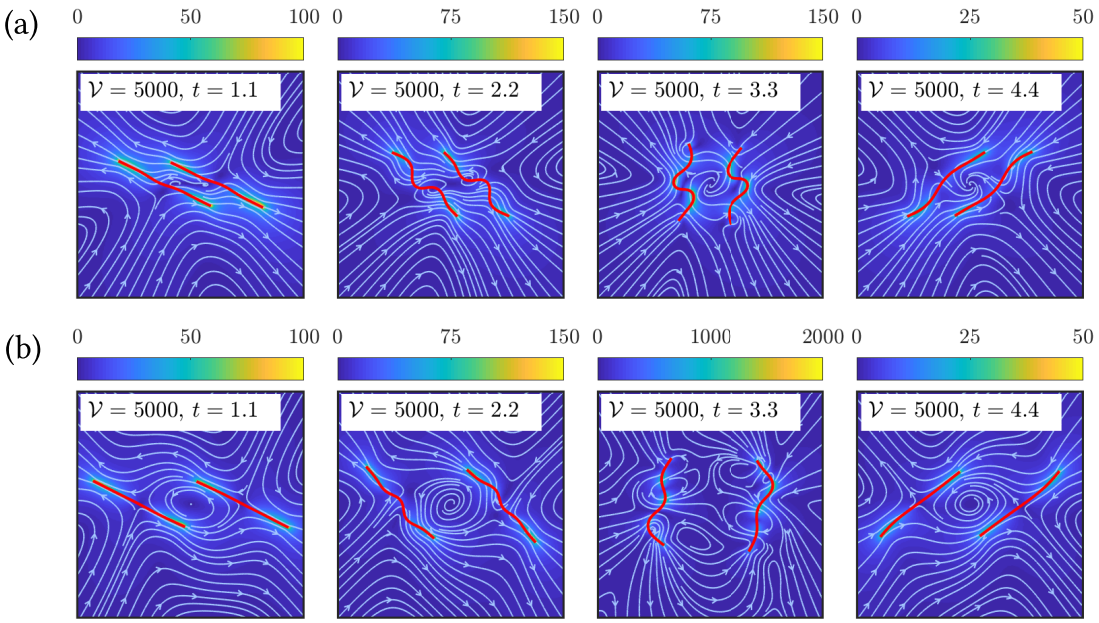

Figure 2.7: Dynamics of two filaments separated by distance (a) $\Delta X_0 = 0.5$, (b) $\Delta X_0 = 1$. The colour bar indicates the magnitude of the relative perturbed fluid velocity $\boldsymbol{u}_p = (\boldsymbol{u}_f - \boldsymbol{u}_b)/\boldsymbol{u}_{\text{ref}}$, where $\boldsymbol{u}_f$ is the fluid flow, $\boldsymbol{u}_b$ is the background shear flow, and $\boldsymbol{u}_{\text{ref}}$ is the flow at an arbitrary reference field point constant to each panel, chosen to be the bottom-left value of each frame. Blue lines with arrows indicate the direction of the flow disturbance, illustrating the filament-fluid interactions and the occlusionary effect the presence of the left-most filament has on the flow reaching the right-most filament.

We next consider the buckling of two proximal filaments in shear flow. Motivated by the work of Young (2009), two filaments of equal length are placed into a linear shear flow so that their midpoints $\boldsymbol{X}(s = 0.5, 0)$ intersect the line $y = 0$, and are separated by a distance ΔX_0. The geometric initial conditions are identical (differing only in $\boldsymbol{X}_0(0)$) and chosen following the perturbation in equation (2.51).

Characterised by the same value of $\mathcal{V}$, the filaments nonetheless develop geometric dissimilarities due to nonlocal hydrodynamic interactions. The choice of $\mathcal{V}$ determines the level of dissimilarity, with higher values leading to larger deviations in shape throughout the rotation. The initial separation distance also has a significant influence

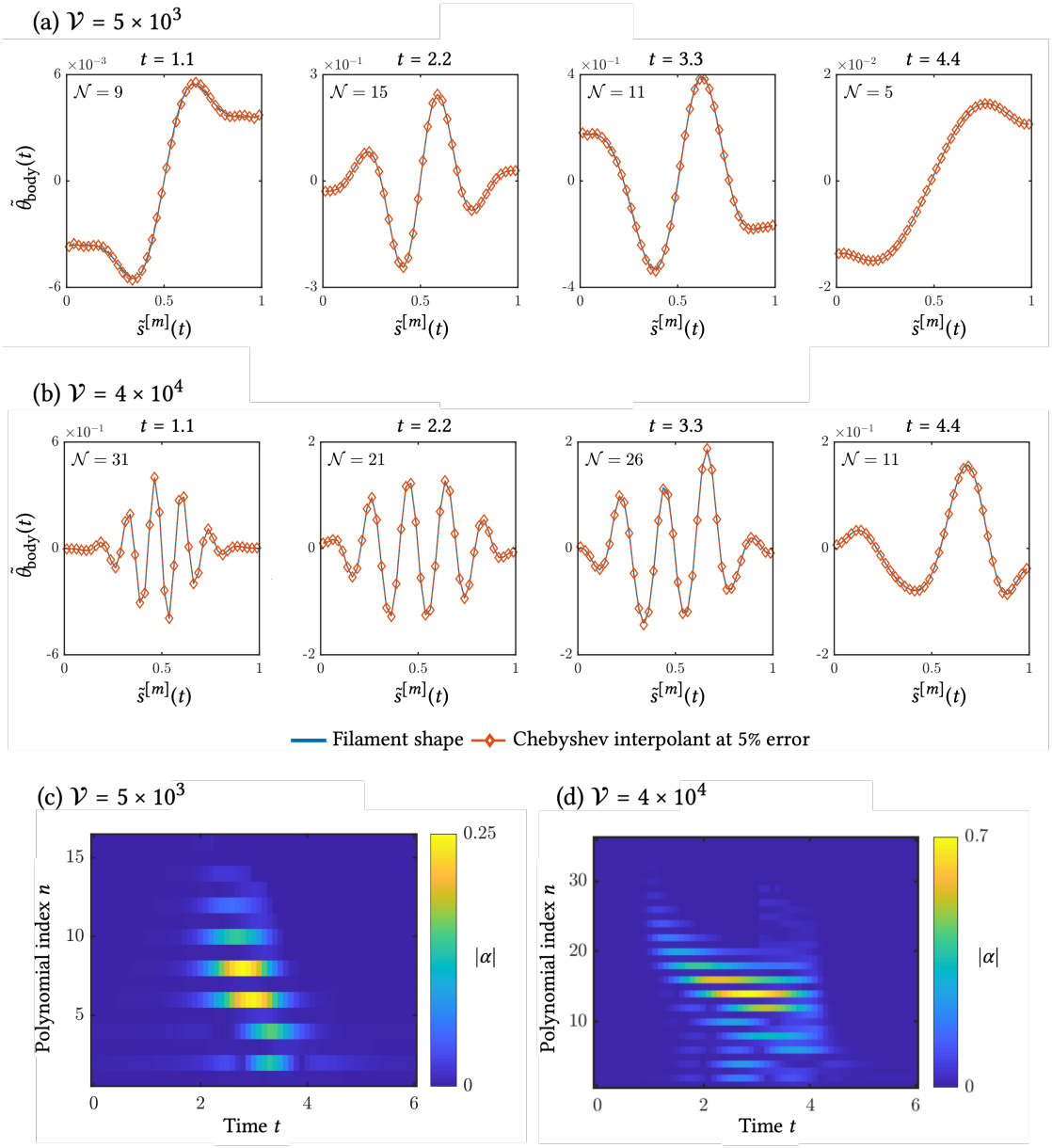

Figure 2.8: Analysis of the buckling modes of a filament in shear flow via polynomial interpolation. At select time points during the filament rotation, the buckled fibre shape is approximated by a series of $n = 1, \ldots, \mathcal{N}$ Chebyshev polynomials $\mathcal{T}_n(\tilde{\theta}_{\text{body}})$, with $\mathcal{N}$ chosen so that the tangent angle curve is interpolated within a 5% error bound. Polynomial coefficients are calculated using `chebfun`. (a) and (b): the tangent angle of a filament undergoing buckling is captured relative to the body frame at four time points. Each subplot implies filament shape via equation (2.52). (c) and (d): the number and magnitude of Chebyshev coefficients for each of the polynomials, for $\mathcal{V} = 5 \times 10^3$ and 4×10^4 respectively.

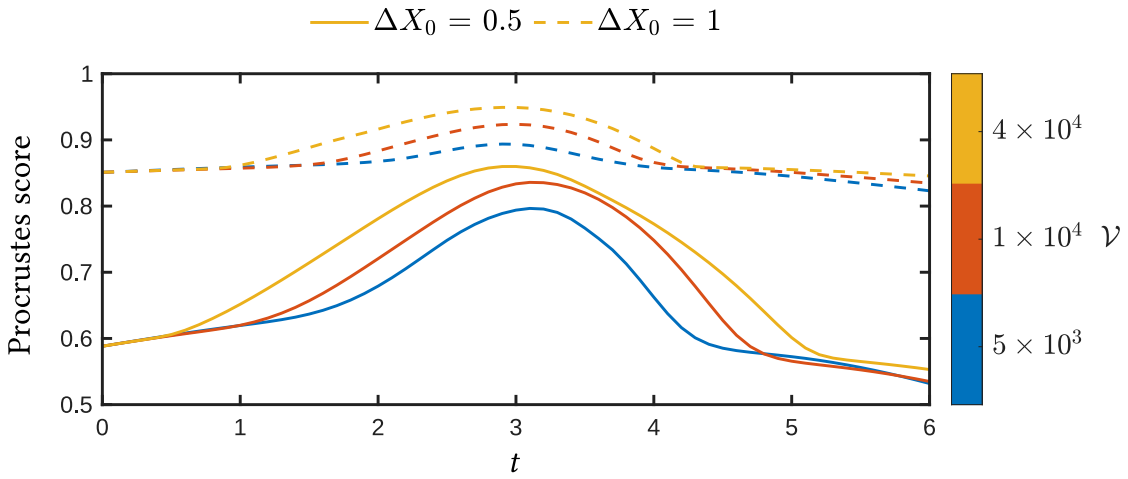

Figure 2.9: The evolving geometric dissimilarity between two proximal filaments of equal stiffness in shear flow, for three values of $\mathcal{V}$. The shape difference is quantified using the Procrustes measure, calculable using the `procrustes` MATLAB® command. Higher values indicate a larger degree of dissimilarity between the two filaments (Gower, 1975).

on the dynamics of each filament. The shapes of initially close filaments evolve in tandem, assuming similar geometries at any given moment (see figure 2.7a). As separation increases, filament shapes become less similar, with notable differences in geometry particularly towards the filament tips (figure 2.7b).

The geometric similarity between filaments can be assessed via their Procrustes score (Gower, 1975), calculable using the `procrustes` MATLAB® command. The MATLAB® algorithm determines a linear transformation mapping one vector of coordinates onto the other, following a sum of least squares goodness-of-fit criterion. We compare pairs of filaments initially separated by $\Delta X_0 = \{0.5, 1\}$ for $\mathcal{V} = \{5 \times 10^3, 1 \times 10^4, 4 \times 10^4\}$. Results are presented in figure 2.9. As $\mathcal{V}$ is increased, hydrodynamic interactions through the fluid cause larger level of asymmetry during the period of maximum buckling, occurring when they are approximately perpendicular to the direction of shear ($t \approx 3$). Increasing the initial filament separation returns a high

baseline Procrustes score, but with reduced variability due to the decaying strength of hydrodynamic interactions.

2.4.2 Filaments sedimenting under gravity

The EIF method can be extended to account for the effects of a body force present within the system. Depending on the size of the fibre and the relative viscosity of the surrounding fluid i.e. the value of the characteristic Reynolds number, this body force may be gravity, or a global magnetic attraction due to a surrounding field. Filaments on the scale of sperm flagella, which operate within very low Reynolds number fluid systems, are effectively neutrally buoyant when observed over short-mid length timescales (i.e. over minutes to hours). With this in mind, the filaments simulated in this section can be assumed to be not flagella, but some other larger-scale slender body object existing within a larger Reynolds number environment. Nonetheless, the techniques described can be used to account for the effects of a different body force which may act upon a body on the length scale of sperm flagella. In this section, simulations of a passive xy-planar filament sedimenting under gravity are considered. Formulations to model different body forces follow in a similar manner, wherein references to "gravity" throughout can be replaced without loss of generality to describe the body force under consideration.

For a filament of uniform mass per unit length ρ subject to a gravitational field acting along the y-axis, the force per unit length due to gravity is $-\rho g \mathbf{e}_y$, where $g = 9.81\text{m/s}^2$ is the acceleration due to gravity. This force appears in the derivations for the force and moment equilibrium equations (2.6) following the physical consideration of forces and moments on an infinitesimal segment of filament. A schematic of

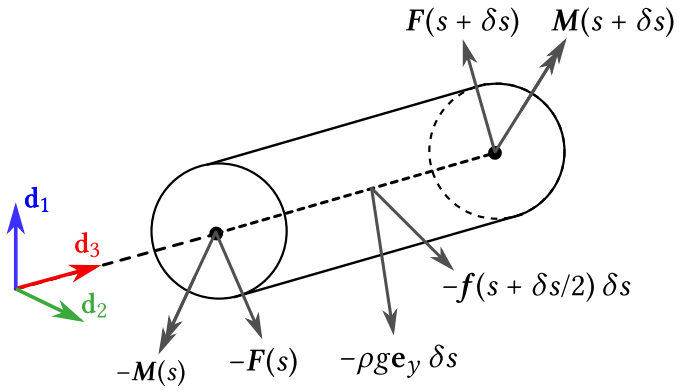

Figure 2.10: Schematic of the force and moment balance about an infinitesimal segment of filament sedimenting under gravity, from which the force and moment equilibrium equations are derived.

this setup is given in figure 2.10. Following the calculations presented in section 1.3.3, the force equilibrium equation becomes

$$\boldsymbol{F}_s(s) - \boldsymbol{f}(s) - \rho g \mathbf{e}_y = \mathbf{0}. \tag{2.53}$$

The moment due to the gravitational force per unit length about the filament segment will be $\mathcal{O}(\delta s^2)$ and so vanishes from the moment equilibrium equation in taking the limit $\delta s \longrightarrow 0$, leaving the moment equilibrium equation unaltered.

In the absence of a natural timescale characterising the system, we nondimensionalise using the same scalings as the passive relaxing problem, given in equation (2.14). The resulting dimensionless total force and total moment balance equations are

$$\int_0^1 \big(-\boldsymbol{f}(\xi,t) - \mathcal{G}\mathbf{e}_y \big)\, d\xi = \mathbf{0}, \tag{2.54a}$$

$$\mathbf{e}_z \cdot \int_0^1 \big(\boldsymbol{X}(\xi,t) - \boldsymbol{X}_c(t) \big) \wedge \big(-\boldsymbol{f}(\xi,t) - \mathcal{G}\mathbf{e}_y \big)\, d\xi = 0, \tag{2.54b}$$

where $\boldsymbol{X}_c(t)$ is the centre of gravity of the filament, $\boldsymbol{f}(s,t)$ is the force per unit length

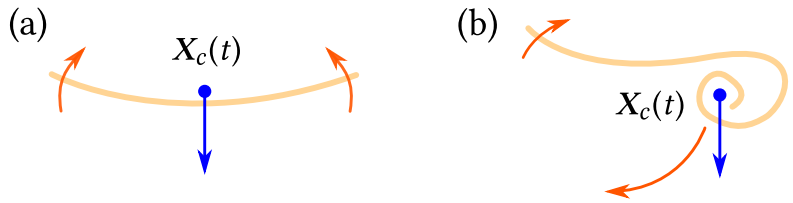

Figure 2.11: For a filament sedimenting under gravity, moment balance across the fibre must be considered about the centre of mass $X_c(t)$ in order to capture potential rotations to filament geometry. In the above diagram, blue arrows indicate the force due to gravity and orange arrows indicate resulting moments. The approximate location of the centre of mass is indicated by the blue circle. (a) The symmetrical configuration results in the filament ends curling upwards upon sedimentation. (b) The highly coiled geometry shifts the centre of mass causing a global rotational moment, balanced by the fluid so that the total moment is zero.

the filament exerts onto the fluid, and the dimensionless group

$$\mathcal{G} = \frac{\rho g L^3}{E} = \frac{\text{gravitational forces}}{\text{elastic forces}} \tag{2.55}$$

is an elastogravitational parameter describing the ratio of gravitational body forces and elastic forces, with large values characterising flexible filaments, and conversely, small values stiff filaments. In equation (2.54b), moments are taken about the the filament centre of mass in order to capture possible rotational effects during sedimentation (see fig 2.11). In problems with a natural pivot, such as the mechanical join between cell body and flagellum, moments should be taken about this point instead.

Following a derivation similar to that presented in section 2.2, the dimensionless elastodynamic equation is found as

$$\theta_s(s,t) + \mathbf{e}_z \cdot \int_s^1 \big(\boldsymbol{X}(\xi,t) - \boldsymbol{X}(s,t)\big) \wedge \big(\boldsymbol{f}(\xi,t) + \mathcal{G}\mathbf{e}_y\big)\, d\xi = 0, \tag{2.56}$$

which, alongside equations (2.54a,2.54b), has spatially discretised form

$$\mathbf{0} = \sum_{n=1}^{N-1} \Delta s\big(-\tilde{\boldsymbol{f}}[n](t) - \mathcal{G}\mathbf{e}_y\big), \tag{2.57a}$$

$$\mathbf{0} = \sum_{n=1}^{N-1} \Delta s\big(\tilde{\boldsymbol{X}}[n](t) - \boldsymbol{X}_c(t)\big) \wedge \big(-\tilde{\boldsymbol{f}}[n](t) - \mathcal{G}\mathbf{e}_y\big), \tag{2.57b}$$

$$\frac{\tilde{\theta}[n+1](t) - \tilde{\theta}[n](t)}{\Delta s} = -\mathbf{e}_z \cdot \sum_{m=n}^{N-2} \Delta s\big(\tilde{\boldsymbol{X}}[m+1](t) - \boldsymbol{X}[n+1](t)\big) \wedge \big(\tilde{\boldsymbol{f}}[n+1](t) + \mathcal{G}\mathbf{e}_y\big), \tag{2.57c}$$

for $n = 1, \ldots, N-2$ in equation (2.57c). The matrix system encoding the sedimenting filament problem is

$$A_g \begin{pmatrix} \dot{\boldsymbol{Z}} \\ \tilde{\boldsymbol{f}} \end{pmatrix} = \boldsymbol{b}_g, \tag{2.58}$$

where the matrix A_g has the same block form as A in section 2.2.3, but with an alteration in the first row of the elasticity block A_E due to the inclusion of the centre of gravity in the total moment balance equation (2.57b). The right hand side vector is constructed as $\boldsymbol{b}_g = \boldsymbol{b} + \boldsymbol{b}'$, where $\boldsymbol{b}'$ encodes the additional gravitational terms arising from the expansion and rearrangement of equations (2.57a,2.57b,2.57c).

We next consider the results of simulations of both single and multiple filaments sedimenting due to gravity for different choices of elastogravitational parameter $\mathcal{G}$. The filament is initialised sampling $\theta(s, 0)$ symmetrically from the very-low amplitude parabola $y = 10^{-7}x^2$, ensuring unit arclength and presolved across the time interval $[0, t_c]$, $t_c \ll t_{\max}$ with a coarse discretisation $N = 11$ until the shape is sufficiently curved i.e. when the maximum curvature exceeds a tolerance of 0.5. The low-resolution coordinate solution is then closely approximated with a cubic smoothing spline generated

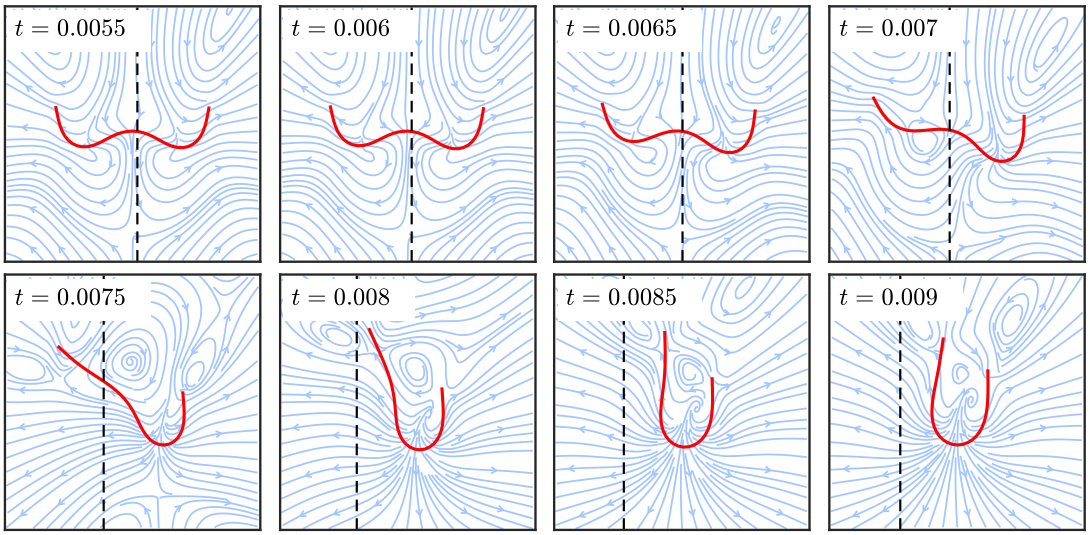

Figure 2.12: Dynamics of a very flexible filament sedimenting under gravity. Here, for $\mathcal{G} = 3500$, the filament first assumes a metastable "W" profile, before instability along the arclength causes a transition to the stable "U" configuration. In each panel, axes are centred on the centre of gravity of the filament at the corresponding time point. The dashed line position of the centre of gravity at $t = 0$, and blue lines with arrows indicate the disturbance in the fluid due to the presence of the filament.

by the MATLAB® function `csaps`, with smoothing parameter chosen so as to maintain unit arclength. This curve is then sampled, again ensuring unit arclength, to obtain a new higher-resolution initial condition for the original problem, which is then simulated over $t \in [0, t_{\max}]$. This presolve enables simulations of multiple high-resolution filaments without needing to vary the discretisation parameters dynamically during the simulation. In the following results, $N = 41$ is used for the upscaled initial condition.

We begin by examining single filament simulations. Different choices of the characteristic parameter $\mathcal{G}$ lead to different sedimentary buckling modes. For $\mathcal{G} < 3000$, a stable "U" configuration is approached whereby the ends of the fibre bend 'upwards' as the filament moves 'downwards', as seen in the model comparisons in 2.3.2. For large

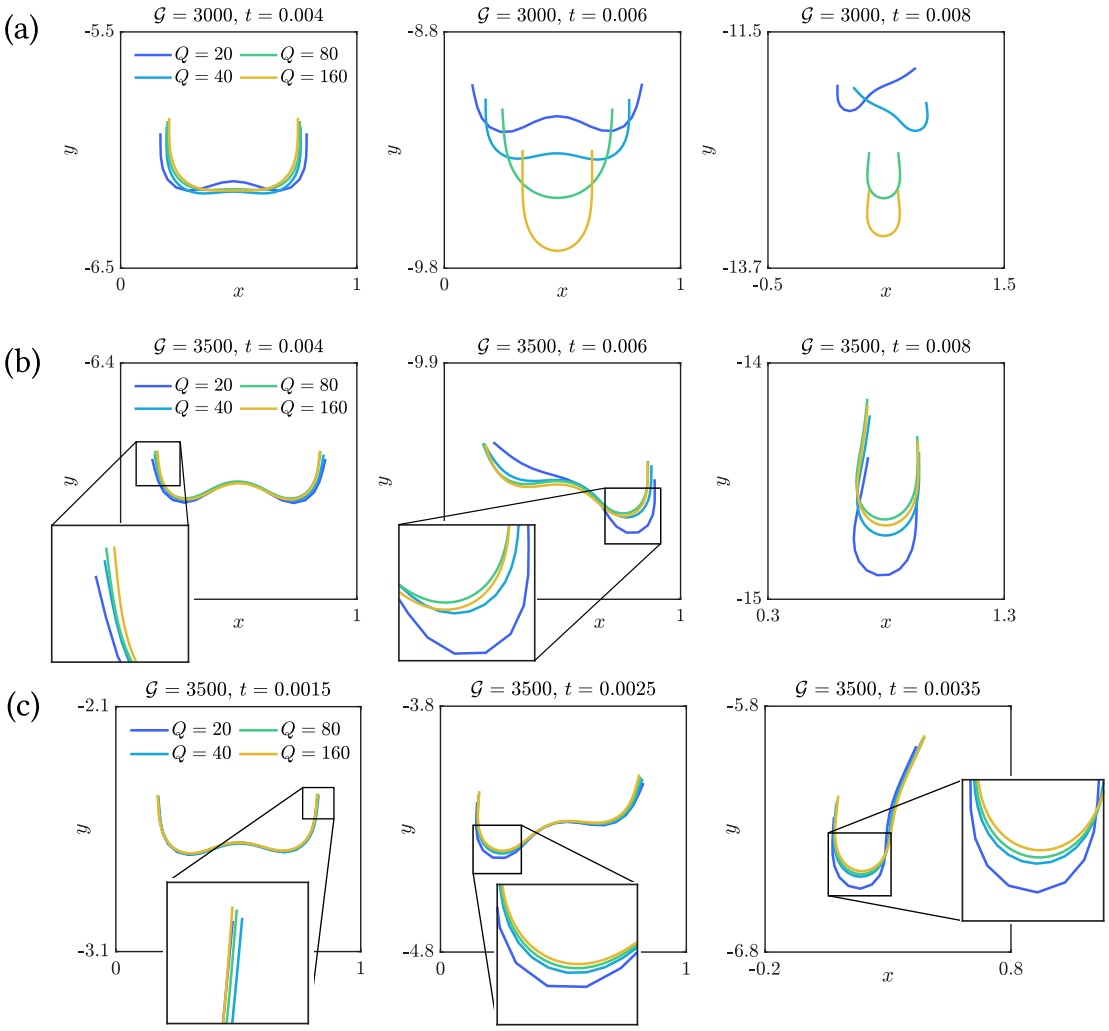

Figure 2.13: Spatial error convergence for a sedimenting filament. (a) The choice of $Q = N - 1$ determines the length of time spent in the metastable "W" configuration. For the critical value of $\mathcal{G} = 3000$, the onset time of the buckling mode transition can lead to large spatial RMSD when refining the filament discretisation. Increasing $\mathcal{G}$, as in (b), guarantees the buckling direction but errors persist. (c) Biasing the initial condition resolves the metastability and convergence results upon doubling Q are improved.

values $\mathcal{G} > 3000$, a metastable "W" configuration forms, transitioning into a stable "U" horseshoe shape, seen in figure 2.12. This behaviour has been previously observed by Cosentino Lagomarsino *et al.* (2005) and Delmotte *et al.* (2015a), who witnessed buckling at the same threshold value for their identically defined elastogravitational parameter. This transition shifts the filament's centre of gravity to the left, creating an asymmetry which is then partially resolved upon approach the horseshoe equilibrium configuration.

As observed for the filaments in shear flow (see 2.4.1), the spatial convergence of solutions for sedimenting problems depends significantly on the choice of initial condition and discretisation. In particular, the choice of N determines the length of time the filament remains in the metastable "W" configuration. When in the "U" configuration, the filament travels faster, resulting in large spatial root mean squared difference (RMSD) if the shape transition occurs at sufficiently different times. This behaviour is most evident at the critical value of $\mathcal{G} = 3000$, where nonunique shape configurations arise (see figure 2.13a). Increasing to $\mathcal{G} = 3500$ guarantees the direction of the buckling, but large variability persists due to differences in the onset time of the transition, as shown in figure 2.13b.

Convergence is improved by using a slightly left/right asymmetrical filament initial condition. Introducing a rotational bias of $\theta_0 = 0.001\pi$ to the initial shape before the presolve reduces the time variance in the "W-U" buckling onset, yielding smaller errors for sufficiently fine discretisations $Q > 40$ (figure 2.13c).

We continue by examining the sedimentary dynamics of arrays of filaments. A range of filament systems with multiple choices of elastogravitational parameter $\mathcal{G}$ are presented in figures 2.14, 2.15, 2.16. In each case, the initial filament shape is as those considered above, and are uniformly separated by $\Delta \boldsymbol{X}_0 = (\Delta X_0, \Delta Y_0)$. A stopping crite-

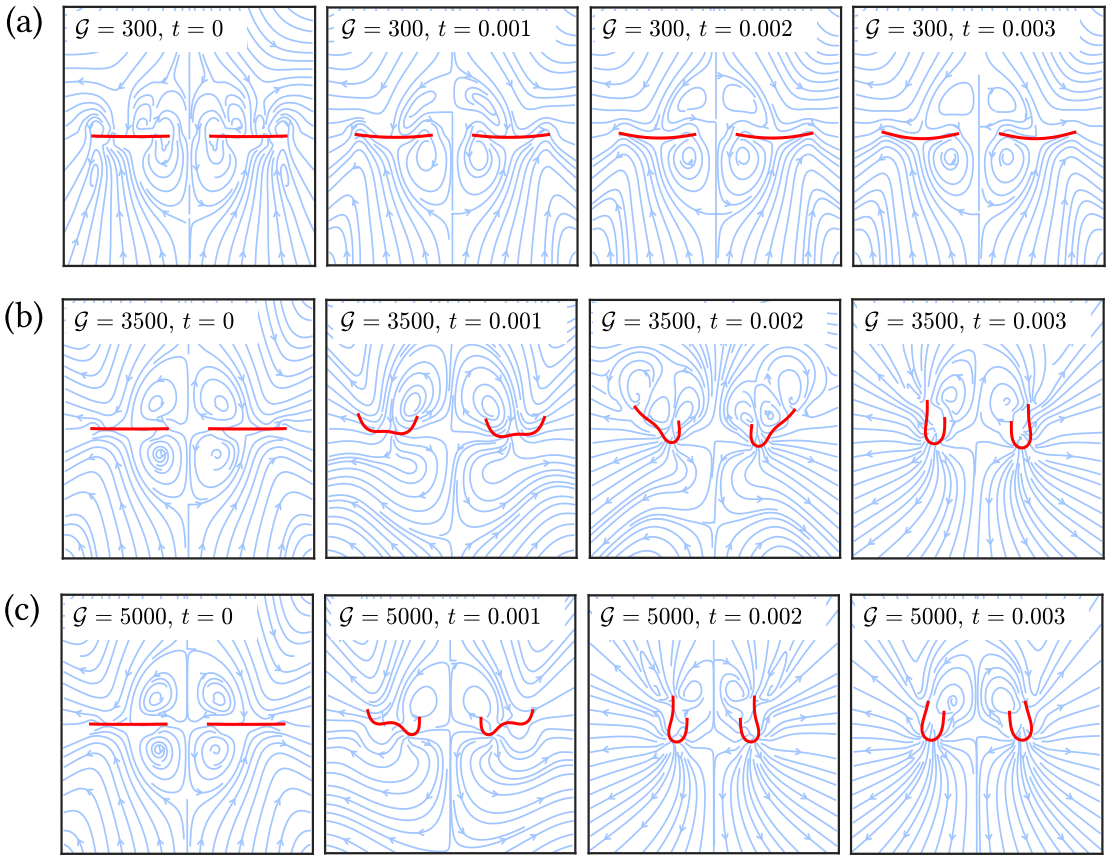

Figure 2.14: Two filament sedimenting under gravity, both characterised by the same elastogravitational parameter $\mathcal{G}$. Blue lines with arrows indicate the direction of the fluid disturbance caused by the presence of the filaments.

rion is implemented which halts the simulation when filaments intersect or otherwise touch.

For small values of $\mathcal{G}$, filaments slide towards each other as they sediment due to the anisotropy of Stokes drag. For larger values (figures 2.14b,c), the metastable and stable buckling modes observed in the single filament experiments (see figure 2.12) are replicated. In these multifilament systems, the hydrodynamic interactions between fibres results in the steady state profiles being reached sooner than in the single fil-

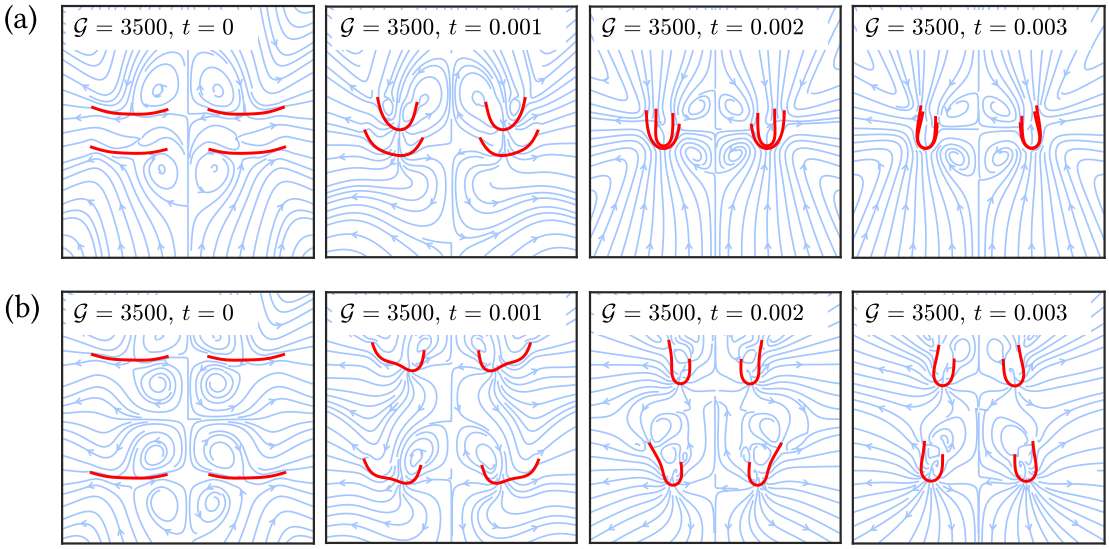

Figure 2.15: The effect of initial filament density on group dynamics when sedimenting under gravity. In both experiments, the horizontal spacing between filaments is equal. A change in the vertical spacing from (a) 0.5 to (b) 1.5 leads to different fluid dynamics and resulting filament configurations. Streamlines indicate the direction of the fluid disturbance caused by filament interactions.

ament experiments. Furthermore, the onset of buckling occurs for reduced $\mathcal{G}$ values when multiple filaments are interacting.

As was the case for multiple filaments in shear flow, the inter-filament spacing $\Delta \boldsymbol{X}_0$ has a significant effect on the resulting group dynamics, and can lead to symmetry breaking in the filament arrangements. Figure 2.15 considers two initial filament placements, with $\Delta X_0 = 1.5$ common to both and $\Delta Y_0 = \{0.5, 1.5\}$ in 2.15a,b respectively. Smaller vertical spacing leads the filaments "nestling" in a horizontally mirrored configuration; when placed further apart, horizontal mirroring still occurs but the fibres do not approach each other.

In figure 2.16 nine filaments of equal length and stiffness are arranged in a grid with initial spacing $\Delta \boldsymbol{X} = (1.5, 1)$. As with the smaller arrays, filaments group and buckle ac-

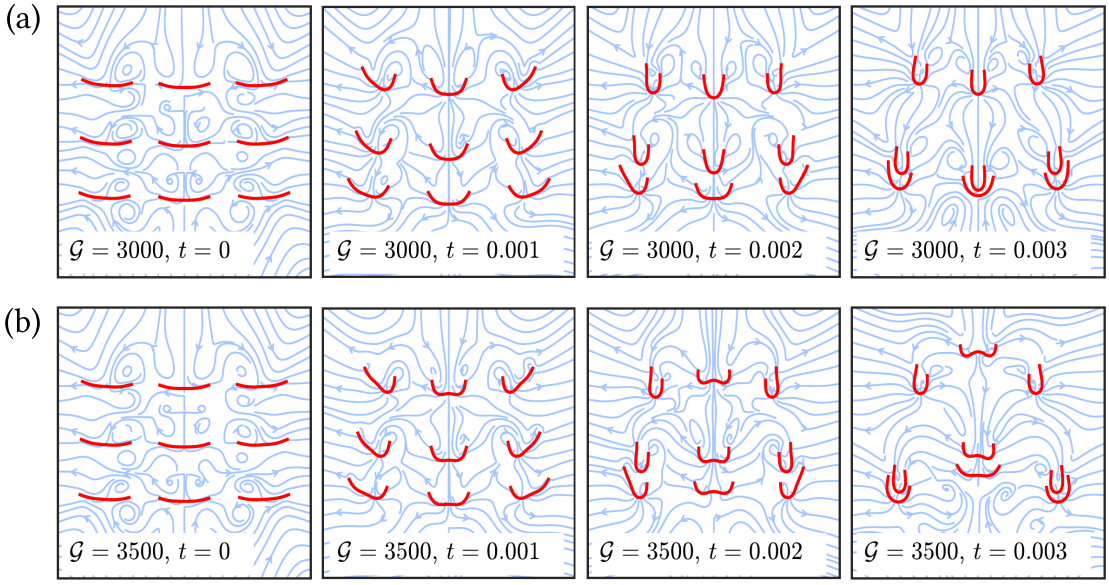

Figure 2.16: Simulation of multiple sedimenting filaments. The EIF framework can also accommodate larger arrays of filaments, such as the 3×3 arrangements above. In each case, the initial filament spacing is $\Delta \boldsymbol{X}_0 = (1.5, 1)$. In all cases, vertical symmetry breaking is apparent when $t > 0.001$. Streamlines indicate the direction of the fluid disturbance caused by the presence of the filaments.

cording to the choice of characteristic parameter $\mathcal{G}$. Despite uniformity between fibres, nonlocal hydrodynamic interactions result in different buckling behaviours depending on location within the array.

For all choices of $\mathcal{G}$, vertical symmetry breaking occurs between the top-most and middle rows of filaments, with the second and third rows of filaments on the left and right of the frame nestling into those below them. For $\mathcal{G} = 3500$, more prominent buckling is apparent, with filaments in the central 'column' approaching a "W" shape, whereas those on the flanks assume a horseshoe configuration. Competing interactions between filaments in the central column and their surrounding neighbours causes them to remain in the metastable "W" configuration longer than would be expected in the single filament experiment.

2.4.3 Internally actuated filaments

Countless microorganisms and organelles use thin elastic bodies to interact with their environment. In particular, filaments are often used as a means of propulsion, either by pushing a body through a fluid, (such as for spermatozoa), pulling a body through a fluid (in the case of *Chlamydomonas reinhardtii* and similar organisms), or themselves being slender and able to move in a way that enables swimming (such as *C. elegans* and other roundworm species). Extending the EIF framework to model actuated fibres enables application to and simulation of many of the swimming problems common in microbiology.

For the problems considered in sections (2.4.1,2.4.2), active filaments can be considered by including a time dependent moment density added to the elastodynamic formulation in equation (2.10).

The equilibrium equations in this case are derived by considering equations (1.89b) and (1.89c), with a planar actuating moment per unit length $m(s,t)$, yielding

$$\boldsymbol{F}_s(s,t) - \boldsymbol{f}(s,t) = \mathbf{0}, \tag{2.59a}$$

$$M_s(s,t) + \mathbf{e}_z \cdot \boldsymbol{X}_s(s,t) \wedge \boldsymbol{F}(s,t) + m(s,t) = 0. \tag{2.59b}$$

In the xy-planar formulation considered here, the active moment per unit length function $m(s,t)$ acts in the same direction as the internal contact moment $M(s,t)$ i.e. in the z-direction, and can be thought of as a dynamic function actively rotating the $(\mathbf{t}(s,t), \mathbf{n}(s,t))$ frame along the length of the filament to produce planar waveforms that will result in cell propulsion. In the following section, we will consider two choices of actuating function, producing *sperm-like* and *worm-like* filament waveforms. The former produces bending moments which grow in amplitude along its arclength, whereas

the second is homogenous. We define these functions as

$$m_1^*\left(\frac{s^*}{L}, t^*\right) = \frac{m_1^0 s^*}{L}\cos\left(\frac{k^* s^*}{L} - \omega^* t^*\right), \tag{2.60a}$$

$$m_2^*(s^*, t^*) = m_2^0\cos(k^* s^* - \omega^* t^*), \tag{2.60b}$$

where k^* is the angular wave number of the beat, ω^* is the beat frequency, L is the filament length, and m^0 is the beat amplitude with units of moment per unit length. Asterisks are used to denote dimensionful variables.

Defining the actuating moment density through either (2.60a) or (2.60b) lends a natural timescale to the problem through the angular frequency of the active beat. Continuing the model derivation as in section 2.2 and using the scalings

$$s^* = Ls, \quad \boldsymbol{X}^* = L\boldsymbol{X}, \quad t^* = \omega^{-1}t, \quad \boldsymbol{f}^* = \mu\omega L\boldsymbol{f}, \quad k^* = L^{-1}k, \tag{2.61}$$
$$m_1^* = m_1^0 m_1, \quad m_2^* = m_2^0 m_2,$$

where $m_1 = s\cos(ks - t)$ and $m_2 = \cos(ks - t)$, yields the dimensionless elastodynamic equation for an active filament as

$$\theta_s(s,t) + \mathbf{e}_3 \cdot \mathcal{S}^4 \int_s^1 \big(\boldsymbol{X}(\xi,t) - \boldsymbol{X}(s,t)\big) \wedge \boldsymbol{f}(\xi,t)\, d\xi - \mathcal{M}_\alpha \mathcal{S}^4 \int_s^1 m_\alpha(\xi,t) d\xi = 0, \tag{2.62}$$

for $\alpha = 1, 2$, determining the choice of actuation function, and where the dimensionless parameters

$$\mathcal{S} = L\left(\frac{\mu\omega}{E}\right)^{1/4}, \qquad \mathcal{M}_1 = \frac{m_1^0}{\mu\omega L^2}, \qquad \mathcal{M}_2 = \frac{m_2^0}{\mu\omega L^2} \tag{2.63}$$

are the *swimming parameter* (comparing the ratio of viscous to elastic forces), and the *actuation parameters* (comparing the ratio of active to viscous forces) for each beat

type respectively. The swimming parameter $\mathcal{S}$ is similar to the commonly-used sperm number Sp (Gadêlha *et al.*, 2010; Montenegro-Johnson *et al.*, 2015), which depends on a chosen resistance coefficient. The dimensionless total moment balance equation is similarly altered owing to the change in equilibrium equation as

$$\int_0^1 \boldsymbol{X}(\xi,t)\wedge\boldsymbol{f}(\xi,t)\,d\xi = \mathcal{M}_\alpha\mathcal{S}^4\int_0^1 m_\alpha(\xi,t)\,d\xi. \tag{2.64}$$

The discretised forms of equations (2.62,2.64) are

$$\mathcal{M}_\alpha\mathcal{S}^4 M_\alpha[1](t) = \sum_{m=1}^{N-1}\Delta s\tilde{\boldsymbol{X}}[m](t)\wedge\tilde{\boldsymbol{f}}[m](t), \tag{2.65a}$$

$$\frac{\tilde{\theta}[n+1](t)-\tilde{\theta}[n](t)}{\Delta s} - \mathcal{M}_\alpha\mathcal{S}^4 M_\alpha[n](t) = -\mathbf{e}_z\cdot\mathcal{S}^4\sum_{m=n}^{N-2}\Delta s\big(\tilde{\boldsymbol{X}}[m+1](t) - \boldsymbol{X}[n+1](t)\big)\wedge\tilde{\boldsymbol{f}}[m+1](t), \tag{2.65b}$$

for $n = 1,\dots,N-2$ and either $\alpha = 1, 2$, and where

$$M_\alpha[n](t) = \int_{\tilde{s}[n]}^1 m_\alpha(\xi,t)\,d\xi, \qquad n = 1,\dots,N-1 \tag{2.66}$$

is the analytically integrated active moment density over the distal discrete filament.

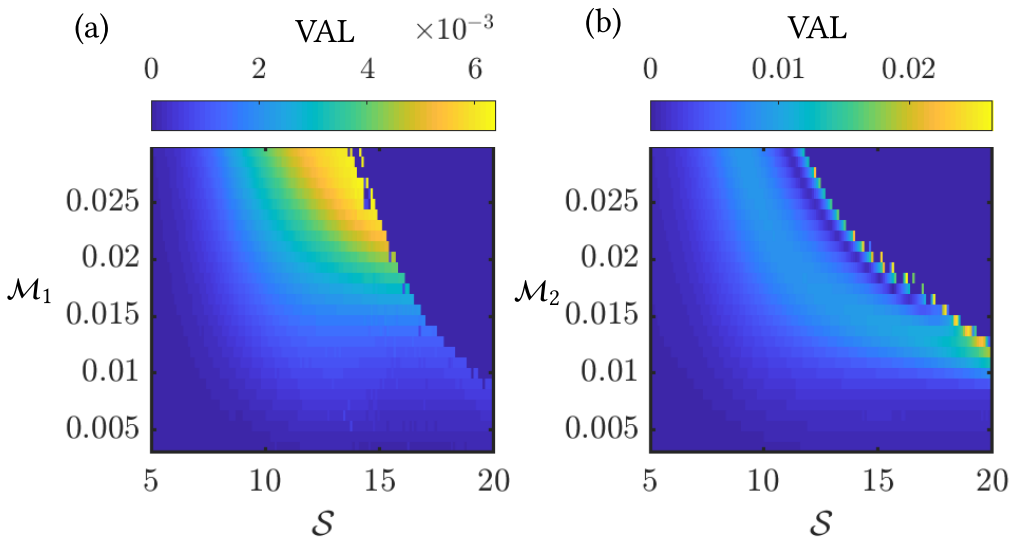

Figure 2.17: Swimming speed of a filament and its relation to parameter choices. For fixed wave number $k = 4\pi$, the velocity along a line (VAL) is calculated for pairs of filament swimming number $\mathcal{S}$ and actuation parameter $\mathcal{M}_\alpha$, with $\alpha = 1, 2$ for a sperm-like beat (a), or worm-like beat (b). The dark blue patches in the top-right of each panel correspond to failed simulations where parameter choices yield filament self-intersection.

The resulting linear system is

$$A_a \begin{pmatrix} \dot{Z} \\ \tilde{f} \end{pmatrix} = \boldsymbol{b}_a, \tag{2.67a}$$

$$\text{where } A_a = \begin{pmatrix} 0 & \mathcal{S}^4 A_E \\ A_K & A_H \end{pmatrix}, \tag{2.67b}$$

$$\text{and } \boldsymbol{b}_a = \boldsymbol{b} - \mathcal{M}_\alpha \mathcal{S}^4 \left(M_\alpha[1](t), \ldots, M_\alpha[N-1](t) \right)^T, \tag{2.67c}$$

such that $\boldsymbol{b}_a$ includes the additional terms required to the right hand side of (2.35) owing to the inclusion of the active moment term.

For appropriate choices of swimming parameter and actuation parameter corre-

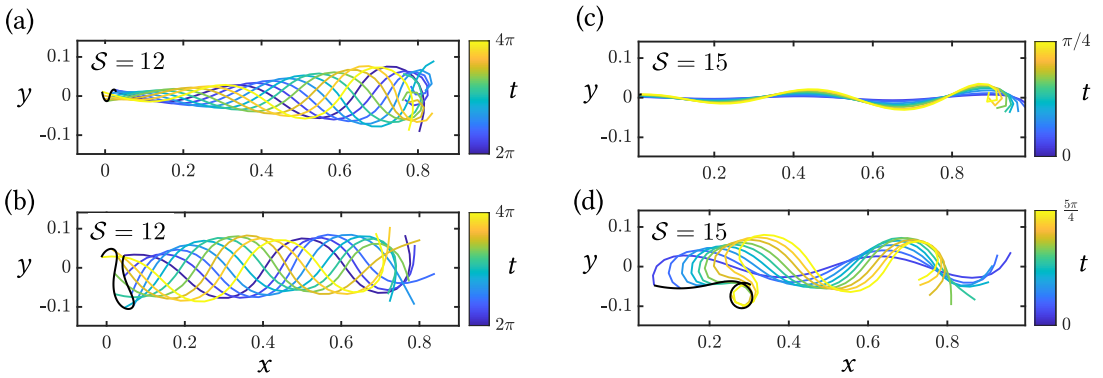

Figure 2.18: Shape configuration of single swimming filaments, propelled by the moment density profiles in equations (2.60a) ((a) and (c)) and (2.60b) ((b) and (c)). Here, $\mathcal{M}_1 = \mathcal{M}_2 = 0.03$, $k = 4\pi$ and $N = 41$. The solid black curve traces the path of the leading point $\boldsymbol{X}_0(t)$. In (a) and (c), $\mathcal{S}$ is approximately optimal for the chosen actuation parameters resulting in fast, directed motion. In figures (b) and (d), extreme filament curvatures lead to self intersection.

sponding to either a sperm-like or worm-like beat, a simulated filament can be induced to swim in a stationary surrounding flow. Fixing the dimensionless wave number $k = 4\pi$, we investigate the relationship between elasticity and choice of driving force (governed by $\mathcal{M}_1$ or $\mathcal{M}_2$) for a single isolated filament. Swimmer performance is qualitatively assessed by its velocity along a line (VAL), a measure of the locomotive speed for a chosen $\mathcal{S}$ and $\mathcal{M}_\alpha$ pair, calculated via

$$\text{VAL} = \frac{\|\boldsymbol{X}_0^{(n)} - \boldsymbol{X}_0^{(n-1)}\|}{T}, \tag{2.68}$$

in which $T = 2\pi$ is the period of the driving wave and $\boldsymbol{X}_0^{(n)} := \boldsymbol{X}(0, 2\pi n)$ is the position of the leading point of the filament after it was travelled n wavelengths, with n chosen such that the filament has established a consistent periodic motion after beginning to swim.

Swimming speed for difference choices of parameter pairings ($\mathcal{S}$, $\mathcal{M}_{1,2}$) for both

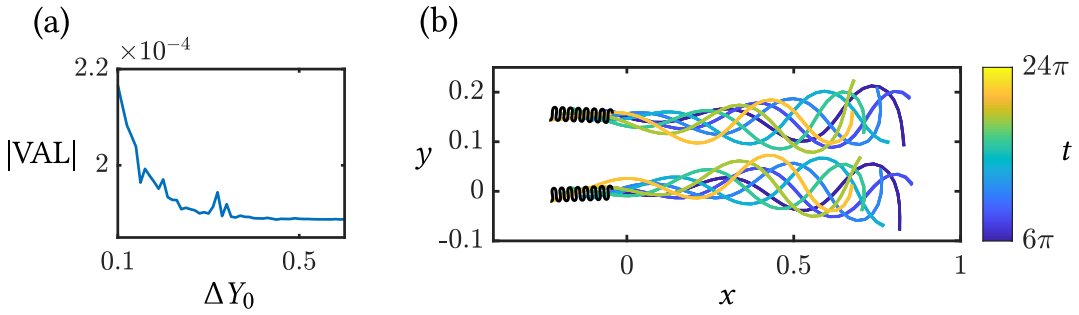

Figure 2.19: Two mechanically identical filaments characterised by $\mathcal{S} = 8$ and $\mathcal{M}_1 = 0.05$, propelled by a sperm-like active moment density function, swimming alongside each other. (a) Filaments in close proximity swim, on average, faster than those further apart. (b) Shapes of the evolving filaments are presented for an initial vertical separation $\Delta Y_0 = 0.1$ for $t \in [6\pi, 24\pi]$. The black curve indicates the paths of the leading points of each filament.

sperm-like and worm-like beat types are presented in figure 2.17. Incompatible parameter pairings result in filament self-intersection, at which point the EIF is inapplicable and the simulation is terminated. Examples of fibre shapes in such cases are given in figures 2.18b and 2.18d. For a sperm-like swimmer (figure 2.17a), swimming speed increased as $\mathcal{M}_1$ and $\mathcal{S}$ are increased in tandem for fixed wave number $k = 4\pi$. In contrast, worm-like swimmers exhibit a clear optimal choice of $\mathcal{M}_2$ for a given $\mathcal{S}$ to induce fastest swimming. Shape profiles for the fastest swimmers of sperm- and worm-type are displayed in figures 2.18a and 2.18c respectively.

As with the previously considered dynamic problems, the EIF can simulate multiple nonlocally interacting swimming filaments. To illustrate this, we consider two filaments swimming alongside each other, in the same direction, at different separation distances ΔY_0. For fixed $\mathcal{S} = 8$ and $\mathcal{M} = 0.05$, the size of the separation effects the resulting average swimming velocity (figure 2.19). At low levels of separation, nonlocal hydrodynamic interactions between the synchronous beats result in a higher average VAL, which decays as the filaments are initialised further apart (figure 2.19a).

2.5 Modelling human spermatozoa using the EIF

An important and prominent application of the EIF is to that of human sperm flagella, the single flexible appendage of the spermatozoon which beats to propel the cell through viscous fluid. Biological features necessitate alterations to the EIF method presented thus far. In this section, we outline extensions to the EIF to model a human spermatozoon, following Neal *et al.* (2020), building from the framework detailed in section 2.4.3.

The largest and most obvious addition to the model is the necessary inclusion of the cell head at the proximal end of the filament. A discretisation for the head surface is obtained by discretising a sphere using the method outlined in section 1.2.6 and then scaled to the desired dimensions. The head is connected to the flagellum at the leading point $\boldsymbol{X}_0(t) := \boldsymbol{X}(0,t)$ and interacts with the rest of the flagellum through the fluid. In the following section, unmarked variables denote dimensionful quantities and hats are used to indicate dimensionless variables. Using the method of regularised stokeslets, the velocity of points $\boldsymbol{Y}(t)$ along the flagellum (enforcing a no-slip condition) can be written in dimensional form

$$\boldsymbol{X}_t(s,t) = \frac{1}{8\pi\mu}\int_0^L \boldsymbol{S}^\varepsilon\big(\boldsymbol{X}(s,t),\boldsymbol{X}(\xi,t)\big)\cdot\boldsymbol{f}(\xi,t)\,d\xi + \frac{1}{8\pi\mu}\iint_{\partial H}\boldsymbol{S}^\varepsilon\big(\boldsymbol{X}(s,t),\boldsymbol{Y}(t)\big)\cdot\boldsymbol{\varphi}(\boldsymbol{Y},t)\,dS_Y, \quad (2.69)$$

where L is the length of the flagellum, ∂H is the surface of the cell head, $\boldsymbol{Y}(t)$ are material points embedded in the head surface, and $\boldsymbol{\varphi}$ is the force per unit area the head exerts on the surrounding fluid. As before, $\boldsymbol{f}$ is the force per unit length the flagellum

exerts onto the fluid. The velocity of points on the head can be similarly written

$$\boldsymbol{Y}_t(t) = \frac{1}{8\pi\mu}\int_0^L \boldsymbol{S}^\varepsilon\big(\boldsymbol{Y}(t), \boldsymbol{X}(\xi,t)\big)\cdot\boldsymbol{f}(\xi,t)\,d\xi + \frac{1}{8\pi\mu}\iint_{\partial H}\boldsymbol{S}^\varepsilon\big(\boldsymbol{Y}(t),\mathrm{y}(t)\big)\cdot\boldsymbol{\varphi}(\mathrm{y},t)\,dS_{\mathrm{y}}. \quad (2.70)$$

The head, through being connected to the flagellum, translates and rotates about the connecting point $\boldsymbol{X}_0(t)$. Modelling the head as a rigid body, the velocities are

$$\boldsymbol{u}(\boldsymbol{Y}(t),t) = \boldsymbol{U}(t) + \Omega(t)\wedge\big(\boldsymbol{Y}(t)-\boldsymbol{X}_0(t)\big), \quad (2.71)$$

where $\boldsymbol{U}(t) = (\boldsymbol{X}_0(t))_t$ and $\Omega(t)$ represent the rigid body translational velocity and rotational velocity of the cell head respectively. For the xy-planar problem considered in this chapter, the angular velocity can be written as

$$\Omega(t) = \phi_t(t)\,\mathbf{e}_z, \quad (2.72)$$

where $\phi(t)$ is the angle formed between the head major-axis and the x-axis, referred to here as the *head angle*. The unit vector $\mathbf{e}_z$ points out of the plane of motion. Enforcing a no-slip condition on the surface of the cell head (as on the surface of the flagellum) and equating equations (2.70) and (2.71) yields an equation for the hydrodynamic velocity of the rigid cell head, accounting for the nonlocal effect of the flagellum. Terms involving the cell head necessarily appear in the total force and total moment balance

equations, which become

$$\int_0^L \boldsymbol{f}(s,t)\,ds + \iint_{\partial H} \boldsymbol{\varphi}(\boldsymbol{Y},t)\,dS_Y = \boldsymbol{0} \tag{2.73a}$$

$$\int_0^L \big(\boldsymbol{X}(s,t) - \boldsymbol{X}_0(t)\big) \wedge \boldsymbol{f}(s,t)\,ds + \iint_{\partial H} \big(\boldsymbol{Y}(t) - \boldsymbol{X}_0(t)\big) \wedge \boldsymbol{\varphi}(\boldsymbol{Y},t)\,dS_Y = \boldsymbol{0}, \tag{2.73b}$$

noting that the flagellar moments taken in (2.73b) are now taken about $\boldsymbol{X}_0(t)$, a natural pivot for the problem. After nondimensionalisation with the same scaling as in section 2.4.3, the coupling of the head to the flagellum is enforced through (see Neal *et al.* (2020) for details)

$$E(0)\kappa(0,t) - \mathbf{e}_z \cdot \mathcal{S}^4 \iint_{\partial H} \big(\boldsymbol{Y}(t) - \boldsymbol{X}_0(t)\big) \wedge \boldsymbol{\varphi}(\boldsymbol{Y},t)\,dS_Y - \int_0^L m(s,t)\,ds = 0, \tag{2.74}$$

where $\mathcal{S}$ is the dimensionless group defined in equation (2.63), m is the active moment per unit length, and E_0 is the bending rigidity of the flagellum at the head-flagellum join. The proximal curvature $\kappa(0,t)$ is approximated as the centred difference between the head angle $\phi(t)$ and the tangent angle at the proximal filament.

Another important biological feature of the human spermatozoon (and observable in many other mammalian sperm) is the tapering structure lending the flagellum different stiffness properties along its length (Cummins & Woodall, 1985). This feature is modelled by varying the elastic rigidity along the flagellum arclength as

$$E(s) = \begin{cases} (E^p - E^d)\left(\dfrac{s - s^d}{s^d}\right)^2 + E^d, & s \leqslant s^d, \\ E^d & s > s^d \end{cases} \tag{2.75}$$

where E^p and E^d are the proximal and distal bending moduli of the flagellum respec-

tively, appropriately chosen to suit the problem at hand. In the subsequent nondimensionalisation, stiffness terms are scaled by the distal bending rigidity so that $\hat{E}(\hat{s}) = E^d E(s)$.

In joint work with Neal *et al.*, the extended EIF as described above is used to investigate the effect upon propulsion of the passive end piece, a mechanically inactive region typically 3–5% of the (human) sperm flagellum length (see section 1.1.1 for details on human sperm structure). Simulations indicate that the presence of the end piece can improve speed and efficiency over cells sporting fully-actuated flagella; these results do not form a part of the present thesis, but detailed results can be found in Neal *et al.* (2020)). The end piece is modelled by multiplying the actuation function $m(s,t)$ with a Heaviside function so that

$$m(s,t) = m_0 \cos(ks - \omega t) H(L - \ell - s), \tag{2.76}$$

where $\ell \in [0, L]$ is the length of the inactive end piece, so that $L - \ell$ is the length of the active region of flagellum. As in section 2.4.3, m_0 is the moment amplitude, k is the wave number of actuation, and ω is the angular frequency of the actuating beat. The dimensional elastodynamics equation is thus

$$E(s)\theta_s(s,t) + \mathbf{e}_z \cdot \int_s^L \big(\boldsymbol{X}(\xi,t) - \boldsymbol{X}(s,t)\big) \wedge \boldsymbol{f}(\xi,t)\, d\xi \\ - \int_s^L m_0 \cos(k\xi - \omega t) H(L - \ell - \xi)\, d\xi = 0, \tag{2.77}$$

with the stiffness coefficient $E(s)$ given by equation (2.75). Nondimensionalising with the scalings in equation (2.4.3) and $\hat{E}(\hat{s}) = E^d E(s)$, the resulting dimensionless elasto-

dynamic equation is

$$\hat{E}(\hat{s})\theta_{\hat{s}}(\hat{s},\hat{t}) + \mathbf{e}_z \cdot \mathcal{S}^4 \int_{\hat{s}}^{1} \left(\hat{\boldsymbol{X}}(\xi,\hat{t}) - \hat{\boldsymbol{X}}(\hat{s},\hat{t})\right) \wedge \hat{\boldsymbol{f}}(\xi,\hat{t})\, d\xi \\ - \mathcal{M}\mathcal{S}^4 \int_{\hat{s}}^{1} \cos(\hat{k}\xi - \hat{t}) H(1 - \hat{\ell} - \xi)\, d\xi = 0, \quad (2.78)$$

where the dimensionless groups $\mathcal{S}$ and $\mathcal{M}$ are the same as those defined in equation (2.63). In simulations, the varying stiffness of the flagellum combined with the presence of the cell head (and the hydrodynamic drag it exerts on the fluid) work together to produce actuation beats that are typically more damped and less writhing (or 'worm-like') in their progression than those observed for the actuated filaments considered in section 2.4.3.

2.6 Conclusions and future extensions

In this chapter, the elastohydrodynamic integral formulation (or EIF) framework is formulated and applied to problems involving single and multiple filaments in shear flows, sedimenting under gravity, and swimming due to a prescribed internal moment density. It is compared to the bead and spring method (or BSM) for modelling elastica, which is presented and benchmarked, establishing the validity of its use to test the EIF method. Due to numerical stiffness arising from the requirement of a large number of beads and sufficiently stiff spring constants to enforce inextensibility, the BSM is unsuitable for general inextensible elastic filament modelling. From the EIF simulations presented in section 2.4, it is apparent how interfilament nonlocal hydrodynamic interactions have an important role in governing filament shapes and buckling behaviour. In particular, these interactions seem to promote shape instabilities for filaments which, in isolation, may not exhibit buckling, showcased by considering arrays of sedimenting filaments (section 2.4.2). By examining actively driven filaments, the relationship between the actuation forces and viscoelastic forces is revealed, with a clear optimum pairing identified.

A key benefit to the integral formulation is that the need for computing Lagrange multipliers of tension is removed; inextensibility of the modelled filament is already guaranteed by the use of the method of lines discretisation. In other methods such as those of Gadêlha *et al.* (2010) and Montenegro-Johnson *et al.* (2015), inextensibility is ensured by coupling the elastodynamic problem with an additional high order nonlinear PDE, which can be difficult to implement and costly to solve. The EIF approach is thus computationally faster than many similar contemporary models. Earlier work by Moreau *et al.* (2018) highlighted the reduction in computational runtime at-

tainable when using an integral formulation applied to elastodynamics, due in part to the reduction in the required degrees of freedom. Alleviating this numerical stiffness facilitates the study of geometrically nonlinear problems, such as those involving filament buckling studied in sections 2.4.1 and 2.4.2. Additional computational costs are incurred by the introduction of nonlocal hydrodynamic modelling to the framework, in line with the increase in the dimension and density of the matrix system solved at each time step. The BSM and EIF (with regularised stokeslets) complete a relaxing rod simulation in approximately equivalent wall time (as expected, since both approaches compute three dimensional nonlocal hydrodynamic interactions), shown in figure 2.2. However, to ensure small pointwise error, the bead model requires a discretisation with $N > 61$, whereas the EIF performs equally well with a much coarser segmentation of the filament $N > 21$. This allows for adequately accurate results to be obtained for reduced computational cost when using the EIF with regularised stokeslets over the bead and link model. In addition, the reduced memory requirements afforded through coarser filament refinements allow more complex problems involving multiple filaments to be simulated for approximately the same computational cost.

The proposed method has the potential to quickly and accurately simulate arrangements of filaments in various flows and surroundings. The EIF method presented here will enable the solution of more challenging problems such as planarly beating cilia sheets, or multiple sperm swimming in a narrow channel. The modular framework of the method allows such problems to be setup and executed in a straightforward and consistent manner. Additionally, the EIF method fits into the family of regularised stokeslet methods (Cortez, 2001; Cortez *et al.*, 2005), which are increasingly widely used for problems in biological fluid mechanics (Smith *et al.*, 2021; Simons & Rosenberger, 2021; Zhao & Koens, 2021). Crucially, the computational efficiency exhibited in

the single filament experiments is retained upon consideration of multiple filaments.

The method could be extended by incorporating the treecode formulation of Wang *et al.* (2019), or equivalent methods, to coarse-grain the far field flow, reducing computational costs and enabling simulation of increasingly large numbers of filaments. The inclusion of a repulsive force term to capture steric effects, such as the Lennard-Jones potential employed by Jayaraman *et al.* (2012), or a barrier force (Wolgemuth *et al.*, 2004; Schoeller *et al.*, 2021), could enable simulation of filaments in close proximity and help avoid filament self-intersection.

The results of section 2.4.1 concerning filaments in shear flow suggest the shape of a buckling fibre can be described to a high degree of accuracy by a relatively low order Chebyshev polynomial (see figure 2.8). These results suggest that a modified discretisation based on orthogonal polynomials, perhaps in concert with suitable quadrature techniques (Muldowney & Higdon, 1995) might provide further improvements in efficiency and scalability. The modularity of the EIF also enables it to be employed inside other problem formulations; recent work by Neal *et al.* (2021, unpublished) models the movement of a filament using an extended version of the EIF, but solved using a finite element method to simulate swimming through non-Newtonian fluids. In addition, regularised stokeslets in the model could be replaced by regularised blakelets (Blake, 1971; Ainley *et al.*, 2008) (see section 1.2.5) to simulate the dynamics of filaments close to domain boundaries, such as sperm cells swimming in a narrow channel (Montenegro-Johnson *et al.*, 2015).

Whilst the EIF method introduced in this chapter calculates hydrodynamic effects using the three dimensional method of regularised stokeslets, we are limited to planar problems by the two dimensional formulation for the filament geometry. Extension to three dimensions would enable simulation of many more biological problems, with

immediate examples including nonplanar rotational beating of cilia and helical swimmers. Recent work by Walker *et al.* (2020) tackles the complex extension of the angle formulation used by the EIF to 3D, requiring careful handling and transformation of orientation angles to avoid ambiguities in segment orientation. In chapter 3 of this thesis, we consider an alternative approach to modelling three dimensional filament geometry through a coordinate representation of the slender body centreline.

Chapter 3

Effects of sperm head morphology on propulsion and efficiency

3.1 Overview

As discussed in section 1.1.1, human spermatozoa comprise a cell head, a stiff midpiece, a long elastic flagellum, and a short end piece. Typically a flattened ellipsoid in shape, the head contains the precious genetic cargo necessary for successful fertilisation. Changes to the cell head dimensions can lead to changes in the storage of the genetic material. In particular, changes in the volume of the cell head can mean that the DNA carried inside is damaged or even missing. Such cells are plainly undesirable for selection in assisted reproduction techniques (ARTs). Understanding the impact of head morphology on cell propulsion through hydrodynamic interactions with its flagellum and the surrounding fluid could provide important insights into sperm rheology, paving the way for improving cell selection mechanisms through a deeper understanding of the elastohydrodynamic behaviour of observed cells.

Prototypical human spermatozoon dimensions are given in the World Health Or-

Head Type	**Length** (μm)	**Width** (μm)	**Topographical Height** (μm)
Normal	4.6 ± 0.26	2.6 ± 0.2	1.03 ± 0.08
Round	2.7 ± 0.03	3.2 ± 0.15	1.8 ± 0.11
Tapered	7.8 ± 0.4	2.6 ± 0.31	1.5 ± 0.06
Amorphous	6.7 ± 0.36	2.6 ± 0.44	1.9 ± 0.1

Table 3.1: Human sperm body dimensions, measured through atomic force microscopy by Sunanda *et al.* (2018). Table recreated from Sunanda *et al.* (2018).

ganisation laboratory manual for the examination and processing of human semen (World Health Organisation, 2010), which states that healthy human spermatozoa (that is, motile cells which are potential candidates for fertilisation of the ovum) have typical median length 4.1μm (95% CI 3.7–4.7μm), and median width 2.8μm (95% CI 2.5–3.2μm). No information is provided for an estimate of the third head dimension.

A recent study by Sunanda *et al.* (2018) has sought to address this quantitative shortcoming by using scanning electron microscopy and atomic force microscopy to produce detailed three-dimensional images of human sperm ultrastructure, measuring and categorising cell types based upon WHO standards. Measurements for the cell body dimensions of a number of phenotypes are given in table 3.1, reproduced from Sunanda *et al.* (2018). Their measurements for the length and width for a normal cell agree with those stated in the WHO manual, and additionally provide mean measurements for the topographical height of the cell.

Both World Health Organisation (2010) and Sunanda *et al.* (2018) provide examples of common defects observed in human spermatozoa. Specific to the cell bodies, deformities can include tapered heads (characterised by highly ellipsoidal shapes) and round pinhead cells, as well as more exotic shapes such as the pyriform type, a com-

bined hemispherical and conical frustum. Sketches of these defective head types are given in figure 1.1. Whilst these cells would never be candidates for artificial insemination, understanding the swimming dynamics of cells with defective geometries may provide insight into the elastohydrodynamic locomotion of sperm cells, and motivate novel new assays for cell selection from cell or flagellum capture.

In section 1.1.1, we discussed previous studies which have sought to examine the effects of varying head morphology on cell swimming dynamics. To briefly recap; in simulations with fixed flagellar beat waveforms, Katz & Phillips (1986) and later Woolley (2003) indicated the large impact head shape can have on cell swimming. Similar fixed-waveform simulations by Smith *et al.* (2009a) suggests that cells with larger bodies exhibit stabilised swimming trajectories, but the effect of this on cell speed and propulsion is unclear. To this end, Gillies *et al.* (2009) noticed cells with elongated heads swam with increased velocity, but as a result of reduced yaw rather than a reduction in drag profile. This study aims to provide further insight into the problem by performing a rigorous simulation assay of swimming cells with systematically varied head geometries. Moreover, unlike previous studies using prescribed waveform models for flagellum actuation, we employ a full elastohydrodynamic model to more accurately capture the fluid-body interactions of the dynamic cell, with more directly applicable insights to the real world problem.

In this chapter, we consider the effects that varying sperm head morphology has on important cell properties, such as its propulsive speed and Lighthill efficiency. Assuming that the cell swims with a planar beat in an infinite fluid, we employ the EIF (discussed in chapter 2), with extensions from Neal *et al.* (2020) as described in section 2.5, to model the dynamic spermatozoa. Cell heads are generated using the experimental data of Sunanda *et al.* (2018), reproduced in table 3.1. In section 3.2, we examine

the effects on VAL (velocity along a line, defined in equation (2.68)) and Lighthill efficiency (to be defined in equation 3.1) of varying cell head dimensions whilst ensuring a fixed body volume. In section (3.3), we consider heads of varying volume of both typical ellipsoidal shape and two common deformities, round and tapered type cells. This chapter concludes with a summary of findings in section 3.4.

3.2 Effects of head dimensions on cell swimming

We begin by considering how cell head dimensions affect the dynamics of a planar swimming cell whilst retaining a fixed volume. As discussed in section 3.1, head volume is an important indicator of the health of the spermatozoa and the integrity of its DNA payload. Here, we consider the ideal volume to be that formed by a body described by the mean dimensions as measured by Sunanda *et al.* (2018), presented in table 3.1, yielding $V_{\text{ideal}} \approx 12.9\,\mu\text{m}^3$. Scaling with respect to an average flagellum length of $\approx 54\,\mu\text{m}$ (Cummins & Woodall, 1985), the ideal dimensionless volume is $\hat{V}_{\text{ideal}} = 7.87 \times 10^{-5}$.

We simulate a number of independent cells swimming in an infinite fluid, with heads generated by perturbing two of the principal axes of the ellipsoidal head, with the other axis determined by fixing the cell volume to be that of the idealised body. Head radii are uniformly sampled across a range of values ±10% about the mean values recorded by Sunanda *et al.* (2018), generating a broad range of head morphologies for use in simulations. The semiaxes of the ellipsoid are (a_1, a_2, a_3), such that a_1 is the long semimajor axis, a_2 is the semiminor axis lying in the plane of beating, and a_3 is the semiminor axis perpendicular to the plane of beating. Noting that the topographical height recorded in table 3.1 is equivalent to the minor radius a_3, the axes for a

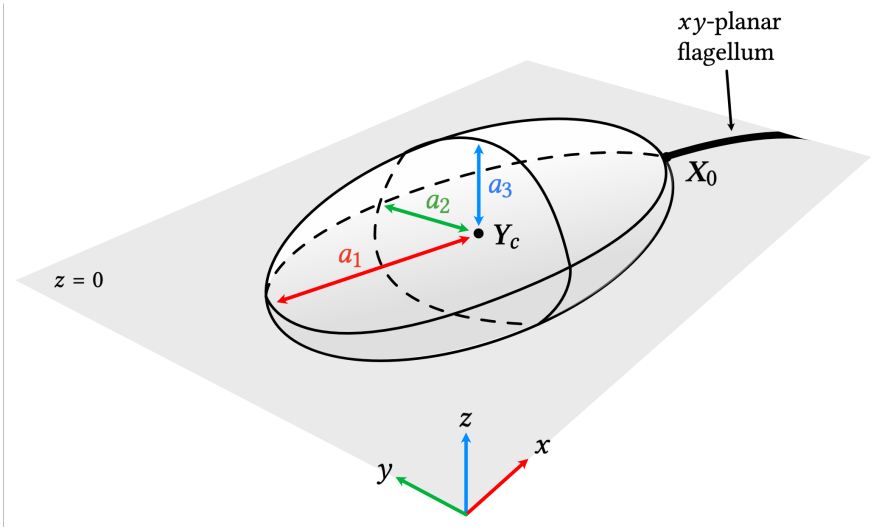

Figure 3.1: Sketch of a generalised sperm body, as included in the EIF model used within chapter 3. The swimming cell is propelled by a flagellum confined to the $z = 0$ plane, connected to the head at $\boldsymbol{X}_0$. The shape of the body is defined by radii a_1, a_2 and a_3 which describe the length of the principal axes in the x, y and z directions respectively.

normal-type cell are $(a_1, a_2, a_3) = (2.3, 1.3, 1.03)\,\mu\text{m}$. In all simulations in this section, the relationship $a_1 > a_2 > a_3$ between axes is ensured so that the aspect ratio pertaining to a physiologically healthy cell is conserved. A sketch of this configuration is provided in figure 3.1.

Each cell head is attached to a flagellum, beating in the xy-plane, described using the extended EIF model of Neal *et al.* (2020), characterised by a selection of swimming parameters $\mathcal{S}$. Fixing the dimensionless passive end piece length $\ell = 0.05$ and wave number $k = 4\pi$, actuation parameters $\mathcal{M}$ are chosen per $\mathcal{S}$ choice in order to optimise VAL for a cell with average body axes. These values, denoted $\mathcal{M}_{\text{VAL}}$, are determined through the MATLAB® minimisation algorithm `fminbnd` and are given in table 3.2. In general, these values are not the same as those which optimise the cell for efficiency (Neal *et al.*, 2020). The initial shape of the cell flagellum is obtained by sampling from

	Swimming parameter, $\mathcal{S}$							
	9	12	13	14	15	16	17	18
$\mathcal{M}_{\mathrm{VAL}}$ ($\times 10^{-2}$)	3.66	1.98	1.80	1.69	1.62	1.58	1.55	1.53

Table 3.2: Values of actuation parameter $\mathcal{M}$ optimising a swimming cell of mean body dimensions, and with passive end piece length $\ell = 0.05$, for velocity along a line (VAL), denoted $\mathcal{M}_{\mathrm{VAL}}$.

a low-amplitude parabola $y = 1 \times 10^{-6} x^2$, ensuring unit arclength through the same procedure as outlined in section 2.4.2. We initialise in this way (as opposed to a perfect straight flagellum) to avoid numerical singularity issues present in angle formulation methods (see section 2.3 for details).

Cells are simulated over 5 beats to ensure a regular periodic motion is established. This number was chosen after repeated manual observations of simulated cells to establish regularity of motion. Following similar use in Hall-McNair *et al.* (2019) and Neal *et al.* (2020), cell motility is quantitatively assessed through velocity along a line (VAL) and Lighthill efficiency. The VAL is defined as in (2.68), with $T = 2\pi$ maintained as the period of the actuating travelling wave. In the following results, we sample across the $j = 4^{\text{th}}$ beat. The Lighthill efficiency (Lighthill, 1975) is defined

$$\eta^{(j)} = \frac{(\mathrm{VAL}^{(j)})^2}{\overline{W}^{(j)}}, \tag{3.1}$$

where $\overline{W}^{(j)}$ is the mean work done by the cell over the j^{th} period, calculated as

$$\overline{W}^{(j)} = \left\langle \int_0^1 \boldsymbol{u}(s) \cdot \boldsymbol{f}(s)\, ds + \iint_{\partial B} \boldsymbol{u}(\boldsymbol{Y}) \cdot \boldsymbol{\varphi}(\boldsymbol{Y})\, dS_Y \right\rangle. \tag{3.2}$$

For each simulation, the VAL and Lighthill efficiency of the cell over a single beat

are calculated. relative to the speed and efficiency of a sperm cell with a mean sized head (i.e. of dimensions given in table 3.1). We refer to such a spermatozoon as the *mean cell* in the following discussion. The mean cell is otherwise characterised by the same dimensionless parameters as the candidate cells. Over the same beat, we additionally calculate the range of values of ϕ, the head tangent angle, to indicate the yaw behaviour of the body. Simulations can be separated into three cases: (a) those featuring cells with head axes determined by fixing a_1 and a_2, (b) those featuring cells with head axes determined by fixing a_1 and a_3, and (c) those featuring cells with head axes determined by fixing a_2 and a_3. In each case, the remaining axis is determined by assuming the volume of the body is $\boldsymbol{V}_{\text{ideal}}$.

A general overview of key results for each axis choice, and for each $\mathcal{S}$ considered, is given in figure 3.2. These star-like diagrams plot each axis value in three-dimensional space, with marker colour representing the percentage VAL difference compared to a mean cell and marker size indicating Lighthill efficiency. Colours corresponding to percentage VAL difference are sampled from a symmetric blue-red spectrum, so that the mean cell (reporting 0% VAL difference) marker is drawn white. For the latter metric, larger markers correspond to more efficient cells. In addition, the fastest cell is indicated by a black ring, and the most efficient by a black cross. The star-like shape arises from the overlaying of three approximate parallelograms generated by each axes sampling procedure, ensuring fixed ideal volume.

For all $\mathcal{S}$ values considered, alterations in head morphology yield percentage differences in VAL over a mean cell of up to ±2%. Broadly, cell heads defined by large choices of a_3 (the shortest axis, pointed out of the plane of beating) swim faster and more efficiently than the converse case. Moreover, cells which yield increases in VAL are in general more efficient swimmers. In the majority of $\mathcal{S}$ values considered, the

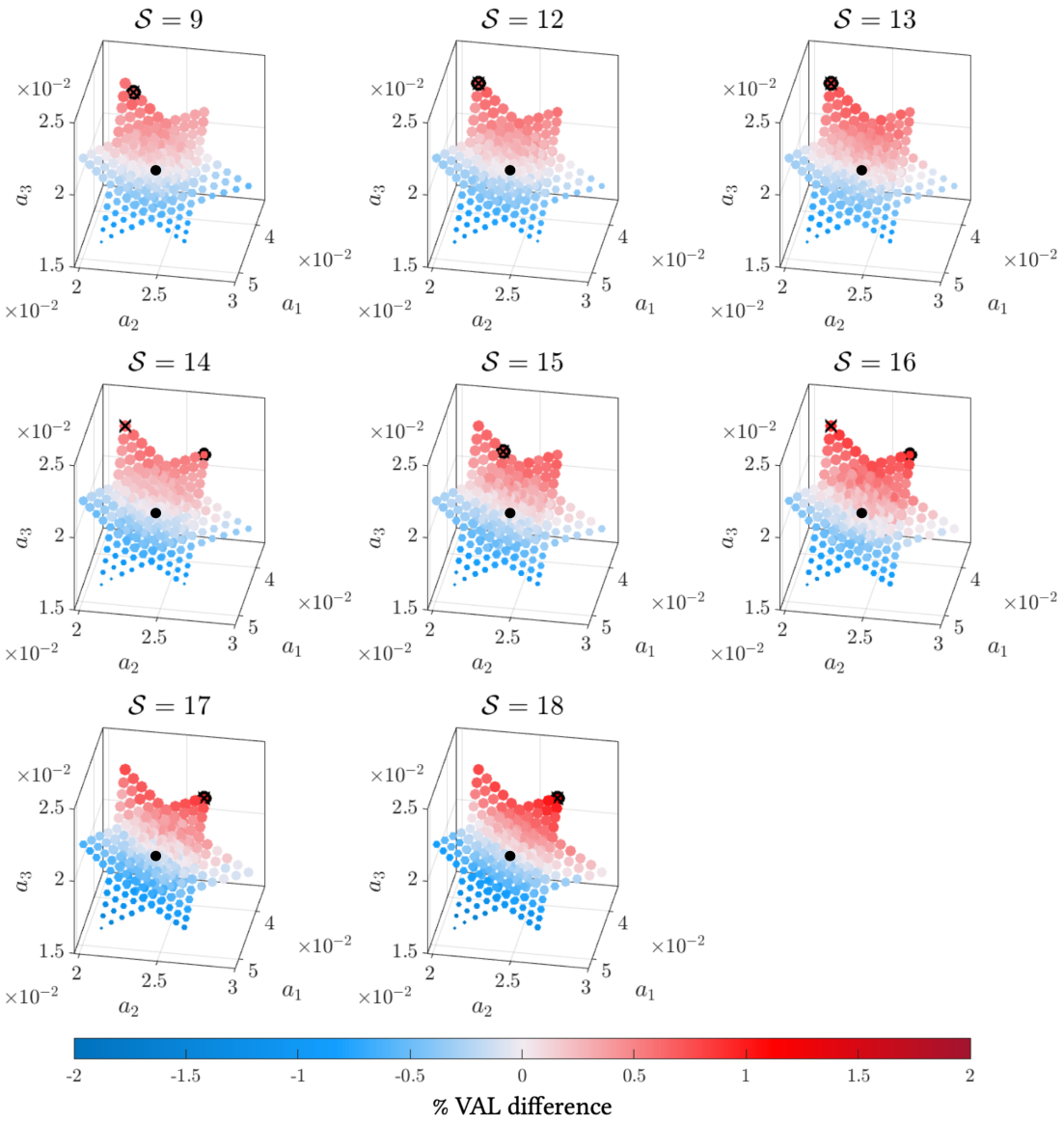

Figure 3.2: For each swimming parameter $\mathcal{S} \in [9, 18]$ considered, each point indicates a simulation with unique cell head axes ensuring fixed ideal volume. Marker colour represents the percentage VAL difference between the given cell and an average cell. Marker size represents cell efficiency, with larger dots indicating more efficient swimmers. The fastest cell is indicated with a black ring; similarly the most efficient is highlighted with a black cross. Average head axes as reported by Sunanda *et al.* (2018) are indicated by a black dot.

axis choices maximising efficiency and percentage VAL difference coincide, with exceptions recorded only in the $S = 14$ and 16 cases. As swimming parameter increases, the range of percentage VAL difference recorded increases. As S increases i.e. as simulations consider regimes in which fluid forces are dominant, the location of the optimal head axes for efficiency and VAL (indicated in figure 3.2 by a black cross and ring respectively) moves clockwise around the edge of the star. This transition is examined further in figure 3.3, which plots the *zeroline* – a linear polynomial generated using the MATLAB® `fit` command through the (a_1, a_2) values of each axis triad, corresponding to cells with absolute percentage VAL differences of $\leqslant 0.02\%$. In this way, axes formed with a_1, a_2 values from underneath each line yield cells which swim faster than a mean cell. Conversely, cells with head axis values from above the zeroline produce cells slower than mean cells. The tolerance for a data point's inclusion in the fitting process is chosen so as to ensure a sufficient number of points are included in the regression procedure whilst removing noise contributed by points whose percentage VAL difference is not close to 0%. Examining figure 3.3, zerolines corresponding to higher values of S have a steeper gradient, reflecting the clockwise travel of optimal head axes in figure 3.2.

The flagellar trace across a single beat corresponding to the fastest swimmer for each S, indicated by black rings in figure 3.2, are displayed in figure 3.4. The flagellum is plotted relative to the motion of the cell head, which is drawn in black and viewed from the xy-plane. Rotating into the body frame, lateral motion is removed from the images so that the head-flagellum join $\boldsymbol{X}_0$ remains pinned at the origin. Cells elongated in the a_1 long-axis optimise for VAL when S is small, with squatter cells where $a_1 \approx a_2$ (yet $a_2 < a_1$) optimal at larger S values. The larger beat envelope in the high-S simulations indicates the transition in beat style exhibited by sperm cells swimming

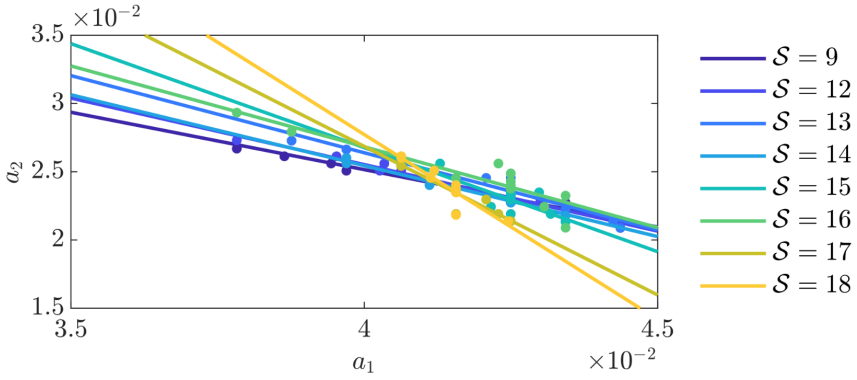

Figure 3.3: Change in 'zeroline' with swimming parameter $\mathcal{S}$. The zeroline is defined as the linear polynomial determined using the MATLAB® `fit` command, through axes values (projected onto the $a_1 a_2$-axis) with percentage VAL difference values less than 0.02. Data points used in each fitting are indicated for each $\mathcal{S}$ case by coloured spherical markers. Cell heads containing values below each line for each $\mathcal{S}$ swim faster than a mean cell, for fixed optimal actuation parameters, corresponding to red-coloured markers in figure 3.2.

in viscous fluids, examined comprehensively in Neal *et al.* (2020).

In figures 3.5 and 3.7, the combined findings displayed in figure 3.2 are separated to examine the relationships between sampled axes values and percentage difference in VAL and Lighthill efficiency, respectively. In both figures, subfigure (a) displays results from experiments where (a_1, a_2) are sampled; similarly subfigures (b) and (c) consider simulations where (a_1, a_3) and (a_2, a_3) are sampled respectively. For each case, slices of head morphologies when moving from the bottom-left (drawn in dark blue) to top-right (drawn in dark red) of each panel are given in figure 3.6. When sampling (a_1, a_2), heads with small values of both a_1 and a_2 yield the greatest uplift of $\approx$ 1.5% over a mean cell (figure 3.5a). Conversely, when sampling (a_2, a_3) (figure 3.5c), the fastest cells comprise large values of both subaxes. In both these cases, larger percentage VAL differences (both uplifts and reductions) are measured in the viscous dominated regimes (large $\mathcal{S}$ values). For the case when (a_1, a_3) is sampled, the VAL values recorded

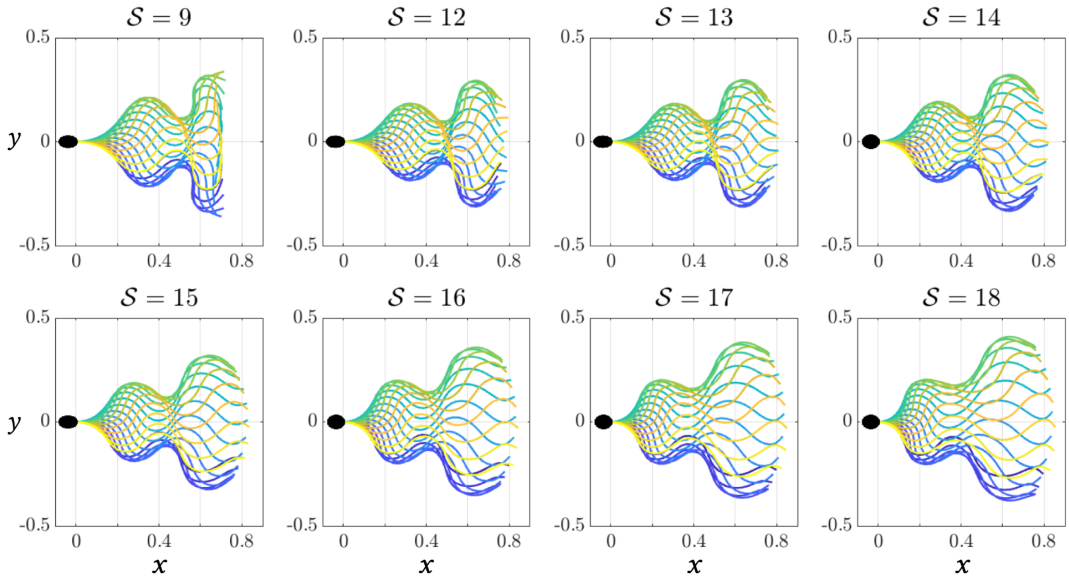

Figure 3.4: Flagellar waveforms (drawn relative to the motion of the cell body) across a single beat of the fastest swimmers for each $\mathcal{S}$ considered, corresponding to those cells marked by a black ring in figure 3.2.

are much smaller, with maximum differences of $\approx 0.5\%$ for most $\mathcal{S}$ values. Since the regularised stokeslet method employed in the fluid dynamic model is itself only order ε accurate, here, with $\varepsilon = 0.01$, these subpercentile differences in swimming dynamics are not large enough to definitively conclude that changes to head morphology arising from sampling (a_1, a_3) significantly affect VAL compared to a mean cell.

Similar trends are observed upon considering the percentage difference in Lighthill efficiency for each case, with results given in figure 3.7. Examining figure 3.7a, heads generated from samples of (a_1, a_2) produce cells with the largest variance in η compared to the mean cell, with differences of $\approx \pm 1.5\%$. These values are additionally reasonably consistent across all $\mathcal{S} \in [9, 18]$ considered, in contrast to the (a_1, a_3) and (a_2, a_3)-sampled results in figures 3.7b and c, where, except in the very-viscous $\mathcal{S} = 18$ case, differences in efficiency are small ($|\%\Delta\eta| \leqslant 0.5\%$ in most cases). These findings

suggest that in all but the most viscous fluid environments, only alterations to the head axes in the plane of beating of the cell have a significant impact on swimming efficiency over a mean cell.

Also of interest is the amount of yawing exhibited by the cell head across the examined beat. In this study, we quantify the body yaw through the range in values assumed by $\phi(t)$, the lab frame angle defining the orientation of the cell body with respect to the positive x-axis. As in previous results, we compare values to those of an identically-actuated mean cell, with results given in figure 3.8. In each (a,b,c) case, percentage differences of up to ±15% are recorded relative to the mean cell. Across all results, increased yawing is observed in the higher-viscosity simulations, reducing to $\approx$ ±6% when $S = 9$. When the long axis a_1 is directly sampled (figures 3.8a and b), percentage range in ϕ decreases inversely proportional to a_1. In the remaining case where (a_2, a_3) are sampled, yaw increases as both minor axes a_2, a_3 increase in tandem, thereby shortening the major a_1 axis (figure 3.8c).

Considering the physics of the swimming cell, it is straightforward to imagine how, given an identically actuated flagellum, differences in head shape affect the drag profile of the body, with differences manifesting most directly as variations in yaw (examined in figure 3.8). An understanding of the drag profile for each cell head can be obtained by examining the entries of the respective grand resistance matrices $\mathcal{R}$ (or GRMs). Resistance problems for each head (of varying dimensions but ideal volume) in a reference configuration aligned with the Cartesian axes are formulated and solved (details in section 1.2.8) to obtain the corresponding GRMs. The grand resistance matrix comprises four 3×3 block matrices

$$\mathcal{R} = \begin{pmatrix} \mathcal{R}^{FU} & \mathcal{R}^{F\Omega} \\ \mathcal{R}^{MU} & \mathcal{R}^{M\Omega} \end{pmatrix}, \tag{3.3}$$

(a) (a_1, a_2) sampled

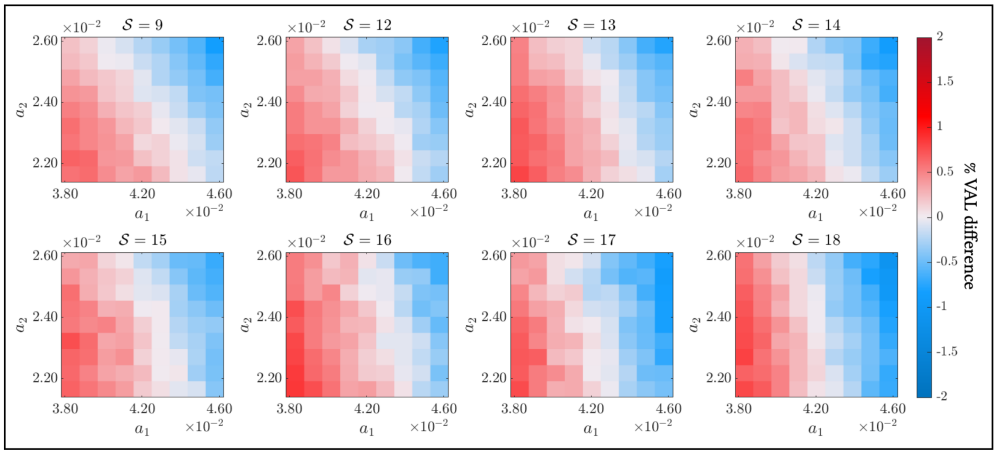

(b) (a_1, a_3) sampled

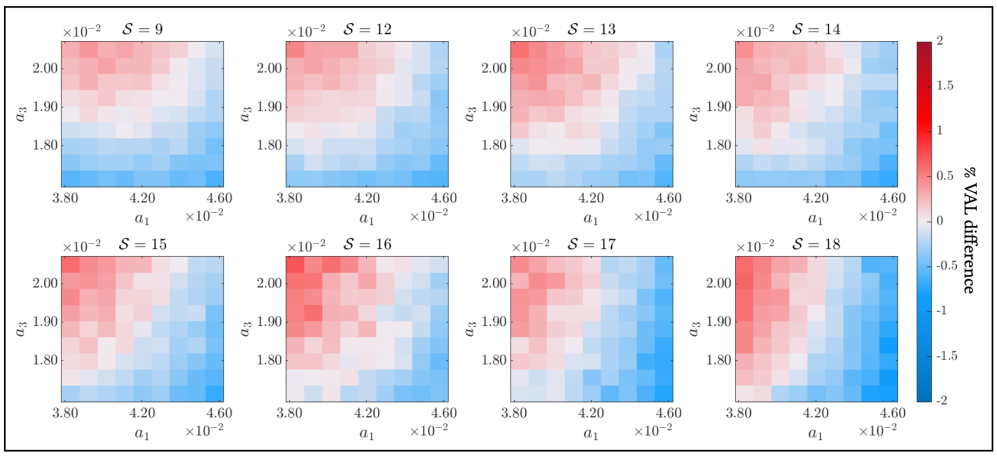

(c) (a_2, a_3) sampled

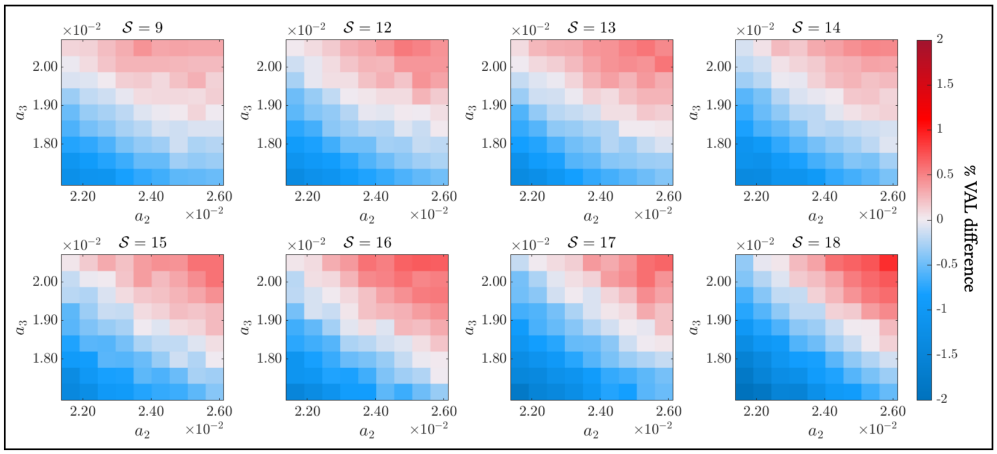

Figure 3.5: Effect of changing head morphology on velocity along a line (VAL) relative to a similarly characterised cell with average head dimensions, when sampling (a) (a_1, a_2), (b) (a_1, a_3), and (c) (a_2, a_3) axis values from fixed intervals. The remaining radius in each case is determined by a fixed ideal volume constraint.

(a) (a_1, a_2) sampled

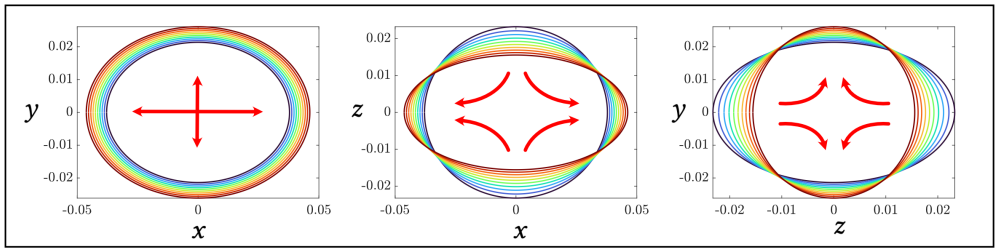

(b) (a_1, a_3) sampled

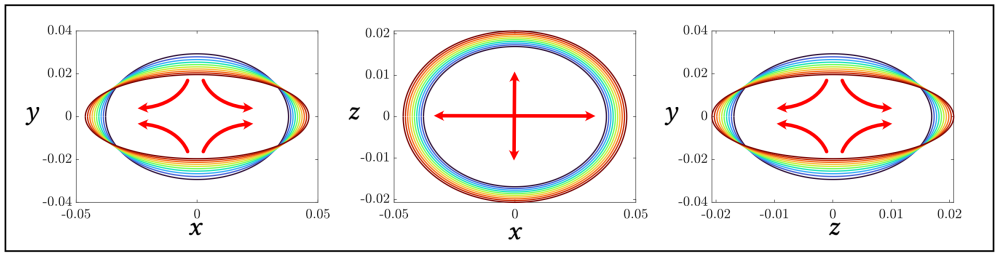

(c) (a_2, a_3) sampled

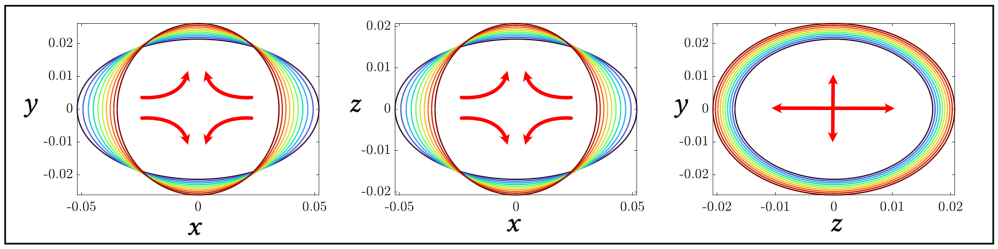

Figure 3.6: Slices through each x, y, z plane of the cell heads used in the simulations generating the results in figures 3.5–3.4. Blue ellipses correspond to heads at the bottom-left, through to red ellipses corresponding to the top-right, of the plots in figures 3.5–3.4.

where $\mathcal{R}^{FU}$ describes the force-translation coupling, $\mathcal{R}^{F\Omega}$ the drag due to rotations, $\mathcal{R}^{MU}$ the rotational moment arising from translations, and $\mathcal{R}^{M\Omega}$ the moment-rotation coupling. For an arbitrarily elliptical body, all of these matrices will contain nonzero entries. In the special case of a perfectly spherical body, $\mathcal{R}^{F\Omega} = \mathcal{R}^{MU} = 0$.

In figure 3.9, we consider two ratios formed between diagonal entries of $\mathcal{R}$, mapping each to percentage VAL difference (on the y-axis) and percentage difference in

(a) (a_1, a_2) sampled

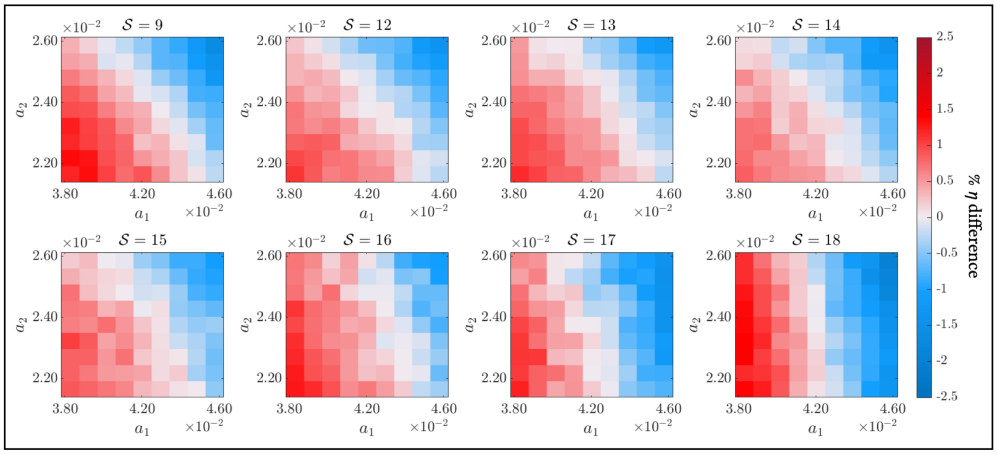

(b) (a_1, a_3) sampled

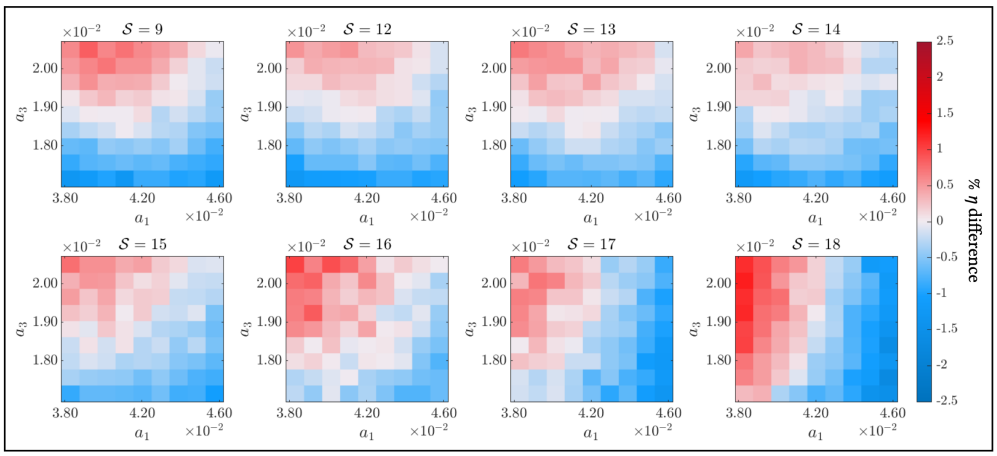

(c) (a_2, a_3) sampled

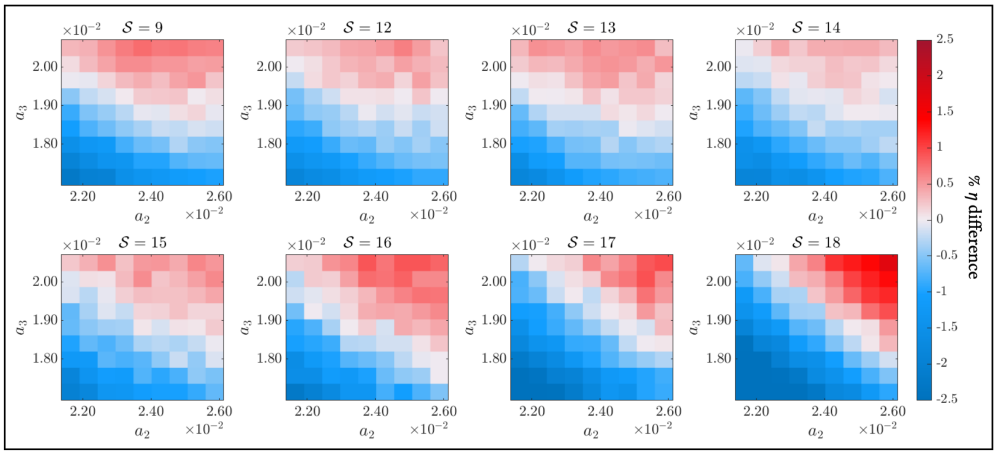

Figure 3.7: Effect of changing head morphology on Lighthill efficiency η relative to a similarly characterised cell with average head dimensions, when sampling (a) (a_1, a_2), (b) (a_1, a_3), and (c) (a_2, a_3) axis values from fixed intervals. The remaining radius in each case is determined by a fixed ideal volume constraint.

(a) (a_1, a_2) sampled

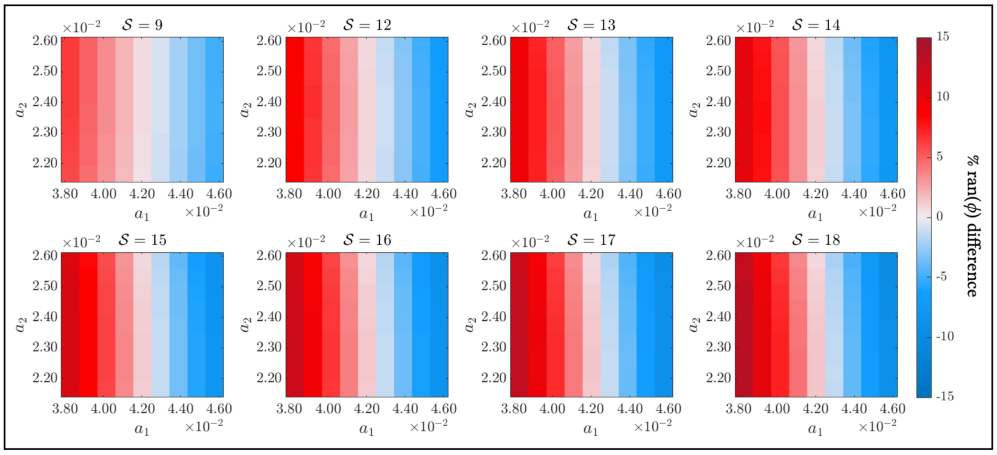

(b) (a_1, a_3) sampled

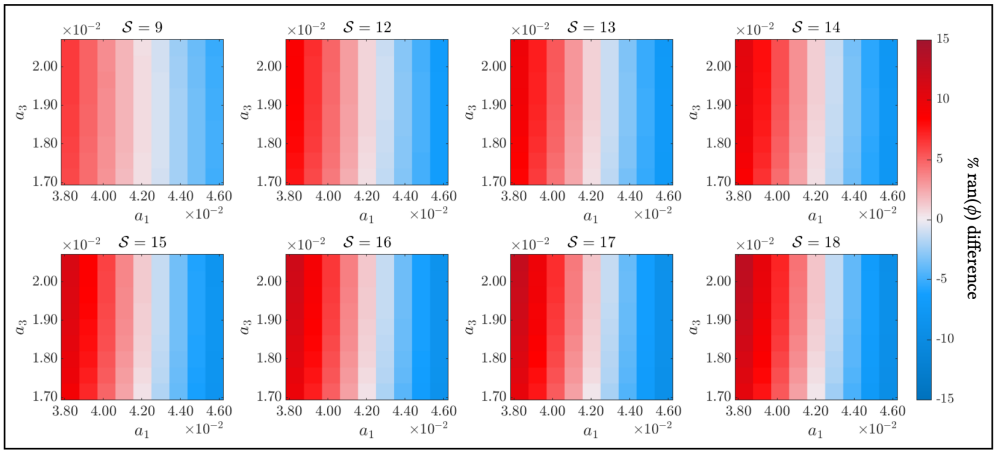

(c) (a_2, a_3) sampled

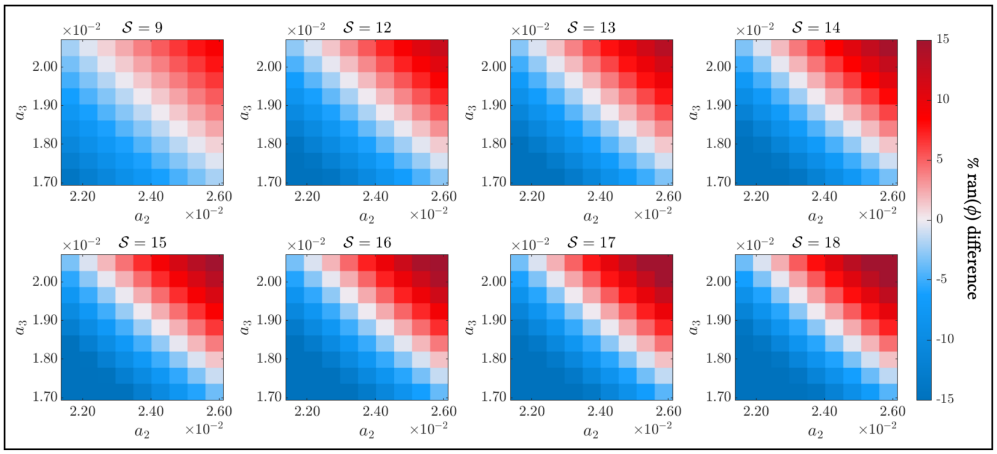

Figure 3.8: Effect of head morphology on head yaw, quantified through the range of head angle ran ϕ across a single beat, relative to a similarly characterised cell with average head dimensions, when sampling (a) (a_1, a_2), (b) (a_1, a_3), and (c) (a_2, a_3) axis values from fixed intervals. The remaining radius in each case is determined by a fixed ideal volume constraint.

Lighthill efficiency, indicated by marker colour. Two ratios are considered; $\mathcal{R}_{11}/\mathcal{R}_{22}$, quantifying the transverse motion in the y-axis (and thus a measure indicating the yawing of the cell), and $\mathcal{R}_{11}/\mathcal{R}_{66}$, describing the resistance to rolling (i.e. rotations about the long-axis of the cell body). Examination of the white markers (representing zero or nearly-zero efficiency improvements over a mean cell) qualitatively illustrates the differences between heads producing average VAL values and those swimming with average efficiency. Both point clouds resemble skewed planar projections of the star arrangements observed in figure 3.2. As $\mathcal{S}$ increases, positive correlations between the ratios $\mathcal{R}_{11}/\mathcal{R}_{22}$, $\mathcal{R}_{11}/\mathcal{R}_{66}$ and percentage VAL difference develop, with the strength of correlation increasing with larger $\mathcal{S}$. In particular, a strong positive correlation between the values $\mathcal{R}_{11}/\mathcal{R}_{66}$ and VAL emerges in the viscous dominated regimes, with data points collapsing onto a thin line of values (see figures 3.9g, h). Whilst the number of data points above and below the zerolines (drawn in black) in the $\mathcal{R}_{11}/\mathcal{R}_{66}$ plots are roughly equal for each $\mathcal{S}$, the increase in strength of correlation upon increasing swimming parameter results in a more even spread of points above and below the zeroline for larger $\mathcal{S}$ values. In the plots in figure 3.9, zerolines are again calculated using the MATLAB® `fit` function to find a linear polynomial through the data points whose absolute percentage efficiency difference value is less than 0.05%. The gradient of these lines is a quantitative measure between the resistance matrix ratios and cell efficiency. For each ratio, swimming parameter $\mathcal{S}$ is plotted against each gradient value, with results in figure 3.10. For both measures, a clear peak in the zeroline gradient is observed for intermediate values of $\mathcal{S} \in [12, 16]$.

Changes in cell body morphology will influence the shape of the elastic flagellum, particularly in the region close the head-flagellum join, due to nonlocal fluid interactions between the head and flagellum. To quantitatively assess changes in flagellar

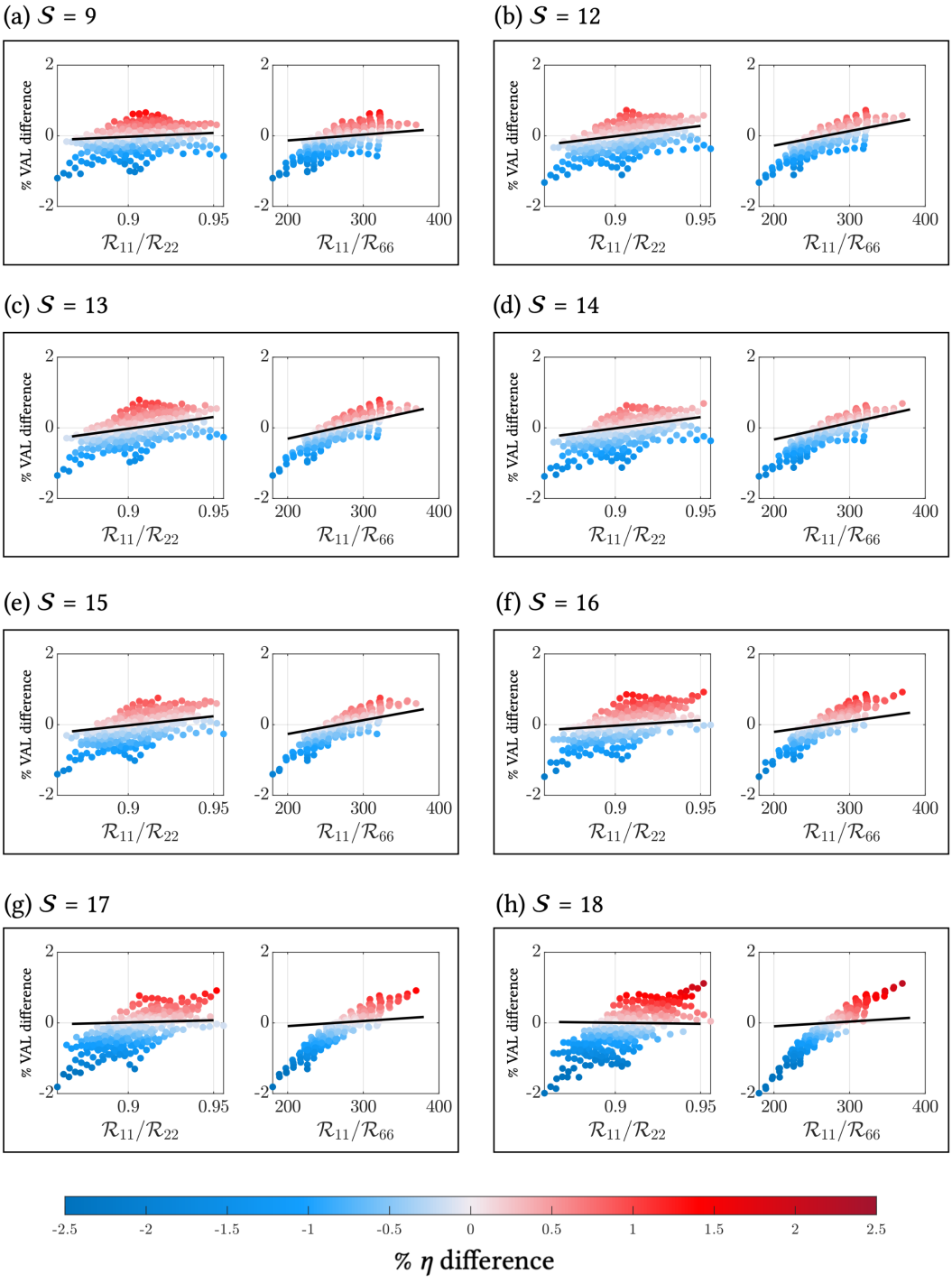

Figure 3.9: For each cell head considered, the ratios $\mathcal{R}_{11}/\mathcal{R}_{22}$ and $\mathcal{R}_{11}/\mathcal{R}_{66}$ are plotted against the percentage VAL difference against a cell with an average-sized body, for a range of swimming parameters $\mathcal{S} \in [9, 18]$. Marker colour indicates the percentage difference in efficiency between each cell and the average cell. The black zeroline in each panel indicates those axes triads corresponding to average efficiency.

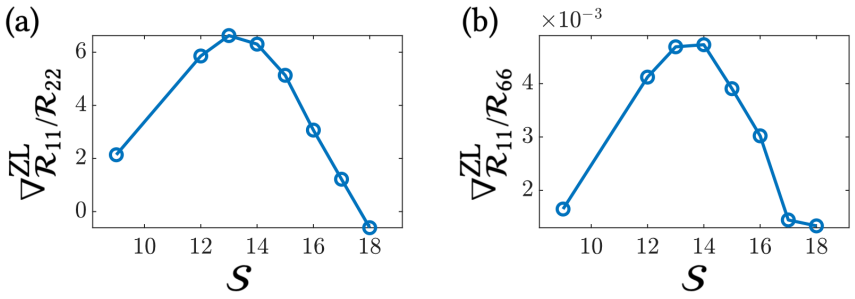

Figure 3.10: Swimming parameter S against gradients of the zerolines for percentage efficiency difference against percentage VAL difference sorted by the ratios (a) $\mathcal{R}_{11}/\mathcal{R}_{22}$ and (b) $\mathcal{R}_{11}/\mathcal{R}_{66}$. Each data point in the above plots corresponds to the gradient of the black line drawn in each panel of figure 3.9.

shape across variations in head axes, we compare time-averaged mean absolute curvature values along the flagellum relative to a mean cell. For each pair of sampled axes, the curves in each panel of figure 3.11 describe the percentage difference (compared to a mean cell) in average curvature at a given material point along the beating flagellum across the course of a single beat. Each coloured line in figures 3.11a,b,c corresponds to a simulation with a cell head of matching colour from the ellipses in figures 3.6a,b,c respectively. Regardless of which axes are sampled to form the body radii triad, variations in head morphology symmetrically about average values produce similarly approximately symmetric deviations in curvature below and above the mean average absolute curvature. Whilst qualitatively similar behaviours are observed across all head choices and all S values, head shapes generated through variations in (a_1, a_2) and (a_2, a_3) pairs yield the largest variations in flagellar shape (figures 3.11a and c respectively). For values of $S < 14$, a single 'envelope' of variation is observed, with direction (i.e. either positive or negative percentage difference) inversely linearly dependent on axis length relative to the mean head dimensions. This variation is largest in the region very close ($s < 0.1$) to $\boldsymbol{X}_0$, the head-flagellum join. As S increases, a

second envelope of opposite polarity forms in the intermediate flagellum, roughly between $0.2 \leqslant s \leqslant 0.6$, which grows in size as swimming parameter increases. In isolated cases ($S = 18$ in figure 3.11a, for example), a third envelope in the distal region is observable; the relatively small variations recorded are deemed not significant compared to the primary and secondary envelopes observed elsewhere. As the hydrodynamic influence of the cell head dissipates with distance from X_0, differences in curvature reduce and all simulations have approximately similar distal curvature profiles.

(a) (a_1, a_2) sampled

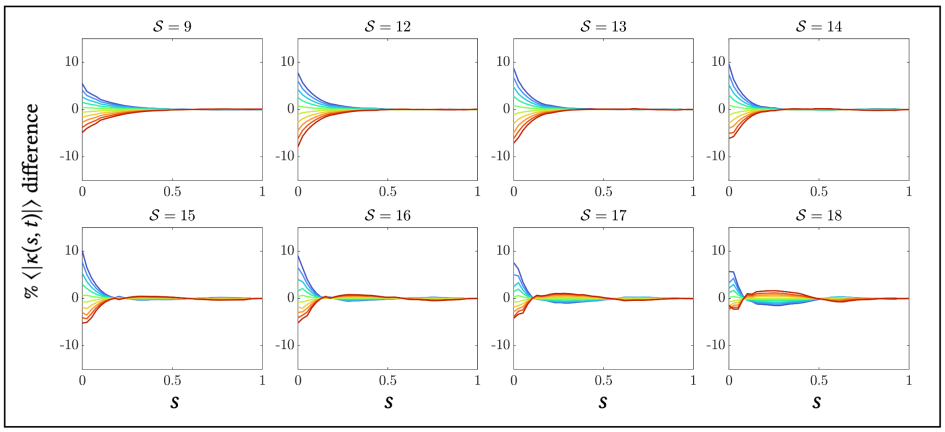

(b) (a_1, a_3) sampled

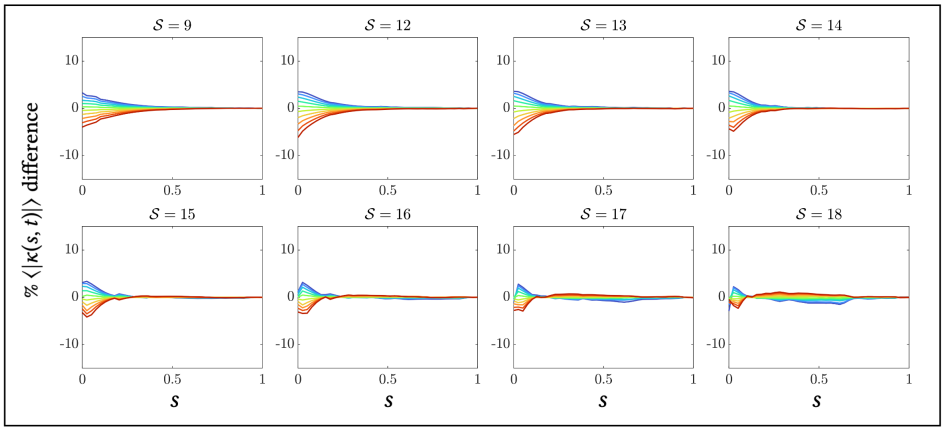

(c) (a_2, a_3) sampled

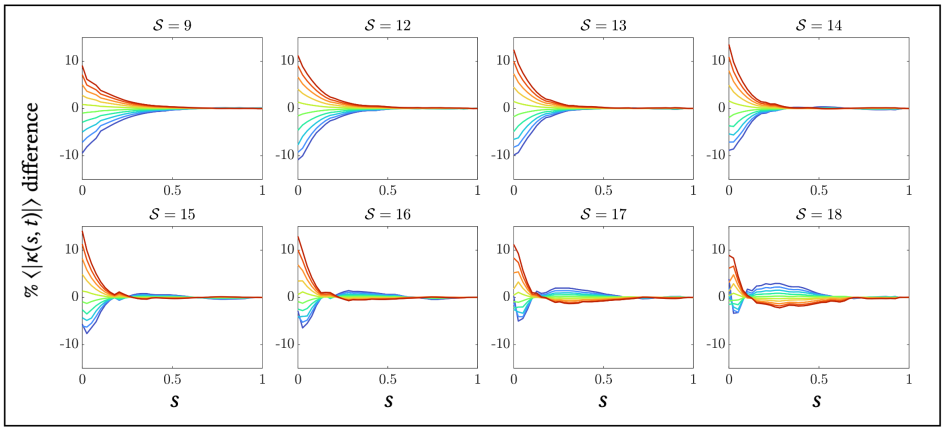

Figure 3.11: Comparisons in the absolute curvature, averaged across a single beat, of simulated cells with head axes linearly varying across (a) the $a_1 a_2$ direction, (b) the $a_1 a_3$ direction, and (c) the $a_2 a_3$ direction. In each case, dark blue lines correspond to combined small value pairs of the sampled axes, through to dark red lines corresponding to conversely large value pairs.

3.3 Effects of head volume on cell swimming

As discussed in section 3.1, changes in volume of the cell body can have a dramatic impact on the viability of the cell, with marked deviations from average head dimensions indicative of a defective cell carrying damaged DNA. Examples of common morphological defects are round cell bodies, with the three axes of the head all being of similar length, and tapering cell bodies, characterised by extreme elongation in the a_1 direction. In section 3.2, we examined the effects that minor variations in each of the axes of the cell head can have on propulsive speed, swimming efficiency, and yaw, whilst ensuring the volume of the body remained fixed at an 'ideal' value determined from average dimensions experimentally observed in healthy cells (Sunanda *et al.*, 2018). In this section, we consider changes in the same metrics upon changes in volume.

Three types of cell body are considered: a normal-type, a round-type, and a tapered-type, each defined in the first instance by the average experimentally observed dimensions given in table 3.1. Identifying the volume of each variant in these cases as the 'mean volume', we consider a range of bodies enclosing between half and double the mean volume for each type. The aspect ratios of each body type are consistent across simulations. We additionally consider a range of swimming parameters $S \in [9, 18]$, with dimensionless wave number $k = 4\pi$ and actuation parameter $\mathcal{M}$ chosen to optimise the cell for swimming speed. As before, the length of the dimensionless end piece is fixed at $\ell = 0.05$. Solution data is then sampled across a single beat, with the VAL and efficiency calculated using equations (2.68) and (3.1) with $j = 4$.

The effects of varying dimensionless volume upon VAL and Lighthill efficiency η for swimming parameters $S \in [9, 18]$ are given in figures 3.12a – 3.12h respectively. The head volume of sperm with tapered-type bodies is typically $\approx 50\%$ larger than those

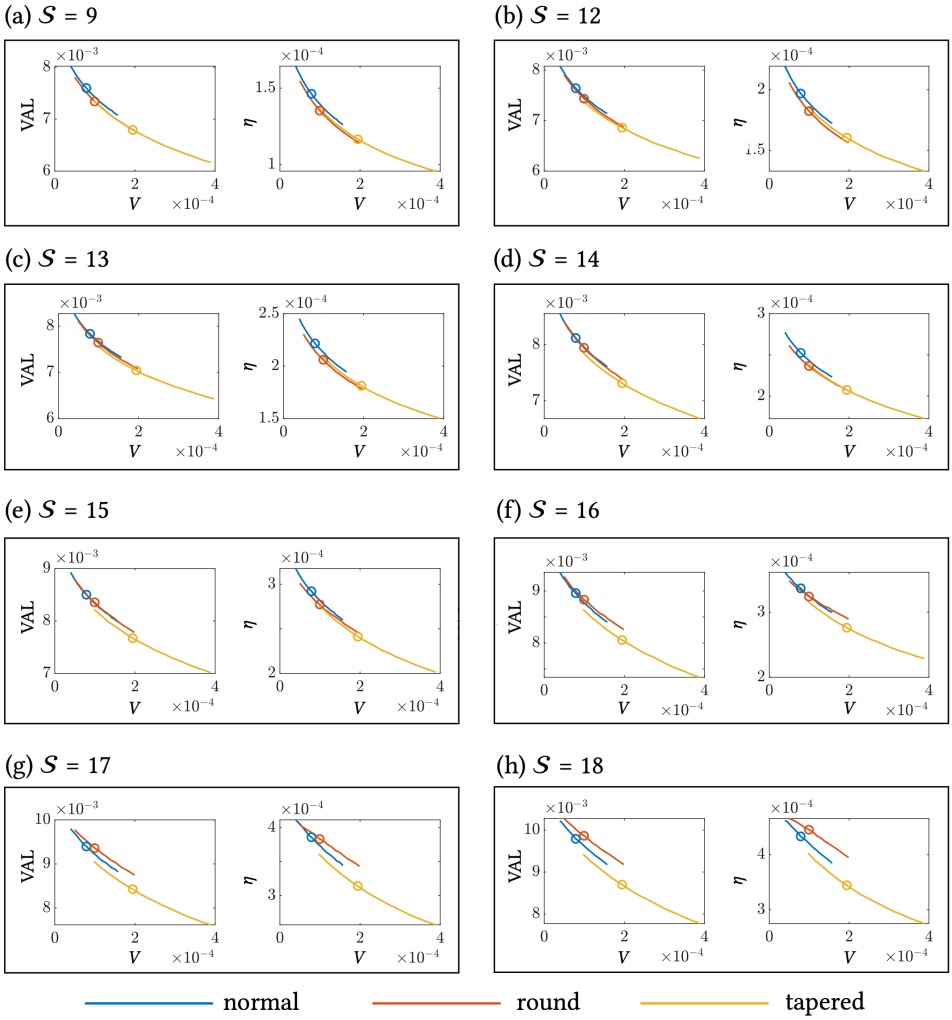

Figure 3.12: Effects of changing cell body volume V on VAL and Lighthill efficiency η, measured across a single beat for a collection of swimming parameter choices $\mathcal{S} \in [9, 18]$. Actuation parameters are $k = 4\pi$ with $\mathcal{M}$ chosen to optimise swimming speed for each $\mathcal{S}$. The dimensionless end piece length is fixed at $\ell = 0.05$. Circled points indicate cell bodies corresponding the mean axes values indicated in table 3.1.

with standard ellipsoidal bodies or round heads. Similarly, in generating bodies from Sunanda *et al.* (2018) measurements, round cell bodies are $\approx$ 20% more voluminous than ellipsoidal types. Relative trends between body volume and each quantity are similar across all choices of $\mathcal{S}$ considered – as cell body volume increases, speed and

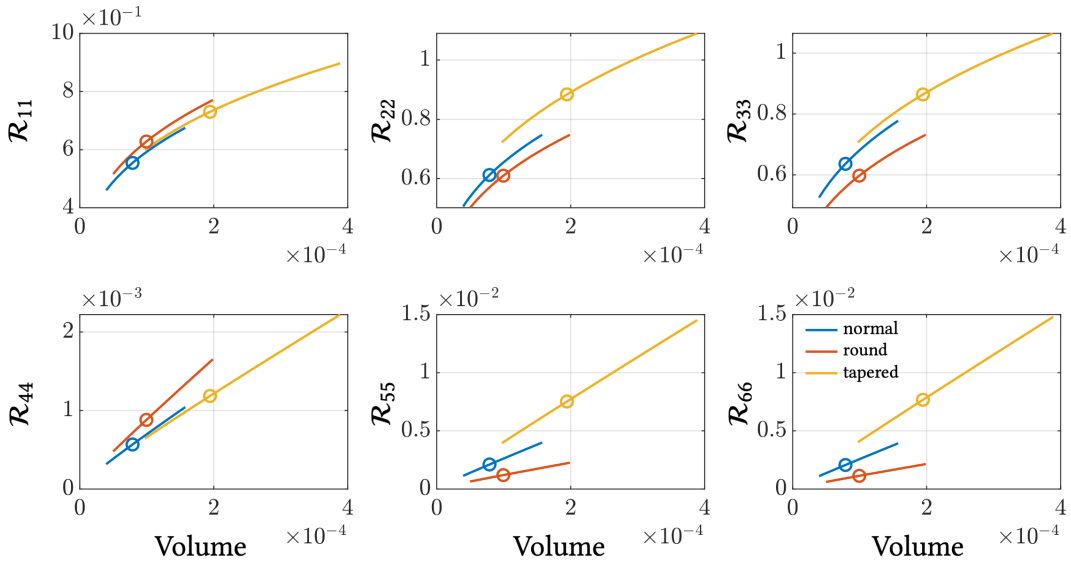

Figure 3.13: As cell body volume increases, the entries of the grand resistance matrix $\mathcal{R}$, measured in a reference configuration, commensurately increase regardless of overall head morphology. Here, blue lines represent normal heads, orange indicates round-type heads, and yellow tapered-type. Circled points indicate bodies corresponding to the mean axes values in table 3.1.

efficiency decrease. For smaller values of $\mathcal{S} \leqslant 15$ (i.e. the relatively more elasticity-dominated regime), all head types closely align along a concave arc. When $\mathcal{S} \leqslant 14$, normal-type heads are marginally more efficient (despite similar VAL measurements) than the two abnormal head types considered. In the more viscous-dominated regimes (i.e. larger values of $\mathcal{S} \geqslant 16$), divergence from this arc develops between head types. In particular, considering cells with approximately equal volume heads, those with round-types heads outperform normal-type cells when $\mathcal{S} \geqslant 17$. Due to their increased volume, tapered type cells consistently perform the worst of all the cell types examined.

In figure 3.13, we examine the values of the diagonal entries of $\mathcal{R}$ for each head type as volume is varied. With the heads oriented pointing in along the x-axis (as indicated in figure 3.1), the values $\mathcal{R}_{11}$, $\mathcal{R}_{22}$ and $\mathcal{R}_{33}$ describe the resistance to translation in

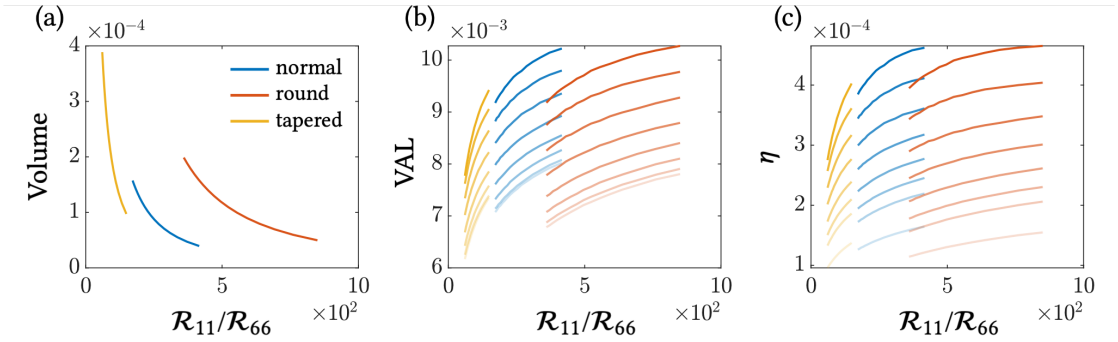

Figure 3.14: Relations between the ratio of grand resistance matrix entries $\mathcal{R}_{11}/\mathcal{R}_{66}$ and (a) body volume (b) VAL and (c) Lighthill efficiency η. In figures (b) and (c), line alpha indicates the value of S, with transparent through to opaque curves corresponding to increasing values from the range $[9, 18]$.

each x, y, z direction respectively. The remaining $\mathcal{R}_{44}$, $\mathcal{R}_{55}$ and $\mathcal{R}_{66}$ values similarly describe the hydrodynamic resistance to rotations about each axis of each body. For all cell head types considered, increases in volume are matched by increases in the values of each diagonal entry of the corresponding grand resistance matrix. All head types have similar drag resistance in the x-direction. Round-type and tapered-typed heads exhibit the smallest and largest drag resistance respectively in the remaining Cartesian directions, with normal-type cells roughly lying between the two curves. Tapered-type cells exhibit markedly larger rotational-moment resistances $\mathcal{R}_{55}$, $\mathcal{R}_{66}$ as a direct consequence of their elongated geometry.

As in section 3.2, describing each considered head through a ratio of grand resistance matrix entries highlights additional distinctions between body shapes. In particular, the ratio $\mathcal{R}_{11}/\mathcal{R}_{66}$ is a convenient metric that cleanly separates values of volume, VAL and efficiency by head type, with only minor overlap in values between normal and round-type cells (see figure 3.14).

3.4 Discussion

In this chapter, we have studied the effects of varying body morphology on overall sperm cell dynamics and performance, with the latter assessed by comparing the velocity along a line (VAL) and Lighthill efficiency for cells with varying-shaped heads. We consider both the effects of varying dimensions whilst conserving a fixed idealised volume, and conserving body proportions whilst linearly scaling the volume enclosed by the cell. Differences in results stem from changes to the drag profile of the head, affecting the amount of yawing exhibited during a beat, as well as from differences in the fluid interactions between head and flagellum upon perturbations in body geometry. We use the previously-discussed EIF model (see chapter 2) augmented by Neal *et al.* (2020) (details in section 2.5) to model the nonlocal elastohydrodynamics of the active planar cell.

In section 3.2, we consider the results of the fixed idealised volume simulations. By defining an 'ideal' cell body volume $\boldsymbol{V}_{\text{ideal}}$, calculated using typical experimentally measured values for each of the cell body radii (Sunanda *et al.*, 2018), a collection of candidate cell heads are generated by selecting two axes, sampling for each from a range ±10% of the mean, and computing the third dimension so as to ensure ideal volume. Each generated cell is repeatedly simulated, varying the characteristic dimensionless swimming parameter $\mathcal{S} \in [9, 18]$, and actuation parameter $\mathcal{M}$ chosen so as to optimise the mean cell for VAL. These optimal $\mathcal{M}_{\text{VAL}}$ parameters are determined algorithmically through a series of separate simulations. In section 3.3, a separate collection of candidate cell heads are generated by scaling the head volume between 50% and 200% of the ideal whilst conserving the average aspect ratio (i.e. the aspect ratio of a head defined by average experimentally observed values). We additionally consider

heads of varying volume with aspect ratios average to round-type and tapered-type cells, two common pathologies.

The star plots presented in figure 3.2 indicate the relative difference in speed and efficiency of each of the candidate cells against one defined with mean head axes. The star-like shape arises from the sampling method chosen for the head morphologies. Increased speed and efficiency are measured for cells with heads which are longer in the a_1 and a_3 axes than a mean cell. However, it should be noted that differences in VAL and efficiency are subpercentile, particularly in the low-viscosity regime for $\mathcal{S} < 14$. This is in part due to characterising the cell actuation by $\mathcal{M}_{\mathrm{VAL}}$ for each $\mathcal{S}$ – choosing nonoptimal $\mathcal{M}$ values results in larger variations in VAL and η. The star plots (figure 3.2) show that many head candidates yield no difference over a mean cell, indicated by the band of near-white points in each panel. As effective viscosity increases (through increasing $\mathcal{S}$), the optimal axes appear to 'rotate' around the star circumference so that cells shorter in the a_1 axis but longer in a_2 yield faster, more efficient cells. This morphological transition can be observed by examining the heads, drawn in a stationary reference frame, in figure 3.4. This transition is accompanied by a rotation of the 'zeroline' (see figure 3.3), a line of best fit in the a_1a_2-plane through those data points in figure 3.2 with approximately zero ($< 0.05\%$) VAL difference to a mean cell. Taken together, figure 3.2 and 3.3 indicate that is variations in the head axes directors coplanar to the plane of swimming that have the largest impact on swimming speed and efficiency.

In examining the relative change in the flagellar mean absolute curvature between each candidate cell and the mean cell, we investigate how changes in head morphology impact waveform, in turn effecting speed and efficiency. The (approximate) horizontal symmetry observed in each panel of figure 3.11 is due to the symmetric sampling

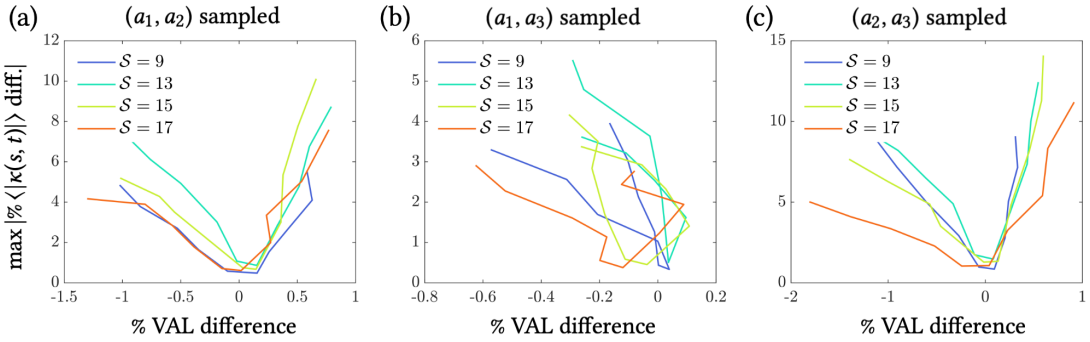

Figure 3.15: For a selection of swimming parameters $\mathcal{S}$ and head axis triads, we plot the % VAL difference against the maximum absolute percentage difference in mean absolute curvature. Differences are between the candidate cell and a mean cell, with the points on each line of each panel corresponding to head axes taken from the diagonal pairings from each figure 3.5a,b,c for the figures a,b,c here respectively.

method by which cell heads were generated. Bringing together panels in figure 3.2 and figure 3.11, in figure 3.15 we plot the percentage difference in VAL against the maximum percentage difference in the mean absolute curvature. In simulations where (a_1, a_2) or (a_2, a_3) are varied, there is an approximately linear relation between the maximum percentage curvature difference and the percentage VAL difference, with the direction of the relation dependant on whether the selected head axes increase or decrease VAL. This trend is much less pronounced when sampling the (a_1, a_3) axis (Fig. 3.15b), which seems to support the hypothesis that changes to head morphology in this plane do not significantly affect cell swimming speed, compared to changes in the two planes perpendicular. In the high-viscosity regimes ($\mathcal{S} \geqslant 15$), changes in proximal curvature are balanced by opposing differences in curvature further down the flagellum, manifesting as a second 'bubble' between $0.2 \leqslant s \leqslant 0.7$. As head geometry changes, the body experiences more or less yaw in the plane of beating according to the size of the long axis a_1 (see figure 3.8). The shorter the a_1 radius, the greater

the yawing of the head. With the elastic flagellum actuated by a constant values of $\mathcal{M}$ for each $\mathcal{S}$, the differences in curvature thus arise from differing drag profiles of each head. The results in figure 3.11 indicate that even minor changes in head morphology have tangible impacts on distal flagellum shape (through fluid interactions), highlighting the importance of nonlocal hydrodynamic effects in elastohydrodynamic modelling.

By solving a resistance problem (discussed in section 1.2.8) for each triad, the candidate heads can be characterised by ratios between entries of their respective grand resistance matrices. In particular, the quantity $\mathcal{R}_{11}/\mathcal{R}_{66}$, the ratio of translational resistance and axial rotational resistance, follows a positive correlation with percentage VAL difference, increasing in strength as swimming parameter $\mathcal{S}$ increases. In the experiments considered heads of scaled volume, the ratio $\mathcal{R}_{11}/\mathcal{R}_{66}$ is an effective measure for head classification, with corresponding volume, VAL and efficiency cleanly separated when plotted against $\mathcal{R}_{11}/\mathcal{R}_{66}$ (see figure 3.14). With significant overlap in recorded values for volume, VAL, and η, the ability of this ratio measure to distinguish between head type suggests its potential use as a new diagnostic measure for experimentalists and clinicians. Outside of use by researchers, clinical adoption of new diagnostic tools is typically a slow process, often taking many years of rigorous testing before full implementation. Nonetheless, used in conjunction with established CASA techniques and sperm tracking software such as FAST (Gallagher *et al.*, 2019), this ratio could be used to effectively select normal-type cells from patient ejaculate samples in IVF or ICSI assistive reproductive techniques.

In summary, the key findings of the presented study are as follows:

- In a relatively more elasticity-dominated regime, cells with heads that are elon-

gated in the $a_1 a_3$-plane exhibit subpercentile increases speed and efficiency over a cell with head of average experimentally-observed dimensions.

- Increasing the effects of viscosity over elasticity changes the optimal head dimensions so that heads short in the a_1 axis and long in the a_2 axis yield cells that swim faster and more efficiently.

- Differences in VAL likely stem from differences in flagellum shape arising from the interactions through the fluid between the altered geometry of the head and the proximal flagellum.

- The ratio $\mathcal{R}_{11}/\mathcal{R}_{66}$ of grand resistance matrix diagonal entries is an effective metric in classifying cell head phenotype, distinguishing normal, round/pin, and tapered-type cells from measurements of volume, VAL, and efficiency.

Beyond expanding the dataset by simulating for a larger range of swimming parameters $\mathcal{S}$, future studies may wish to investigate the effects of head morphology upon swimming when actuated by a nonplanar beat, a scenario not able to be modelled by the EIF. To this end, we will next develop and present in chapter 4 a fully three-dimensional framework for simulating elastohydrodynamic slender bodies and thus nonplanarly swimming human spermatozoa.

Chapter 4

A three-dimensional elastohydrodynamic model for Stokesian monoflagellate swimmers via centreline position

4.1 Motivation

In the proceeding work of this thesis, we have only considered models for planar dynamics of elastohydrodynamic filaments and sperm cells. For these cases, we have shown that the nonlocal integral equation formulation introduced in chapter 2 (referred to as the EIF method) can provide accurate solutions quickly and efficiently. The tangent angle formulation allows a reduction in the degrees of freedom of the problem, whilst simultaneously guaranteeing that the filaments being modelled are inextensible. Use of efficient numerical algorithms such as the built-in black box ODE solver suite within MATLAB® enables rapid solutions to be obtained, at the cost of methodological transparency and flexibility.

The requirement for planarity in scenarios describable by the EIF method greatly

reduces its applicability to general slender body Stokes flow problems. Human sperm, and many other microbiological swimmers, exhibit nonplanar beat patterns such as helical or quasi-helical beats (Woolley, 2003; Simons *et al.*, 2015). More broadly, planar models are incapable of modelling the mechanical twisting of filaments, crucial to the dynamics of microfibres and polymers, and which could play a large role in beat modulation for spermatozoa. Indeed, axonemal twist has been shown to be essential in beat regulation in cilia (Sartori *et al.*, 2016a). Recent approaches to extend angle formulation descriptions of flagellum geometry have employed novel mapping techniques (Walker *et al.*, 2020) or quaternions (Schoeller *et al.*, 2021) to track rotations in three dimensions. Simpler approaches, such as Euler angle representations, are prone to gimbal lock issues hampering the generality of the resulting frameworks. Methods to avoid these problems can significantly increase the complexity of the geometric model, negating much of the simplicity and ease of applicability enjoyed in planar angle formulation models.

In this chapter, we present a framework for elastohydrodynamic modelling of filaments and monoflagellate cells in three dimensions, herein referred to as the *SPX method* ("SP" indicating sperm, the central focus of the model, and "X" representing the position formulation for geometry). The proposed model is able to simulate slender bodies and swimming cells bending and twisting in three dimensions, accounting for nonlocal hydrodynamic interactions through the fluid between the cell and itself, the fluid, and with surrounding structures. Nonlinear geometry is described in terms of the flagellum centreline $\boldsymbol{X}(s)$, avoiding the need for complex rotational bases to avoid gimbal lock, but requiring additional constraints to enforce inextensibility. The SPX method improves upon previous work by Gadêlha *et al.* (2010), which accounts for only local hydrodynamic interactions, and by Montenegro-Johnson *et al.* (2015), by improv-

ing the hydrodynamic model and fully generalising to allowing bending, twisting, and actuation in any direction.

The remainder of this chapter is structured as follows: in section 4.2, the steps in the derivation of the SPX model are described, with additional working presented in appendices A, C and E. Accuracy is assessed in section 4.3 through comparisons to the aforementioned EIF (chapter 2) and a bead and spring model (see appendix B). In sections 4.4.1, we demonstrate the SPX model by investigating the nonplanar beating of a human sperm cell actuated through a 'twist and bend' style beat pattern, both in an infinite fluid and in proximity of an infinite plane wall (section 4.4.2). This chapter concludes with a discussion and summary of the method in section 4.5.

4.2 Derivation of the elastohydrodynamic model

In the following section we derive the proposed three-dimensional nonlocal elastohydrodynamic model. In section 4.2.1, the hydrodynamic model is formulated, using a nonlocal approximation inspired by resistive force theory combined with the method of regularised stokeslets to model nonlocal fluid interactions. Section 4.2.2 derives expressions for the internal elastic force and moment, which are subsequently combined with the hydrodynamic model to arrive at the desired elastohydrodynamic model. Extensions to the model equations to account for nonconstant bending stiffness along the flagellum arclength (a feature common to many flagellated swimmers) are discussed in section 4.2.3. Boundary conditions closing the problem are derived in section 4.2.4. Complete summaries of the final dimensional and dimensionless coupled systems of partial differential equations are given in sections 4.2.5 and 4.2.6 respectively. Finally, steps in the numerical discretisation and code implementation are detailed and discussed in section 4.2.7.

4.2.1 Nonlocal hydrodynamic model

We again consider a slender body comprised of a rigid cell body connected to an elastic flagellum swimming in Stokes flow, with the aim to model human spermatozoa or other monoflagellate swimmers. As discussed in section 1.2.2, the fluid velocity anywhere in the fluid can be described by combining fundamental stokeslet solutions. In section 1.2.6, the method of regularised stokeslets (Cortez, 2001; Cortez *et al.*, 2005) was introduced as a way to conveniently avoid singularities common in problems involving slender bodies. In this manner, the fluid velocity at a material point $\mathbf{x}$ anywhere in

the fluid domain is

$$\boldsymbol{u}(\mathbf{x}) = \int_0^L \boldsymbol{S}^\varepsilon\big(\mathbf{x}, \boldsymbol{X}(s)\big) \cdot \boldsymbol{f}(s)\, ds + \iint_{\partial B} \boldsymbol{S}^\varepsilon\big(\mathbf{x}, Y\big) \cdot \boldsymbol{\varphi}(Y)\, dS_Y, \tag{4.1}$$

where $\boldsymbol{X}(s)$ are flagellum centreline positions, parametrised by arclength $s \in [0, L]$ and ∂B is the surface of the cell body (or cell head; these terms are used here interchangeably), described by material points Y placed across its surface. The filament and body exert a viscous force per unit length $\boldsymbol{f}(s)$ and force per unit area $\boldsymbol{\varphi}(Y)$ onto the fluid, respectively. The kernels of the integrals are regularised stokeslets, as defined in equation (1.40). Time dependence, common to all variables, is suppressed for conciseness. Assuming no slip conditions of the surface of the flagellum and body so that $\boldsymbol{u}(\boldsymbol{X}(s)) = \boldsymbol{X}_t$ and $\boldsymbol{u}(Y) = Y_t$, the velocity of the cell is described by the equations

$$\boldsymbol{X}_t(s) = \int_0^L \boldsymbol{S}^\varepsilon\big(\boldsymbol{X}(s), \boldsymbol{X}(s')\big) \cdot \boldsymbol{f}(s')\, ds', + \iint_{\partial B} \boldsymbol{S}^\varepsilon\big(\boldsymbol{X}(s), \mathrm{y}\big) \cdot \boldsymbol{\varphi}(\mathrm{y})\, dS_\mathrm{y}, \tag{4.2a}$$

$$Y_t = \int_0^L \boldsymbol{S}^\varepsilon\big(Y, \boldsymbol{X}(s)\big) \cdot \boldsymbol{f}(s)\, ds + \iint_{\partial B} \boldsymbol{S}^\varepsilon\big(Y, \mathrm{y}\big) \cdot \boldsymbol{\varphi}(\mathrm{y})\, dS_\mathrm{y}. \tag{4.2b}$$

The cell head moves as a rigid body, allowing its velocity to be expressed as a combination of translational and rotational motion through

$$Y_t = \boldsymbol{X}_{0,t} + \Omega_0 \wedge (Y - \boldsymbol{X}_0), \tag{4.3}$$

where $\boldsymbol{X}_{0,t}$ is the translational velocity of the body, equal to the flagellar velocity at $\boldsymbol{X}_0 := \boldsymbol{X}(0)$, and $\Omega_0 := \Omega(0)$ is the angular velocity about the head-flagellum. The cell body is attached to the flagellum so that the tangent plane to the cell surface at $\boldsymbol{X}_0$ and the tangent to the curve at $s = 0$ are perpendicular. Additional equations ensuring

compatibility between the motion of the head and the proximal flagellum at the head-flagellum join are considered later in section 4.2.4.

The hydrodynamic velocity at a point along the flagellum centreline is decomposed into a contribution from a local neighbourhood of curve, and from the distal curve outside this region, and given as

$$\boldsymbol{X}_t = \int_{|s-s'|\leqslant q} \boldsymbol{S}^{\varepsilon}\big(\boldsymbol{X}(s), \boldsymbol{X}(s')\big) \cdot \boldsymbol{f}(s')\, ds' + \int_{|s-s'|>q} \boldsymbol{S}^{\varepsilon}\big(\boldsymbol{X}(s), \boldsymbol{X}(s')\big) \cdot \boldsymbol{f}(s')\, ds' + \cdots \tag{4.4}$$

where ellipses denote additional integral terms describing the interaction of the flagellum with the cell body and/or other cells and structures. The parameter $0 \leqslant q \leqslant L$ governs the size of the locally-treated region of curve. In previous works by Gadêlha *et al.* (2010) and Montenegro-Johnson *et al.* (2015), the integral across the local neighbourhood of curve (or *inner region*) i.e. across $|s - s'| \leqslant q$, $s' \in [0, L]$ for some $s \in [0, L]$, is approximated using a resistive drag law. In particular, Gadêlha *et al.* (2010) used resistive force theory and neglected all other contributions; Montenegro-Johnson *et al.* (2015) used a modified theory via Gueron & Liron (1992) to account for nonlocal interactions. Assuming that the force per unit length is constant across the inner region, and denoting $\mathbf{d}_3 := \boldsymbol{X}_s$, one can write

$$\int_{|s-s'|\leqslant q} \boldsymbol{S}^{\varepsilon}\big(\boldsymbol{X}(s), \boldsymbol{X}(s')\big) \cdot \boldsymbol{f}(s')\, ds' \approx \int_{|s-s'|\leqslant q} \boldsymbol{S}^{\varepsilon}\big(\boldsymbol{X}(s), \boldsymbol{X}(s')\big) ds' \cdot \boldsymbol{f}(s), \tag{4.5a}$$

$$\approx \frac{1}{c_{\perp}}\big(I + (\gamma - 1)\boldsymbol{X}_s\boldsymbol{X}_s\big) \cdot \boldsymbol{f}, \tag{4.5b}$$

where $\gamma = c_{\perp}/c_{\parallel}$ and $\boldsymbol{X}_s\boldsymbol{X}_s := \boldsymbol{X}_s \otimes \boldsymbol{X}_s$. The steps taken to obtain the final expression are described in appendix C. The parameters $c_{\perp}$ and $c_{\parallel}$ are referred to here as *resistance coefficients* of the hydrodynamic approximation.

In this work, rather than using resistance parameter values from Gray & Hancock (1955) or Gueron & Liron (1992), we derive new expressions stemming directly from the regularised stokeslet integral equation, thereby keeping the hydrodynamic model within the family of the regularised stokeslet methods. This contrasts with the previous approach of Montenegro-Johnson *et al.* (2015), which features a mixed hydrodynamic description. Consider the inner q–region of the regularised stokeslet integral, expanded into cases,

$$\int_{|s-s'|\leqslant q} \boldsymbol{S}^{\varepsilon}\big(\boldsymbol{X}(s),\boldsymbol{X}(s')\big)\,ds' = \begin{cases} \displaystyle\int_{0}^{s+q} \boldsymbol{S}^{\varepsilon}\big(\boldsymbol{X}(s),\boldsymbol{X}(s')\big)\,ds' & s < q, \\ \displaystyle\int_{s-q/2}^{s+q/2} \boldsymbol{S}^{\varepsilon}\big(\boldsymbol{X}(s),\boldsymbol{X}(s')\big)\,ds' & q \leqslant s \leqslant L-q, \\ \displaystyle\int_{s-q}^{L} \boldsymbol{S}^{\varepsilon}\big(\boldsymbol{X}(s),\boldsymbol{X}(s')\big)\,ds' & s > L-q. \end{cases} \tag{4.6}$$

We approximate the region of curve in each integral as a linear rod and, through the regularised stokeslet segments method (Smith, 2009; Cortez, 2018) described in section 1.2.9, obtain coefficients analogous to those of Gray & Hancock resistive force theory (Gray & Hancock, 1955). The regularised stokeslet integral across the q-inner region of flagellum can be then be approximated

$$\int_{|s-s'|\leqslant q} \boldsymbol{S}^{\varepsilon}\big(\boldsymbol{X}(s),\boldsymbol{X}(s')\big)\cdot\boldsymbol{f}(s')\,ds' \approx \frac{1}{\xi_{\perp}}\big(\boldsymbol{I}+(\gamma-1)\boldsymbol{X}_s(s)\boldsymbol{X}_s(s)\big)\cdot\boldsymbol{f}(s), \tag{4.7}$$

where $\xi_{\perp} = 8\pi\mu/D_{22}^{L}$, $\xi_{\parallel} = 8\pi\mu/D_{11}^{L}$ and $\gamma = \xi_{\perp}/\xi_{\parallel}$, with analytic expressions for D_{11}^{L} and D_{22}^{L} given in equations (1.65g) and (1.66) respectively. Suppressing arclength dependence, the final equation for the hydrodynamic velocity is

$$\boldsymbol{X}_t - \boldsymbol{V} = \frac{1}{\xi_{\perp}}\big(\boldsymbol{I}+(\gamma-1)\boldsymbol{X}_s\boldsymbol{X}_s\big)\cdot\boldsymbol{f}, \tag{4.8}$$

where the nonlocal contribution to the flagellar velocity is given by

$$\boldsymbol{V}(s) = \int_{|s-s'|>q} \boldsymbol{S}^{\varepsilon}\big(\boldsymbol{X}(s), \boldsymbol{X}(s')\big) \cdot \boldsymbol{f}(s')\, ds' + \iint_{\partial B} \boldsymbol{S}^{\varepsilon}\big(\boldsymbol{X}(s), \boldsymbol{Y}\big) \cdot \boldsymbol{\varphi}(\boldsymbol{Y})\, dS_{\boldsymbol{Y}}. \tag{4.9}$$

Equation 4.7 provides an approximation for the integrated inner region stokeslet through analytical integration of a hydrodynamically exact but geometrically approximate regularised stokeslet integral. In this manner, the error arising from the inner approximation stems only from the straight line approximation and not as a result of using resistance coefficients derived from a less accurate hydrodynamic model. Through nonlocal contributions encompassed by $\boldsymbol{V}$, equation (4.8) describes the nonlocal hydrodynamic velocity of the flagellum centreline.

4.2.2 Elasticity model with bend and twist

The hydrodynamic model derived in section 4.2.1, and the equation for the filament velocity, given in equation (4.8), are coupled to the elasticity model by finding an expression for the hydrodynamic force per unit length $\boldsymbol{f}$ in terms of the internal filament elasticity. In the following section, we derive an expression for $\boldsymbol{f}$, building upon the equations presented in section 1.3.1 for a general filament.

The three dimensional nonlinear flagellum geometry is described using a Kirchhoff rod model, as given in section (1.3.1). The orientation of the flagellum is defined by a director basis $\{\mathbf{d}_1, \mathbf{d}_2, \mathbf{d}_3\}$ with $\mathbf{d}_3 = \boldsymbol{X}_s$ and $\mathbf{d}_2 = \mathbf{d}_3 \wedge \mathbf{d}_1$. Additionally, the $\mathbf{d}_1\mathbf{d}_3$-plane at $s = 0$ corresponds to the plane of flattening of the cell head. The internal elastic force $\boldsymbol{F}_{\text{int}}$ and moment $\boldsymbol{M}_{\text{int}}$ transmitted by the downstream ($s_0 \in [s, L]$) flagellum on

the upstream section ($s_0 \in [0, s)$) are given by the equilibrium equations

$$\boldsymbol{F}_{\text{int},s} - \boldsymbol{f} = \mathbf{0}, \tag{4.10a}$$

$$\boldsymbol{M}_{\text{int},s} + \mathbf{d}_3 \wedge \boldsymbol{F}_{\text{int}} + \boldsymbol{m} = \mathbf{0}, \tag{4.10b}$$

where $\boldsymbol{f}$ is the viscous force per unit length the flagellum exerts onto the fluid, and $\boldsymbol{m}$ is an internal actuating moment per unit length. Constitutively linear elasticity relates the internal contact moment $\boldsymbol{M}_{\text{int}}$ to the curvatures of the rod through (Landau & Lifshitz, 1965)

$$\boldsymbol{M}_{\text{int}} = E(\kappa_1 \mathbf{d}_1 + \kappa_2 \mathbf{d}_2) + C\kappa_3 \mathbf{d}_3, \tag{4.11a}$$

$$= E\boldsymbol{X}_s \wedge \boldsymbol{X}_{ss} + C\kappa_3 \boldsymbol{X}_s, \tag{4.11b}$$

where E is the bending rigidity of the flagellum and C is the twist rigidity. The twist curvature κ_3 describes the rate of rotation of the frame with respect to arclength and hence the amount of twist the filament experiences along its length. Substituting (4.11b) into the moment equilibrium equation (4.10b), assuming for now that both E and C are constant, we obtain

$$E\boldsymbol{X}_s \wedge \boldsymbol{X}_{sss} + C\kappa_{3,s}\boldsymbol{X}_s + C\kappa_3 \boldsymbol{X}_{ss} + \boldsymbol{X}_s \wedge \boldsymbol{F}_{\text{int}} + \boldsymbol{m} = \mathbf{0}. \tag{4.12}$$

Multiplying vectorially from the left by $\boldsymbol{X}_s$ yields

$$E\boldsymbol{X}_s \wedge (\boldsymbol{X}_s \wedge \boldsymbol{X}_{sss}) + C\kappa_3 \boldsymbol{X}_s \wedge \boldsymbol{X}_{ss} + \boldsymbol{X}_s \wedge (\boldsymbol{X}_s \wedge \boldsymbol{F}_{\text{int}}) + \boldsymbol{X}_s \wedge \boldsymbol{m} = \mathbf{0}, \tag{4.13}$$

which, simplified using the triple vector product identity, yields an expression for the

internal contact force as

$$\boldsymbol{F}_{\text{int}} = -E\boldsymbol{X}_{sss} + C\kappa_3\boldsymbol{X}_s \wedge \boldsymbol{X}_{ss} + T\boldsymbol{X}_s + \boldsymbol{X}_s \wedge \boldsymbol{m}, \tag{4.14}$$

where T is the internal tension, introduced as a new unknown since (4.14) contains no information on the tangential force components. Substituting equation (4.14) into the force equilibrium equation (4.10a), provides an expression for the hydrodynamic force per unit $\boldsymbol{f}$ length in terms of centreline elastics as

$$\boldsymbol{f} = -E\boldsymbol{X}_{ssss} + C[\kappa_3(\boldsymbol{X}_s \wedge \boldsymbol{X}_{ss})]_s + [T\boldsymbol{X}_s]_s + [\boldsymbol{X}_s \wedge \boldsymbol{m}]_s \tag{4.15}$$

The active torque term in equation (4.15) contains only terms arising from rotations about $\mathbf{d}_1$ and $\mathbf{d}_2$. We refer to these components as the *active bending* components of the actuating torque. For the general form $\boldsymbol{m} = m_i\mathbf{d}_i$, the scalar functions of arclength m_1, m_2 and m_3 describe the active rotation of the frame about the $\mathbf{d}_1$, $\mathbf{d}_2$ and $\mathbf{d}_3$ axes respectively. Expressions for these functions, specific to a human spermatozoa, will be given later in section 4.3.3. The elastohydrodynamic equation is thus obtained by substituting equation (4.15) into equation (4.8), yielding

$$\boldsymbol{X}_t - \boldsymbol{V} = \frac{1}{\xi_\perp}\big(\boldsymbol{I} + (\gamma - 1)\boldsymbol{X}_s\boldsymbol{X}_s\big) \cdot \big(- E\boldsymbol{X}_{ssss} + C[\kappa_3\boldsymbol{X}_s \wedge \boldsymbol{X}_{ss}]_s + [T\boldsymbol{X}_s]_s + [\boldsymbol{X}_s \wedge \boldsymbol{m}]_s\big), \tag{4.16}$$

Following Gadêlha *et al.* (2010) and Montenegro-Johnson *et al.* (2015), we expand (4.16)

(details in appendix E) to obtain the *nonlocal and nonplanar sperm equation* as

$$\begin{aligned}\xi_\perp(\boldsymbol{X}_t - \boldsymbol{V}) = -E\boldsymbol{X}_{ssss} - E(\gamma - 1)(\boldsymbol{X}_s \cdot \boldsymbol{X}_{ssss})\boldsymbol{X}_s + C\kappa_{3,s}(\boldsymbol{X}_s \wedge \boldsymbol{X}_{ss}) \\ + C\kappa_3(\boldsymbol{X}_s \wedge \boldsymbol{X}_{sss}) + T\boldsymbol{X}_{ss} + \gamma T_s \boldsymbol{X}_s + \boldsymbol{X}_{ss} \wedge \boldsymbol{m} \\ + \boldsymbol{X}_s \wedge \boldsymbol{m}_s + (\gamma - 1)\boldsymbol{X}_s \boldsymbol{X}_s \cdot (\boldsymbol{X}_{ss} \wedge \boldsymbol{m}). \quad (4.17)\end{aligned}$$

Since we aim to model cells actuated by nonplanar internal moments per unit length, we retain the vector form for $\boldsymbol{m}$ and terms arising from it, rather than expand into components as in other centreline models (Gadêlha *et al.*, 2010; Montenegro-Johnson *et al.*, 2015).

An auxiliary equation for the tension T is obtained through manipulation of the inextensibility constraint $\boldsymbol{X}_s \cdot \boldsymbol{X}_s = 1$. Following Tornberg & Shelley (2004) and Montenegro-Johnson *et al.* (2015), the constraint is included in the model through the approximately equivalent but numerically tractable condition

$$\frac{1}{2}(\boldsymbol{X}_s \cdot \boldsymbol{X}_s)_t = (\boldsymbol{X}_t)_s \cdot \boldsymbol{X}_s = \lambda(1 - \boldsymbol{X}_s \cdot \boldsymbol{X}_s), \quad (4.18)$$

which works to remove numerical length errors at the expense of including a numerical damping parameter λ, which governs the strength of the conservative restorative action. The expression on the right hand side of (4.18) can be thought of as spring with spring constant proportional to λ remove any axial growth. Results are generally insensitive to a broad range of λ values (to be discussed in section 4.3). Rearranging

equation (4.17) for $\boldsymbol{X}_t$ and substituting into equation (4.18) yields the *tension equation*

$$\begin{aligned}\lambda(1 - \boldsymbol{X}_s \cdot \boldsymbol{X}_s) - \boldsymbol{V}_s \cdot \boldsymbol{X}_s \\ = \frac{1}{\xi_\perp}\big[\gamma T_{ss} - (\boldsymbol{X}_{ss} \cdot \boldsymbol{X}_{ss})T + E(1 + 3\gamma)\boldsymbol{X}_{ss} \cdot \boldsymbol{X}_{ssss} \\ + 3E\gamma \boldsymbol{X}_{sss} \cdot \boldsymbol{X}_{sss} + C\kappa_{3,s}(\boldsymbol{X}_s \wedge \boldsymbol{X}_{ss}) \cdot \boldsymbol{X}_{sss} \\ + \gamma(\boldsymbol{X}_{sss} \wedge \boldsymbol{m}) \cdot \boldsymbol{X}_s + (\gamma + 1)(\boldsymbol{X}_{ss} \wedge \boldsymbol{m}_s) \cdot \boldsymbol{X}_s\big]. \quad (4.19)\end{aligned}$$

Full details of the expansion are provided in appendix E.

There remains to consider the geometric coupling between curvature and angular velocity arising from elasticity. Adopting a local approximation to the hydrodynamic drag arising from twist (Gueron & Levit-Gurevich, 2001b; Wolgemuth *et al.*, 2004), the elastic and viscous twist moments balance as

$$\xi_R \Omega_3 = C\kappa_{3,s} + m_3, \quad (4.20)$$

where $\xi_R = 4\pi\mu a^2$ is the viscous drag coefficient, with a the cross-sectional radius of the flagellum. Rearranging equation (4.20) for Ω_3, and substituting into the compatibility condition equation (1.74c) yields

$$\kappa_{3,t} = \frac{C}{\xi_R}\kappa_{3,ss} + \frac{1}{\xi_R} m_{3,s} + (\boldsymbol{X}_s \wedge \boldsymbol{X}_{ss}) \cdot \boldsymbol{X}_{st}. \quad (4.21)$$

The full derivation of the geometric compatibility equation (4.21) is provided in appendix A. Equation (4.21) is coupled to the hydrodynamic model in equation (4.8) by noting that, upon differentiation with respect to arclength, the dimensional hydrody-

namic velocity can be written

$$\boldsymbol{X}_{ts} = \frac{1}{\xi_\perp}\boldsymbol{f}_s + \frac{\gamma-1}{\xi_\perp}(\boldsymbol{X}_s \cdot \boldsymbol{f})_s \boldsymbol{X}_s + \frac{\gamma-1}{\xi_\perp}(\boldsymbol{X}_s \cdot \boldsymbol{f})\boldsymbol{X}_{ss} + \boldsymbol{V}_s. \tag{4.22}$$

Since the result of the vector product in equation (4.21) is by definition perpendicular to both $\boldsymbol{X}_s$ and $\boldsymbol{X}_{ss}$, substituting (4.22) into (4.21) yields an equation for the elastohydrodynamic twist of the flagellum as

$$\kappa_{3,t} = \frac{C}{\xi_R}\kappa_{3,ss} + \frac{1}{\xi_R}m_{3,s} + \frac{1}{\xi_\perp}(\boldsymbol{X}_s \wedge \boldsymbol{X}_{ss}) \cdot \boldsymbol{f}_s + (\boldsymbol{X}_s \wedge \boldsymbol{X}_{ss}) \cdot \boldsymbol{V}_s. \tag{4.23}$$

The third term in the above equation is nonzero when the flagellum is out of elastic equilibrium. The final term incorporates the nonlocal hydrodynamic effects of the distal flagellum on the local twist. Taken together, these terms act as sinks, restoring the flagellum to an untwisted state. For a pure bending problem, $\kappa_3 = 0$ can be prescribed without loss of generality.

4.2.3 Varying flagellar stiffness

A key physiological feature of human spermatozoa is the tapering sheath surrounding the 9+2 axonemal structure of the flagellum. As discussed in section 1.1.2, and represented in figure 1.1, the tapering structure produces different elastic properties along the length of the flagellum. The varying bending stiffness $E(s)$ is modelled as in chapter 2, following Neal *et al.* (2020), and as given in equation (2.75).

Accounting for the bending stiffness as a function of arclength requires alterations to the elastohydrodynamic model. The internal elastic moment is defined through the equilibrium equation and constitutive bending law, given in equations (4.10b) and

(4.11b) respectively. Substituting the elastic moment expression into the equilibrium equation yields

$$E\boldsymbol{X}_s \wedge \boldsymbol{X}_{sss} + E_s\boldsymbol{X}_s \wedge \boldsymbol{X}_{ss} + C[\kappa_3\boldsymbol{X}_s]_s + \boldsymbol{X}_s \wedge \boldsymbol{F}_{\text{int}} + \boldsymbol{m} = \boldsymbol{0}. \tag{4.24}$$

Following the same procedure as in section 4.2.2, the internal contact force now includes additional bending stiffness derivative terms, and is given by

$$\boldsymbol{F}_{\text{int}} = -E\boldsymbol{X}_{sss} - E_s\boldsymbol{X}_{ss} + C\kappa_3\boldsymbol{X}_s \wedge \boldsymbol{X}_{ss} + T\boldsymbol{X}_s + \boldsymbol{X}_s \wedge \boldsymbol{m}. \tag{4.25}$$

The resulting viscous force per unit length, exerted by the flagellum onto the fluid, obtained via the force equilibrium equation (4.10a) and (4.25), is

$$\boldsymbol{f} = -E\boldsymbol{X}_{ssss} - 2E_s\boldsymbol{X}_{sss} - E_{ss}\boldsymbol{X}_{ss} + C[\kappa_3\boldsymbol{X}_s \wedge \boldsymbol{X}_{ss}]_s + [T\boldsymbol{X}_s]_s + [\boldsymbol{X}_s \wedge \boldsymbol{m}]_s, \tag{4.26}$$

yielding the extended elastohydrodynamic equation, replacing (4.17), as

$$\begin{aligned}\xi_\perp(\boldsymbol{X}_t - \boldsymbol{V}) = {} & -E\boldsymbol{X}_{ssss} - 2E_s\boldsymbol{X}_{sss} - E_{ss}\boldsymbol{X}_{ss} \\ & - E(\gamma-1)(\boldsymbol{X}_s \cdot \boldsymbol{X}_{ssss})\boldsymbol{X}_s - 2E_s(\gamma-1)(\boldsymbol{X}_{ss} \cdot \boldsymbol{X}_{sss})\boldsymbol{X}_s \\ & + C\kappa_{3,s}\boldsymbol{X}_s \wedge \boldsymbol{X}_{ss} + C\kappa_3\boldsymbol{X}_s \wedge \boldsymbol{X}_{sss} \\ & + T\boldsymbol{X}_{ss} + \gamma T_s\boldsymbol{X}_s + \boldsymbol{X}_{ss} \wedge \boldsymbol{m} \\ & + \boldsymbol{X}_s \wedge \boldsymbol{m}_s + (\gamma-1)\boldsymbol{X}_s\boldsymbol{X}_s \cdot (\boldsymbol{X}_{ss} \wedge \boldsymbol{m}).\end{aligned} \tag{4.27}$$

Similarly, the resulting auxiliary tension equation, replacing (4.19), is

$$\begin{aligned}\lambda(1 - \boldsymbol{X}_s \cdot \boldsymbol{X}_s) - \boldsymbol{V}_s \cdot \boldsymbol{X}_s = \frac{1}{\xi_\perp}\big[&\gamma T_{ss} + [E_{ss}(1 + 2\gamma) - T]\boldsymbol{X}_{ss} \cdot \boldsymbol{X}_{ss} \\ &- 3E_s\gamma \boldsymbol{X}_s \cdot \boldsymbol{X}_{ssss} - 2E_s(\gamma - 1)\boldsymbol{X}_{ss} \cdot \boldsymbol{X}_{sss} + C\kappa_{3,s}(\boldsymbol{X}_s \wedge \boldsymbol{X}_{ss}) \cdot \boldsymbol{X}_{sss} \\ &+ E(1 + 3\gamma)\boldsymbol{X}_{ss} \cdot \boldsymbol{X}_{ssss} + 3E\gamma \boldsymbol{X}_{sss} \cdot \boldsymbol{X}_{sss} \\ &+ \gamma(\boldsymbol{X}_{sss} \wedge \boldsymbol{m}) \cdot \boldsymbol{X}_s + (\gamma + 1)(\boldsymbol{X}_{ss} \wedge \boldsymbol{m}_s) \cdot \boldsymbol{X}_s\big]. \quad (4.28)\end{aligned}$$

The hydrodynamics and kinematic equations for the model remain unchanged. The original *constant stiffness* model can be recovered from the varying stiffness equations by noting that terms involving derivatives of the bending stiffness disappear when E is constant.

4.2.4 Boundary conditions

We next consider boundary conditions for the problem. When modelling monoflagellate swimmers such as sperm, the proximal boundary conditions (i.e. at $\boldsymbol{X}_0 := \boldsymbol{X}(0)$) need to account for the presence of the cell body exerting a force and moment onto the connected flagellum. The derivations here are similar to the steps used in chapter 3, generalised to account for full 3D elastodynamics. We begin by noting that in the Stokes flow regime, the total viscous force and moment on the cell are zero, so that

$$\int_0^L \boldsymbol{f}(s)\, ds + \iint_{\partial B} \boldsymbol{\varphi}(Y)\, dS_Y = \boldsymbol{0}, \quad (4.29a)$$

$$\int_0^L \big(\boldsymbol{X}(s) - \boldsymbol{X}_0\big) \wedge \boldsymbol{f}(s)\, ds + \iint_{\partial B} (Y - \boldsymbol{X}_0) \wedge \boldsymbol{\varphi}(Y)\, dS_Y = \boldsymbol{0}, \quad (4.29b)$$

where $\boldsymbol{f}$ and $\boldsymbol{\varphi}$ are the force per unit length and force per unit area the filament and body exert onto the fluid, respectively. Integration of the force equilibrium equation yields

$$\boldsymbol{F}_{\text{int},s} = \boldsymbol{f} \implies \int_s^L \boldsymbol{F}_{\text{int},s'}(s')\, ds' = \boldsymbol{F}_{\text{int}}(L) - \boldsymbol{F}_{\text{int}}(s) = \int_s^L \boldsymbol{f}(s')\, ds'. \tag{4.30}$$

Since the distal tip of flagellum is unconstrained, $\boldsymbol{F}_{\text{int}}(L) = \boldsymbol{M}_{\text{int}}(L) = \boldsymbol{0}$, and equation (4.30) yields $-\boldsymbol{F}_{\text{int}}(0) = \int_0^L \boldsymbol{f}(s)\, ds$. Combining with equation (4.29a),

$$\int_0^L \boldsymbol{f}(s)\, ds + \iint_{\partial B} \boldsymbol{\varphi}(\boldsymbol{Y})\, dS_Y = -\boldsymbol{F}_{\text{int}}(0) + \iint_{\partial B} \boldsymbol{\varphi}(\boldsymbol{Y})\, dS_Y = \boldsymbol{0}. \tag{4.31}$$

Substituting for the elastic expression of the internal contact force, we obtain the proximal force boundary condition as

$$\big(- E\boldsymbol{X}_{sss} - E_s\boldsymbol{X}_{ss} + C\kappa_3\boldsymbol{X}_s \wedge \boldsymbol{X}_{ss} + T\boldsymbol{X}_s + \boldsymbol{X}_s \wedge \boldsymbol{m}\big)\big|_{s=0} = \iint_{\partial B} \boldsymbol{\varphi}(\boldsymbol{Y})\, dS_Y. \tag{4.32}$$

The proximal boundary condition for the tension T is obtained by writing the axial component of equation (4.32) by projecting along the tangent at $\boldsymbol{X}_0$, yielding

$$\left(\iint_{\partial B} \boldsymbol{\varphi}(\boldsymbol{Y})\, dS_Y \right) \cdot \boldsymbol{X}_s\big|_{s=0} = \big(E\boldsymbol{X}_{ss} \cdot \boldsymbol{X}_{ss}\big)\big|_{s=0} + T(0), \tag{4.33}$$

where simplifications are afforded using the differential identities given in appendix E. The proximal boundary condition for the moment is obtained by first considering the moment equilibrium equation

$$\boldsymbol{M}_{\text{int},s} + \boldsymbol{X}_s \wedge \boldsymbol{F}_{\text{int}} + \boldsymbol{m} = \boldsymbol{0}, \tag{4.34}$$

where $\boldsymbol{M}_{\text{int}}$ is the internal elastic contact moment and $\boldsymbol{m}$ is the active moment per unit length. As in the derivation presented in section 2.2, integrating the above over the distal segment $[s, L]$, and noting that $\boldsymbol{M}_{\text{int}}(L) = \boldsymbol{0}$, provides the equation

$$-\boldsymbol{M}_{\text{int}}(s) - \int_s^L \big(\boldsymbol{X}(s') - \boldsymbol{X}(s)\big) \wedge \boldsymbol{f}(s')\, ds' + \int_s^L \boldsymbol{m}(s')\, ds' = \boldsymbol{0}. \tag{4.35}$$

Evaluating equation (4.35) at $s = 0$ and rearranging yields

$$\int_0^L \big(\boldsymbol{X}(s) - \boldsymbol{X}_0\big) \wedge \boldsymbol{f}(s)\, ds = -\boldsymbol{M}_{\text{int}}(0) + \int_0^L \boldsymbol{m}(s)\, ds. \tag{4.36}$$

Substituting this expression into the total moment balance equation (4.29b),

$$-\boldsymbol{M}_{\text{int}}(0) + \int_0^L \boldsymbol{m}(s)\, ds + \iint_{\partial B} (\boldsymbol{Y} - \boldsymbol{X}_0) \wedge \boldsymbol{\varphi}(\boldsymbol{Y})\, dS_Y = \boldsymbol{0}. \tag{4.37}$$

Using the constitutive equation for linear elasticity (equation (1.87)), we substitute and rearrange to obtain the proximal moment boundary condition

$$\iint_{\partial B} (\boldsymbol{Y} - \boldsymbol{X}_0) \wedge \boldsymbol{\varphi}(\boldsymbol{Y})\, dS_Y = \big(E\boldsymbol{X}_s \wedge \boldsymbol{X}_{ss} + C\kappa_3 \boldsymbol{X}_s\big)\big|_{s=0} - \int_0^L \boldsymbol{m}(s)\, ds. \tag{4.38}$$

Taking the vector product of equation (4.38) with $\boldsymbol{X}_s(0)$ from the right provides a boundary condition for the bending moment as

$$\left(\iint_{\partial B} (\boldsymbol{Y} - \boldsymbol{X}_0) \wedge \boldsymbol{\varphi}(\boldsymbol{Y})\, dS_Y\right) \wedge \boldsymbol{X}_s\big|_{s=0} = E\boldsymbol{X}_{ss}\big|_{s=0} - \boldsymbol{M} \wedge \boldsymbol{X}_s\big|_{s=0} \tag{4.39}$$

simplified using triple vector product identities, where, recalling $\boldsymbol{m} = m_i \mathbf{d}_i$,

$$\boldsymbol{M} = \int_0^L m_1(s)\mathbf{d}_1(s) + m_2(s)\mathbf{d}_2(s) + m_3(s)\mathbf{d}_3(s)\, ds. \tag{4.40}$$

A boundary condition for the moment due to twist at $\boldsymbol{X}_0$ is obtained by taking the scalar product between equation (4.38) and $\boldsymbol{X}_s(0)$, yielding

$$\left(\iint_{\partial B} (\boldsymbol{Y} - \boldsymbol{X}_0) \wedge \boldsymbol{\varphi}(\boldsymbol{Y})\, dS_Y \right) \cdot \boldsymbol{X}_s\big|_{s=0} = C\kappa_3(0) - \boldsymbol{M} \cdot \boldsymbol{X}_s\big|_{s=0}. \tag{4.41}$$

At the distal end, the flagellum is force and moment free. The zero force condition provides the boundary condition

$$\boldsymbol{F}_{\text{int}}(L) = \big(- E\boldsymbol{X}_{sss} - E_s\boldsymbol{X}_{ss} + C\kappa_3\boldsymbol{X}_s \wedge \boldsymbol{X}_{ss} + T\boldsymbol{X}_s + \boldsymbol{X}_s \wedge \boldsymbol{m}\big)\big|_{s=L} = \mathbf{0}. \tag{4.42}$$

The tangential component of equation (4.42) yields the distal tension condition to be $T(L) = 0$. The zero moment condition provides a boundary condition for the centreline as

$$\big(E\boldsymbol{X}_s \wedge \boldsymbol{X}_{ss} + C\kappa_3\boldsymbol{X}_s\big)\big|_{s=L} = \mathbf{0}. \tag{4.43}$$

The condition on the bending moment is obtained by taking the cross product of equation (4.43) with $\boldsymbol{X}_s(L)$, yielding

$$\big(E\boldsymbol{X}_s \wedge (\boldsymbol{X}_s \wedge \boldsymbol{X}_{ss})\big)\big|_{s=L} = -E\boldsymbol{X}_{ss}(L) = \mathbf{0}. \tag{4.44}$$

Similarly, the distal boundary condition for the twist moment is

$$C\kappa_3(L) = 0. \tag{4.45}$$

For the reduced problem considering a headless cell i.e. a filament, the distal conditions (4.42–4.45) evaluated at $s = 0$ replace the proximal boundary conditions (4.32–4.41).

An expression for the angular velocity of the frame at $s = 0$, which we assume to also be the angular velocity of the cell head, is obtained through manipulations of the rigid body rotation formula $\boldsymbol{X}_{st} = \boldsymbol{\Omega} \wedge \boldsymbol{X}_s$. Multiplying vectorally from the left by $\boldsymbol{X}_s$, and using the kinematic constraint given in equation (4.20), yields the equation

$$\boldsymbol{\Omega} = \boldsymbol{X}_s \wedge \boldsymbol{X}_{st} + \left(\frac{C}{\xi_R} \kappa_{3,s} + \frac{1}{\xi_R} m_3 \right) \boldsymbol{X}_s, \tag{4.46}$$

where ξ_R is the hydrodynamic twist resistance and m_3 is the active twist moment per unit length.

Defining the director frame along the flagellum as $\mathbf{d}_3 = \boldsymbol{X}_s$ and $\mathbf{d}_2 = \mathbf{d}_3 \wedge \mathbf{d}_1$, the *a priori* unknowns $\mathbf{d}_1(s)$ are computable by noting $\kappa_2 = \mathbf{d}_{3,s} \cdot \mathbf{d}_1$, which requires knowledge of $\mathbf{d}_1(0)$ as a boundary condition for the resulting system partial differential equations. Thus, we include a final equation for the director at $s = 0$ through

$$\mathbf{d}_{1,t} = \boldsymbol{\Omega} \wedge \mathbf{d}_1, \qquad \text{at } s = 0, \tag{4.47}$$

thereby closing the problem. Physically, $\mathbf{d}_1$ is a material direction which rotates with the head at $s = 0$, and coincides with the plane of flattening of the head. Removing the cell head from the model (for example, to model filaments) removes the need to include equations (4.46) and (4.47).

4.2.5 Summary of the dimensional model

The complete dimensional model comprises equations for the elastohydrodynamics of the flagellum, subject to the auxiliary equation which enforces inextensibility. The elastohydrodynamic velocity matches the hydrodynamic velocity of the cell, described by regularised stokeslet integral equations along the filament centreline and across the surface of the cell body. The kinematic constraints connecting the body to the flagellum at their junction point provides additional equations for the angular velocity of the body and the dynamics of the material normal to the plane of the cell body. The dimensional model equations are

$$\begin{aligned}\xi_\perp(\boldsymbol{X}_t - \boldsymbol{V}) = &- E\boldsymbol{X}_{ssss} - E(\gamma-1)(\boldsymbol{X}_s\cdot\boldsymbol{X}_{ssss})\boldsymbol{X}_s \\ &- 2E_s[\boldsymbol{X}_{sss} + (\gamma-1)(\boldsymbol{X}_s\cdot\boldsymbol{X}_{sss})\boldsymbol{X}_s] - E_{ss}\boldsymbol{X}_{ss} + T\boldsymbol{X}_{ss} \\ &+ \gamma T_s\boldsymbol{X}_s + C\kappa_{3,s}\boldsymbol{X}_s\wedge\boldsymbol{X}_{ss} + C\kappa_3\boldsymbol{X}_s\wedge\boldsymbol{X}_{sss} \\ &+ \boldsymbol{X}_{ss}\wedge\boldsymbol{m} + \boldsymbol{X}_s\wedge\boldsymbol{m}_s + (\gamma-1)\boldsymbol{X}_s\boldsymbol{X}_s\cdot(\boldsymbol{X}_{ss}\wedge\boldsymbol{m}),\end{aligned} \tag{4.48a}$$

$$\begin{aligned}\lambda(1-\boldsymbol{X}_s\cdot\boldsymbol{X}_s) - \boldsymbol{V}_s\cdot\boldsymbol{X}_s = \frac{1}{\xi_\perp}\big[&\gamma T_{ss} + [E_{ss}(1+2\gamma) - T]\boldsymbol{X}_{ss}\cdot\boldsymbol{X}_{ss} \\ &- 3E_s\gamma\boldsymbol{X}_s\cdot\boldsymbol{X}_{ssss} - 2E_s(\gamma-1)\boldsymbol{X}_{ss}\cdot\boldsymbol{X}_{sss} + 3E\gamma\boldsymbol{X}_{sss}\cdot\boldsymbol{X}_{sss} \\ &+ E(1+3\gamma)\boldsymbol{X}_{ss}\cdot\boldsymbol{X}_{ssss} + C\kappa_{3,s}(\boldsymbol{X}_s\wedge\boldsymbol{X}_{ss})\cdot\boldsymbol{X}_{sss} \\ &+ \gamma(\boldsymbol{X}_{sss}\wedge\boldsymbol{m})\cdot\boldsymbol{X}_s + (\gamma+1)(\boldsymbol{X}_{ss}\wedge\boldsymbol{m}_s)\cdot\boldsymbol{X}_s\big],\end{aligned} \tag{4.48b}$$

$$\begin{aligned}\boldsymbol{X}_t = \frac{1}{\xi_\perp}\big(I + (\gamma-1)\boldsymbol{X}_s\boldsymbol{X}_s\big)\cdot\boldsymbol{f} &+ \int_{|s-s'|>q}\boldsymbol{S}^\varepsilon\big(\boldsymbol{X},\boldsymbol{X}(s')\big)\cdot\boldsymbol{f}(s')\,ds' \\ &+ \iint_{\partial B}\boldsymbol{S}^\varepsilon\big(\boldsymbol{X},\boldsymbol{Y}\big)\cdot\boldsymbol{\varphi}(Y)\,dS_Y,\end{aligned} \tag{4.48c}$$

$$\boldsymbol{X}_{0,t} + \boldsymbol{\Omega}_0 \wedge (\boldsymbol{Y} - \boldsymbol{X}_0) = \int_0^L \boldsymbol{S}^\varepsilon\big(\boldsymbol{Y}, \boldsymbol{X}(s)\big) \cdot \boldsymbol{f}(s)\, ds + \iint_{\partial B} \boldsymbol{S}^\varepsilon\big(\boldsymbol{Y}, \mathrm{y}\big) \cdot \boldsymbol{\varphi}(\mathrm{y})\, dS_{\mathrm{y}}, \tag{4.48d}$$

$$\boldsymbol{V} = \int_{|s-s'|>q} \boldsymbol{S}^\varepsilon\big(\boldsymbol{X}, \boldsymbol{X}(s')\big) \cdot \boldsymbol{f}(s')\, ds' + \iint_{\partial B} \boldsymbol{S}^\varepsilon\big(\boldsymbol{X}, \boldsymbol{Y}\big) \cdot \boldsymbol{\varphi}(\boldsymbol{Y})\, dS_{\boldsymbol{Y}}, \tag{4.48e}$$

$$\kappa_{3,t} = \frac{C}{\xi_R}\kappa_{3,ss} + \frac{1}{\xi_R} m_{3,s} + \frac{1}{\xi_\perp}(\boldsymbol{X}_s \wedge \boldsymbol{X}_{ss}) \cdot \boldsymbol{f}_s + (\boldsymbol{X}_s \wedge \boldsymbol{X}_{ss}) \cdot \boldsymbol{V}_s, \tag{4.48f}$$

for $0 < s < L$ and $t > 0$, where

$$\boldsymbol{\Omega} = \boldsymbol{X}_s \wedge \boldsymbol{X}_{st} + \left(\frac{C}{\xi_R}\kappa_{3,s} + \frac{1}{\xi_R} m_3\right) \boldsymbol{X}_s, \qquad \text{at } s = 0, \tag{4.49a}$$

$$\mathbf{d}_{1,t} = \boldsymbol{\Omega} \wedge \mathbf{d}_1, \qquad \text{at } s = 0, \tag{4.49b}$$

and subject to the boundary conditions

$$\iint_{\partial B} \boldsymbol{\varphi}(\boldsymbol{Y})\, dS_{\boldsymbol{Y}} = \big(- E\boldsymbol{X}_{sss} - E_s \boldsymbol{X}_{ss} + C\kappa_3 \boldsymbol{X}_s \wedge \boldsymbol{X}_{ss} + T\boldsymbol{X}_s + \boldsymbol{X}_s \wedge \boldsymbol{m}\big)\big|_{s=0}, \tag{4.50a}$$

$$\left(\iint_{\partial B} \boldsymbol{\varphi}(\boldsymbol{Y})\, dS_{\boldsymbol{Y}}\right) \cdot \boldsymbol{X}_s\big|_{s=0} = \big(E\boldsymbol{X}_{ss} \cdot \boldsymbol{X}_{ss}\big)\big|_{s=0} + T(0), \tag{4.50b}$$

$$\left(\iint_{\partial B} (\boldsymbol{Y} - \boldsymbol{X}_0) \wedge \boldsymbol{\varphi}(\boldsymbol{Y})\, dS_{\boldsymbol{Y}}\right) \wedge \boldsymbol{X}_s\big|_{s=0} = \big(E\boldsymbol{X}_{ss}\big)\big|_{s=0} - \boldsymbol{M} \wedge \boldsymbol{X}_s\big|_{s=0}, \tag{4.50c}$$

$$\left(\iint_{\partial B} (\boldsymbol{Y} - \boldsymbol{X}_0) \wedge \boldsymbol{\varphi}(\boldsymbol{Y})\, dS_{\boldsymbol{Y}}\right) \cdot \boldsymbol{X}_s\big|_{s=0} = C\kappa_3(0) - \boldsymbol{M} \cdot \boldsymbol{X}_s\big|_{s=0}, \tag{4.50d}$$

$$\mathbf{0} = \big(- E\boldsymbol{X}_{sss} - E_s \boldsymbol{X}_{ss} + C\kappa_3 \boldsymbol{X}_s \wedge \boldsymbol{X}_{ss} + T\boldsymbol{X}_s + \boldsymbol{X}_s \wedge \boldsymbol{m}\big)\big|_{s=L}, \tag{4.50e}$$

$$0 = T(L), \tag{4.50f}$$

$$\mathbf{0} = (E\boldsymbol{X}_{ss})\big|_{s=L}, \tag{4.50g}$$

$$0 = \kappa_3(L), \tag{4.50h}$$

where $\boldsymbol{M} = \int_0^L m_i(s)\mathbf{d}_i(s)\,ds$ is the integrated active moment per unit length, and where $\varepsilon \ll q \ll L$ and $\lambda > 0$ are parameters to be chosen. For clarity, the space and time dependency of each variable has been suppressed. The model is closed by specification of the initial filament shapes $\boldsymbol{X}(s,0)$, director $\mathbf{d}_1(0,0)$, and twist curvature $\kappa_3(s,0)$.

4.2.6 Nondimensionalisation and summary

The mathematical model is nondimensionsalised using the scalings

$$\begin{gathered}
\hat{s} = Ls, \quad \hat{\boldsymbol{X}} = L\boldsymbol{X}, \quad \hat{\boldsymbol{Y}} = L\boldsymbol{Y}, \quad \hat{\boldsymbol{f}} = \frac{E^d}{L^3}\boldsymbol{f}, \quad \hat{\boldsymbol{\varphi}} = \frac{E^d}{L^4}\boldsymbol{\varphi}, \quad \hat{T} = \frac{E^d}{L^2}T, \\
\hat{t} = \frac{1}{\omega}t, \quad \hat{E} = E^d E, \quad \hat{\varepsilon} = L\varepsilon, \quad \hat{q} = Lq, \quad \hat{\boldsymbol{V}} = \frac{E^d}{\mu L^3}\boldsymbol{V}, \\
\hat{m}_i = m_i^0 m_i, \quad \hat{\Omega} = \frac{1}{\omega}\Omega, \quad \hat{\boldsymbol{\kappa}} = \frac{1}{L}\boldsymbol{\kappa},
\end{gathered} \tag{4.51}$$

for $i = 1, 2, 3$, where L is the length of the flagellum, ω is the time scale associated with the actuation of the cell, E^d is the bending rigidity of the flagellum at the distal end, C is the twist rigidity, and m_i^0 are the amplitudes of the active moment per unit length functions $m_i(s)$ about each director director.

The regularised stokeslet and varying bending stiffness function scale as discussed previously in section 2.2.2. In what follows, hats are used to indicate dimensionless variables, and index notation implies summation over repeated indices. The complete dimensionless problem is then given by the following system of continuous equations,

$$\mathcal{S}^4\hat{\boldsymbol{X}}_{\hat{t}} - \hat{\boldsymbol{V}} = \frac{\mu}{\xi_\perp}\Big[- \hat{E}\hat{\boldsymbol{X}}_{\hat{s}\hat{s}\hat{s}\hat{s}} - \hat{E}(\gamma-1)(\hat{\boldsymbol{X}}_{\hat{s}}\cdot\hat{\boldsymbol{X}}_{\hat{s}\hat{s}\hat{s}\hat{s}})\hat{\boldsymbol{X}}_{\hat{s}} \tag{4.52a}$$
$$- 2\hat{E}_{\hat{s}}[\hat{\boldsymbol{X}}_{\hat{s}\hat{s}\hat{s}} + (\gamma-1)(\hat{\boldsymbol{X}}_{\hat{s}}\cdot\hat{\boldsymbol{X}}_{\hat{s}\hat{s}\hat{s}})\hat{\boldsymbol{X}}_{\hat{s}}] - \hat{E}_{\hat{s}\hat{s}}\hat{\boldsymbol{X}}_{\hat{s}\hat{s}} + \hat{T}\hat{\boldsymbol{X}}_{\hat{s}\hat{s}}$$
$$+ \gamma\hat{T}_{\hat{s}}\hat{\boldsymbol{X}}_{\hat{s}} + \Gamma_s\hat{\kappa}_{3,\hat{s}}\hat{\boldsymbol{X}}_{\hat{s}}\wedge\hat{\boldsymbol{X}}_{\hat{s}\hat{s}} + \Gamma_s\hat{\kappa}_3\hat{\boldsymbol{X}}_{\hat{s}}\wedge\hat{\boldsymbol{X}}_{\hat{s}\hat{s}\hat{s}}$$
$$+ \mathcal{S}^4\hat{\boldsymbol{X}}_{\hat{s}\hat{s}}\wedge\mathcal{M}_i\hat{m}_i\mathbf{d}_i + \mathcal{S}^4\hat{\boldsymbol{X}}_{\hat{s}}\wedge\mathcal{M}_i(\hat{m}_i\mathbf{d}_i)_{\hat{s}}$$
$$+ \mathcal{S}^4(\gamma-1)\hat{\boldsymbol{X}}_{\hat{s}}\hat{\boldsymbol{X}}_{\hat{s}}\cdot(\hat{\boldsymbol{X}}_{\hat{s}}\wedge\mathcal{M}_i\hat{m}_i\mathbf{d}_i)\Big],$$

$$\mathcal{S}^4\hat{\lambda}(1-\hat{\boldsymbol{X}}_{\hat{s}}\cdot\hat{\boldsymbol{X}}_{\hat{s}}) - \hat{\boldsymbol{V}}_{\hat{s}}\cdot\hat{\boldsymbol{X}}_{\hat{s}} = \frac{\mu}{\xi_\perp}\Big[\gamma\hat{T}_{\hat{s}\hat{s}} + [\hat{E}_{\hat{s}\hat{s}}(1+2\gamma) - \hat{T}]\hat{\boldsymbol{X}}_{\hat{s}\hat{s}}\cdot\hat{\boldsymbol{X}}_{\hat{s}\hat{s}} \tag{4.52b}$$
$$- 3\hat{E}_{\hat{s}}\gamma\hat{\boldsymbol{X}}_{\hat{s}}\cdot\hat{\boldsymbol{X}}_{\hat{s}\hat{s}\hat{s}\hat{s}} - 2\hat{E}_{\hat{s}}(\gamma-1)\hat{\boldsymbol{X}}_{\hat{s}\hat{s}}\cdot\hat{\boldsymbol{X}}_{\hat{s}\hat{s}\hat{s}}$$
$$+ 3\hat{E}\gamma\hat{\boldsymbol{X}}_{\hat{s}\hat{s}\hat{s}}\cdot\hat{\boldsymbol{X}}_{\hat{s}\hat{s}\hat{s}} + \hat{E}(1+3\gamma)\hat{\boldsymbol{X}}_{\hat{s}\hat{s}}\cdot\hat{\boldsymbol{X}}_{\hat{s}\hat{s}\hat{s}\hat{s}}$$
$$+ \Gamma_s\hat{\kappa}_{3,\hat{s}}(\hat{\boldsymbol{X}}_{\hat{s}}\wedge\hat{\boldsymbol{X}}_{\hat{s}\hat{s}})\cdot\hat{\boldsymbol{X}}_{\hat{s}\hat{s}\hat{s}} + \mathcal{S}^4\gamma(\hat{\boldsymbol{X}}_{\hat{s}\hat{s}\hat{s}}\wedge\mathcal{M}_i\hat{m}_i\mathbf{d}_i)\cdot\hat{\boldsymbol{X}}_{\hat{s}}$$
$$+ \mathcal{S}^4(\gamma+1)(\hat{\boldsymbol{X}}_{\hat{s}\hat{s}}\wedge\mathcal{M}_i\hat{m}_i\mathbf{d}_i)\cdot\hat{\boldsymbol{X}}_{\hat{s}}\Big],$$

$$\mathcal{S}^4\hat{\boldsymbol{X}}_{\hat{t}} = \frac{\mu}{\xi_\perp}\big(I + (\gamma-1)\hat{\boldsymbol{X}}_{\hat{s}}\hat{\boldsymbol{X}}_{\hat{s}}\big)\cdot\hat{\boldsymbol{f}} \tag{4.52c}$$
$$+ \int_{|\hat{s}-\hat{s}'|>\hat{q}} \hat{\boldsymbol{S}}^{\hat{\varepsilon}}\big(\hat{\boldsymbol{X}}, \hat{\boldsymbol{X}}(\hat{s}')\big)\cdot\hat{\boldsymbol{f}}(\hat{s}')\,d\hat{s}'$$
$$+ \iint_{\partial\hat{B}} \hat{\boldsymbol{S}}^{\hat{\varepsilon}}\big(\hat{\boldsymbol{X}}, \hat{\boldsymbol{Y}}\big)\cdot\hat{\boldsymbol{\varphi}}(\hat{\boldsymbol{Y}})\,dS_{\hat{Y}},$$

$$\mathcal{S}^4\big(\hat{\boldsymbol{X}}_{0,\hat{t}} + \hat{\boldsymbol{\Omega}}_0\wedge(\hat{\boldsymbol{Y}} - \hat{\boldsymbol{X}}_0)\big) = \int_0^1 \hat{\boldsymbol{S}}^{\hat{\varepsilon}}\big(\hat{\boldsymbol{Y}}, \hat{\boldsymbol{X}}(\hat{s}')\big)\cdot\hat{\boldsymbol{f}}(\hat{s}')\,d\hat{s}' \tag{4.52d}$$
$$+ \iint_{\partial\hat{B}} \hat{\boldsymbol{S}}^{\hat{\varepsilon}}\big(\hat{\boldsymbol{Y}}, \hat{\boldsymbol{y}}\big)\cdot\hat{\boldsymbol{\varphi}}(\hat{\boldsymbol{y}})\,dS_{\hat{y}},$$

$$\hat{\boldsymbol{V}} = \int_{|\hat{s}-\hat{s}'|>\hat{q}} \hat{\boldsymbol{S}}^{\hat{\varepsilon}}\big(\hat{\boldsymbol{X}}, \hat{\boldsymbol{X}}(\hat{s}')\big)\cdot\hat{\boldsymbol{f}}(\hat{s}')\,d\hat{s}' \tag{4.52e}$$
$$+ \iint_{\partial\hat{B}} \hat{\boldsymbol{S}}^{\hat{\varepsilon}}\big(\hat{\boldsymbol{X}}, \hat{\boldsymbol{Y}}\big)\cdot\hat{\boldsymbol{\varphi}}(\hat{\boldsymbol{Y}})\,dS_{\hat{Y}},$$

$$\mathcal{S}^4\hat{\kappa}_{3,\hat{t}} = \Gamma_d\Gamma_s\hat{\kappa}_{3,\hat{s}\hat{s}} + \mathcal{S}^4\mathcal{M}_3\Gamma_d\hat{m}_{3,\hat{s}} \tag{4.52f}$$
$$+ \frac{\mu}{\xi_\perp}(\hat{\boldsymbol{X}}_{\hat{s}}\wedge\hat{\boldsymbol{X}}_{\hat{s}\hat{s}})\cdot\hat{\boldsymbol{f}}_{\hat{s}} + (\hat{\boldsymbol{X}}_{\hat{s}}\wedge\hat{\boldsymbol{X}}_{\hat{s}\hat{s}})\cdot\hat{\boldsymbol{V}}_{\hat{s}}$$

where $0 < \hat{s} < 1$ and $\hat{t} > 0$, and with

$$\mathcal{S}^4 \hat{\boldsymbol{\Omega}} = \mathcal{S}^4 \hat{\boldsymbol{X}}_{\hat{s}} \wedge \hat{\boldsymbol{X}}_{\hat{s}\hat{t}} + \Gamma_d (\Gamma_s \hat{\kappa}_{3,\hat{s}} + \mathcal{S}^4 \mathcal{M}_3 \hat{m}_3) \hat{\boldsymbol{X}}_{\hat{s}}, \qquad \text{at } \hat{s} = 0, \tag{4.53a}$$

$$\mathbf{d}_{1,\hat{t}} = \hat{\boldsymbol{\Omega}} \wedge \mathbf{d}_1, \qquad \text{at } \hat{s} = 0, \tag{4.53b}$$

subject to the boundary conditions

$$\begin{aligned}
\iint_{\partial \hat{B}} \hat{\boldsymbol{\varphi}}(\hat{\boldsymbol{Y}}) \, dS_{\hat{\boldsymbol{Y}}} &= \big(- \hat{E} \hat{\boldsymbol{X}}_{\hat{s}\hat{s}\hat{s}} - \hat{E}_{\hat{s}} \hat{\boldsymbol{X}}_{\hat{s}\hat{s}} + \Gamma_s \hat{\kappa}_3 \hat{\boldsymbol{X}}_{\hat{s}} \wedge \hat{\boldsymbol{X}}_{\hat{s}\hat{s}} \\
&\qquad + \hat{T} \hat{\boldsymbol{X}}_{\hat{s}} + \mathcal{S}^4 \hat{\boldsymbol{X}}_{\hat{s}} \wedge \mathcal{M}_i \hat{m}_i \mathbf{d}_i \big)\big|_{\hat{s}=0}, && (4.54a) \\
\left(\iint_{\partial \hat{B}} \hat{\boldsymbol{\varphi}}(\hat{\boldsymbol{Y}}) \, dS_{\hat{\boldsymbol{Y}}} \right) \cdot \hat{\boldsymbol{X}}_{\hat{s}}\big|_{\hat{s}=0} &= \big(\hat{E} \hat{\boldsymbol{X}}_{\hat{s}\hat{s}} \cdot \hat{\boldsymbol{X}}_{\hat{s}\hat{s}} \big)\big|_{\hat{s}=0} + \hat{T}(0), && (4.54b) \\
\left(\iint_{\partial \hat{B}} (\hat{\boldsymbol{Y}} - \hat{\boldsymbol{X}}_0) \wedge \hat{\boldsymbol{\varphi}}(\hat{\boldsymbol{Y}}) \, dS_{\hat{\boldsymbol{Y}}} \right) \wedge \hat{\boldsymbol{X}}_{\hat{s}}\big|_{\hat{s}=0} &= \big(\hat{E} \hat{\boldsymbol{X}}_{\hat{s}\hat{s}} \big)\big|_{\hat{s}=0} - \mathcal{S}^4 \hat{\boldsymbol{M}} \wedge \hat{\boldsymbol{X}}_{\hat{s}}\big|_{\hat{s}=0}, && (4.54c) \\
\left(\iint_{\partial \hat{B}} (\hat{\boldsymbol{Y}} - \hat{\boldsymbol{X}}_0) \wedge \hat{\boldsymbol{\varphi}}(\hat{\boldsymbol{Y}}) \, dS_{\hat{\boldsymbol{Y}}} \right) \cdot \hat{\boldsymbol{X}}_{\hat{s}}\big|_{\hat{s}=0} &= \Gamma_s \hat{\kappa}_3(0) - \mathcal{S}^4 \hat{\boldsymbol{M}} \cdot \hat{\boldsymbol{X}}_{\hat{s}}\big|_{\hat{s}=0}, && (4.54d) \\
\mathbf{0} &= \big(- \hat{E} \hat{\boldsymbol{X}}_{\hat{s}\hat{s}\hat{s}} - \hat{E}_{\hat{s}} \hat{\boldsymbol{X}}_{\hat{s}\hat{s}} + \Gamma_s \hat{\kappa}_3 \hat{\boldsymbol{X}}_{\hat{s}} \wedge \hat{\boldsymbol{X}}_{\hat{s}\hat{s}} \\
&\qquad + \hat{T} \hat{\boldsymbol{X}}_{\hat{s}} + \mathcal{S}^4 \hat{\boldsymbol{X}}_{\hat{s}} \wedge \mathcal{M}_i \hat{m}_i \mathbf{d}_i \big)\big|_{\hat{s}=1}, && (4.54e) \\
0 &= \hat{T}(1), && (4.54f) \\
\mathbf{0} &= (\hat{E} \hat{\boldsymbol{X}}_{\hat{s}\hat{s}})\big|_{\hat{s}=1}, && (4.54g) \\
0 &= \hat{\kappa}_3(1), && (4.54h)
\end{aligned}$$

where

$$\hat{\boldsymbol{M}}(\hat{s}) = \int_{\hat{s}}^{1} \mathcal{M}_i \hat{m}_i(\hat{s}) \mathbf{d}_i(\hat{s}) \, d\hat{s}, \tag{4.55}$$

is the distal integral of the dimensionless active moment per unit length, and where $\hat{\varepsilon} \ll \hat{q} \ll 1$ and $\hat{\lambda} > 0$ are parameters to be chosen. The surface $\partial \hat{B}$ is the dimensionless surface of the cell body, scaled by the total flagellum length.

The dimensionless ratios $\Gamma_s = C/E_d$ and $\Gamma_d = \mu L^2/\xi_R$ describe the relative strength of twist to bending stiffness and bending to twist drag, and are dubbed the *stiffness ratio* and *drag ratio* respectively. The dimensionless groups, referred to as the *swimming parameter* and *actuation parameters* respectively are

$$\mathcal{S} = L\left(\frac{\mu\omega}{E^d}\right)^{\frac{1}{4}} = \frac{\text{viscous forces}}{\text{elastic bending forces}}, \tag{4.56a}$$

$$\mathcal{M}_i = \frac{m_i^0}{\mu\omega L^2} = \frac{\text{active forces}}{\text{viscous forces}}, \quad i = 1, 2, 3, \tag{4.56b}$$

In what follows, we will refer exclusively to the dimensionless model described above unless otherwise declared, and drop the hat notation for clarity.

4.2.7 Numerical implementation

The system of equations forming the dimensionless model given in 4.2.6 is numerically integrated in time using a backwards (i.e. implicit) Euler scheme. For a general ordinary differential equation

$$u_t = \mathcal{F}(u, u', u'', \dots) \tag{4.57}$$

where primes denote differentiation with respect to the independent variable, discretised in time by $t^n = n\Delta t$, the backwards Euler method provides a solution via

$$u^{n+1} = u^n + \Delta t \mathcal{F}^{n+1}(u, u', u'', \dots). \tag{4.58}$$

Whilst other time stepping schemes are available, such as a Crank-Nicolson type scheme (Montenegro-Johnson *et al.*, 2015), or a mixed implicit-explicit ImEx scheme

(Tornberg & Shelley, 2004; Lim *et al.*, 2008; Gadêlha *et al.*, 2010), we use the backwards Euler method for its conceptual simplicity and ease of implementation, finding that improvements in other areas of the numerical implementation compensate for the common drawbacks of using such first-order time stepping approaches.

Labelling temporally discrete filament positions as $\boldsymbol{X}^n := \boldsymbol{X}(s, n\Delta t)$ (and other variables similarly), applying the backward Euler scheme to the elastohydrodynamic equation (4.52a) yields

$$\begin{aligned}\mathcal{S}^4\boldsymbol{X}^{n+1} - \Delta t\boldsymbol{V}^{n+1} = \mathcal{S}^4\boldsymbol{X}^n + \frac{\mu\Delta t}{\xi_\perp}\Big(&- E\boldsymbol{X}_{ssss}^{n+1} - E(\gamma-1)(\boldsymbol{X}_s^{n+1}\cdot\boldsymbol{X}_{ssss}^{n+1})\boldsymbol{X}_s^{n+1} \\ &- 2E_s\big(\boldsymbol{X}_{sss}^{n+1} + (\gamma-1)(\boldsymbol{X}_s^{n+1}\cdot\boldsymbol{X}_{sss}^{n+1})\boldsymbol{X}_s^{n+1}\big) - E_{ss}\boldsymbol{X}_{ss}^{n+1} + T^{n+1}\boldsymbol{X}_{ss}^{n+1} \\ &+ \gamma T_s^{n+1}\boldsymbol{X}_s^{n+1} + \Gamma_d\kappa_{3,s}^{n+1}\boldsymbol{X}_s^{n+1}\wedge\boldsymbol{X}_{ss}^{n+1} + \Gamma_d\kappa_3^{n+1}\boldsymbol{X}_s^{n+1}\wedge\boldsymbol{X}_{sss}^{n+1} \\ &+ \mathcal{S}^4\boldsymbol{X}_{ss}^{n+1}\wedge\mathcal{M}_i m_i^{n+1}\mathbf{d}_i^{n+1} + \mathcal{S}^4\boldsymbol{X}_s^{n+1}\wedge\mathcal{M}_i(m_i^{n+1}\mathbf{d}_i^{n+1})_s \\ &+ \mathcal{S}^4(\gamma-1)\boldsymbol{X}_s^{n+1}\boldsymbol{X}_s^{n+1}\cdot(\boldsymbol{X}_s^{n+1}\wedge\mathcal{M}_i m_i^{n+1}\mathbf{d}_i^{n+1})\Big), \end{aligned} \tag{4.59}$$

which is nonlinear in the unknown filament positions $\boldsymbol{X}^{n+1}$. Note that as the actuation functions $m_i(s,t)$ are prescribed, their values at all time points is automatically known. Calculation of the line tensions T^{n+1} requires solving the auxiliary equation (4.52b) evaluated at time t^{n+1}, which is also nonlinear in the filament shape. The nonlinearity of these equations, as well as others in the system, is tackled by linearising the model equations and employing Picard fixed point iteration until the iterated solutions converge to within a chosen tolerance. Denoting by $\boldsymbol{X}^m$ the m^{th} iterate approximating

$\boldsymbol{X}^{n+1}$, and labelling other variables similarly, the linearised system of equations is

$$\begin{aligned}
\mathcal{S}^4\boldsymbol{X}^{m+1} - \Delta t\boldsymbol{V}^{m+1} = \mathcal{S}^4\boldsymbol{X}^n + \frac{\mu}{\xi_\perp}\Big[& - E\boldsymbol{X}_{ssss}^{m+1} \\
& - E(\gamma-1)(\boldsymbol{X}_s^m\cdot\boldsymbol{X}_{ssss}^{m+1})\boldsymbol{X}_s^m - E_s\boldsymbol{X}_{ss}^{m+1} \\
& - 2E_s[\boldsymbol{X}_{sss}^{m+1} + (\gamma-1)(\boldsymbol{X}_s^m\cdot\boldsymbol{X}_{sss}^{m+1})\boldsymbol{X}_s^m] \\
& + T^{m+1}\boldsymbol{X}_{ss}^m + \gamma T_s^{m+1}\boldsymbol{X}_s^m + \Gamma_s\hat{\kappa}_{3,s}^m\boldsymbol{X}_s^m\wedge\boldsymbol{X}_{ss}^{m+1} \\
& + \Gamma_s\hat{\kappa}_3^m\boldsymbol{X}_s^m\wedge\boldsymbol{X}_{sss}^{m+1} + \mathcal{S}^4\boldsymbol{X}_{ss}^m\wedge\mathcal{M}_i m_i^{n+1}\mathbf{d}_i^m \\
& + \mathcal{S}^4(\gamma-1)\boldsymbol{X}_s^m\boldsymbol{X}_s^m\cdot(\boldsymbol{X}_s^m\wedge\mathcal{M}_i\hat{m}_i^{m+1}\mathbf{d}_i^m) \\
& + \mathcal{S}^4\boldsymbol{X}_s^m\wedge\mathcal{M}_i(m_i^{n+1}\mathbf{d}_i^m)_s\Big],
\end{aligned} \tag{4.60a}$$

$$\begin{aligned}
\mathcal{S}^4\lambda(1-\boldsymbol{X}_s^m\cdot\boldsymbol{X}_s^{m+1}) = \boldsymbol{V}_s^m\cdot\boldsymbol{X}_s^{m+1} + \frac{\mu}{\xi_\perp}\Big[& \gamma T_{ss}^{m+1} - (\boldsymbol{X}_{ss}^m\cdot\boldsymbol{X}_{ss}^m)T^{m+1} \\
& + E_s(1+2\gamma)\boldsymbol{X}_{ss}^m\cdot\boldsymbol{X}_{ss}^{m+1} - 3E_s\gamma\boldsymbol{X}_s^m\cdot\boldsymbol{X}_{ssss}^{m+1} \\
& - 2E_s(\gamma-1)\boldsymbol{X}_{ss}^m\cdot\boldsymbol{X}_{sss}^{m+1} + 3E\gamma\boldsymbol{X}_{sss}^m\cdot\boldsymbol{X}_{sss}^{m+1} \\
& + E(1+3\gamma)\boldsymbol{X}_{ss}^m\cdot\boldsymbol{X}_{ssss}^{m+1} + \Gamma_s\hat{\kappa}_{3,s}^m(\boldsymbol{X}_s^m\wedge\boldsymbol{X}_{ss}^m)\cdot\boldsymbol{X}_{sss}^{m+1} \\
& + \mathcal{S}^4\gamma(\boldsymbol{X}_{sss}^m\wedge\mathcal{M}_i m_i^{n+1}\mathbf{d}_i^m)\cdot\boldsymbol{X}_s^m \\
& + \mathcal{S}^4(\gamma+1)(\boldsymbol{X}_{ss}^m\wedge\mathcal{M}_i m_i^{n+1}\mathbf{d}_i^m)\cdot\boldsymbol{X}_s^m\Big],
\end{aligned} \tag{4.60b}$$

$$\begin{aligned}
\mathcal{S}^4\boldsymbol{X}^{m+1} = \mathcal{S}^4\boldsymbol{X}^n + \frac{\Delta t\mu}{\xi_\perp}\big(I + (\gamma-1)\boldsymbol{X}_s^m\boldsymbol{X}_s^m\big)\cdot\boldsymbol{f}^{m+1} \\
+ \Delta t\int_{|s-s'|>q} S^\varepsilon\big(\boldsymbol{X}^m,\boldsymbol{X}^m(s')\big)\cdot\boldsymbol{f}^{m+1}(s')\,ds' \\
+ \Delta t\iint_{\partial B} S^\varepsilon\big(\boldsymbol{X}^m,\boldsymbol{Y}^m\big)\cdot\boldsymbol{\varphi}^{m+1}(Y)\,dS_Y,
\end{aligned} \tag{4.60c}$$

$$\begin{aligned}
\mathcal{S}^4\boldsymbol{X}_0^{m+1} = \mathcal{S}^4\boldsymbol{X}_0^n - \Delta t\,\mathcal{S}^4\boldsymbol{\Omega}_0^{m+1}\wedge(\boldsymbol{Y}^m - \boldsymbol{X}_0^m) \\
+ \Delta t\int_0^1 S^\varepsilon\big(\boldsymbol{Y}^m,\boldsymbol{X}^m(s')\big)\cdot\boldsymbol{f}^{m+1}(s')\,ds' \\
+ \Delta t\iint_{\partial B} S^\varepsilon\big(\boldsymbol{Y}^m,\mathbf{y}^m\big)\cdot\boldsymbol{\varphi}^{m+1}(\mathrm{y})\,dS_\mathrm{y},
\end{aligned} \tag{4.60d}$$

$$\boldsymbol{V}^{m+1} = \int_{|s-s'|>q} \mathcal{S}^{\varepsilon}\left(\boldsymbol{X}^{m}, \boldsymbol{X}^{m}(s')\right) \cdot \boldsymbol{f}^{m+1}(s')\, ds' + \iint_{\partial B} \mathcal{S}^{\varepsilon}\left(\boldsymbol{X}^{m}, \boldsymbol{Y}^{m}\right) \cdot \boldsymbol{\varphi}^{m+1}(\boldsymbol{Y})\, dS_{Y}, \tag{4.60e}$$

$$\mathcal{S}^{4}(\kappa_{3}^{m+1} - \kappa_{3}^{n}) = \Delta t\, \Gamma_{d}\Gamma_{s}\kappa_{3,ss}^{m+1} + \Delta t \mathcal{S}^{4}\mathcal{M}_{3}\Gamma_{d}\, m_{3,s}^{n+1} + \Delta t \frac{\mu}{\xi_{\perp}}(\boldsymbol{X}_{s}^{m} \wedge \boldsymbol{X}_{ss}^{m}) \cdot \boldsymbol{f}_{s}^{m+1} + \Delta t\, (\boldsymbol{X}_{s}^{m} \wedge \boldsymbol{X}_{ss}^{m+1}) \cdot \boldsymbol{V}_{s}^{m}, \tag{4.60f}$$

The kinematic equations for the angular velocity and director normal at the body-flagellum join linearise as

$$\Delta t \mathcal{S}^{4}\boldsymbol{\Omega}^{m+1} = \mathcal{S}^{4}\boldsymbol{X}_{s}^{m} \wedge (\boldsymbol{X}_{s}^{m+1} - \boldsymbol{X}_{s}^{n}) + \Delta t\, \Gamma_{d}\left(\Gamma_{s}\kappa_{3,s}^{m+1} + \mathcal{S}^{4}\mathcal{M}_{3}\, m_{3}^{n+1}\right)\boldsymbol{X}_{s}^{m}, \qquad \text{at } s = 0, \tag{4.61a}$$

$$\mathbf{d}_{1}^{m+1} = \mathbf{d}_{1}^{n} + \Delta t\, \boldsymbol{\Omega}^{m} \wedge \mathbf{d}_{1}^{m+1} \qquad \text{at } s = 0. \tag{4.61b}$$

The boundary conditions linearise as

$$\iint_{\partial B} \boldsymbol{\varphi}^{m+1}(\boldsymbol{Y})\, dS_{Y} = \Big(- E\boldsymbol{X}_{sss}^{m+1} - E_{s}\boldsymbol{X}_{ss}^{m+1} + \Gamma_{s}\kappa_{3}^{m}\boldsymbol{X}_{s}^{m} \wedge \boldsymbol{X}_{ss}^{m+1} + T^{m}\boldsymbol{X}_{s}^{m} + \mathcal{S}^{4}\boldsymbol{X}_{s}^{m} \wedge \mathcal{M}_{i}\, m_{i}^{n+1}\mathbf{d}_{i}^{m}\Big)\Big|_{s=0}, \tag{4.62a}$$

$$\left(\iint_{\partial B} \boldsymbol{\varphi}^{m+1}(\boldsymbol{Y})\, dS_{Y}\right) \cdot \boldsymbol{X}_{s}^{m}\Big|_{s=0} = \left(E\boldsymbol{X}_{ss}^{m} \cdot \boldsymbol{X}_{ss}^{m+1}\right)\Big|_{s=0} + T^{m+1}(0), \tag{4.62b}$$

$$\left(\iint_{\partial B} (\boldsymbol{Y}^{m} - \boldsymbol{X}_{0}^{m}) \wedge \boldsymbol{\varphi}^{m+1}(\boldsymbol{Y})\, dS_{Y}\right) \wedge \boldsymbol{X}_{s}^{m}\Big|_{s=0} = \left(E\boldsymbol{X}_{ss}^{m+1}\right)\Big|_{s=0} - \mathcal{S}^{4}\boldsymbol{M}^{m+1} \wedge \boldsymbol{X}_{s}^{m}\Big|_{s=0}, \tag{4.62c}$$

$$\left(\iint_{\partial B} (\boldsymbol{Y}^{m} - \boldsymbol{X}_{0}^{m}) \wedge \boldsymbol{\varphi}^{m+1}(\boldsymbol{Y})\, dS_{Y}\right) \cdot \boldsymbol{X}_{s}^{m}\Big|_{s=0} = \Gamma_{s}\kappa_{3}^{m+1}(0) - \mathcal{S}^{4}\boldsymbol{M}^{m+1} \cdot \boldsymbol{X}_{s}^{m}\Big|_{s=0}, \tag{4.62d}$$

$$\mathbf{0} = \Big(- E\boldsymbol{X}_{sss}^{m+1} - E_s \boldsymbol{X}_{ss}^{m+1} \tag{4.62e}$$
$$+ \Gamma_s \kappa_3^m \boldsymbol{X}_s^m \wedge \boldsymbol{X}_{ss}^{m+1} + T^m \boldsymbol{X}_s^m$$
$$+ \mathcal{S}^4 \boldsymbol{X}_s^m \wedge \mathcal{M}_i m_i^{n+1} \mathbf{d}_i^m \Big)\Big|_{s=1},$$
$$0 = T^{m+1}(1), \tag{4.62f}$$
$$\mathbf{0} = (E\boldsymbol{X}_{ss}^{m+1})\Big|_{s=1}, \tag{4.62g}$$
$$0 = \kappa_3^{m+1}(1), \tag{4.62h}$$

where

$$\boldsymbol{M}^{m+1}(s) = \int_s^1 \mathcal{M}_i m_i^{n+1}(s') \, \mathbf{d}_i^m(s') \, ds'. \tag{4.63}$$

At each iteration, the director frame is updated using the most recent iterates by solving the separate system of partial differential equations given by the linearised equations

$$\mathbf{d}_{1,s}^{m+1} = \kappa_3^m \mathbf{d}_2^{m+1} - \kappa_2^{m+1} \boldsymbol{X}_s^m, \tag{4.64a}$$
$$\mathbf{d}_2^{m+1} = \boldsymbol{X}_s^m \wedge \mathbf{d}_1^{m+1}, \tag{4.64b}$$
$$\kappa_2^{m+1} = \boldsymbol{X}_{ss}^m \cdot \mathbf{d}_1^{m+1}, \tag{4.64c}$$

closed by the boundary condition prescribing $\mathbf{d}_1^{m+1}(0)$ equal to the most recent iterate for $\mathbf{d}_1(0)$ provided by the solution of equation (4.61b).

The flagellum is spatially discretised by $i = 1, \dots, N$ equally spaced nodes along its arclength at discrete values $s[i] := (i-1)\Delta s$. The cell body is discretised by M nodes distributed across its surface, obtained through a cubic projection method as outlined in section 1.2.8. Derivatives with respect to s are approximated using second order accurate central finite difference schemes for variables positioned at interior nodes.

Derivatives of variables at the boundaries (that is, each end of the flagellum) are approximated using third order accurate one-sided finite differences.

Integrals of the active moment vector and director vectors are numerically approximated using the trapezium rule. The regularised stokeslet integrals across the body surface in equations (4.60c–4.60e) and the boundary conditions are approximated using a nearest neighbour discretisation as described in section 1.2.8, which requires the additional generation of a higher resolution discretisation of the cell head. These discretisations are generated in a reference configuration during initialisation, and then rotated by a rigid body transformation as required at each iteration according to the values of Ω and $\boldsymbol{X}_{0,t}$ calculated upon each solve. The boundary conditions involving integrals across the surface of the cell body are formulated as operators onto the unknown head forces. Steps taken to obtain the required linear operators are described in appendix F.

Applying the aforementioned finite difference scheme to approximate spatial derivatives, equations (4.60a–4.61b), closed by the boundary conditions (4.62a–4.62h) form a linear system solveable at each time step for the unknown positions $\boldsymbol{X}^{m+1}$, tensions T^{m+1}, force densities $\boldsymbol{f}^{m+1}$ and $\boldsymbol{\varphi}^{m+1}$, angular velocity Ω_0^{m+1}, director $\mathbf{d}_1^{m+1}[1]$, and twist curvature κ_3^{m+1}. This system can be written as a matrix equation,

$$A\boldsymbol{b} = \boldsymbol{Z}, \tag{4.65}$$

where A is a $(8N+3M+6)\times(8N+3M+6)$ square matrix, $\boldsymbol{Z}$ is an $(8N+3M+6)\times 1$ column vector of unknowns, and $\boldsymbol{b}$ is an identically sized vector encoding the right hand sides of the model equations.

The linear system at each iteration is solved in a monolithic fashion, differing from

other nonlocal methods by Gueron & Levit-Gurevich (2001a) and Montenegro-Johnson *et al.* (2015), which tackle the hydrodynamic problem separately from the elastohydrodynamics. The left hand side operator, expressed in matrix blocks, is

$$A = \begin{pmatrix} A_X^E & A_T^E & A_{f,\varphi}^E & 0 & 0 & 0 \\ A_X^T & A_T^T & 0 & 0 & 0 & 0 \\ A_X^H & 0 & A_{f,\varphi}^H & 0 & 0 & 0 \\ A_X^K & 0 & 0 & A_\Omega^K & A_{\mathrm{d}_{10}}^K & 0 \\ A_X^C & 0 & A_{f,\varphi}^C & 0 & 0 & A_{\kappa_3}^C \end{pmatrix}, \tag{4.66}$$

where the subscript of each block matrix indicates onto which of the unknowns of the iterative problem the operator multiplies. Respectively, the matrices A^E, A^T, A^H, A^K, and A^C encode the linearised elastohydrodynamic equation (4.60a), auxiliary equation (4.60b), hydrodynamics equations (4.60c,4.60d), kinematic equations (4.61a,4.61b), and compatibility relation (4.60f). The matrix block $A_{f,\varphi}^E$ encodes the nonlocal velocity contribution (equation (4.60e)) appearing on the left hand side of the elastohydrodynamic equation (4.60a). The vector of unknowns is

$$\boldsymbol{b} = \left(\boldsymbol{b}^E, \boldsymbol{b}^T, \boldsymbol{b}^H, \boldsymbol{b}^K, \boldsymbol{b}^C\right)^T, \tag{4.67}$$

where

$$\boldsymbol{b}^E = \left(X_1^{m+1}[1], \dots, X_1^{m+1}[N], X_2^{m+1}[1], \dots, X_2^{m+1}[N], X_3^{m+1}[1], \dots, X_3^{m+1}[N]\right), \tag{4.68a}$$

$$\boldsymbol{b}^T = \left(T^{m+1}[1], \dots, T^{m+1}[N]\right), \tag{4.68b}$$

$$\boldsymbol{b}^H = \left(f_1^{m+1}[1], \dots, f_1^{m+1}[N], \Phi_1^{m+1}[1], \dots, \Phi_1^{m+1}[M], \right. \tag{4.68c}$$

$$\left. f_2^{m+1}[1], \dots, f_2^{m+1}[N], \Phi_2^{m+1}[1], \dots, \Phi_2^{m+1}[M], \right. \tag{4.68d}$$

$$f_3^{m+1}[1], \dots, f_3^{m+1}[N], \Phi_3^{m+1}[1], \dots, \Phi_3^{m+1}[M], \big), \tag{4.68e}$$

$$\boldsymbol{b}^K = \left(\Omega_0^{m+1}, \mathbf{d}_{10}^{m+1}\right), \tag{4.68f}$$

$$\boldsymbol{b}^C = \left(\kappa_3^{m+1}[1], \dots, \kappa_3^{m+1}[N]\right), \tag{4.68g}$$

where the subscripts $1, 2, 3$ indicate the x, y, z components of the respective variables. The force quantities $\Phi[1], \dots, \Phi[M]$ are the combined forces per unit area the cell body exerted by the body onto the fluid, with their associated weights,

$$\Phi[j] = \boldsymbol{\varphi}[j] dS_{Y[j]}, \qquad j = 1, \dots, M, \tag{4.69}$$

arising due to the choice of nearest-neighbour discretisation for the regularised stokeslet surface integrals, which does not require explicit knowledge of the force per unit area $\boldsymbol{\varphi}$.

The linear system is preconditioned using the MATLAB® `equilibrate` function, which reduces the condition number of the matrix (measured for a typical swimming cell simulation) from $\mathcal{O}(10^{16})$ to $\mathcal{O}(10^9)$, aiding in numerical stability. Since the order of the condition number of the matrix is approximately temporally constant, the scaling matrices are computed on the first time step and then reused on all subsequent time steps in order to reduce computational expense. Additionally, for problems not involving any mechanical twist (such as a planar beating problem), the linear system may be reduced by removing the rows of the matrix containing the block matrices A^C, and their corresponding right hand sides $\boldsymbol{b}^C$ from $\boldsymbol{b}$, since $\kappa_3[1] = \cdots = \kappa_3[N] = 0$ can be prescribed in these cases. The system is solved using the MATLAB® `mldivide` command to obtain new iterates for the model unknowns. The system is then rebuilt

with the new information and repeatedly solved until

$$\max |\boldsymbol{X}^{m+1} - \boldsymbol{X}^{m}| \leqslant \tau, \tag{4.70}$$

where τ is the desired tolerance of the iterative solver. In what follows, we choose $\tau = 10^{-4}$ unless otherwise stated. Depending on the problem under consideration, convergence to this tolerance is typically achieved with 1–5 iterations per time step. Upon satisfying the tolerance, the converged values are stored as the solutions to the problem at t^{n+1}, and used as initial guesses for variables at the next time step.

4.3 Model comparisons

In the following section we compare the accuracy and performance of the proposed framework, hereafter referred to as the *SPX method*, against the previously developed EIF method (see chapter 2 for details). Additionally, as in section 2.3, we compare against a nonlocal bead and spring model (labelled *BSM*), and the nonlinear model of Moreau *et al.* (2018) (labelled *MGG*), which contrasts in that it employs resistive force theory to model only local hydrodynamic interactions. In all of the following, unless otherwise stated, the regularisation parameter is set at $\varepsilon = 0.01$, and the tolerance for the nonlinear iterative solver is $\tau = 10^{-4}$. As described previously, iterations are considered converged when the maximum absolute difference in centreline positions $\boldsymbol{X}$ is below τ, as opposed to convergence in the full vector of unknowns $\boldsymbol{Z}$. In practice, $\boldsymbol{X}$-convergence at each time step is sufficient for an accurate and stable algorithm, and converges in fewer iterations than waiting for full $\boldsymbol{Z}$-convergence.

4.3.1 Passively relaxing filament

A headless cell (i.e. a filament) is initially deformed into a planar semicircle of unit arclength. The initial condition is obtained by prescribing $\kappa_1(s) = 0$, $\kappa_2(s) = \pi$ and $\kappa_3(s) = 0$ along with proximal directors $\mathbf{d}_1(0)$, $\mathbf{d}_2(0)$ and $\mathbf{d}_3(0)$ and solving the linear system given in equations (1.70). Since $\boldsymbol{X}_s = \mathbf{d}_3$, the resulting centreline coordinates can be obtained through numerical integration. The corresponding initial condition for the angle formulation methods is obtained through basic trigonometric formulas.

At $t = 0$, the simulation begins and the filament relaxes towards its equilibrium configuration of a straight line. In the absence of any external or internal actuation forces, we characterise the filaments by $\mathcal{S} = 1$ without loss of generality. A trace of

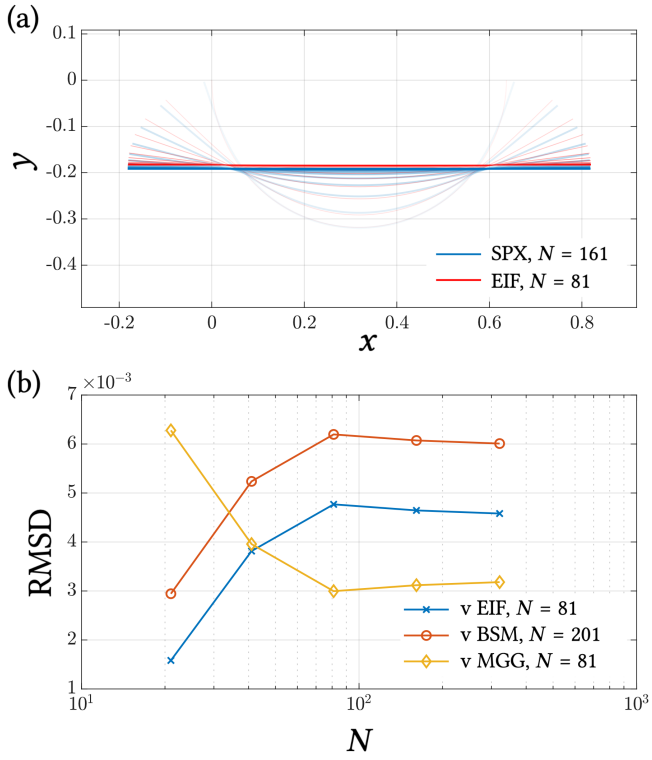

Figure 4.1: Comparisons between the SPX method and alternate planar filament modelling codes. In all SPX simulations, the damping parameter is $\lambda = 200$. (a) The trace of the fibre as it relaxes during the simulation over $0 \leqslant t \leqslant 0.06$. (b) Relative differences in the final position of the centre of mass between the SPX method and the (i) EIF (blue crosses) (ii) BSM (orange circles) and (iii) MGG (yellow diamonds) models, for increasing spatial discretisation parameter N.

the planar fibre configuration, produced by the SPX and EIF methods respectively, is shown in figure 4.1a. For a sufficiently finely discretised filament, the SPX method agrees well with a converged result using the EIF method (see section 2.3.1 for details on the convergence properties of the EIF method).

The root mean squared difference in the final position of the filament centre of mass between the SPX solution and the EIF, BSM, and MGG solutions respectively are presented in figure 4.1b. For $N > 100$, the SPX solution agrees to within $\leqslant 1\%$ with the

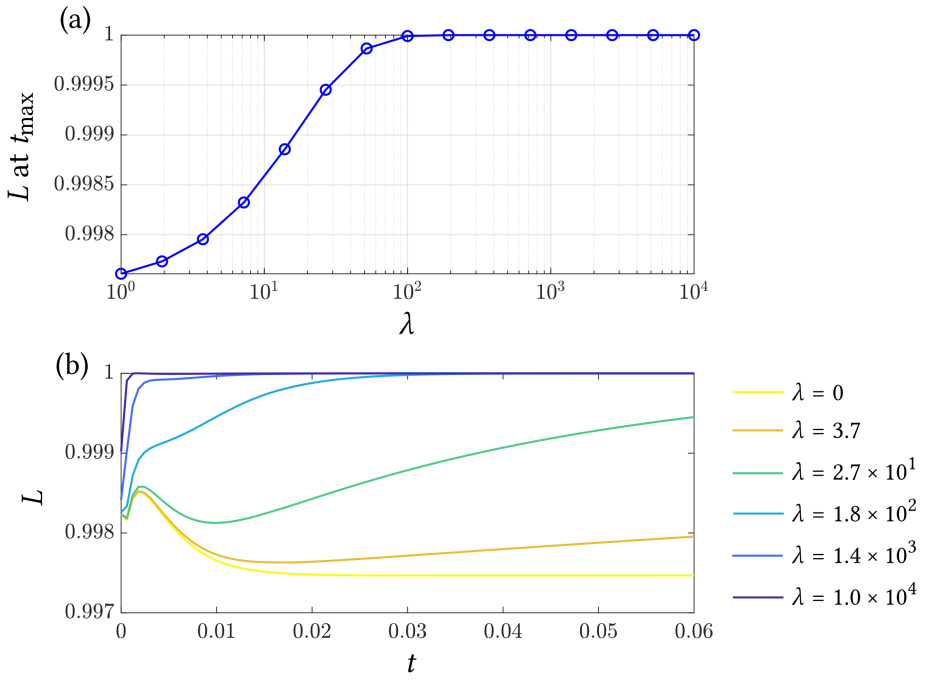

Figure 4.2: Effects of the choice of tension damping parameter λ on dimensionless filament arclength L. A filament discretised with $N = 161$ relaxes from an initial semicircular initial condition towards a straight line equilibrium. (a) Arclength measured at the end of the simulation ($t = 0.06$) for increasing λ. (b) Arclength over the course of the relaxing filament simulation ($0 \leqslant t \leqslant 0.06$), for a selection of λ values.

nonlocal EIF and BSM methods. The marginally improved agreement with the local MGG approach is due to the hybridised nonlocal hydrodynamic model the SPX employs, with a small neighbourhood around each collocation point approximated with a local expression, complemented by a full nonlocal approximation outside this area. The reported lower error for $N < 100$ when compared with the nonlocal methods is a result of unconverged SPX simulations, since the accuracy of derivatives of variables, and the extent to which the inextensibility constraint is successfully enforced, both scale with the refinement of the filament discretisation.

Motivated by the comparison results in figure 4.1, we choose $N = 161$ and simulate

a relaxing filament using the SPX method for a range of values of λ, the parameter governing the strength of the inextensibility correction. Results are shown in figure 4.2. For $\lambda \geqslant 100$, unit arclength is ensured at the end of the relaxing filament simulation, as seen in figure 4.2a. In figure 4.2b, the total arclength throughout the relaxing filament simulation is tracked for a selection of $\lambda \in [0, 10^4]$. Whilst larger values tightly enforce the unit arclength requirement, in all cases the deviation of the total flagellum length is $< 0.25\%$.

4.3.2 Passively relaxing cell

We next assess the SPX model for the case of a passively relaxing planar sperm cell. We compare against the EIF with the extensions described in section 2.5. In both approaches, the cell flagellum is assumed to extend perpendicular from the surface of the cell body at the head-flagellum join $\boldsymbol{X}_0$, so that both methods describe the same dynamic physical problem, allowing appropriate comparisons between simulation results to be made.

As in section 4.3.1, the cell is initialised in a semicircular configuration and is allowed to relax over $t \in [0, 0.06]$, with the dimensionless swimming parameter set at $S = 1$. The presence of the cell head provides additional drag to the proximal flagellum, altering the final rest state of the cell. The dimensionless head axes are prescribed as $\boldsymbol{a} = [2, 1.6, 1]/45 \approx [0.044, 0.036, 0.022]$. In both methods, integrals over the cell head are included using nearest-neighbour methods, requiring the generation of a refined quadrature discretisation and a coarser traction discretisation. The cell body discretisations in both SPX and EIF methods are fixed with $M_q = 600$ and $M_t = 149$ for the quadrature and traction respectively, which arise from cubic projections with $H_q = 10$

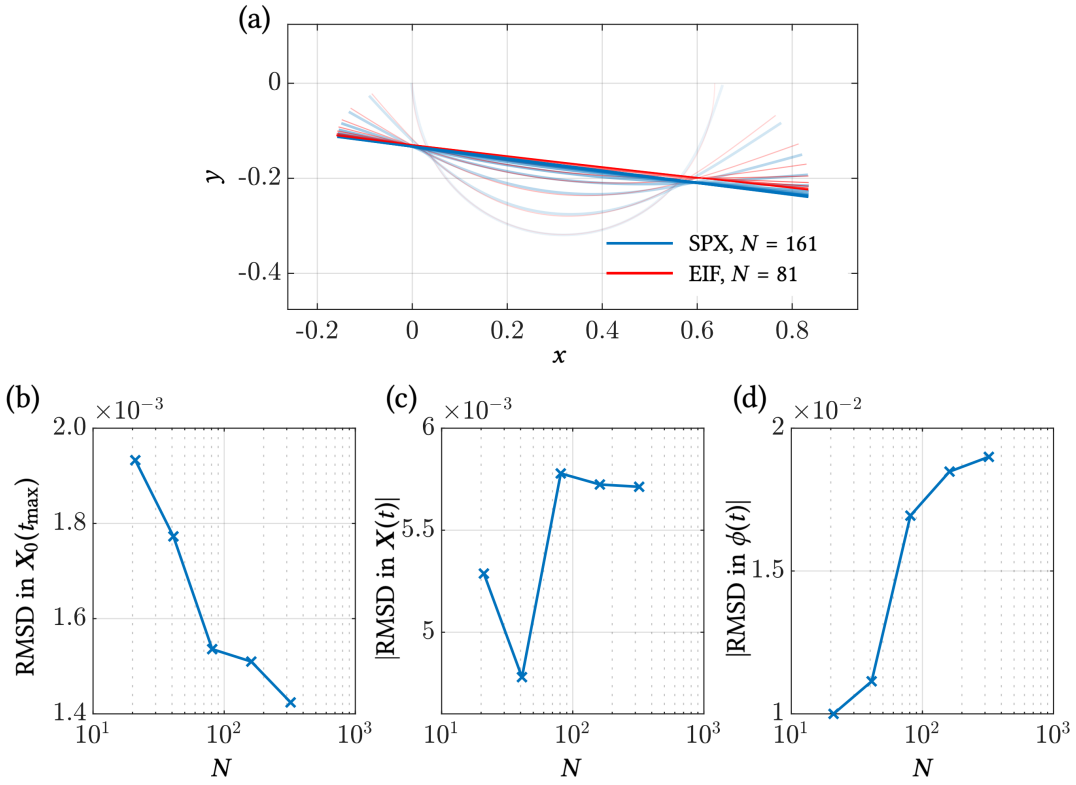

Figure 4.3: Comparisons between the SPX method and the EIF method for modelling a planar relaxing cell. The cell body, with dimensionless axes lengths $[2, 1.6, 1]/45$, is attached at the left-most end of the filament, though is omitted from the plots for clarity. (a) Trace of the cell flagellum over $t \in [0, 0.06]$. Root mean squared differences (RMSD) upon increasing N in (b) the final position of the head-flagellum join $\boldsymbol{X}_0$, (c) the flagella curves, averaged across t, and (d) the head angle ϕ, averaged across t.

and $H_t = 5$ nodes per face respectively. These values are deemed sufficient to provide converged results following the convergence testing presented in section 1.2.8 (see figure 1.6), as well as in Neal *et al.* (2020). The number of flagella segments in the EIF method is chosen as $Q = 80$, sufficient for a converged result (see section 2.3.1 for details).

The trace of the cell across the simulation, with the head omitted for clarity, is displayed in figure 4.3a, illustrating the good qualitative agreement between the $N = 81$

SPX result and SPX solution with $N = 161$. The RMSD between the final positions of the head-flagellum join $\boldsymbol{X}_0$ upon increasing the number of flagellum nodes N is given in figure 4.3b, with the error $\leqslant 2 \times 10^{-3}$ for all $N \geqslant 50$ considered. The MATLAB® spline function is used to generate a smooth interpolating cubic polynomial closely matching the discrete solution; the SPX solutions for varying N can be then be sampled from the spline at arclength values matching those used in the EIF simulation. The RMSD between these two vectors, calculated at each time point and then averaged across the interval, is presented in figure 4.3c. This curve exhibits the same misleading reduced differences for $N < 100$ as observed in figure 4.1 arising from the the SPX method being underresolved in these cases. For $N \geqslant 100$, this difference remains below 6×10^{-3}.

A similar metric is applied to the body tangent angle ϕ, with results given in 4.3d. Despite convergence in the head-flagellum join coordinate $\boldsymbol{X}_0$, larger differences are observed in the tangent angle. In these methods we enforce $\phi = \tan^{-1} \boldsymbol{X}_s(0, t)$, and thus differences previously established in the flagellar model (section 4.3.1) manifest here in the observed discrepancy. Nevertheless, taken together these results indicate that the SPX method accurately accounts for the additional physics associated with the inclusion of a cell body. Since the error associated with the regularised stokeslet method itself is order ε, with $\varepsilon = 0.01$ as in these simulations, we consider these convergence and difference statistics as satisfactory.

4.3.3 Planar beating sperm cell

In the following section, we examine the convergence properties of the SPX method when used to simulate a planar swimming cell. To model human spermatozoa, we employ the varying stiffness model as described in section 4.2.3. Additionally, motivated

by the recent findings of Neal *et al.* (2020), we choose the scalar actuation function $m_2(s)$ so as to model the inactive end piece observable at the distal few microns of human sperm flagella. In the aforementioned work, and in the method used in chapter 3, this is implemented by combining a travelling wave function with a Heaviside function, so that

$$m_2(s,t) = \cos(ks - t)\, H((1-\ell) - s), \tag{4.71}$$

where $0 \leqslant \ell \leqslant 1$ is the length of the inactive distal end piece, k is the dimensionless wave number of the actuating travelling wave, and t is time. Implementing the passive end piece in this manner introduces a discontinuity in the values for m_2; moreover the analytical derivative $m_{2,s}$ at $s = 1 - \ell$ is infinite. However, for levels of discretisation which ensure a converged result (see sections 4.3.1 and 4.3.2), these derivatives are not so large as to cause numerical instability.

A cell is characterised by swimming parameter $\mathcal{S} = 14$ and actuation parameter $\mathcal{M}_2 = 0.015$, fixing $q = 0.1$ and the dimensionless wave number $k = 4\pi$. The passive end piece is modelled as described above by including $\boldsymbol{m} = m_2\mathbf{d}_2$, with $m_2(s)$ given by equation (4.71), in the SPX model equations detailed in section 4.2.6. In all simulations, the time step is fixed at $\Delta t = 0.01$ and the tolerance of the iterative solver is $\epsilon = 1 \times 10^{-4}$. With these values, solutions at each time step converge in between 2 and 5 iterations. The cell body is discretised identically as in section 4.3.2, with $H_t = 5$ and $H_q = 10$ defining the discretisations for the head traction and kernel discretisations respectively.

The flagellum is initialised as a straight line, and the cell swims across the time interval $t \in [0, 4\pi]$ in the xy-plane, in the negative-x direction. Fixing $\lambda = 200$, the number of nodes N along the flagellum is varied between 17 and 501, with intermediate

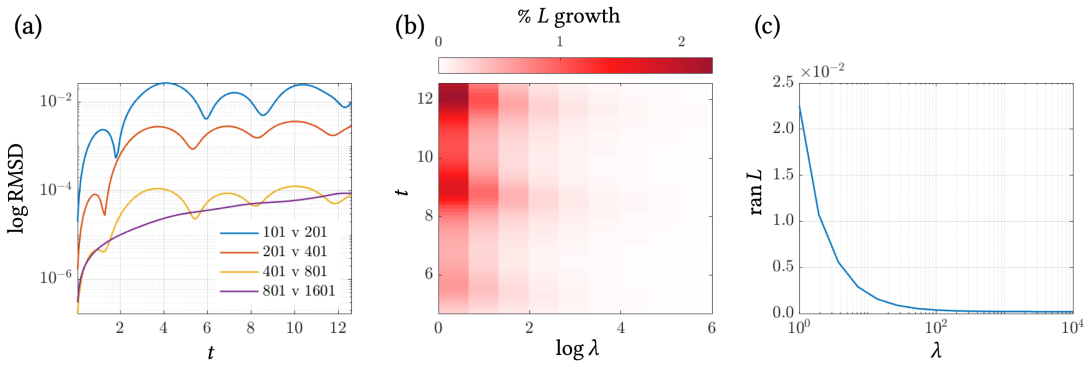

Figure 4.4: Spatial convergence properties of the SPX method when used to simulate a swimming human sperm cell, for varying (a) level of discretisation N, and (b,c) inextensibility enforcement parameter λ. In all simulations, the cell is characterised by swimming parameter $\mathcal{S} = 14$ and actuation parameter $\mathcal{M}_2 = 0.015$, and simulated over $t \in [0, 4\pi]$. (a) Convergence of the relative error of the final position of $\boldsymbol{X}_0$ between the highly-refined solution and simulations with varying $N \in [91, 501]$. Choosing $N = 201$, (b) variation in total arclength L across each simulation for varying $\lambda \in [1, 10^4]$, and (c) convergence in the range of L as λ increases.

values chosen from a logarithmic scale. Simulations with $N \lessapprox 90$ did not converge due to underrefinement of the auxiliary equation leading to violation of the inextensibility constraint. Such cases are omitted from consideration in the following results.

Figures 4.4a and 4.4b indicate the effect of increasing spatial refinement upon simulated swimming dynamics. The final flagellum configuration from simulations with $N = 501$ (blue line) and $N = 91$ (orange line) nodes respectively is displayed in figure 4.4a, illustrating that coarsely discretised cells can exhibit underresolved dynamics, particularly in the distal $s > 0.6$ region, despite convergence of the numerical method. Note that the cell bodies in each simulation are omitted from the plot for clarity. The relative error in the final $\boldsymbol{X}_0$ coordinate between each varied-N simulation and the highest resolution ($N = 501$) simulation is presented in figure 4.4b, indicating that relative errors are small $\leqslant 1\%$ for $N \gtrapprox 151$. Motivated by these results, in all subsequent

simulations, unless otherwise stated, we choose $N = 201$.

We additionally consider the effect of varying the inextensibility parameter λ for a swimming cell. The problem is setup exactly as before, but fixing $N = 201$ and varying $\lambda \in [1, 10^4]$ between multiple simulations. Results are presented in figures 4.4b and 4.4c. Despite an adequately refined flagellum discretisation, insufficiently large values of λ lead to undesirable growth in the total arclength L, up to $\approx 2\%$, as shown in figure 4.4b. Maximum extension occurs at moments of extreme dynamics, in particular at the moment when the distal flagellum changes direction. In figure 4.4c, the absolute difference between the maximum and minimum recorded total arclength values for each simulation are presented, indicating that $\lambda \geqslant 100$ is sufficient to ensure that the total arclength never varies by more than $\approx 0.25\%$. The size of this range will be affected by choices of S and $\mathcal{M}_2$, both of which will alter the cell dynamics. To this end, to ensure filament inextensibility in a range of scenarios, all subsequent simulations will use $\lambda = 200$ unless otherwise indicated.

4.3.4 Temporal stability

In the following section, we briefly assess the temporal stability of the SPX method. Here, the method is labelled *stable* if, for a given value of Δt, the nonlinear solver converges. A "brute force" approach is used, whereby stability regions are found through repeated simulation runs, changing the time step on each run and noting which simulations succeed or fail. Analytical methods were not attempted due to the complexity of the SPX model, confounding the construction of eigenvalue problems or analytical linearisations required for such techniques. Moreover, a full analysis of the stability of the method was deemed outside the scope of the present work, but remains an avenue

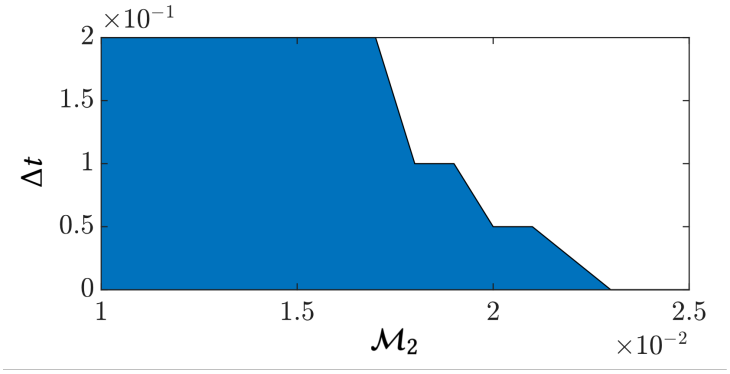

Figure 4.5: Measuring the temporal stability of the SPX framework applied to a planar swimming sperm cell characterised by $\mathcal{S} = 14$. Increasing actuation parameter $\mathcal{M}_2$ produces larger amplitude bending deformations, requiring smaller time steps Δt to ensure a temporally stable result. Simulations lying within the shaded region above are stable and numerical solutions can be found.

of potential future study.

As described in section 4.2.7, the system of nondimensionalised PDEs comprising the model (see section 4.2.6) are numerically discretised in time using an implicit Euler method. Thus, we expect solutions to be $\mathcal{O}(\Delta t)$ accurate in time. In order to ascertain suitable choices for Δt for use in subsequent problems, we simulate planar swimming sperm cells, characterised by $\mathcal{S} = 14$ with a variety of actuation parameters $\mathcal{M}_2$. For a fixed choice of swimming parameter, increasing the value of the actuation parameter yields more dynamic cells exhibiting larger amplitude flagellar bending; examining performance in these cases thereby increases understanding of the stability of the numerical method across a variety of setups.

For each $\mathcal{M}_2 \in [0.01, 0.025]$, the simulation is initially attempted using the largest considered time step $\Delta t_0 = 0.02$. Using the MATLAB® `try` and `catch` functions, should the simulation fail it is repeated using $\Delta t_{n+1} = \Delta t_n/2$ with $n = 1, \ldots$, until the code successfully completes. The critical value of Δt allowing the simulation to complete is thus

marked as sufficient for the given $(\mathcal{S}, \mathcal{M}_2)$ parameter pair. Results of this procedure are presented in figure 4.5. Simulations lying within the shaded region are temporally stable and solutions can be found. In the region $\mathcal{M}_2 > 0.022$, actuation parameters are too large for the selected $\mathcal{S} = 14$ value, producing a self-intersecting flagellum, violating the model and causing the code to exit without solving regardless of time step used. In the remaining white region above the critical line, temporal instability results in nonconvergence in the nonlinear iterative solver. From the results in figure 4.5, more dynamic swimming cell problems require smaller time step values in order to solve. For all but the most dynamic problems, $\Delta t = 5 \times 10^{-2}$ is sufficient in this problem for stability of the implicit Euler method. In practice, issues are easily identified as any potential nonconvergence arising from temporal instability often occurs within the first few time steps of the numerical solve regardless of initial condition or time step size, allowing rapid reselection of a new, smaller time step.

The backwards Euler method implemented here is desirable in that it can be applied easily and consistently to all time derivatives of variables across the model equations (summarised in (4.2.6)). Higher-order schemes, such as the Crank-Nicolson method, require greater care to implement and can significantly increase the complexity of the temporally discretised model and associated numerical implementation. By choosing the time step as $\Delta t = 5 \times 10^{-2}$ in conjunction with a tolerance of $\tau = 10^{-4}$ for the nonlinear iterative solver, converged solutions at each time step are obtained in between 2 and 5 iterations for the aforementioned planar beating problem; a simulation of a swimming cell across 5 beat cycles thus takes approximately 10 minutes on an Apple M1 Macbook Pro (2021 model). With the typical runtime tractable, the first-order temporal scheme currently used is considered adequate, with the implementation of higher-order schemes left as potential future work (see section 4.5 for additional dis-

cussion of future improvements to the SPX model).

4.4 Three dimensional swimming with twist and bend elasticity

In the following section we employ the SPX method as described in section 4.2 to simulate human sperm cells swimming with nonplanar beats. In section 4.4.1 we consider cells swimming with a 'twist and bend' beat, examining viable parameter choices to produce progressive swimmers. In section 4.4.2 we consider the effects on flagellum geometry and swimming performance when progressing over and towards an infinite plane wall.

4.4.1 'Twist and bend' beating

Bending moments within the flagellum arise from systematic rhythmic engaging and disengaging of dynein arms within the 9+2 axoneme. Early experimental imaging of hamster spermatozoa highlighted the complex three-dimensional geometry arising from the development of torsion within the flagellum axoneme (Woolley & Osborn, 1984; Yeung & Woolley, 1984). Subsequent studies have observed that, particularly in the absence of solid boundaries, sperm exhibit complex nonplanar beats, causing cells to roll and follow curved trajectories (Woolley, 2003; Simons *et al.*, 2015). Previous modelling approaches, with prescribed waveform flagella or no-twist bending models, have approximated idealised helical beats by applying internal active moments acting about the cross-sectional $\mathbf{d}_1, \mathbf{d}_2$ directions of the flagellum. Assuming a sliding filament model for actuation, the asymmetry of the axoneme due to the central pair suggests that this is unlikely to be the true physical mechanism by which helical beat patterns arise in motile sperm. With the exact mechanisms resulting in bending within the axoneme still mysterious (see section 1.1.1 for details), it can be reasonably assumed

that in generating a bending moment, the internal actuating motors may also give rise to some degree of twisting moment. It is then a combination of active bending and twisting that results in the nonplanar flagellar waveform propelling the cell. Active twisting can be modelled in the SPX framework by setting $\mathcal{M}_3 > 0$ and choosing a suitable scalar function of arclength for $m_3(s)$, the active twist moment per unit length.

Generation of a viable progressive beat depends greatly on the values of the dimensionless groups $\mathcal{S}, \mathcal{M}_3$ and Γ_d. In the latter case, by recalling that $\xi_R \approx 4\pi\mu a^2$ (where a is the radius of the flagellum) and assuming $a \approx L/100$, an approximate value for Γ_d can be obtained as

$$\Gamma_d \approx \frac{\mu L^2}{4\pi\mu a^2} = \frac{L^2}{4\pi(L/100)^2} \approx 10^4, \tag{4.72}$$

motivating choices for $\Gamma_d \in [10^3, 10^5]$. The stiffness ratio $\Gamma_s = C/E^d$ is assumed to be constant along the flagellum and, in lieu of empirical measurements of sperm flagellum stiffness values, we choose $\Gamma_s = 4$ i.e. the flagellum is assumed to be four times resistant to twist deformations than to bending deformations at the distal tip. Experimental values for the stiffness parameters Γ_s, Γ_d are not known; indeed, due to the difficulty of imaging in particular cells swimming in three dimensions, and in general capturing the flagellum with any reasonable clarity, values are unlikely to be determined through experimental procedures for some time. Rather, experimentation *in silico* and subsequent comparison to experimental images and videos is much more likely to yield approximate realistic values for these parameters. Such comparison is outside the scope of this thesis; here, we select values that produce actuation patterns qualitatively similar to those seen through the microscope.

Despite this uncertainty, in practice, simulation results are largely insensitive to the choice of Γ_s, with the values of $\mathcal{S}$ and Γ_d dominating the dynamics. Variations in

varying stiffness arclength threshold value s^d (see equation (2.75)) additionally alter the envelope of the developing beat. In what follows, we choose $s^d = 0.5$ unless otherwise stated.

As the nonplanar beat develops, nonlocal hydrodynamic interactions between the proximal and distal flagellum can promote unpredictable dynamics. In the passive end piece, the shape of which is not directly driven by any active internal bending or twisting moments, this can result in flagellum self-intersection, particularly in viscous-dominated (i.e. large $\mathcal{S}$) regimes where fluid effects are dominant over elasticity. With this in mind, we consider problems characterised by lower values of $\mathcal{S}$, so that flagellar shapes are influenced more by elasticity, allowing for greater control of the simulated beats. Unless otherwise declared, we fix $\mathcal{S} = 12$ across all simulations.

In what follows, we perform a systematic parameter sweep in order to determine values which yield progressive swimming cells. The bending and twist moment per unit length are chosen as trigonometric functions of arclength as

$$m_1(s) = 0, \tag{4.73a}$$

$$m_2(s) = \cos(ks - t)\, H(1 - \ell - s), \tag{4.73b}$$

$$m_3(s) = -\cos(ks - t)\, H(1 - \ell - s), \tag{4.73c}$$

for $0 \leqslant s \leqslant 1$, where k is the dimensionless wave number for the bending and twist actuating travelling waves. The Heaviside functions $H(s)$ account for the presence of the passive distal end piece. In assuming the twisting moment arises from the same mechanical process which generates the bending moment, we assume both travelling waves are defined with the same wave number. The dimensionless length of the end piece is fixed across all simulations at $\ell = 0.05$.

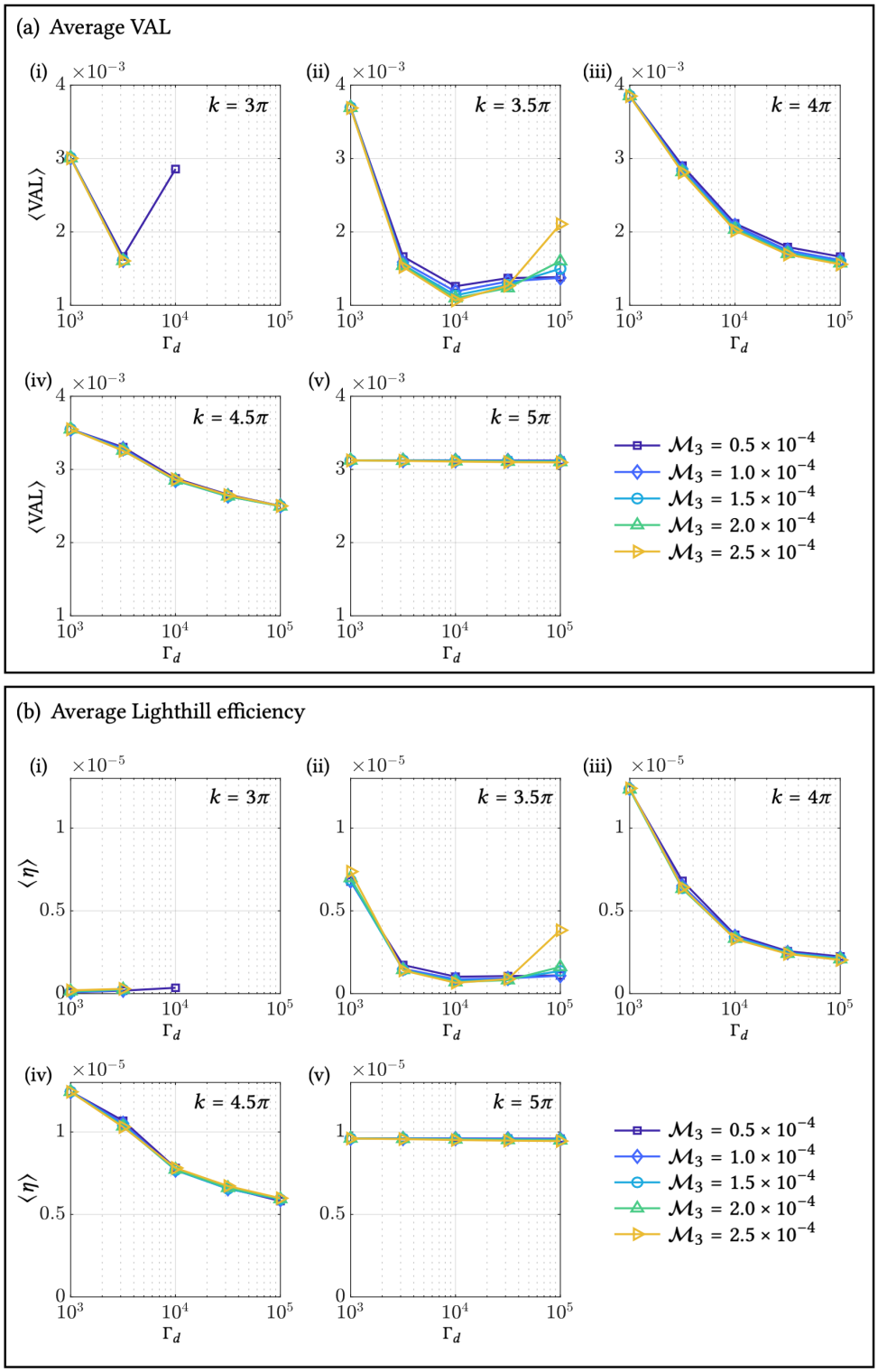

Figure 4.6: Average (a) VAL and (b) Lighthill efficiency of cells actuated with a twist and bend beat, characterised through wave numbers $k \in [3\pi, 5\pi]$, drag ratios $\Gamma_d \in [10^3, 10^5]$ and twist actuation parameters $\mathcal{M}_3 \in [0.5, 2.5] \times 10^{-4}$.

The flagellum is discretised using $N = 251$ equally-spaced points along the centreline. The ellipsoidal body is assumed to have mean dimensions as reported by Sunanda *et al.* (2018) (values in table 3.1), and its surface is discretised through a cubic projection method using $H_t = 4$ and $H_q = 8$ nodes per face (see section 1.2.8 for details), yielding a traction discretisation of $M_t = 96$ nodes and a quadrature discretisation of $M_q = 384$ nodes. The time step is set at $\Delta t = 2\pi/60 \approx 0.1$ in accordance with the stability results in figure 4.5. Since the time step is chosen as a regular fraction of the beat period $T = 2\pi$, the simulated beats can be precisely sampled at regular intervals throughout each beat.

In each simulation, the cell is initialised with an exactly straight flagellum, so that the director frames are all parallel at $t = 0$, and point along the negative x-axis. Simulations are run over ten flagellar beats i.e. over $0 \leqslant t \leqslant 10T$, with $T = 2\pi$ the period of the actuating travelling waves, to ensure periodic nonplanar beating is established before sampling for results. The first cycle ($t \in [0, T]$) is considered a *warmup beat*, with $\mathcal{M}_2$ and $\mathcal{M}_3$ linearly increased over the period to smoothly accelerate the cell.

Across multiple repeated simulations, we vary the twist actuation parameter $\mathcal{M}_3$, the drag ratio Γ_d, and the wave number of actuation k, so as to consider a broad range of cells representing swimmers characteristic of differing viscosities (through $\mathcal{M}_3$ and k) and stiffness (through Γ_d). The velocity along a line (VAL, see equation 2.68), measured at the head-flagellum join $\boldsymbol{X}_0$, is computed across each beat period (after the warmup period) and averaged to obtain a measure, denoted $\langle \text{VAL} \rangle$ for the mean speed of the cell. The average Lighthill efficiency $\langle \eta \rangle$ is similarly computed over the same period. Results are displayed in figure 4.6. Altering parameters has a similar effect on both VAL and η results. Cell speed and efficiency is largely unaffected by choices of $\mathcal{M}_3$, with little appreciable variation in values upon changes in actuation parameter

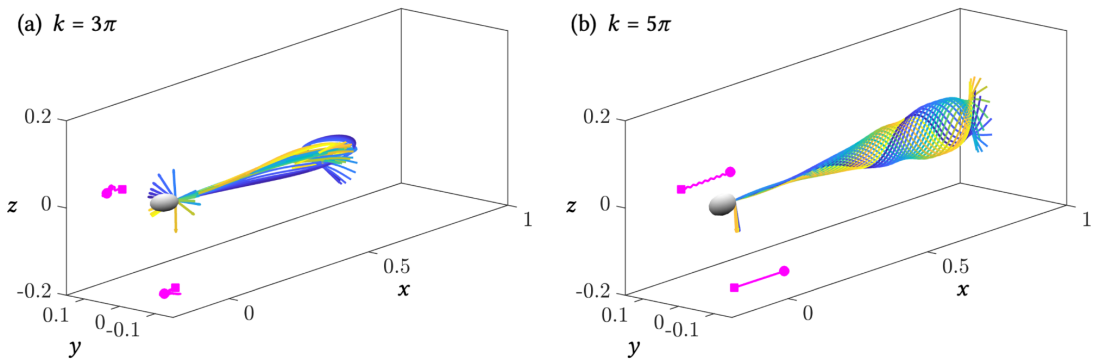

Figure 4.7: Flagellar traces across a single beat, plotted relative to the head-flagellum join position $\boldsymbol{X}_0$ for cells characterised by $\mathcal{M}_3 = 5{\times}10^{-5}$ and $\Gamma_d = 10^4$, for wave numbers (a) $k = 3\pi$ and (b) $k = 5\pi$. Relative trajectories of $\boldsymbol{X}_0$ over the full simulation are indicated by projections in magenta onto the xy and xz planes. Arrows at $\boldsymbol{X}_0$ indicate the rolling of the cell body across the considered beat.

across the range $[5 \times 10^{-5}, 2.5 \times 10^{-4}]$. For intermediate values of $k \in [3.5\pi, 4.5\pi]$, reductions in speed and efficiency are observed as drag ratio Γ_d, a pseudo-analogue for flagellum stiffness, is increased. This degradation occurs as the cell transitions from planar beating at low values of Γ_d to nonplanar beating as Γ_d increases (discussed further later on). For extremes $k = 3\pi, 5\pi$, the aforementioned trends in $\langle \text{VAL} \rangle$ and $\langle \eta \rangle$ are not observed. Missing values in the plots of figures 4.6 and 4.8 correspond to the $k = 3\pi$ case, where extreme flagellum curvature causes self intersection and the simulation terminates. When $k = 5\pi$, the short wavelength of the active twist moment does not produce nonplanar motion, with the beat remaining planar across the simulation. Examples of cells exhibiting both these behaviours are given in figure 4.7.

Depending on the stiffness of the flagellum, the cell either (a) progresses with a beat approximately confined to a plane through the nearly-parallel $\mathbf{d}_1$ directors, or (b) develops a nonplanar beat, which initiates rolling about its long axis. By rotating the cell head frame at each instant so that $\mathbf{d}_3(0)$ and $\mathbf{e}_1$ are parallel, the angle between $\mathbf{d}_1(0)$

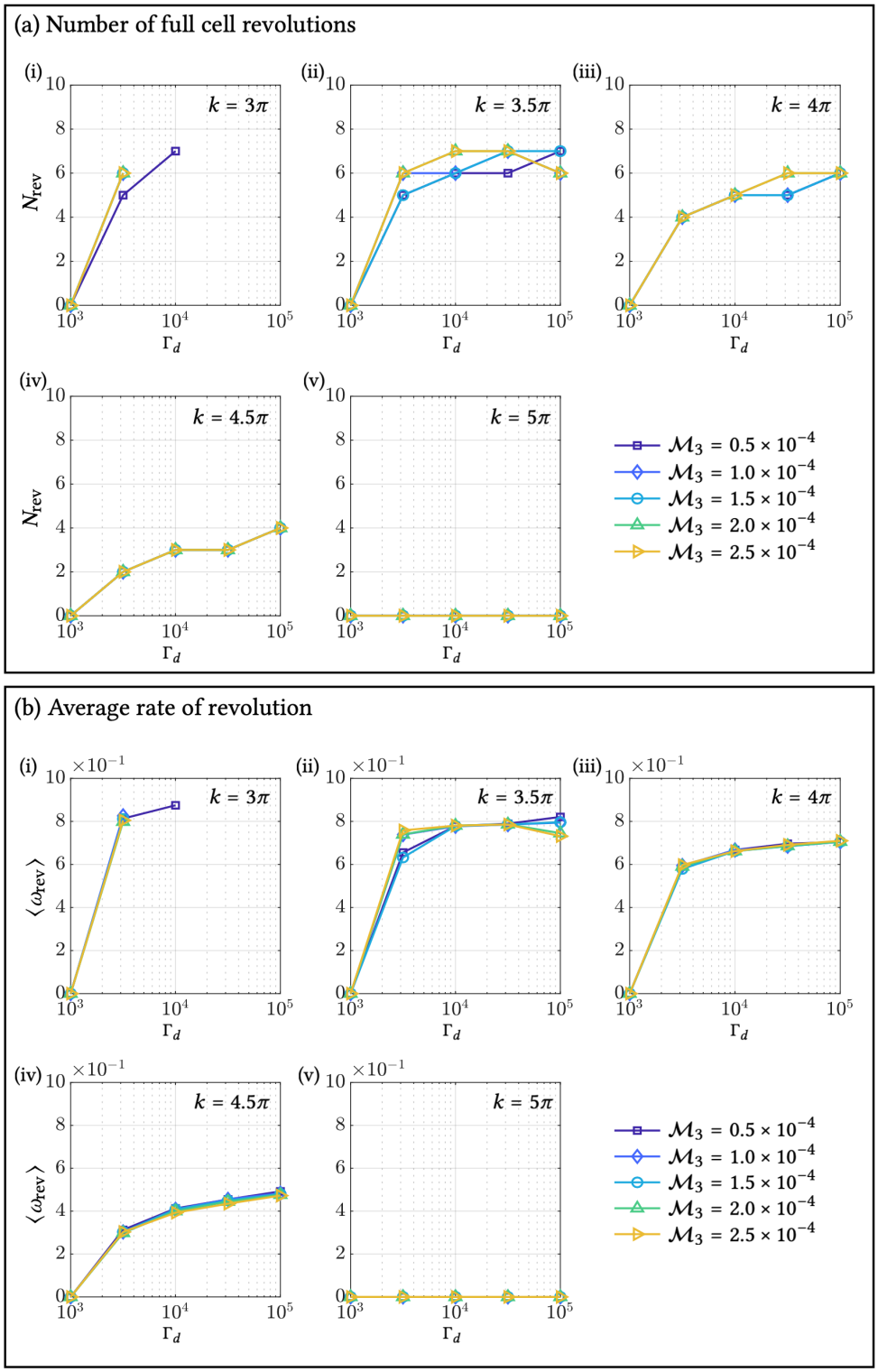

Figure 4.8: Effects of varying twist drag ratio Γ_d, twist actuation parameter $\mathcal{M}_3$, and actuation wave number k on (a) the number of full axial cell revolutions N_{rev} over a ten beat period, and (b) average rate of revolution $\langle \omega_{\text{rev}} \rangle$. In both cases, a zero value indicates no axial rolling motion.

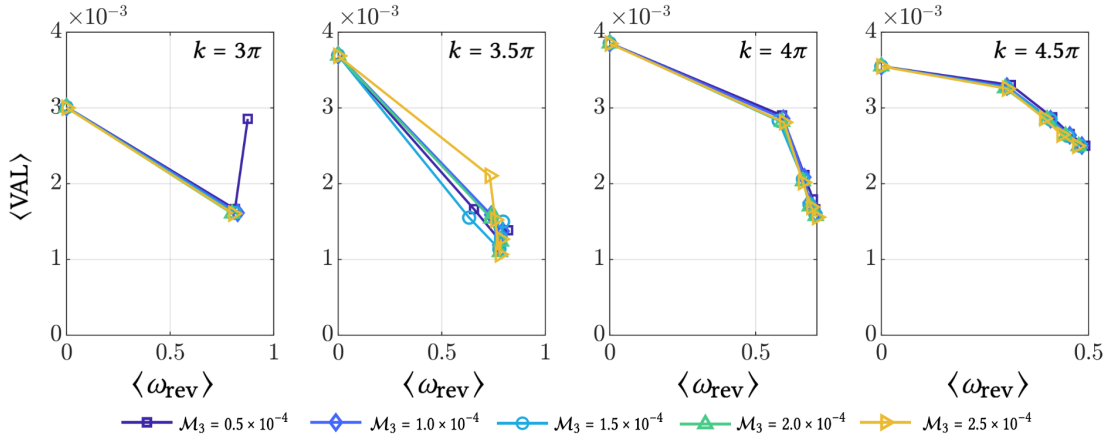

Figure 4.9: Relationships between mean rate of axial revolution $\langle \omega_{\text{rev}} \rangle$ and average VAL, for varying wave numbers $3\pi \leqslant k \leqslant 4.5\pi$ and twist actuation parameters $\mathcal{M}_3$. Simulations with $k = 5\pi$ are excluded since no cell rolling occurs.

and $\mathbf{e}_3$ can be determined, and thus the number of full 2π rotations of the head can be counted. The rate of axial rolling of the cell, measured over the j^{th} revolution, is calculated as

$$\omega_{\text{rev}}^{(j)} = \frac{2\pi}{T_{\text{rev}}^{(j)}}, \tag{4.74}$$

where $T_{\text{rev}}^{(j)}$ is the time taken for the cell to complete the j^{th} full rotation. These quantities can vary across the simulation, and so we additionally consider the mean axial rotational rate

$$\langle \omega_{\text{rev}} \rangle = \frac{1}{N_{\text{rev}}} \sum_{j=1}^{N_{\text{rev}}} \omega_{\text{rev}}^{(j)}, \tag{4.75}$$

where N_{rev} is the total number of revolutions the cell exhibits. Figure 4.8 examines the relations between the varied parameters Γ_d, k, $\mathcal{M}_3$, and the rolling behaviour of the cell. In these plots, a zero value indicates planar motion with no cell rolling having occurred. As observed in the relationships with cell VAL and efficiency, the value of $\mathcal{M}_3$ has little effect on the amount or rate of revolution of the cell. When $\Gamma_d = 10^3$, the

cell beats in a planar manner and does not roll. As Γ_d increases for $k < 5\pi$, nonplanar motion develops and cells roll about their long axis between 3 and 9 times over a ten beat period. The periodic nonplanar beat takes a number of beat periods to establish, accounting for the difference in the number of simulated beats and the number of cell revolutions. The maximum number of revolutions decreases as k increases; when $k = 5\pi$, no nonplanar motion arises and thus zero revolutions are recorded (see figure 4.7). Within each k case, the number of revolutions increases as Γ_d increases. Similar trends are observed in the relationship between Γ_d, k, and $\langle \omega_{\text{rev}} \rangle$, the average rate of revolution. As Γ_d increases beyond 10^3, $\langle \omega_{\text{rev}} \rangle$ initially increases with Γ_d before plateauing to a value between 0.4 and 0.8 depending on the choice of k. Larger k values exhibit a lower maximum $\langle \omega_{\text{rev}} \rangle$ value, and vice versa.

Neglecting the trivial $k = 5\pi$ case, by plotting the mean rate of revolution $\langle \omega_{\text{rev}} \rangle$ against the average VAL (figure 4.75), we note that the average VAL decreases as the rate of axial revolution increases, a trend observed for each choice of actuation wave number k and twist parameter $\mathcal{M}_3$ (discounting the anomalous result in the first panel of figure 4.9). Taking together the trends in figures 4.6, 4.8 and 4.9, we can determine that increases in drag ratio Γ_d yield nonplanar swimming, leading to cell rolling that decreases swimming speed as measured through VAL.

The three-dimensional cell shape is examined by considering the trace the flagellum, moving from yellow through to blue over the final beat period. In figures 4.7, 4.10, we consider motion relative to the position of the head-flagellum join $\boldsymbol{X}_0$ so that the cell appears not to progress (though we stress that the cells *in silico* are unconstrained). We refer to cells rendered in this approach as being viewed from the *fixed laboratory frame*. The cell body position at the beginning of the beat is drawn in greyscale. The coloured arrows radiating from $\boldsymbol{X}_0$ represent $\mathbf{d}_1(0)$ at each sampled time point, thus

giving an indication of the rolling of the cell about its long axis. Additionally, projections onto the xy- and xz-axis of the trajectory of $\boldsymbol{X}_0$ (relative to final position) across the entire simulation are shown through magenta lines, moving from the circled end to the squared end as t increases.

For the remainder of this section, we will consider only parameter combinations which yield progressive cells which do not self-intersect. In figure 4.10, we observe waveforms of pinned cells characterised by $k = 4\pi$ and $\mathcal{M}_3 = 1.5 \times 10^{-4}$, for a variety of drag ratios Γ_d. Cells are observed and flagella traced over their final simulated beat. For $\Gamma_d = 10^3$, the flagella beat remains approximately planar (figure 4.10a), with little deviation when observed from the xy-plane. Rotations to the cell head are predominantly xz-planar. Larger values for Γ_d reduce the effective resistance to twisting deformations, allowing nonplanar beats to develop. The subsequent axial rolling of the cell is indicated in figures 4.10b,c by the fan-like director vectors at $\boldsymbol{X}_0$. Body rotation is approximately confined to the xy-plane. Reading from figure 4.6a, the cell characterised with $\Gamma_d = 10^5$ (figure 4.10c) swims slower and is less efficient than the same cell with $\Gamma_d = 10^4$ (figure 4.10b), observable in figures 4.10b,c as a reduction in the length of the projected $\boldsymbol{X}_0$ trajectory. Comparing the planar projections of the waveform traces, increased distal curvature is apparent in figure 4.10c, potentially contributing to the reduction in efficiency (Neal *et al.*, 2020).

The geometry of an evolving nonplanar beat can be further understood by considering the flagellum shape relative to the motion of the cell body. At each time point, a rotation matrix mapping the orthonormal director frame of the head to the identity I^3 is determined and applied to the position vector of each flagellum coordinate. We refer to cells presented in this manner as viewed in the *fixed body/head frame*. The three dimensional trace and planar projections of the same cells considered in figure

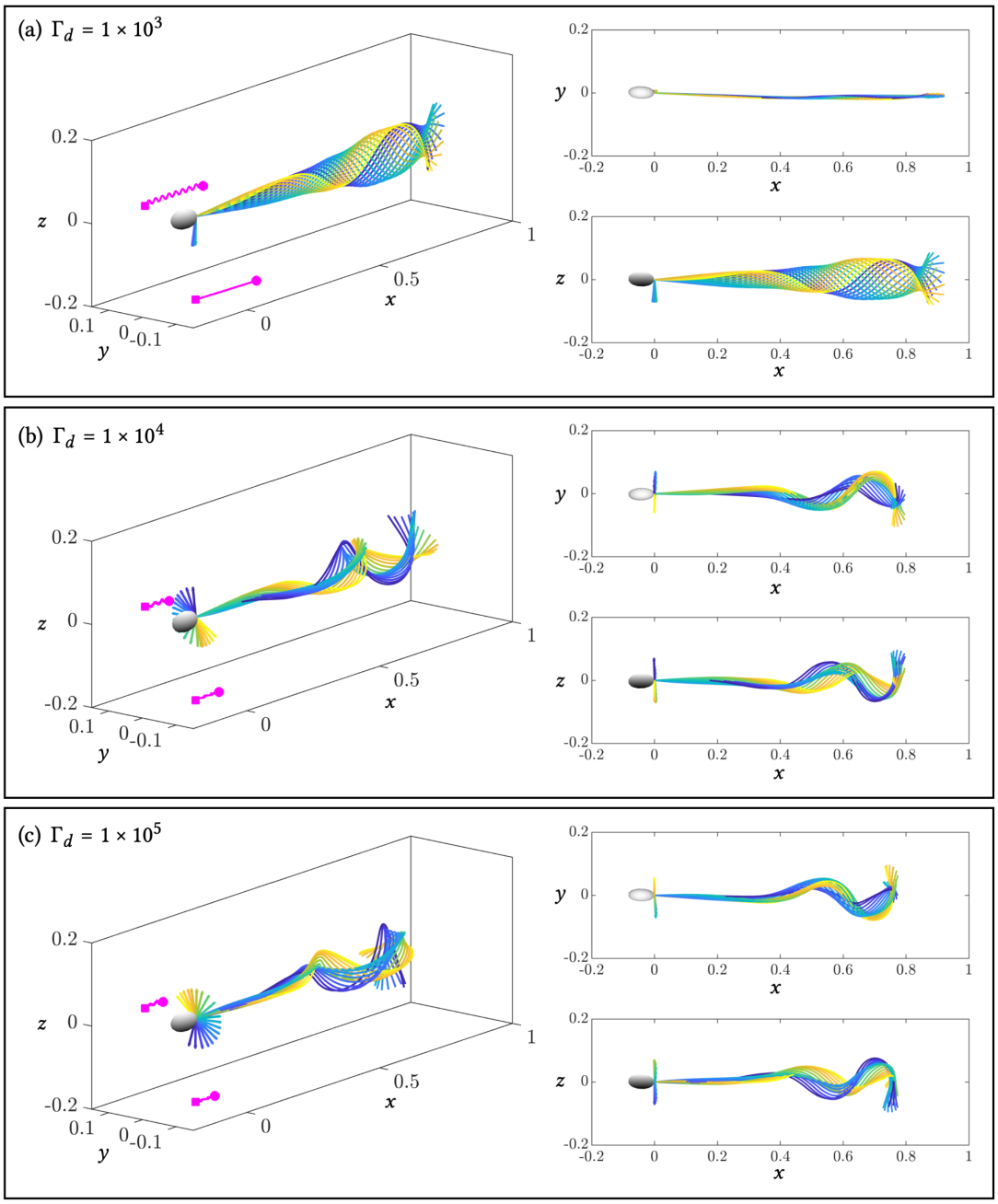

Figure 4.10: Effects of varying the viscous drag ratio Γ_d on nonplanar twist and bend beating. Cells are characterised by $k = 4\pi$, $\mathcal{M}_3 = 1.5 \times 10^{-4}$, and $\Gamma_d \in [10^3, 10^5]$. Flagellum motion is indicated by lines of blue through yellow, plotted relative to the head-flagellum join $\boldsymbol{X}_0$. Short arrows at $\boldsymbol{X}_0$ represent the roll of the cell over the beat. The head position at the start of the beat is drawn in greyscale. The trajectory of $\boldsymbol{X}_0$, projected onto the xy- and xz-planes, is indicated in magenta, moving from the circle through to the square marker.

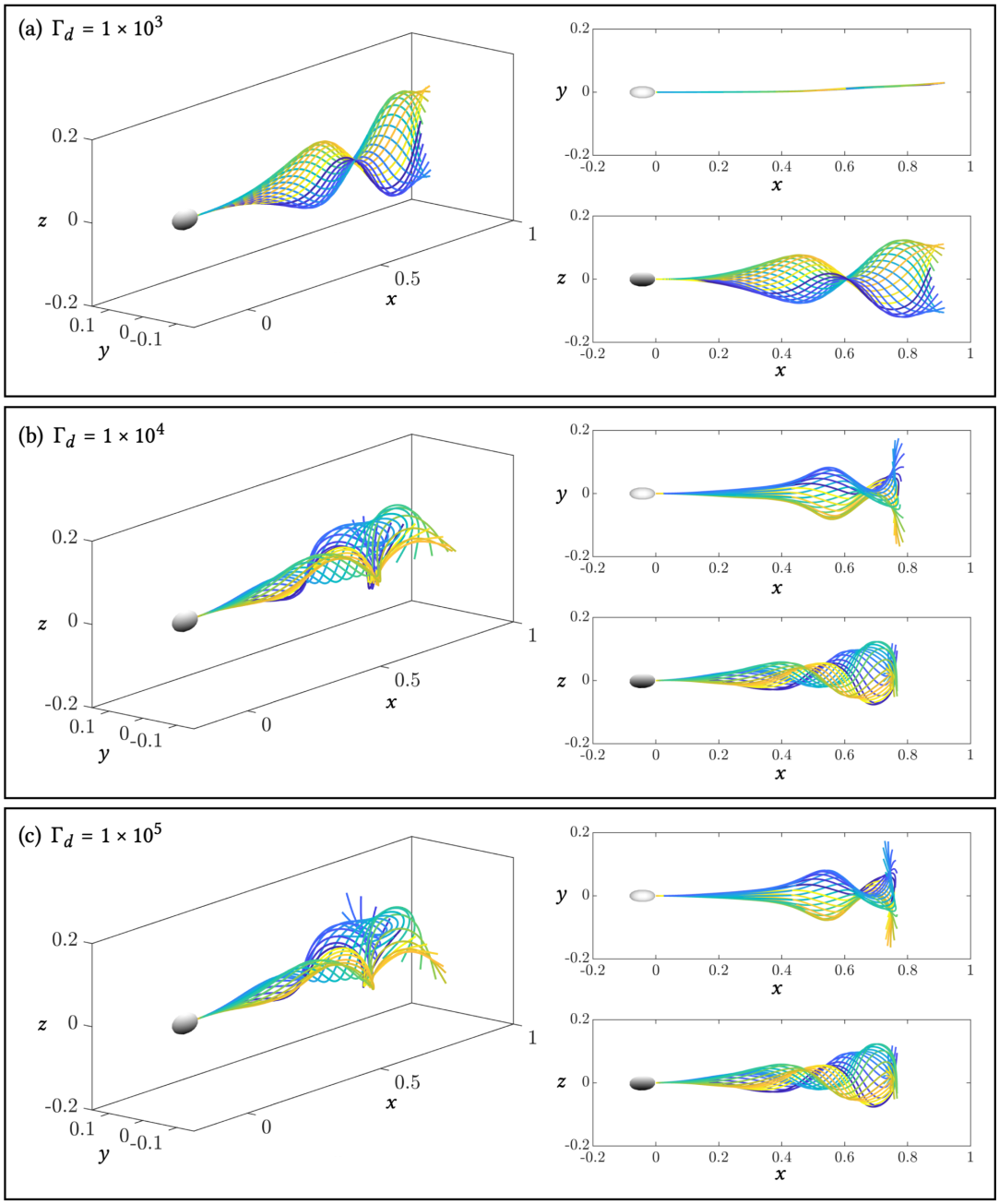

Figure 4.11: Effects of varying the viscous drag ratio $\Gamma_d \in [10^3, 10^5]$ on nonplanar twist and bend beating. Cells considered are the same as those in figure 4.10, but here plotted in a frame of reference which translates and rotates with the head.

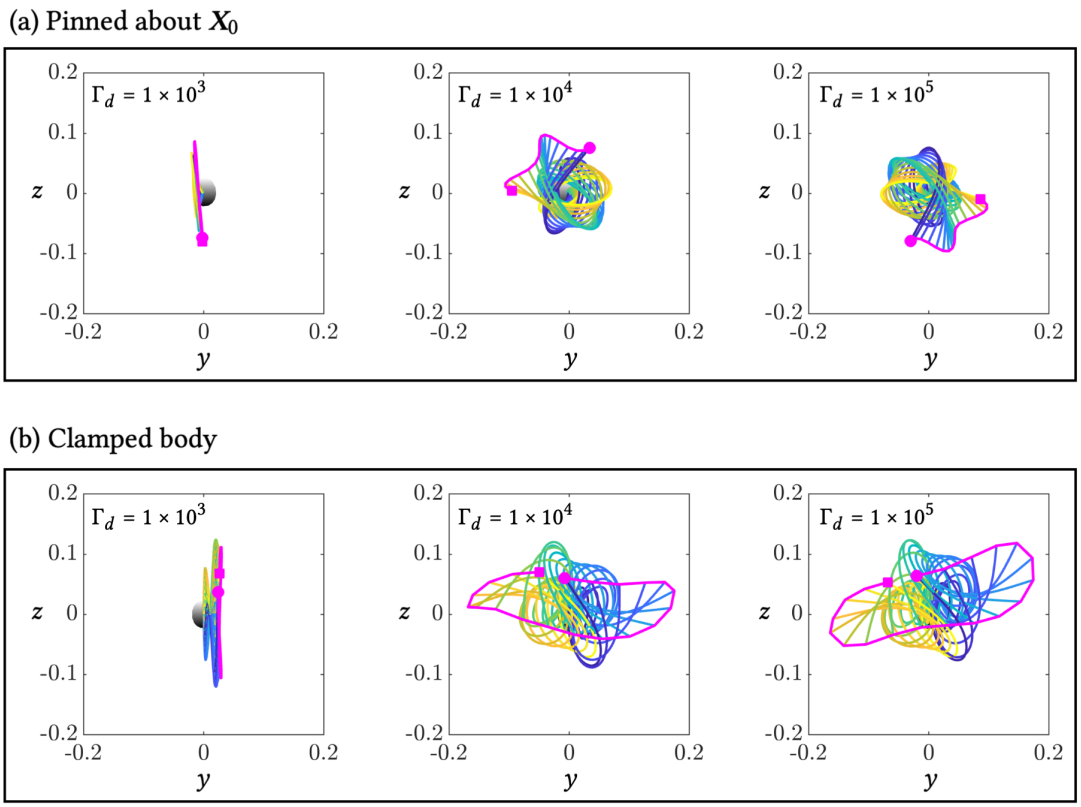

Figure 4.12: Cell traces across a single beat viewed from the yz-plane, relative to (a) the head-flagellum join $\boldsymbol{X}_0$ (in the fixed laboratory frame) and (b) the motion of the cell head (in the fixed head frame). Cells are identical to those considered in figures 4.10 and 4.11. The motion of the distal flagellum tip $\boldsymbol{X}(L)$ is superimposed in magenta, moving from the circular marker through to the square over the beat.

4.10 are presented in the body frame in figure 4.11. Viewed this way, the waveform arising from the cell with $\Gamma_d = 10^3$ (figure 4.11a) closely resembles planarly beating cells considered elsewhere in this thesis (chapters 2, 3), and in studies of planar swimming (Gadêlha *et al.*, 2010; Montenegro-Johnson *et al.*, 2015; Neal *et al.*, 2020). For the nonplanar cells (figures 4.11b,c), a clear distinction between the plane projections is apparent, in contrast to the beat projections in figure 4.10.

The periodicity of the nonplanar beats considered in figures 4.10 and 4.11 is further

examined through the trace of the distal flagellum tip $\boldsymbol{X}(L)$ over a single beat (figure 4.12). The trajectory is drawn in magenta, with the point following the path travelling from the circle-marked end to the square-marked end over a single period. When the beating is xz-planar, such as for $\Gamma_d = 10^3$, the distal trace moves in a vertical linear pattern. For the nonplanar cells, in the laboratory reference frame (figures 4.12b), $\boldsymbol{X}(L)$ appears to trace part of a larger geometric pattern (examined further shortly). Plotted in the fixed head frame, the trajectory is smoothed and approximately ellipsoidal.

Expanding to consider cell motion from the fourth beat onwards (qualitatively determined as a time by which a periodic nonplanar beat has been established), we see the complete geometric patterns traced by $\boldsymbol{X}(L)$ across each simulation. In figure 4.13, we consider the distal traces of cells characterised by $k = 4\pi$ and $\mathcal{M}_3 = 1.5{\times}10^4$, for various Γ_d, neglecting trivial planar trace generated when $\Gamma_d = 10^3$. For each cell, the yz-plane projection over time in both the fixed lab and head frames of reference is drawn. To the top-right of each trace, the y and z trajectory components as functions of time are plotted. To the bottom-right, absolute half-space of the discrete Fourier transform of the coordinate 'signals' is plotted, computed using the MATLAB® fft built-in function. Qualitatively, in the laboratory frame, the distal tip traces trace star-like patterns, with the number and smoothness of the peaks dependent on Γ_d. The projected components form noisy sinusoidal curves with a period of $\approx 2\pi$, matching the period of the actuating bending and twist waves. Viewed in the fixed body frame, the distal tip traces a flattened ellipsoid, with the ellipsoid tips become more rounded as Γ_d increases. In this frame, the projected components are similarly sinusoidal in appearance but have wavelength $\approx \pi$.

Both y and z Fourier signals exhibit peaks at the same frequencies, differing only in amplitude. The frequency associated with these peaks is determined using the

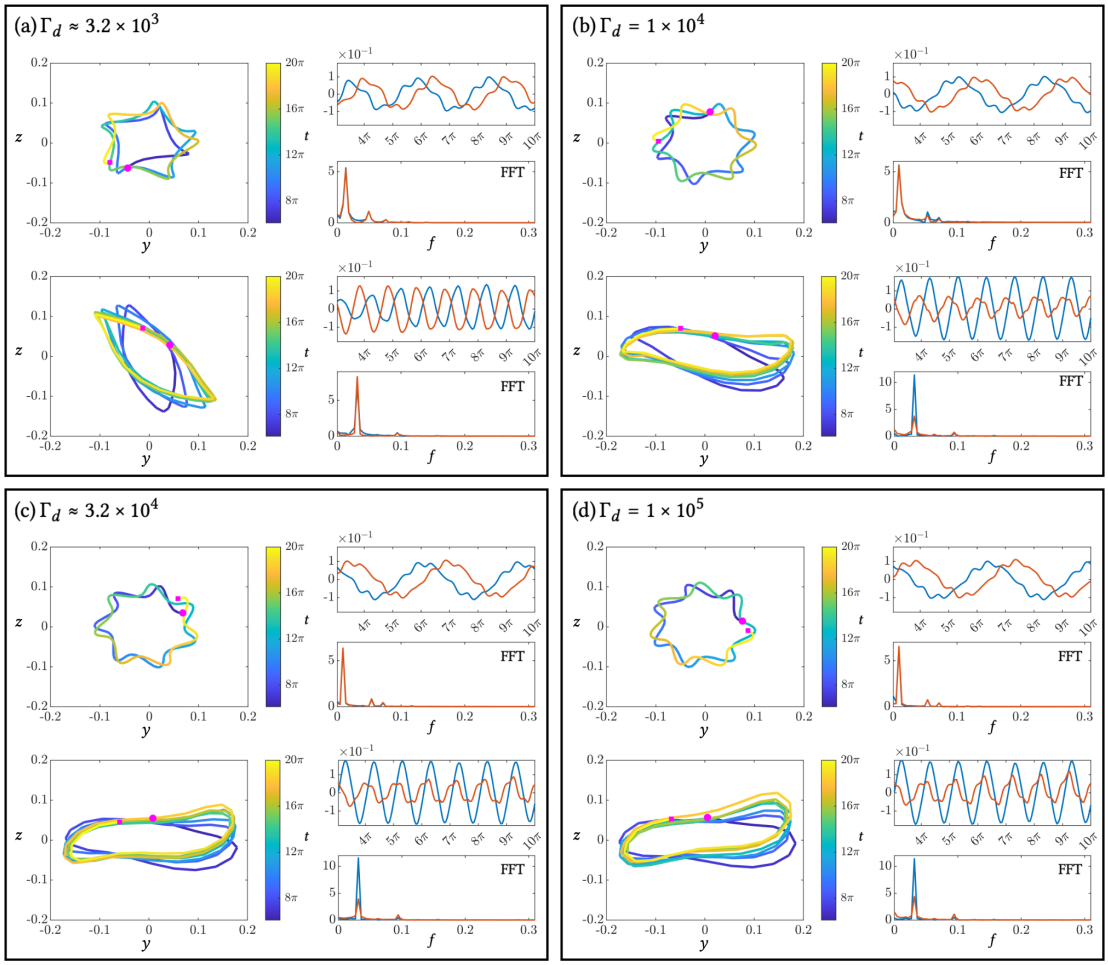

Figure 4.13: Trace of the distal flagellum tip across established nonplanar beats, projected onto the yz-plane and considered relative to $\boldsymbol{X}_0$ (top plots) and to the fixed body frame (bottom plots) in each panel. The start and end of the traces are indicated by magenta circles and squares respectively. To the top-right; the y (blue line) and z (orange line) components of the projected trace against time. To the bottom-right; the ones-sided absolute discrete Fourier transform of the y trace (blue) and z trace (orange). Cells considered are characterised by parameters $k = 4\pi$ and $\mathcal{M}_3 = 1.5 \times 10^4$, with viscous drag ratio Γ_d varied between panels.

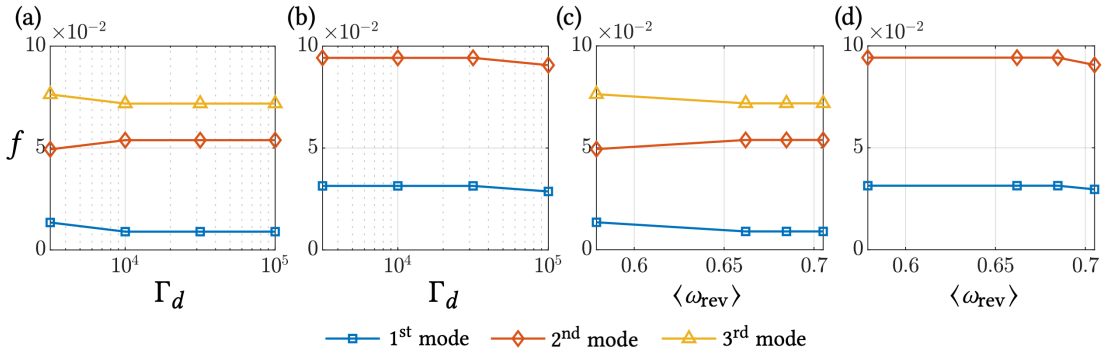

Figure 4.14: Effects of varying the drag stiffness ratio Γ_d and cell mean rate of revolution $\langle \omega_{\mathrm{rev}} \rangle$ on the frequency of the distal flagellum tip Fourier modes (plotted in figure 4.13), as viewed from (a,c) the fixed laboratory frame, and (b,d) the fixed head frame, which rotates with the motion of the cell.

MATLAB® `findpeaks` function, with the detection threshold chosen as 0.1. This analysis reveals the existence of three dominant frequencies in the lab frame signal, and two in the body frame signal. The additional signal arises from the global rotation of the cell, a dynamic captured in the laboratory frame plots but absent by definition from the head frame cell trajectories. In the laboratory frame, the frequencies of the Fourier modes remain approximately constant regardless of the choice of Γ_d and value of ω_{rev}, with approximate values 0.015, 0.05 and 0.075 (see figure 4.14). Viewed relative to the body motion, the two characteristic frequencies are approximately 0.03 and 0.095. The near-invariance in the characteristic Fourier mode frequencies of the distal flagellum tip trajectory with respect to the drag ratio Γ_d suggests that the periodic motion is not determined by the elastic twist resistance, but instead regulated by hydrodynamic interactions, provided that the value of Γ_d is sufficiently large to lead to nonplanar beating in the first instance.

4.4.2 Nonplanar beating over an infinite wall

Of particular interest is understanding how cells modulate or alter their beating upon approaching a planar wall. Previous studies have focused on planar beats (Montenegro-Johnson *et al.*, 2015; Walker & Gaffney, 2021a), or used prescribed-beat models for the cell flagellum (Smith *et al.*, 2009a); the SPX model allows for simulation of full three-dimensional elastohydrodynamic beating to be considered, with nonlocal interactions between the wall and flagellum affecting the cell geometry. In this section we describe the changes required to the SPX framework to accommodate a rigid boundary, and present some example simulations of cells approaching a plane wall.

The equation for the dimensionless hydrodynamic velocity of the flagellum, via the method of regularised stokeslets, can be extended to account for the presence of the wall as

$$\mathcal{S}^4\boldsymbol{X}_t = \frac{\mu}{\xi_\perp}\big(I + (\gamma-1)\boldsymbol{X}_s\boldsymbol{X}_s\big)\cdot\boldsymbol{f} + \int_{|s-s'|>q} \boldsymbol{S}^\varepsilon\big(\boldsymbol{X}, \boldsymbol{X}(s')\big)\cdot\boldsymbol{f}(s')\,ds' + \iint_{\partial B} \boldsymbol{S}^\varepsilon\big(\boldsymbol{X}, \boldsymbol{Y}\big)\cdot\boldsymbol{\varphi}(\boldsymbol{Y})\,dS_Y + \iint_{\partial W} \boldsymbol{S}^\varepsilon\big(\boldsymbol{X}, \mathbf{x}\big)\cdot\boldsymbol{\psi}(\mathbf{x})\,dS_{\mathbf{x}}, \quad (4.76)$$

where $\boldsymbol{X}$ are nodes along the flagellum, $\boldsymbol{Y}$ are material points on the surface of the cell head, and $\mathbf{x}$ are material points on the surface of the boundary wall; $\boldsymbol{f}$ is the force per unit length the flagellum exerts onto the surrounding fluid; similarly $\boldsymbol{\varphi}$ and $\boldsymbol{\psi}$ are the forces per unit area exerted onto the fluid by the cell body and wall respectively. However, as discussed in section 1.2.5, the stokeslet does not accurately capture the hydrodynamic effects of the presence of the boundary wall, motivating the use of regularised blakelets in place of regularised stokeslets. Derived by Ainley *et al.* (2008), the

regularised blakelet is defined

$$B_{ij}^{\varepsilon}(\mathbf{x},\mathbf{y}) = \frac{\delta_{ij}(r^2+2\varepsilon^2)+r_i r_j}{r_\varepsilon^3} - \frac{\delta_{ij}(R^2+2\varepsilon^2)+R_i R_j}{R_\varepsilon^3} + 2h\Delta_{jk}\left(\frac{\partial}{\partial R_k}\left\{\frac{hR_i}{R_\varepsilon^3} - \frac{\delta_{i3}(R^2+2\varepsilon^2)+R_i R_3}{R_\varepsilon^3}\right\} - 4\pi h\delta_{ik}\phi_\varepsilon(R)\right) - \frac{6h\varepsilon^2}{R_\varepsilon^5}(\delta_{i3}R_j - \delta_{ij}R_3), \quad (4.77)$$

where $r_\varepsilon = \sqrt{r^2+\varepsilon^2}$, $R_\varepsilon = \sqrt{R^2+\varepsilon^2}$ and

$$\Delta_{jk} = \begin{cases} +1 & j=k=1,2, \\ -1 & j=k=3, \\ 0 & \text{otherwise} \end{cases}. \quad (4.78)$$

The blob function in equation (4.77) is chosen as $\phi_\varepsilon(R) = 3\varepsilon^2/(4\pi R_\varepsilon^5)$, modified to decay more slowly than the analogous function ϕ_ε in the regularised stokeslet (see section 1.2.6 for details).

Replacing the regularised stokeslet kernel with regularised blakelets, the hydrodynamic velocity of the flagellum can be thus written as

$$\mathcal{S}^4\boldsymbol{X}_t = \frac{\mu}{\xi_\perp}\big(I+(\gamma-1)\boldsymbol{X}_s\boldsymbol{X}_s\big)\cdot\boldsymbol{f} + \int_{|s-s'|>q}\boldsymbol{B}^{\varepsilon}\big(\boldsymbol{X},\boldsymbol{X}(s')\big)\cdot\boldsymbol{f}(s')\,ds' + \iint_{\partial B}\boldsymbol{B}^{\varepsilon}\big(\boldsymbol{X},\boldsymbol{Y}\big)\cdot\boldsymbol{\varphi}(\boldsymbol{Y})\,dS_Y + \iint_{\partial W}\boldsymbol{B}^{\varepsilon}\big(\boldsymbol{X},\mathbf{x}\big)\cdot\boldsymbol{\psi}(\mathbf{x})\,dS_{\mathbf{x}}, \quad (4.79)$$

The nonlocal contribution to the flagellar velocity $\boldsymbol{V}$ (equation (4.52e)), which appears in the elastohydrodynamic equation (4.52a), auxiliary equation (4.52b) and twist equation (4.52f), is similarly extended, with the kernels of the integrals replaced by regu-

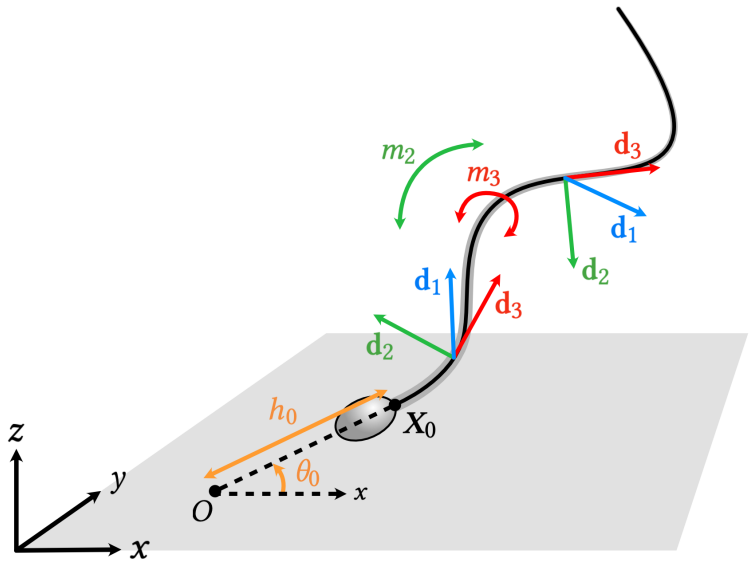

Figure 4.15: Sketch of the problem setup considered in section 4.4.2. The cell is initialised at a distance h_0 and at an angle θ_0 (relative to the x-axis) above the $z = 0$ plane, which is an infinite plane solid wall. Active bending and twisting moments per unit length m_2, m_3 respectively produce a nonplanar waveform which is hydrodynamically influenced by the proximal wall. The orthonormal triad $\{\mathbf{d}_1, \mathbf{d}_2, \mathbf{d}_3\}$ describes the orientation of the cross section at each point along the flagellum centreline.

larised blakelets.

In the resulting discretised system, blakelet integrals are treated using a nearest neighbour discretisation in the same way as the previous regularised stokeslet integrals, as described in section 1.2.8. The unknown forces $\boldsymbol{\Psi}[n] := \boldsymbol{\psi}[n]dS(\mathbf{x}[n])$, with $n = 1, \ldots, P$, are treated as unknowns of the resulting linear system alongside the forces per unit length $\boldsymbol{f}$ and forces $\boldsymbol{\Phi}$ (define in equation (4.69)). The matrix in equation (4.66) similarly expands to accommodate the additional degrees of freedom for the wall. The process for solving and iterating the problem is the same as described in section 4.2.7.

A number of individual cells are simulated swimming with nonplanar beats towards an infinite plane solid boundary $z = 0$. The flagellum is initialised as a straight

line (so that all tangent directors $\mathbf{d}_3$ are parallel at $t = 0$), lying within the xz-plane, and at an angle θ_0 (with respect to the x-axis) pointing towards the wall. In what follows, we refer to θ_0 as the *incidence angle*. Cells are initialised so that the head-flagellum join $\boldsymbol{X}_0$ is a distance h_0 from the origin i.e. $\boldsymbol{X}_0 = (h_0 \cos\theta_0, 0, h_0 \sin\theta_0)$. We choose $h_0 = 0.25$ so that the cell is in close proximity of the wall within a reasonable number of beats. In total, we simulate 40 beats. The starting orientation is such that the director vectors $\mathbf{d}_1$ lie in the xz-plane. Note that the initial inclination due to $\theta_0 > 0$ means they are not perpendicular to the boundary. A sketch of the problem setup is provided in figure 4.15. Cells are discretised in the same way as described in section 4.4.1. Note that the plane wall does not need to be discretised since is it accounted for analytically within the regularised blakelet. Owing to the increased nonlocal fluid dynamic interactions due to the presence of the wall, the time step is reduced to $\Delta t = 2\pi/100$ to ensure stability of the time stepping method.

Across simulations, we vary the drag ratio $\Gamma_d \in [10^3, 10^4]$ and incidence angle $\theta_0 \in [\pi/16, 3\pi/16]$, so as to consider a range of swimmers approaching the surface with beats characteristic of different stiffness profiles. In all simulations, we fix $S = 12$, $\mathcal{M}_1 = 0$, $\mathcal{M}_2 = 1.5 \times 10^{-2}$, and $\mathcal{M}_3 = 1.5 \times 10^{-4}$. Results comparing the trajectories of cells for different values of Γ_d and θ_0 are presented in figure 4.16. The solid plane boundary at $z = 0$ is indicated in grey, and projections of each trajectory onto the xy- and xz-planes are drawn in transparent dotted lines on the bounding walls of each panel. For $\Gamma_d = 10^3$, the resistance to twist is large enough to suppress periodic non-planar motion. However, as proximity to the wall increases, the approximate plane of beating rotates from being predominantly xz-planar to increasingly xy-planar.

For the larger values of Γ_d, a periodic nonplanar beat pattern develops after approximately 2 or 3 beats. As in the infinite fluid (see figure 4.6), cells with a nonplanar

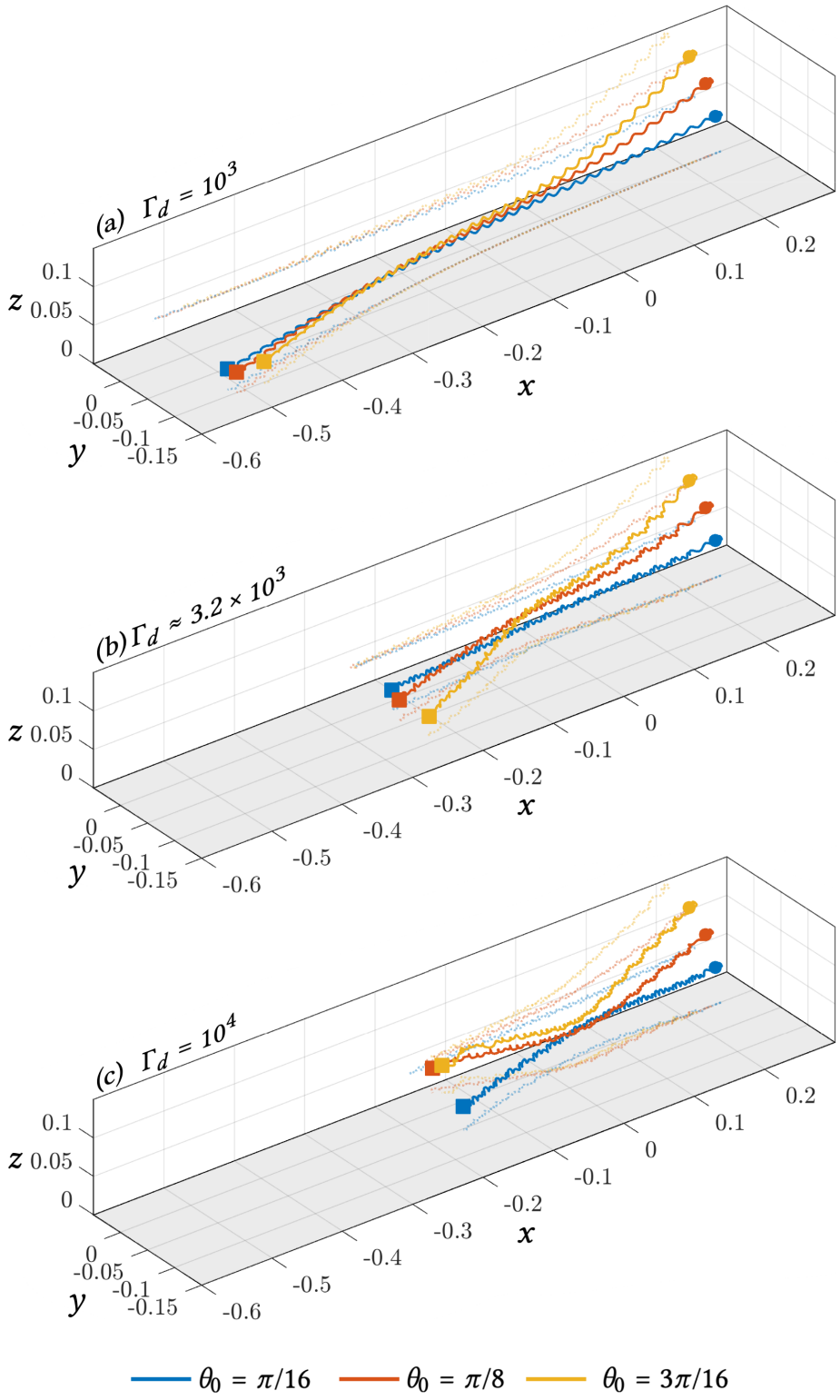

Figure 4.16: Trajectories, progressing from circle to square, of cells approaching a planar rigid wall at $z = 0$ (shaded in grey). We consider three different drag ratios Γ_d (in (a), (b) and (c)), and three angles of incidence θ_0 (indicated by line colour). Projections of each trajectory onto the xz and xy planes are indicated by transparent dotted lines of the matching colour.

beat traverse less distance over the same simulation time. In all cases, hydrodynamic interactions between the cell and the plane wall affect the large-scale trajectory of the cell. In the stiffer case (figure 4.16a), the cells bank left upon approaching the wall, regardless of incidence angle θ_0. Changing the sign of the twist actuation causes the cells to bank in the opposite direction. This banking behaviour is observed for moderately-nonplanar cells, with the amount of deviation affected by the angle of incidence (figure 4.16). The deviation of cell trajectories is considered further shortly.

The flagellum waveforms of the cells considered in an infinite fluid in figure 4.16 are presented in figure 4.10 approaching the plane wall. As in section 4.4.1, cells are plotted with the head-flagellum join $\boldsymbol{X}_0$ translated at each instant to coincide with the origin. Solutions are sampled stroboscopically once per beat, so that regular periodic motion appears stationary. In general, the choice of the angle of incidence θ_0 appears to have little qualitative impact on the developing flagellum waveform, instead affecting the deflection angle of the head as it gets close to the wall. In the twist-resistant ($\Gamma_d = 10^3$) case, the plane of beating rotates from being predominantly xz-aligned to being largely in the xy-plane. This is due to a rotation of the cell by $\approx \pi/2$, evidenced by the fact that the flagellum motion remains approximately planar when viewed in the cell body (or clamped) frame (bottom right of figure 4.18a). Indeed, viewing the planar projections of the pinned trace in figure 4.18a clearly illustrates the change of plane of beating and of direction of the cell as it advances towards the wall. As above, we consider this behaviour in more detail later in this section.

As Γ_d increases from 10^3 , nonplanar progressive motion develops and the cells adopt a rolling, twisting gait as they approach the wall. For the larger value $\Gamma_d = 10^4$ considered, a regular twist and bend swimming pattern develops, indicated by the 'threads' of similar flagellum lines, reminiscent of a weave or plait, seen in figures

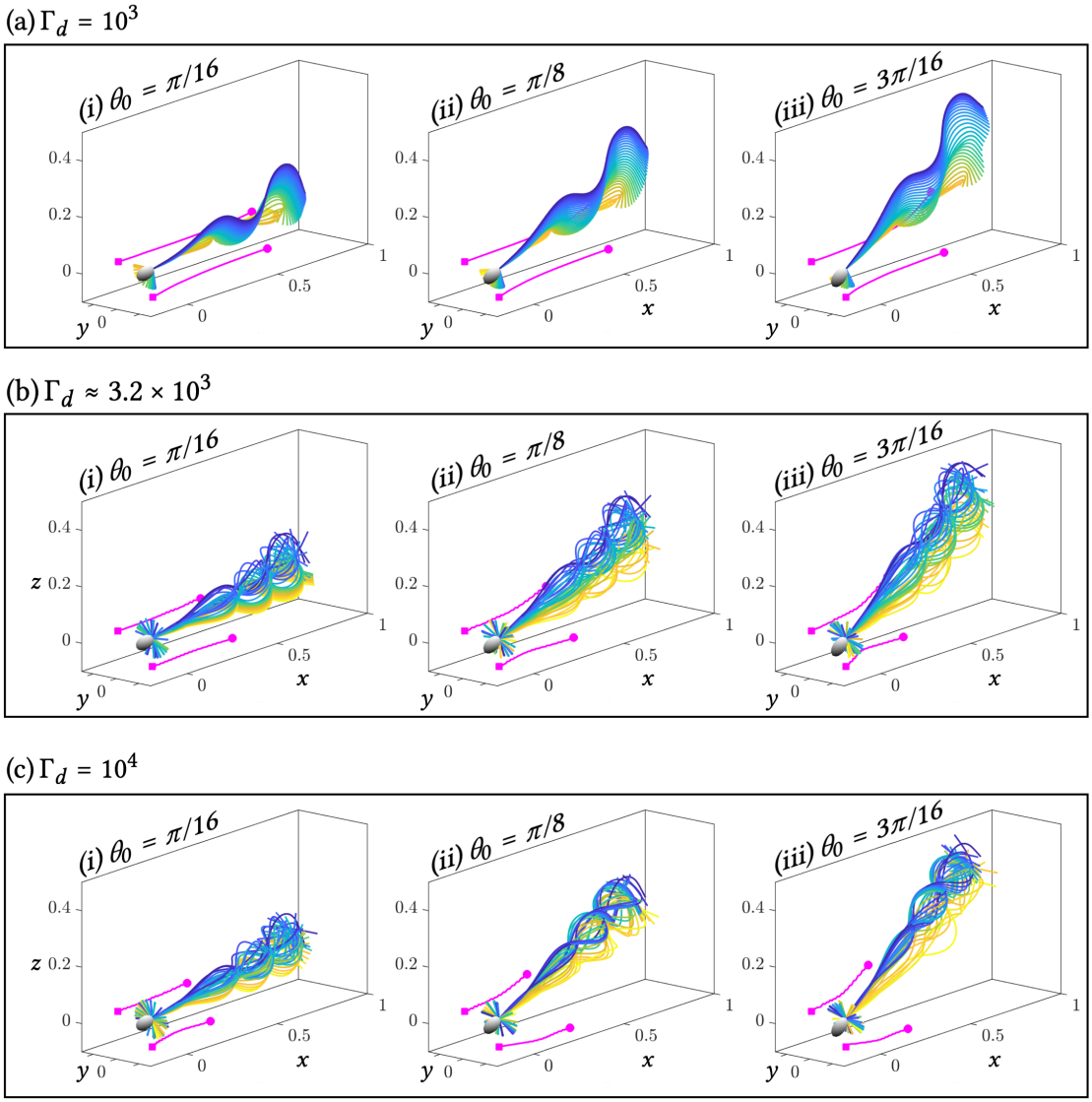

Figure 4.17: Waveforms in the fixed laboratory frame of cells differing in drag ratio Γ_d as they approach a rigid plane boundary from varying incidence angles θ_0. Cells are plotted with $\boldsymbol{X}_0$ translated to the origin O, and flagellum shapes sampled stroboscopically so that consistent periodic motion appears motionless. Flagellum colour, from blue through to yellow, indicates time $t \in [3T, 40T]$ where $T = 2\pi$ is the period of the actuating beat. Magenta lines represent the trajectory of $\boldsymbol{X}_0$ across the same period, projected onto the xy- and xz-walls of each panel. Arrows at $\boldsymbol{X}_0$ indicate the rolling of the cell over the simulation.

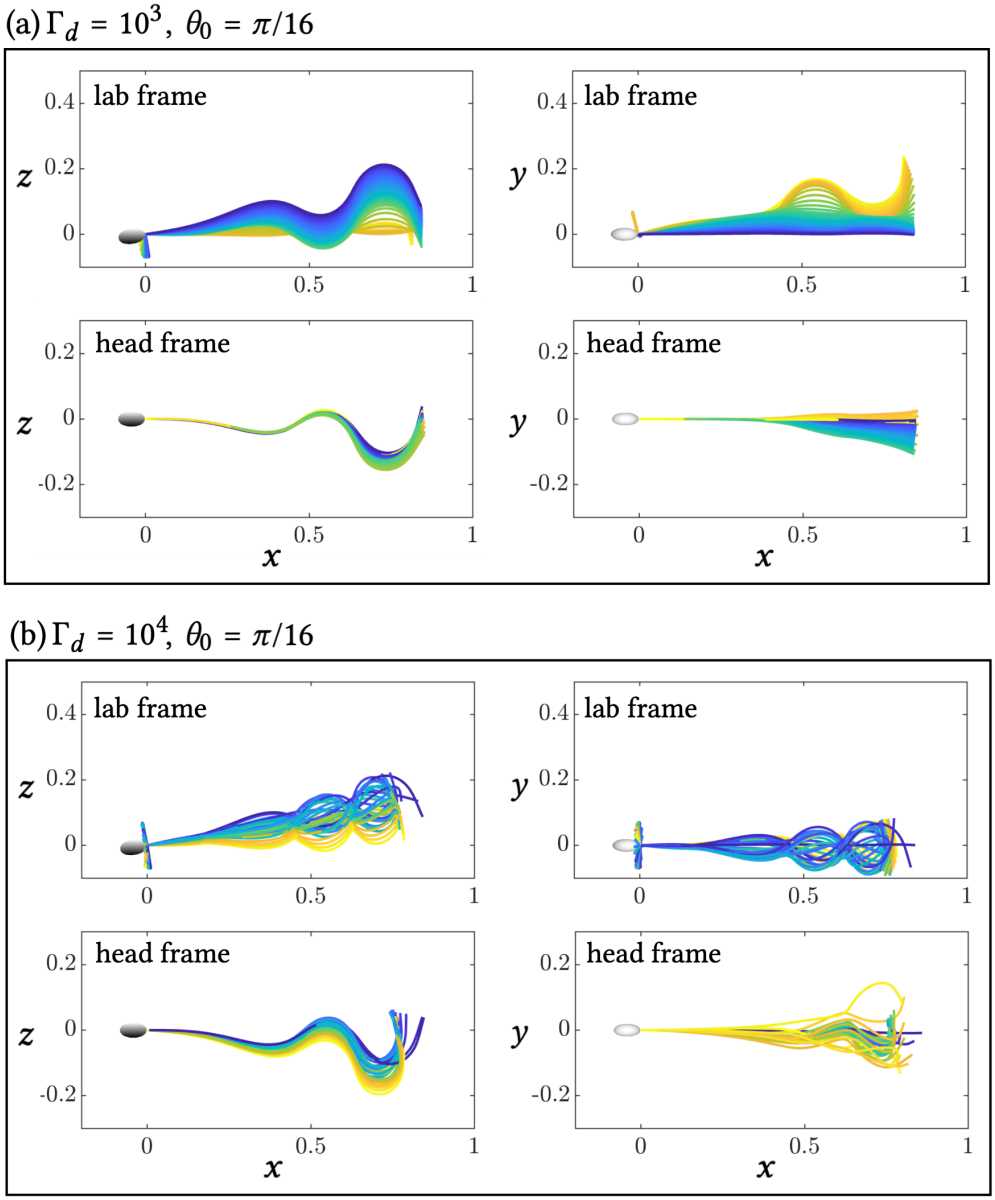

Figure 4.18: Planar projections of cells in the presence of a solid boundary onto the xz- and xy-planes (left and right of each panel respectively) of cells characterised by drag ratios (a) $\Gamma_d = 10^3$ and (b) $\Gamma_d = 10^4$, viewed both from the fixed laboratory frame (top of each panel) and relative to the rotation of the cell head (bottom of each panel). Line colour indicates the evolving beat across the interval $t \in [3T, 40T]$, with $T = 2\pi$ the period of the actuating beat.

4.10 and 4.11. Such a pattern is not as evident for the intermediate $\Gamma_d \approx 3.2 \times 10^3$ case, suggesting that the competing balance of elasticity and fluid dynamics in that scenario works against the formation of a nonplanar beat that is regular across a larger time interval. By way of example, figure 4.18b examines the planar projections of a nonplanarly beating cell with $\Gamma_d = 10^4$. The geometric regularity of the nonplanar flagellum is well illustrated by examining the projections in the fixed head frame, with motion between lines in the bottom-left panel indicating the alteration in trajectory the cell exhibits as it approaches the wall.

The trajectories of the cells as they approach the wall can be more quantitatively understood through examination of the tangent angles of the trajectory of $\boldsymbol{X}_0$ when projected onto the xy- and xz-planes. We label these quantities θ_{xy} and θ_{xz} respectively, which imply the motion and deviation of the cell; if one or the other is zero at any time, then the flagellum waveform is not beating in the corresponding plane. In addition, we track the angle of revolution of the cell head θ_{rev}, which indicates the axial rotation of the cell. These quantities, for the cells drawn in figure 4.17, are presented plotted against time in figure 4.19, starting from $t = 4\pi$. For clarity, we plot the two lines enveloping the oscillating θ_{xy},θ_{xz} waveforms (which are not drawn). These lines are computed using the MATLAB® `envelope` function, with smoothing parameter chosen as 200.

For the cell most resistant to twist (with $\Gamma_d = 10^3$), figure 4.19 supports the earlier qualitative observations by clearly indicating the transition from predominantly xz-planar beating to xy-planar beating upon approaching the wall. The initial incidence angle biases the initial θ_{xz} curve (drawn in light blue), which reduces to nearly zero upon approaching the wall. At a critical time t_c, the cell head undergoes a partial roll of approximately $\pi/4 < \theta_{\text{rev}} < \pi/2$, shown by the orange line. Small oscillations in the

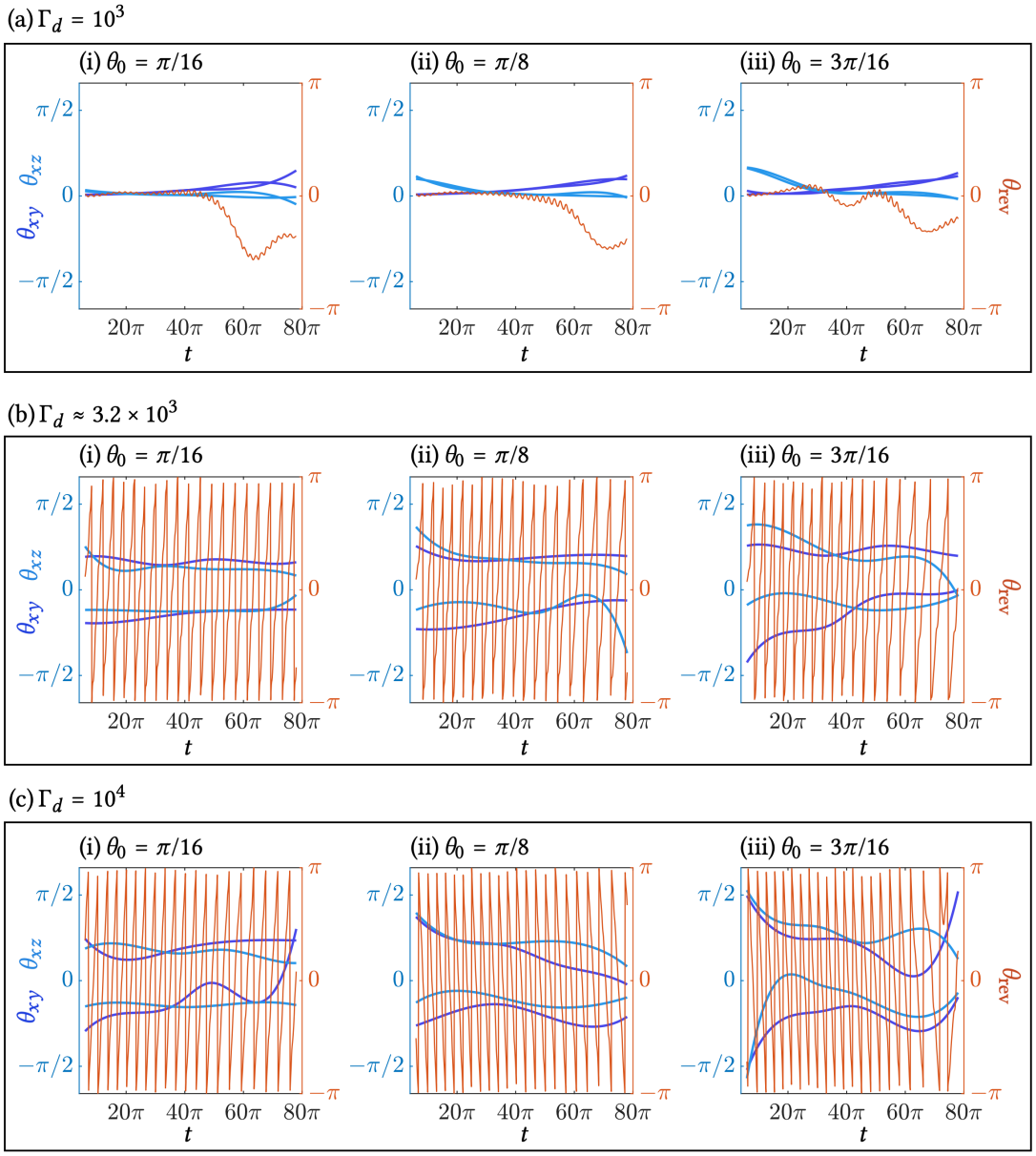

Figure 4.19: Evolving tangent angles θ_{xy} (light blue) and θ_{xz} (dark blue) to the curves formed by projecting the trajectory of $\boldsymbol{X}_0$ onto the xy- and xz-planes respectively. Angles are plotted against time $t \in [4\pi, 80\pi]$. Corresponding to the blue axes of each panel, the trajectory tangent angles are each implied through two lines enveloping the oscillating curve (not drawn for clarity). Corresponding to the oranges axes; the evolving angle of revolution of the cell, varying across $-\pi \leqslant \theta_{\text{rev}} < \pi$, so that each period represents a complete axial rotation.

θ_{rev} curve imply the 2π periodic beat pattern of the flagellum. The size of the deviation in orientation depends on θ_0, and is greater for smaller θ_0, since the perpendicular height of the cell above the wall is smaller and as such experiences greater and more prolonged hydrodynamic interaction with the wall over the course of the simulation. After the onset of this roll (initiated at a value $20\pi < t_c < 40\pi$ depending on θ_0), the θ_{xy} curve (drawn in dark blue) grows, indicating the change in the plane of beating of the cell. The close proximity of the enveloping lines for both θ_{xy} and θ_{xz} in this case indicate the tight (but slowly rolling) planarity of the flagellar waveform, as seen previously in figures 4.17a and 4.18a.

Figures 4.19b and 4.19c track the same angular quantities for the nonplanar swimmers characterised by $\Gamma_d \approx 3.2\times10^3$ and $\Gamma_d = 10^4$ respectively. The periodic axial rolling of the cell is immediately evident in the oscillatory curve for θ_{rev}, shown in orange, with the number of peaks being the number of complete revolutions N_{rev} exhibited across the selected period. In both Γ_d cases, and for all θ_0 considered, the separation between both the θ_{xy} and θ_{xz} lines indicates the nonplanarity of the flagellar waveforms. The levels of separation are approximately equal at each instant, suggesting that the motion has no preferential plane of beating. With $\Gamma_d \approx 3.2 \times 10^3$ and $\theta_0 = \pi/16$ (figure 4.19bi), the relation $\theta_{xy} \approx \theta_{xz}$ is maintained across the simulation, producing an approximately linear cell trajectory without deviations (also viewable in figure 4.16b, blue line). This behaviour appears to be the outlier; as suggested by figures 4.16b and 4.16c, other cells characterised by $\Gamma > 3 \times 10^3$ exhibit less discernable (if any) relationships between θ_{xy} and θ_{xz} through erratic trajectories. Nonetheless, the increase in the relative importance of hydrodynamic interactions (despite fixing $S = 12$) by increasing $\Gamma_d = 10^4$ leads to pronounced trajectory deviations of $\approx -\pi/4$ (figure 4.19cii) and $\approx \pi/2$ (figure 4.19ciii).

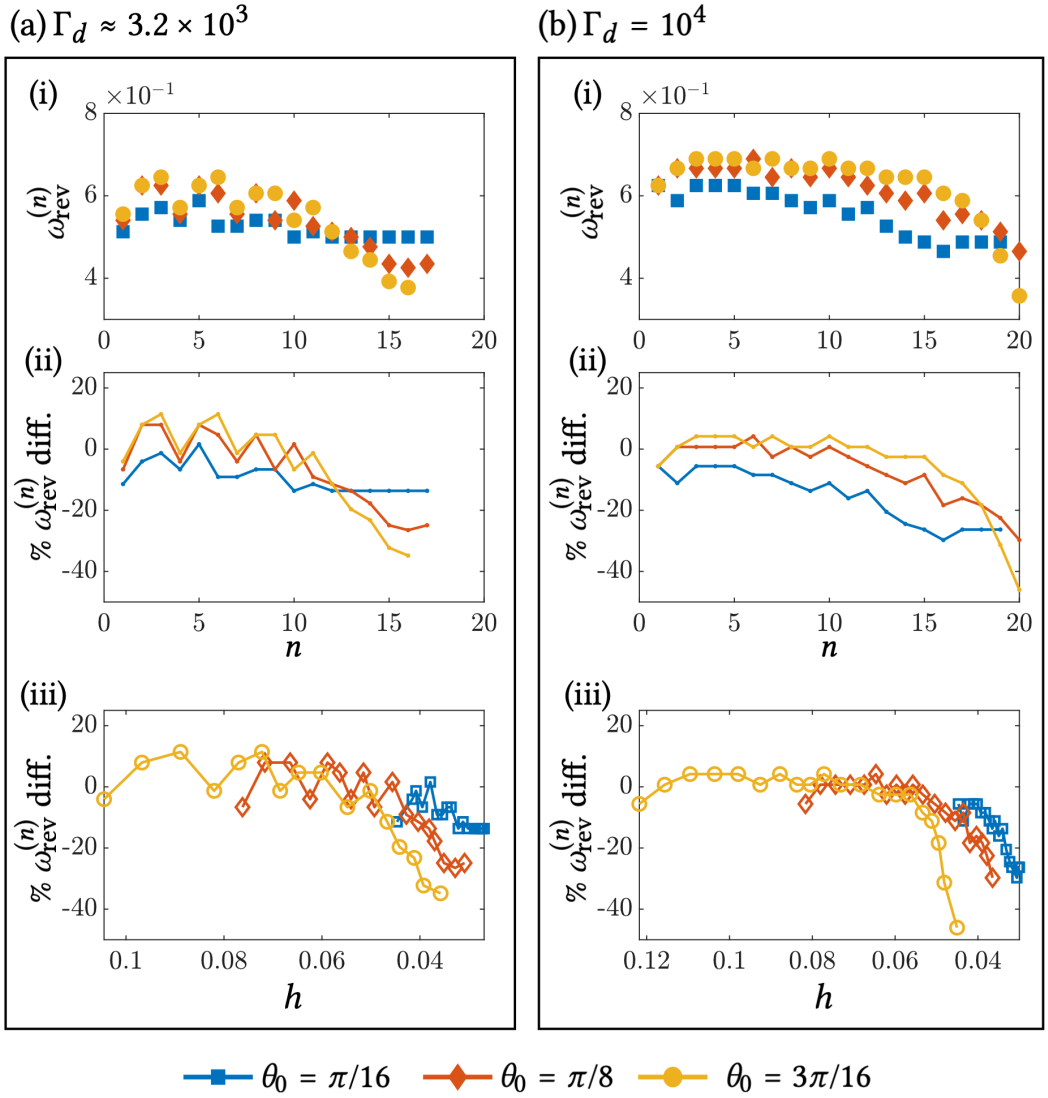

Figure 4.20: Quantifying the rolling behaviour of cells as they approach a plane wall from three different angles of incidence, for cells characterised by (a) $\Gamma_d \approx 3.2 \times 10^3$ and (b) $\Gamma_d = 10^4$. (i) Roll rate $\omega_{\text{rev}}^{(n)}$ against n, the index of the revolution to which it corresponds. Marker shape and colour indicates the initial incidence angle θ_0. In (ii), index n against the percentage difference between the roll rate $\omega_{\text{rev}}^{(n)}$ and the mean roll rate $\langle \omega_{\text{rev}} \rangle$ for an identical cell in an infinite fluid. (iii) Percentage differences in roll rate plotted against the smoothed perpendicular height h of $\boldsymbol{X}_0$ above the plane wall.

As in section 4.4.1, the rolling behaviour of the simulated cells can be measured through ω_{rev}, the axial rate of revolution (or rate of rolling) as defined in equation (4.74). Considering only those values of Γ_d which yield nonplanar beating, in figure 4.20 we examine how the rate of rolling is affected by proximity to the cell wall. For both $\Gamma_d \approx 3.2 \times 10^3$ (figure 4.20a) and $\Gamma_d = 10^4$ (figure 4.20b), trends between ω_{rev} and wall proximity are similar. In panels (i), the rate of rotation for a single complete revolution (labelled $\omega_{\text{rev}}^{(n)}$) is marked against the index n of the roll to which it corresponds. In this way, rates for larger n values correspond to cell revolutions later in the simulation when the cell is closer to the plane wall. As n increases, the roll rate $\omega_{\text{rev}}^{(n)}$ decreases from ≈ 0.7 to < 0.4, depending on the angle of incidence θ_0. To better understand the retarding effect of the wall upon the cell, in panels (ii) we consider the percentage difference between each roll rate and the average roll rate for an identically characterised cell swimming in an infinite fluid. Plotted against revolution index n, we see that cells roll approximately at the same rate as those in an infinite fluid for $\lessapprox 10$ revolutions, before rolling slower upon approaching the wall (i.e. as n increases). Cells that approach the wall from a steeper initial angle (through larger θ_0) more rapidly reduce their rotation rate in close proximity of the wall, as they 'ram' into the surface and are required to rapidly change orientation (here driven through elastohydrodynamic interactions, rather than any sensory intelligence). This rapid change in direction is indicated by the sharp bends in the θ_{xy} and θ_{xz} line pairs in both figures 4.19b and c.

Finally, we consider the change in the aforementioned percentage difference with respect to perpendicular height above the plane wall at $z = 0$. As indicated in figure 4.16, the evolving trajectory at $\boldsymbol{X}_0$ oscillates with the motion of cell. With this in mind, the height above the wall is sampled at the start of each new revolution, and smoothed using the MATLAB® `smooth` function (with a moving average size of 200 points), to

obtain an injective curve closely approximating the path taken by the cell towards the wall. Since more acute incidence angles initialise the cell closer to the surface, measurements corresponding to smaller values of θ_0 are concentrated at one end of the x-axes of figures 4.20aiii and biii. A rapid reduction in the relative roll rate between 10% and 40% occurs when $h < 0.05$ for both Γ_d values considered. The reduction is more severe and occurs sooner upon approaching from a steeper incidence angle; since the height h is measured from the plane to $\boldsymbol{X}_0$, this difference is accounted for by the physical presence of the head, defined by axes $\boldsymbol{a} = [0.044, 0.036, 0.022]$ (see section 4.3). Nonetheless, percentage reductions in the roll rate are more severe in the case with $\Gamma_d = 10^4$, with differences of over 40% recorded in extremes (e.g when $\Gamma_d = 10^4$ and $\theta_0 = 3\pi/16$).

4.5 Summary and discussion

In this chapter we have introduced and benchmarked the SPX method, a newly developed framework for modelling the elastohydrodynamics of slender bodies and actuated monoflagellate cells. The method couples a nonlinear elasticity model accounting for mechanical bending and twisting of a flexible filament, connected to a rigid-body head, with a nonlocal expression for the surrounding fluid enabling interactions between the cell, itself, and surrounding structures.

The SPX model is derived from the general equations for linear elasticity in three dimensions, and thus accounts for both bending and twisting deformations within a slender body. By actuating the cell flagellum through the application of internally-driven bend and twist moments, a geometrically complex, rolling, writhing motion is generated, which, through interaction with surrounding fluid, induces progressive swimming. Examining the behaviour of such cells in section 4.4.1, we find that nonplanar swimmers are less effective at fast and efficient motion than a purely planar beat, in agreement with Huang *et al.* (2018). In the space of parameters considered here, dynamics are dominated by the choice of Γ_d, a ratio between the viscous bending and twist drag of the flagellum, and which governs the effective resistance to nonplanar motion. In contrast to planar swimming, where the value of $\mathcal{M}_2$ broadly determines cell dynamics (for a given $\mathcal{S}$), nonplanar motion is largely invariant to the choice of $\mathcal{M}_3$. Through Fourier analysis of the motion of the distal flagellum tip, characteristic frequencies corresponding to the three types of motion the cell experiences can be determined: a bending and twisting motion in the flagellum, and a global cell rotation arising from the nonplanar beat (see figures 4.13 and 4.14).

To our knowledge, the SPX enables for the first time explorations into the effects of

solid boundaries upon the beat plane of an active, elastohydrodynamically-accurate, sperm cell. In section 4.4.2, we consider the dynamics of cells approaching an infinite plane wall, varying the effective resistance to twist through Γ_d and the incidence angle θ_0. For smaller values of Γ_d, a cell that originally beats in the plane perpendicular to the surface rotates by $\approx \pi/2$ as it approaches, so that the plane of beating and the wall are approximately parallel. Whilst previous studies have used elastohydrodynamic models to simulate planar swimmers above a wall (Montenegro-Johnson *et al.*, 2015), through generalisation of the elasticity and hydrodynamic models, the SPX allows for changes in the plane of beating to be caused dynamically through interactions between the cell and the rigid boundary. In addition, the SPX enables pioneering simulations of progressive cells actuated through a combined twist-and-bend motion in the presence of a wall; results presented in figure 4.20 indicate that such nonplanar swimmers exhibit markedly less rolling than those progressing in an infinite fluid, with reductions in the rate of rotation up to and exceeding 40% in extremes.

The rotation in the plane of beating for twist-resistant cells (observed in figures 4.16, 4.17, and 4.19) seems to agree with experimental observations (Woolley, 2003; Nosrati *et al.*, 2015). We do not, however, observe the adoption of planar beat patterns by those cells exhibiting nonplanar beats. Since proximity to the wall is maintained throughout the simulation, it is unlikely that this is due to the simulations not being run for a long enough time period. Instead, we hypothesise that this nonplanar dampening does not occur since we have considered only $S = 12$, a relatively elasticity-dominated regime. This value was chosen to allow for greater control in investigating the inducement of nonplanar swimming in section 4.4.1; it is possible that for larger choices for S, characteristic of viscosity-dominant scenarios, this behaviour is observed.

Advancements in elastohydrodynamic modelling offered by the SPX method fall

into two categories: improvements relating to the inclusion of nonplanar bending and twist elastic deformations, and improvements relating to the use of the nonlocal method of regularised stokeslets for hydrodynamics. In the former category, the SPX immediately improves over planar models (Tornberg & Shelley, 2004; Moreau *et al.*, 2018; Hall-McNair *et al.*, 2019; Neal *et al.*, 2020) by allowing for full bending deformations in three dimensions. Indeed, by additionally accounting for mechanical twisting of the flagellar axoneme as well as varying bending stiffness, SPX improves over those 3D methods which allow for bending but not twist, such as the methods used by Gadêlha *et al.* (2010) and Montenegro-Johnson *et al.* (2015). Considering only the elasticity model, the SPX method differs from previous elastohydrodynamic frameworks accounting for bend and twist by formulating the motion of the flagellum in terms of its centreline; in contrast, methods by Wolgemuth *et al.* (2000; 2004) track filament motion through the integrated complex curvature, and Schoeller *et al.* (2021) use a quaternion basis for describing elastic geometry of fibres. In both these cases, additional transformations to the constitutive equations are necessary, increasing complexity over the direct position formulation adopted by SPX. The nonlinear elasticity equations used in the proposed method differ only superficially from the equations in methods by Gueron & Levit-Gurevich (2001a; 2001b), which can be obtained by considering the scalar components of equations in section 4.2.6 expressed in terms of director curvatures $\kappa_1, \kappa_2, \kappa_3$ following substitutions using equations in 1.3.1. Moreover, the proposed SPX method expands upon the above fully 3D models by considering the addition of a rigid body cell head connected to the elastohydrodynamic flagellum at one end, significantly increasing the complexity of the model boundary conditions.

The use of the nonlocal regularised stokeslet method provides immediate improvements in flow accuracy over local methods, which have frequently been employed to

reduce model complexity (Wolgemuth *et al.*, 2000, 2004; Gadêlha *et al.*, 2010). Whilst structurally similar to the hydrodynamic model used in Montenegro-Johnson *et al.* (2015), by using resistance coefficients directly computed from regularised stokeslet integrals (see section 4.2.1 for details) over coefficients derived from resistive force theory (or indeed, the nonlocally extended L.G.L. theory in Gueron & Levit-Gurevich (2001b)), the hydrodynamic model in the SPX can be considered wholly a member of the regularised stokeslet family of fluid models, unifying the hydrodynamic model compared to those previous approaches utilising hybridised descriptions.

A potential improvement to the SPX model would be the implementation of a more sophisticated time integration algorithm. In the current numerical scheme, we use the implicit Euler method, though higher-order time stepping schemes (e.g. Crank-Nicolson) could be implemented to improve accuracy and stability. Indeed, the similar framework by Montenegro-Johnson *et al.* (2015) employs a Crank-Nicolson Adams-Bashforth (CNAB) method for integration. Such methods can be straightforwardly implemented onto the elastohydrodynamic equation (4.52a), but require care when applied to equations containing time derivatives of variables other than centreline position. Since there is no overly-hampering restriction on time step size in the current SPX implementation (see section 4.3 for details), this additional complexity was deemed unnecessary for the current study. Other models, including those by Tornberg & Shelley (2004) and Gadêlha *et al.* (2010) use so-called ImEx (IMplicit-EXplicit) methods, splitting the model equations into those requiring implicit integration (e.g. high-order derivatives and other numerically stiff terms), and those where explicit integration is acceptable. Such an approach could help control the complexity of the discrete model by only requiring selected equations to be written implicitly, enabling higher-order implicit methods for those terms, while allowing the remainder to be straightforwardly

treated using explicit techniques. More advanced numerical integration techniques, such as Jacobian-free Newton Krylov or Broyden's method (both discussed in detail by Schoeller *et al.* (2021)) could further enhance stability and accuracy of SPX model solutions. In addition, a better understanding of the temporal stability of the method could be obtained through analytical analysis techniques, building upon on the "brute force" approach described and performed in Sec. 4.3.4.

Morphological accuracy, particularly to human sperm, could be improved by allowing for flexibility at the head-flagellum join. In the current implementation, the orientation of the cell head is determined by the proximal director frame such that the flagellum connects perpendicular to the surface, an approach inherited from previous centreline models by Gadêlha *et al.* (2010); Montenegro-Johnson *et al.* (2015). Adapting recent methods by Neal *et al.* (2020), head-flagellum flexibility could be included by decoupling the head orientation basis from the flagellum director. The elasticity model could be generalised further by allowing for anisotropic bending stiffness. However, a crucial early step in the SPX derivation requires allowing $E_1\kappa_1\mathbf{d}_1 + E_2\kappa_2\mathbf{d}_2 = E\boldsymbol{X}_s \wedge \boldsymbol{X}_{ss}$, so that $E = E_1 = E_2$. In removing this constraint, the resulting model cannot be formulated in terms of the flagellum centreline coordinates; rather the centreline curvatures κ_i become the principal unknowns of the model, as in methods by Gueron & Levit-Gurevich (2001a,b), with positions obtainable through a geometric relation integrating along $\mathbf{d}_3$. Decoupling the bending moduli would better model the cross-sectional asymmetry of the 9+2 axoneme and could promote more morphologically accurate nonplanar beats.

Currently, the current SPX formulation only allows for simulations of individual isolated cells. Allowing for simulation of multiple interacting cells in 3D could enable many more problems to be considered, in particular, building upon large-scale fibre studies by Schoeller *et al.* (2021) to investigate the three-dimensional bundling

of sperm cells, either in infinite fluid or near boundaries, or upon nodal cilia studies by Gallagher *et al.* (2020) by incorporating elastohydrodynamic effects in the nonlocal fluid flow model. Since the SPX requires many times more degrees of freedom than the EIF to model a single cell, the monolithic approach to include multiple filaments in that model would be ill-advised; simulations of only two or three cells would rapidly produce dense matrices with many thousands of rows, ballooning the memory requirements and slowing solve times. Using an aforementioned ImEx method, or alternate hydrodynamic method (e.g. fast-multipole or RPY-tensor, as used by Schoeller *et al.* (2021)), could allow the linear system to be solved nonmonolithically and thus avoid extreme memory requirements while retaining computational efficiency.

The SPX is explicitly designed to enable accurate simulations of microbiological slender bodies, and thus has great potential to contribute to future studies within the mathematical biology community. The presence of a nearby plane wall has already been shown to reduce axial rolling of nonplanarly beating cells (see figure 4.20); this result may have applications into studies considering sperm locomotion near boundaries, and in particular upon investigations of cell slipstreaming (Ishimoto & Gaffney, 2015) and surface attachment (Woolley, 2003; Simons *et al.*, 2014, 2015). With relatively little alterations, the SPX can be applied to model cilia attached to a planar surface, building upon previous simulation studies (Gueron & Levit-Gurevich, 2001b; Sartori *et al.*, 2016a) through improved hydrodynamics modelling to investigate the regulatory role twist elasticity plays in ciliary actuation. The generality of the driving moment terms in the SPX formulation make it well suited for future studies comparing and contrasting alternative theories of actuation (such as those discussed in section 1.1.2); potential research inspired by the recent findings of Carichino & Olson (2019) could involve coupling the SPX model for actuation with a calcium gradient response, improving

knowledge of the mechanosensory and chemotactic behaviours of sperm (and other cells), and with applications to cell steering and selection procedures. Novel biotechnological propulsion techniques could be adapted for use with SPX, including slender bodies actuated by phoretic responses (Katsamba *et al.*, 2020), and shape-change elastic mechanisms (Sharan *et al.*, 2021).

The results in section 4.4.2 reveal that cells characterised by lower values of the drag ratio $\Gamma_d = 10^3$ exhibit a planar beat pattern by suppressing nonplanar motion. Such cells swim faster than those exhibiting nonplanar beats, which arise with larger choices of Γ_d. This finding may be biologically relevant for motility in polymeric fluids such as cervical mucus, and upon swimming across step-changes in viscosity (e.g the semen/cervical mucus boundary). Since the drag ratio Γ_d defines in essence the behaviour of the surrounding fluid (unlike, for example, the stiffness ratio $\Gamma_s = C/E^d$, which describes only flagellum properties), we hypothesise that polymeric fluids may effectively reduce the value of Γ_d by making axial rotations relatively harder than translation, producing more planar beats and thus enabling more effective swimmers. Further investigations into the relationship between Γ_d and viscosity (through the swimming parameter $\mathcal{S}$) may additionally help to explain the planar nature of flagellar beats in high viscosity and complex fluids. The SPX itself could be used to simulate the constituent polymer chains themselves, with the inextensibility requirement made lax to enable filament stretching, or dynamic fibre extension enabled by including additional growth terms (Wolgemuth *et al.*, 2004). Rigid boundaries more complex than the infinite plane considered in section 4.4.2 can be included through distributions of stokeslets across the surface in conjunction with the regularised blakelet image system (Ainley *et al.*, 2008) already implemented. The SPX could thus enable accurate assessment and development of novel microchannel designs,without the requirement for

planar swimming cells present in previous studies (Montenegro-Johnson *et al.*, 2015).

Chapter 5

Conclusion

In this thesis, we have developed two distinct frameworks for describing and simulating the motion of elastohydrodynamic slender bodies in viscous flows. These methods, referred to throughout as the *EIF* and *SPX* methods respectively, have been derived from basic physical constitutive laws, benchmarked for both accuracy and computational efficiency, and used to simulate dynamic filaments and propulsive human spermatozoa in both two and three dimensions. MATLAB® codes for both methods are made available in online GitLab repositories (Hall-McNair, 2019, 2021). In this conclusion, we briefly recap each approach in sections 5.1 and 5.2 for the EIF and SPX methods respectively. We conclude with summarising remarks in section 5.3.

5.1 Summary of the EIF

Developed to simulate planar passive filaments and swimming monoflagellates, the *Elastohydrodynamic Integral Formulation* (or EIF, introduced in chapter 2) provides an efficient framework for rapidly simulating fibres and cells in isolation or in small groups. Interactions between the distal filament (or flagellum), and between any poten-

tial neighbours are included in the nonlocal hydrodynamic model by incorporating the method of regularised stokeslets. The titular integral equations, describing the elastic bending of the filament, arise from integration of the moment equilibrium equation (in (1.86)) for a generalised deforming slender body, combined with a linear constitutive law relating the bending moment to the centreline tangent angle. The elastic representation is coupled to the hydrodynamics through the force equilibrium equation (in (1.84)) and the regularised stokeslet boundary integral equation, reducible to a one-dimensional integral along the centreline since the volume of the flagellum does not change (see section 1.2.3).

Previous position-based elastohydrodynamic methods, such as those by Goldstein *et al.* (1998); Wolgemuth *et al.* (2004); Tornberg & Shelley (2004); Gadêlha *et al.* (2010); Montenegro-Johnson *et al.* (2015), require auxiliary equations enforcing filament inextensibility to be included in their models. Additionally, sufficiently resolving the line tension can require large numbers of discretising nodes, yielding numerical implementations prone to stiffness, requiring small time steps to ensure stability. Work by Moreau *et al.* (2018) demonstrated that describing filaments by centreline tangent angle, in conjunction with an integral formulation of the elastodynamic equations, enabled large increases in efficiency and reductions in computational cost. These gains derive from a reduction in the required degrees of freedom and implicit enforcement of the inextensibility constraint through the angle formulation. The EIF presented in this thesis improves on the Moreau *et al.* formulation by replacing the local hydrodynamic model with a regularised stokeslet method to include nonlocal interactions. Judicial use of commercial-grade built-in MATLAB® ODE solvers further improves computational efficiency, allowing simulations involving multiple interacting filaments to be completed on a timescale of minutes (rather than hours or even days) with remarkably

few constraints on computational hardware.

A keen focus has been kept on adaptability of the EIF to many problem scenarios. Within this thesis, the EIF is used to examine (a) filaments in a linear shear flow, (b) sedimenting due to gravity, and (c) self-propulsive swimming. These varied scenarios are describable through the EIF with relatively minor alterations to the model equations, and similarly straightforward tweaks to the MATLAB® code. Despite the one-dimensional description of the filament, the method exhibits buckling phenomena when in compressing shear flows, in agreement with previous findings (Tornberg & Shelley, 2004). Similar geometric instabilities are observed for sedimenting filaments, with close agreement to methods by Schoeller *et al.* (2021).

In chapter 3, extensions to the EIF by Neal *et al.* (2020) are incorporated to model planar human spermatozoa, examining the effect of varying head morphology on swimming speed and efficiency. The rigid body head is included in the method through a nearest-neighbour regularised stokeslet discretisation (Smith, 2018). The flagellar axonemal structure is modelled by varying the elastic bending stiffness E along the arclength, producing propulsive waveforms typical of cells swimming in high-viscosity fluids (Neal *et al.*, 2020). For cells optimised for swimming speed, variations in head dimensions agreeing to a fixed idealised volume constraint produce percentile differences in speed and efficiency over a similarly-actuated cell with a head of average observed dimensions. These performance differences arise from changes in head sway in the plane of the beat, which leads to changes in both the proximal flagellum shape (dominated by altered dynamics of the head-flagellum joint) and distal curvature (due to nonlocal hydrodynamic interactions).

Use of angle formulation methods to model slender bodies deforming in three-dimensions is an active avenue of research, with early work by Walker *et al.* (2020)

demonstrating their applicability to simulate passive unbending and active clamped filaments. Difficulties arise in correctly tracking the rotations of flagellar segments in 3D space, with care required to ensure uniqueness and avoid so-called "gimbal lock". With this in mind, Walker *et al.* use a spherical mapping to write model equations in a transformed singularity-free basis. The aforementioned study by Schoeller *et al.* (2021), whilst not an angle formulation method in the sense described here, uses a quaternion representation to track rotations in 3D, an approach which could be applied to the EIF to enable nonplanar bending.

With the elastodynamic integral equation a key feature of the EIF, it is natural that it be a focus for potential improvements. The results in section 2.4.1 indicate that the shape of a buckled filament can be well described using interpolating Chebyshev polynomials, suggesting the applicability of alternate spectral integral techniques, such as those by Muldowney & Higdon (1995), enabling increases in efficiency and accuracy with potentially fewer degrees of freedom. Recent work by Gallagher & Smith (2021) reveals the gains in efficiency at no loss of accuracy available when applying Richardson extrapolation to the nearest neighbour regularised stokeslet method, allowing for larger choices of the regularisation parameter ε to be chosen, particularly applicable to the surface integral arising from the cell body hydrodynamics. Coarse graining the far-field flow using a treecode formulation similar to Wang *et al.* (2019) (or equivalent methods) would simplify the computational cost and enable simulation of increasingly large numbers of filaments. Fibre self intersections could be avoided through inclusion of a Lennard-Jones potential acting between each segment, as used in other methods (Wolgemuth *et al.*, 2004; Jayaraman *et al.*, 2012).

5.2 Summary of the SPX method

The *Sperm-X* (SPX) method developed in chapter 4 provides a framework for modelling monoflagellate cells bending, twisting, relaxing and swimming in three dimensions. Both linear bend and twist deformations are included in the elastics model, coupled to a nonlocal hydrodynamic model in the form of the method of regularised stokeslets. The hydrodynamic model is easily replaced by the method of regularised blakelets to incorporate fluid interactions between a slender body and an infinite plane boundary. Designed primarily for simulating human spermatozoa, morphological features characteristic of sperm, namely a rigid body cell head, varying flagella stiffness, and a distal end piece region of mechanically inactive flagellum are present in the model.

To avoid the complexities arising from a three dimensional angle formulation for nonlinear filament geometry (discussed above), the model is formulated in terms of the coordinates of the flagellum centreline. As a result, conservation of arclength is enforced through coupling to an auxiliary equation derived directly from the inextensibility constraint and the elastohydrodynamic equation for the slender body. Centreline models have previously been used effectively to model planar cells in shear flows (Tornberg & Shelley, 2004), investigate the importance of nonlinear geometry on cell trajectory (Gadêlha *et al.*, 2010), and quantify hydrodynamic scattering upon traversing a microchannel backstep (Montenegro-Johnson *et al.*, 2015). Here, inclusion of mechanical twist necessitates tracking both the orthonormal director frame (which describes the orientation of the flagellum) and the twist curvature. These additions dramatically increase the complexity of the SPX over other centreline models and the aforementioned EIF approach, but enables for the first time investigations into non-planar swimming near rigid boundaries. In section 4.4, the SPX is used to simulate

a variety of progressive cells actuated through a dynamic 'twist and bend' procedure originating within the axonemal ultrastructure. In doing so, we highlight the intricate balance between geometry, elasticity and hydrodynamics crucial to promoting successful sperm locomotion. In section 4.4.2, we examine the hydrodynamic impact of a proximal plane wall upon axial rolling (exhibited by nonplanar swimming cells). We find that the rate of cell rolling is determined by effective twist resistance and angle of approach towards the wall, and that wall effects reduce rates of revolution by up to 40% compared to identical cells swimming in an infinite fluid.

The SPX could be extended in various ways. Allowing for anisotropic bending stiffness, through reformulation of the model unknowns, may improve the regulation and stability of nonplanar beats through better mechanical likeness to the 9+2 axoneme. Additionally, the SPX can only simulate a single cell. Whilst nonlocal hydrodynamic effects between multiple cells are straightforward to implement (as discussed in chapter 2), a monolithic approach in SPX as used in the EIF extension to multiple filaments would rapidly produce extremely large matrix systems due to the larger degrees of freedom required to describe a cell in the SPX formulation as opposed to the EIF. These complexities could be addressed by employing a fast-multipole or RPY-tensor approach for the far field hydrodynamics, previously used with success in modelling large numbers of interacting filaments and cells (Delmotte *et al.*, 2015b; Schoeller *et al.*, 2021). Computational expense resulting from large linear systems could be managed effectively and efficiently by utilising GPUs, recently shown to enable large speed increases in fluid simulations over comparable CPU-driven experiments (Gallagher & Smith, 2020). Temporal accuracy and stability could be improved by employing a higher-order time stepping scheme, such as a Crank-Nicolson or Runge-Kutta method, at the expensive of more complex temporal discretisations, with particular care required

when treating those equations containing time derivatives of multiple variables. Alternatively, ImEx (Implicit-Explicit) methods have been used to great effect in many previous models (Camalet & Jülicher, 2000; Tornberg & Shelley, 2004; Gadêlha *et al.*, 2010; Montenegro-Johnson *et al.*, 2015) and could reduce computational expense whilst improving accuracy. Other previously discussed improvements to the EIF, such as inclusion of a Lennard-Jones potential to avoid self-intersections, or far-field flow coarse graining, are equally applicable to the SPX.

A number of potential avenues for further study are possible. Some key questions include, (i) how do changes in the viscoelastic swimming parameter change twisting and bending cells? (ii) For a given swimming parameter, what collection of parameters optimise the cell for speed and efficiency when locomoting with a nonplanar beat? (iii) With the effect of head morphology on planar beating investigated in chapter 3, how does body shape impact the motion of nonplanar beating cells, and is a head that is optimal for planar beating similarly effective for a rolling, twisting cell? And (iv) how can SPX be applied to model other (potentially multiflagelleted) cells?

The SPX can be immediately applied to many problems comprising biologically-driven fluids and slender bodies, including (but not limited to) the modelling of cilia (Gueron & Liron, 1993; Pozrikidis, 2011; Sartori *et al.*, 2016a; Gallagher *et al.*, 2020), stability analysis of stretching and twisting polymer chains (Wolgemuth *et al.*, 2004; Jayaraman *et al.*, 2012), cell swimming in the presence of geometrically complex rigid boundaries (Montenegro-Johnson *et al.*, 2015; Walker *et al.*, 2019), as well to as biotechnological innovations such as phoretic swimmers (Katsamba *et al.*, 2020). It is our hope that the code (provided via open-source repository (Hall-McNair, 2021)) is used by peers working within the larger mathematical biology worldwide community to expedite their own studies and inspire pioneering research.

5.3 Closing remarks

In this thesis, we have introduced, derived, and benchmarked two new modelling frameworks for elastohydrodynamic problems, labelled the EIF and SPX respectively. Particular focus has been on modelling both planar and nonplanar human spermatozoa, actuated through a variety of physiologically realistic means in both infinite fluid and in proximity of a rigid boundary. Through a broad simulation study using the EIF, we have assessed the effect of head shape upon sperm speed and efficiency, for morphologies common to both healthy and defective cell types, leading to the proposal of new metrics to determine cell viability, with applications in cell classification methods. The axial rolling behaviour exhibited by spermatozoa driven by an actively bending and twisting flagellum, particularly upon approaching a wall, enables new possibilities for simulations of nonplanarly beating cells near boundaries, and providing useful insights for researchers and technicians alike in designing microtubule devices for cell selection.

Both of the presented methods are accurate, performant, and generalisable, allowing for their use in a variety of other microbiological fluid flow problems in addition to the examples presented in this thesis. The approaches are presented in detail, with the aim of clearly describing the complex mathematical derivations so that they may be adapted for future research in the rich world of slender body elastohydrodynamics, and provide insights useful to both experimentalists and clinicians. Finally, MATLAB® codes implementing the numerical schemes for both methods are made available via open-source repositories (Hall-McNair, 2019, 2021). It is our hope that these codes are used, modified, inspected and critiqued to benefit future researchers in the field, and aid them in their own scientific endeavours.

Appendix A

Deriving the three-dimensional geometric compatibility equations

In chapter 1, we present the compatibility equations relating slender body curvature and angular rotation. These equations are crucial in closing the formulation of the SPX method in chapter 4. In this appendix, the equations (1.74a–1.74c) are derived. The argument here follows from Gueron & Levit-Gurevich (2001b) and Wolgemuth *et al.* (2004), with minor typographical corrections.

We begin by reaffirming equations for the components of curvature and angular rotation. The director frame of the filament is the collection of orthonormal vectors $\mathbf{d}_1$, $\mathbf{d}_2$ and $\mathbf{d}_3 = \boldsymbol{X}_s$, where $\boldsymbol{X} = \boldsymbol{X}(s)$ are material points along the centreline, parametrised by arclength s. As in chapter 1, time dependence of all variables is suppressed for notational clarity. The frame rotates along the filament length according to the curvatures $\boldsymbol{\kappa} = \kappa_i \mathbf{d}_i$ and rotates in time according to the angular velocities $\boldsymbol{\Omega} = \Omega_i \mathbf{d}_i$, as

$$\mathbf{d}_{i,s} = \boldsymbol{\kappa} \wedge \mathbf{d}_i, \qquad \mathbf{d}_{i,t} = \boldsymbol{\Omega} \wedge \mathbf{d}_i. \tag{A.1}$$

These relations yield equations for the components of curvature and angular velocity

as

$$\kappa_1 = \mathbf{d}_{2,s} \cdot \mathbf{d}_3, \qquad \Omega_1 = \mathbf{d}_{2,t} \cdot \mathbf{d}_3, \tag{A.2a}$$

$$\kappa_2 = \mathbf{d}_{3,s} \cdot \mathbf{d}_1, \qquad \Omega_2 = \mathbf{d}_{3,t} \cdot \mathbf{d}_1, \tag{A.2b}$$

$$\kappa_3 = \mathbf{d}_{1,s} \cdot \mathbf{d}_2, \qquad \Omega_3 = \mathbf{d}_{1,t} \cdot \mathbf{d}_2, \tag{A.2c}$$

Additionally, note that since $\mathbf{d}_i \cdot \mathbf{d}_j = \delta_{ij}$, we obtain an additional identity

$$(\mathbf{d}_1 \cdot \mathbf{d}_2)_t = \mathbf{d}_{1,t} \cdot \mathbf{d}_2 + \mathbf{d}_1 \cdot \mathbf{d}_{2,t} = (\delta_{12})_t = 0, \tag{A.3a}$$

$$\implies \mathbf{d}_{1,t} \cdot \mathbf{d}_2 = -\mathbf{d}_1 \cdot \mathbf{d}_{2,t}. \tag{A.3b}$$

Similarly, $\mathbf{d}_{1,s} \cdot \mathbf{d}_2 = -\mathbf{d}_1 \cdot \mathbf{d}_{2,s}$. These relations are used repeatedly throughout the following derivations. The compatibility equations are calculated by differentiating the components of curvature given in equations (A.2a–A.2c) with respect to time. We consider each component in turn. Then,

$$\kappa_{1,t} = (\mathbf{d}_{2,s} \cdot \mathbf{d}_3)_t = (-\mathbf{d}_2 \cdot \mathbf{d}_{3,s})_t, \tag{A.4a}$$

$$= -\mathbf{d}_{2,t} \cdot \mathbf{d}_{3,s} - \mathbf{d}_2 \cdot \mathbf{d}_{3,st}, \tag{A.4b}$$

$$= (\Omega_3 \mathbf{d}_1 - \Omega_1 \mathbf{d}_3) \cdot \mathbf{d}_{3,s} - \mathbf{d}_2 \cdot \boldsymbol{X}_{sst}, \tag{A.4c}$$

$$= \Omega_3 \mathbf{d}_1 \cdot \mathbf{d}_{3,s} - \mathbf{d}_2 \cdot \boldsymbol{X}_{sst} = \Omega_3 \kappa_2 - \mathbf{d}_2 \cdot \boldsymbol{X}_{sst}. \tag{A.4d}$$

The second compatibility equation is computed in a similar manner as

$$\kappa_{2,t} = (\mathbf{d}_{3,s} \cdot \mathbf{d}_1)_t, \tag{A.5a}$$

$$= (\mathbf{d}_{3,t} \cdot \mathbf{d}_1 + \mathbf{d}_{3,s} \cdot \mathbf{d}_{1,t}), \tag{A.5b}$$

$$= (\Omega_3 \mathbf{d}_2 - \Omega_2 \mathbf{d}_3) \cdot \mathbf{d}_{3,s} + \mathbf{d}_1 \cdot \boldsymbol{X}_{sst}, \tag{A.5c}$$

$$= \Omega_3 \mathbf{d}_2 \cdot \mathbf{d}_{3,s} + \mathbf{d}_1 \cdot \boldsymbol{X}_{sst} = -\Omega_3 \kappa_1 + \mathbf{d}_1 \cdot \boldsymbol{X}_{sst}. \tag{A.5d}$$

The final condition is more involved, but follows the same logical arguments to yield

$$\kappa_{3,t} = (\mathbf{d}_{1,s} \cdot \mathbf{d}_2)_t = \mathbf{d}_{1,st} \cdot \mathbf{d}_2 + \mathbf{d}_{1,s} \cdot \mathbf{d}_{2,t} \tag{A.6a}$$

$$= (\Omega_3 \mathbf{d}_2 - \Omega_2 \mathbf{d}_3)_s \cdot \mathbf{d}_2 + (\kappa_3 \mathbf{d}_2 - \kappa_2 \mathbf{d}_3) \cdot \mathbf{d}_{2,t}, \tag{A.6b}$$

$$= (\Omega_{3,s} \cdot \mathbf{d}_2 + \Omega_3 \mathbf{d}_{2,s} - \Omega_{2,s} \cdot \mathbf{d}_3 - \Omega_2 \mathbf{d}_{3,s}) \cdot \mathbf{d}_2 - \kappa_2 \mathbf{d}_3 \cdot \mathbf{d}_{2,t}, \tag{A.6c}$$

$$= \Omega_{3,s} - \Omega_2 \mathbf{d}_{3,s} \cdot \mathbf{d}_2 - \kappa_2 \Omega_1, \tag{A.6d}$$

$$= \Omega_{3,s} + \Omega_2 \kappa_1 - \kappa_2 \Omega_1. \tag{A.6e}$$

Noting that $\Omega_1 = \mathbf{d}_{2,t} \cdot \mathbf{d}_3 = -\mathbf{d}_2 \cdot \mathbf{d}_{3,t}$, and $\mathbf{d}_3 = \boldsymbol{X}_s$, this can be further simplified to obtain

$$\kappa_{3,t} = \Omega_{3,s} + \kappa_1 \mathbf{d}_1 \cdot \boldsymbol{X}_{st} + \kappa_2 \mathbf{d}_2 \cdot \boldsymbol{X}_{st}, \tag{A.7a}$$

$$= \Omega_{3,s} + (\kappa_1 \mathbf{d}_1 + \kappa_2 \mathbf{d}_2) \cdot \boldsymbol{X}_{st}, \tag{A.7b}$$

$$= \Omega_{3,s} + (\boldsymbol{X}_s \wedge \boldsymbol{X}_{ss}) \cdot \boldsymbol{X}_{st}, \tag{A.7c}$$

with the bending moment equivalency in the final step following from the discussion in section 1.3.1 and Landau & Lifshitz (1965).

Appendix B

A bead and spring method for elastic filaments

The bead and link model is used in chapter 2 of this thesis as a baseline against which to assess the accuracy of both the EIF and SPX methods for a passively relaxing filament experiment (see section 2.3.1 and 4.3.1). In this appendix we define and verify the BSM as it is employed within this thesis.

Based upon work by Jayaraman *et al.* (2012), the filament is modelled as a chain of discrete spherical beads connected by elastic Hookean springs, with elastic bending and inextensibility properties fulfilled by a prescribed force potential at each bead. Bead and spring models have been extensively used in polymer modelling (see section 1.4.2 for examples), and where the requirement of fibre inextensibility is less essential (Wolgemuth *et al.*, 2004). A sketch of the construction is given in figure B.1. For a chain of N beads placed along the centreline of a planar filament, the n^{th} bead experiences

the force

$$\begin{aligned} \boldsymbol{f}_e[n](t) &= -\frac{\partial \mathcal{E}}{\partial \boldsymbol{X}[n]}, \\ &= -\frac{\partial}{\partial \boldsymbol{X}[n]}\left(\sum_{m=1}^{N-1}\frac{\mathcal{K}}{2}(b[m](t)-b_0)^2+\sum_{m=1}^{N-2}(N-1)\big(1-\cos\alpha[m](t)\big)\right), \end{aligned} \tag{B.1}$$

for $n = 1, \dots, N-1$, and where

$$b[m](t) = \|\boldsymbol{b}[m](t)\| := \|\boldsymbol{X}[m+1](t) - \boldsymbol{X}[m](t)\|, \qquad m = 1, \dots, N-1, \tag{B.2}$$

is the size of the *bond vector* between adjacent beads. The bead separation at elastic equilibrium is denoted by b_0. The angle α is the angle formed between the tangents at adjacent beads. Filament flexibility is described by the dimensionless group

$$\mathcal{K} = \frac{kL^3}{E} = \frac{\text{spring forces}}{\text{bending forces}}, \tag{B.3}$$

where k is the Hookean spring constant of the structural springs, with a single value common to all springs in the model, and E is the mechanical bending rigidity of the filament. To ensure inextensibility, very large values of k are typically required. Beads are sized so that their diameter matches the radius of the filament, ensuring the correct aspect ratio.

In Stokes flow, the filament is force and moment free at each instant, and so elastic forces must balance hydrodynamic forces i.e. $\boldsymbol{f}_e + \boldsymbol{f}_h = \boldsymbol{0}$, where $\boldsymbol{f}_e$ is the elastic force density and $\boldsymbol{f}_h$ the hydrodynamic force density. Employing the method of regularised stokeslets (Cortez, 2001; Cortez *et al.*, 2005), the dimensionless velocity of each bead is

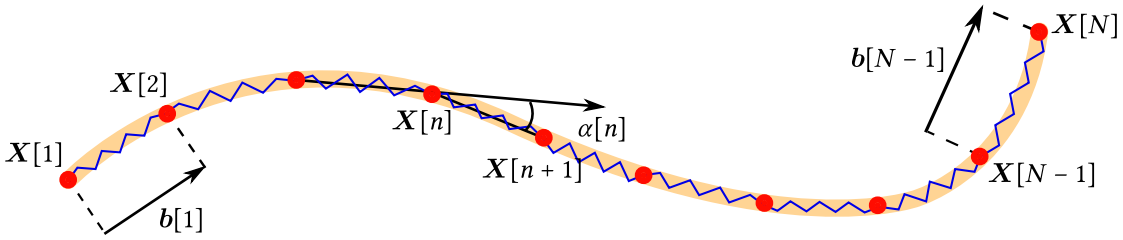

Figure B.1: Geometry of a continuous filament as approximated by the discrete bead and spring model. Spherical beads with centres $\boldsymbol{X}[1], \dots, \boldsymbol{X}[N]$ are connected by Hookean springs with resting length b_0 and spring constant k. The bond vectors $\boldsymbol{b}[n] = \boldsymbol{X}[n+1] - \boldsymbol{X}[n]$ indicate the direction of the linear springs.

then given

$$\boldsymbol{X}_t[n](t) = \frac{1}{8\pi} \sum_{m=1}^{N} S^{\varepsilon}\big(\boldsymbol{X}[n](t), \boldsymbol{X}[m](t)\big) \cdot \boldsymbol{f}_e[n](t), \qquad n = 1, \dots, N, \tag{B.4}$$

with the force per unit length $\boldsymbol{f}_e$ given in equation (B.1). Given a discrete configuration, the elastic forces per unit length are calculable through (B.1), at which point equation (B.4) is integrated in time to obtain updated bead positions.

To assess the BSM formulation, a planarly relaxing low amplitude parabolic filament is considered, which, assuming a local hydrodynamic drag law, can be expressed as a hyperdiffusive partial differential equation IBVP, given by

$$y_t(x,t) = -\frac{8\pi\mu}{c_\perp} y_{xxxx}(x,t), \qquad x \in [0,1],\ t > 0, \tag{B.5a}$$

$$y_{xx}(0,t) = y_{xx}(1,t) = 0, \qquad t > 0, \tag{B.5b}$$

$$y_{xxx}(0,t) = y_{xxx}(1,t) = 0, \qquad t > 0, \tag{B.5c}$$

$$y(x,0) = g(x), \qquad x \in [0,1], \tag{B.5d}$$

where $g(x)$ defines the deformed initial condition of the filament. The normal resis-

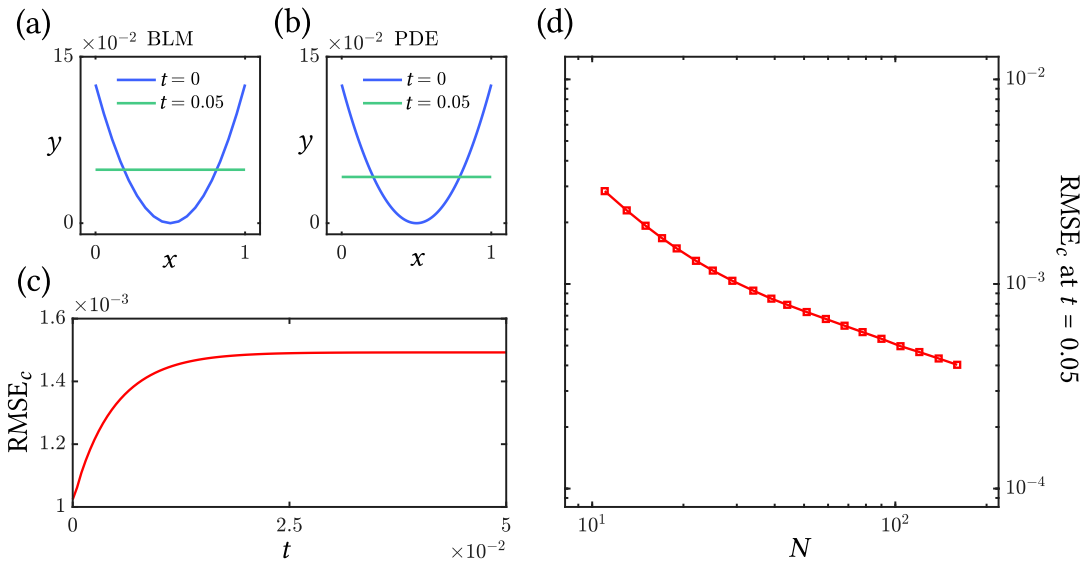

Figure B.2: Comparison of the bead and spring model (BSM) to a finite difference implementation of the hyperdiffusion PDE for a low amplitude relaxing filament. (a) and (b): The initial and final fibre shapes when modelled with each method. (c) RMS error between the coordinates of the centres of mass over time between the BSM solution (with $N = 41$) and the finite difference solution with grid spacings $\Delta x = 2\times10^{-3}, \Delta t = 1\times10^{-6}$. (d) RMSE$_c$ convergence at $t = 0.05$ for increasing N.

tive force coefficient is $c_\perp = 4\pi\mu/(1/2 + \log(2q/a))$ where $a = 0.01$ is the radius of the filament and q is the characteristic wavelength of deformation, set to be $L/2$. The system in equations (B.5a)–(B.5d) is numerically implemented using second-order central differences in space and the backward Euler method in time. The initial condition is given by the parabola $g(x) = 0.5(x - 0.5)^2$.

Results of the comparison between the hyperdiffusive equation and the bead and link model are presented in figure B.2. The initial larger errors between these two methods is sue to the violation of the no-penetration condition when using coarse discretisations in the BSM. The bead model is accurate for sufficiently large N, with clear convergence to the numerical implementation of the hyperdiffusion equation

model shown in B.2d.

The requirement for large values of $\mathcal{K}$, and the resulting numerical stiffness, produces a computationally expensive method for modelling naturally inextensible biological filaments. Furthermore, shape dynamics can only be accurately captured for fine discretisations using lots of beads, increasing the degrees of freedom for adequate accuracy and increasing this cost. The discrete construction of the bead and spring method makes additional problems such as those involving surrounding flows, body forces, or active propulsion, nontrivial to formulate, as they must derive from discrete formulations of naturally continuous problems. These limitations are crucial in motivating the alternative EIF framework discussed in chapter 2 of this thesis.

Appendix C

Hydrodynamic velocity of a rod via a resistance drag law

In the classical resistive force theory of Gray & Hancock (1955), the hydrodynamic force acting on a slender body is described by considering the velocity of the rod in each direction associated with a frame describing the orientation of the rod in space. That is,

$$\boldsymbol{f} = (c_{\perp}\mathbf{nn} + c_{\perp}\mathbf{bb} + c_{\parallel}\mathbf{tt}) \cdot \boldsymbol{u}, \tag{C.1}$$

where $\mathbf{n}$, $\mathbf{b}$ and $\mathbf{t}$ are the unit normal, unit binormal, and unit tangent vectors to the rod respectively. The rod velocity is $\boldsymbol{u}$, $\boldsymbol{f}$ is the hydrodynamic force per unit length the rod exerts onto the surrounding fluid, and $\mathbf{tt} := \mathbf{t} \otimes \mathbf{t}$ is a dyadic product (similarly for $\mathbf{nn}$ and $\mathbf{bb}$). The parameters $c_{\perp}$ and $c_{\parallel}$ are resistance coefficients, the values of which vary with rod dimensions, as well as the accuracy of the hydrodynamic approximation (see section 1.1.2 for details). A sketch of this model applied to human sperm is provided in figure 1.2.

Since the mobility problems considered in this thesis often involve unknown body forces, we desire an equation for the velocity $\boldsymbol{u}$ in terms of $\boldsymbol{f}$, rather than an equation

for $\boldsymbol{f}$ in terms of $\boldsymbol{u}$. Rearranging,

$$\boldsymbol{f} = \Big(c_\perp \mathbf{nn}\cdot\boldsymbol{u} + c_\perp \mathbf{bb}\cdot\boldsymbol{u} + c_\parallel \mathbf{tt}\cdot\boldsymbol{u}\Big), \tag{C.2a}$$

$$= \Big(c_\perp(\boldsymbol{u}\cdot\mathbf{n})\mathbf{n} + c_\perp(\boldsymbol{u}\cdot\mathbf{b})\mathbf{b} + c_\parallel(\boldsymbol{u}\cdot\mathbf{t})\mathbf{t}\Big), \tag{C.2b}$$

$$= c_\perp\Big((\boldsymbol{u} - (\boldsymbol{u}\cdot\mathbf{t})\mathbf{t} - (\boldsymbol{u}\cdot\mathbf{b})\mathbf{b}) + (\boldsymbol{u}\cdot\mathbf{b})\mathbf{b} + \gamma^{-1}(\boldsymbol{u}\cdot\mathbf{t})\mathbf{t}\Big), \tag{C.2c}$$

$$= c_\perp\Big(I + (\gamma^{-1}-1)\mathbf{tt}\Big)\cdot\boldsymbol{u}, \tag{C.2d}$$

$$= c_\perp\left[I + \left(\frac{1-\gamma}{\gamma}\right)\mathbf{tt}\right]\cdot\boldsymbol{u}, \tag{C.2e}$$

$$\implies \boldsymbol{u} = \frac{1}{c_\perp}\left[I + \left(\frac{1-\gamma}{\gamma}\right)\mathbf{tt}\right]^{-1}\cdot\boldsymbol{f}, \tag{C.2f}$$

where I is the three dimensional identity matrix, and $\gamma = c_\perp/c_\parallel$ (sometimes referred to as the *anisotropy ratio*). We write the velocity decomposed into components i.e. $\boldsymbol{u} = (\boldsymbol{u}\cdot\mathbf{t})\mathbf{t} + (\boldsymbol{u}\cdot\mathbf{b})\mathbf{b} + (\boldsymbol{u}\cdot\mathbf{n})\mathbf{n}$ to eliminate the nontangential dyadic products. To compute the inverse on the final line, consider

$$\left[I + \left(\frac{1-\gamma}{\gamma}\right)\mathbf{tt}\right]\cdot(I - \alpha\mathbf{tt}) = I + \left[-\alpha + \frac{1-\gamma}{\gamma} - \alpha\left(\frac{1-\gamma}{\gamma}\right)\right]\mathbf{tt}, \tag{C.3}$$

for some α. By inspection we must have that

$$-\alpha + \frac{1-\gamma}{\gamma} - \alpha\left(\frac{1-\gamma}{\gamma}\right) = 0, \tag{C.4a}$$

$$\implies \alpha = \frac{1-\gamma}{\gamma\left(1 + \frac{1-\gamma}{\gamma}\right)} = 1-\gamma, \tag{C.4b}$$

and thus the desired inverse operator is

$$\left[I + \frac{1-\gamma}{\gamma}\mathbf{tt}\right]^{-1} = I - (1-\gamma)\mathbf{tt} = I + (\gamma-1)\mathbf{tt}. \tag{C.5}$$

We can therefore write

$$\boldsymbol{u} = \frac{1}{c_\perp}\big(I + (\gamma - 1)\mathbf{tt}\big) \cdot \boldsymbol{f}, \tag{C.6}$$

expressing the hydrodynamic velocity $\boldsymbol{u}$ in terms of the hydrodynamic force per unit length exerted by the filament on the fluid $\boldsymbol{f}$, the tangents $\mathbf{t}$, and resistance parameters $c_\perp$ and $\gamma = c_\perp / c_\parallel$.

Appendix D

Angle formulation model with a local hydrodynamic approximation

The elastohydrodynamic integral formulation (EIF) model for planar elastic filaments, as defined in section 2.2, employs the method of regularised stokeslets to model nonlocal hydrodynamic interactions of the fibre with itself, other filaments, and surrounding structures. In section 2.3.1, the EIF is compared to a version of itself which instead uses a local hydrodynamic model.

The hydrodynamic force per unit length acting on a planar linear rod can be written in terms of the velocity as (details in appendix C)

$$\boldsymbol{f} = c_{\parallel}(\boldsymbol{u}\cdot\mathbf{t})\mathbf{t} + c_{\perp}(\boldsymbol{u}\cdot\mathbf{n})\mathbf{n}, \tag{D.1a}$$

$$\implies \boldsymbol{f} = c_{\parallel}\big(\mathbf{tt} + \gamma(I - \mathbf{tt})\big)\cdot\boldsymbol{u}, \tag{D.1b}$$

where $\mathbf{t}$ and $\mathbf{n}$ are unit vectors tangential and normal to the rod, and where $\gamma = c_{\perp}/c_{\parallel}$ is the *anisotropy ratio*. Filament planarity means that $\boldsymbol{u}\cdot\mathbf{b} = 0$, hence the lack of binormal terms in equation (D.1b). The resistance coefficients $c_{\perp}$ and $c_{\parallel}$ are chosen according to the choice of hydrodynamic model. The dyadic product is defined $\mathbf{tt} := \mathbf{t}\otimes\mathbf{t}$. In section

2.3.1, following Lighthill (1975) and Moreau *et al.* (2018), we choose

$$c_{\parallel} = \frac{2\pi\mu}{-1/2 + \log(2q/b)}, \qquad \gamma \approx 1.8, \tag{D.2}$$

where $q = 0.1$ and $b = 0.01$ is the radius of the filament. In the EIF, the continuous geometrically nonlinear filament is modelled as a connected sequence of linear rods. For a sequence of $m = 1, \dots, Q$ linear segments with tangents $\mathbf{t}[m] = \big(t_1[m], t_2[m]\big)$ and velocities $\tilde{\boldsymbol{u}} = \big(\tilde{u}_1[m], \tilde{u}_2[m]\big)$ (where a tilde indicates measurement at the segment midpoints), the component of velocity in the tangential direction can be written

$$\big(\tilde{u}[m] \cdot \mathbf{t}[m]\big)\mathbf{t}[m] = \begin{pmatrix} \tilde{u}_1[m]t_1^2[m] + \tilde{u}_2[m]t_1[m]t_2[m] \\ \tilde{u}_1[m]t_1[m]t_2[m] + \tilde{u}_2[m]t_2^2[m] \end{pmatrix}. \tag{D.3}$$

Ordering the tangent and velocity vectors by components enables the hydrodynamic problem to be written as a $2Q \times 2Q$ system of linear equations. The resistive force equation is thus

$$\tilde{\boldsymbol{F}} = c_{\parallel}\big[\boldsymbol{T}\boldsymbol{T} + \gamma(I - \boldsymbol{T}\boldsymbol{T})\big] \cdot \tilde{\boldsymbol{U}} = C\tilde{\boldsymbol{U}}, \tag{D.4a}$$

$$\implies \tilde{\boldsymbol{U}} = C^{-1}\tilde{\boldsymbol{F}}, \tag{D.4b}$$

where $\tilde{\boldsymbol{F}} = \big(\tilde{f}_1[1], \dots, \tilde{f}_1[Q], \tilde{f}_2[1], \dots, \tilde{f}_2[Q]\big)^T$ is the $2Q$ column vector of forces per unit length acting upon each segment comprising the filament. In this way, by replacing the hydrodynamic matrix block A_H with C^{-1} in equation (2.35), we obtain an version of the EIF using resistive force theory. The kinematic, geometric, and elastic equations remain unaltered from their definitions in section 2.2.

Appendix E

Steps in the derivation of the three dimensional centreline model

In chapter 3 we propose the elastohydrodynamic model

$$\xi_{\perp}(\boldsymbol{X}_t - \boldsymbol{V}) = \left(\boldsymbol{I} + (\gamma - 1)\boldsymbol{X}_s\boldsymbol{X}_s\right) \cdot \left(- E\boldsymbol{X}_{ssss} + C[\kappa_3(\boldsymbol{X}_s \wedge \boldsymbol{X}_{ss})]_s + [T\boldsymbol{X}_s]_s + [\boldsymbol{X}_s \wedge \boldsymbol{m}]_s\right), \quad \text{(E.1)}$$

which is then manipulated to obtain an the nonlocal sperm equation in (4.17), as well as an auxiliary equation for the internal tension T, given in (4.19). In this appendix, we detail the steps in the derivation of each of these equations. For brevity we assume that the bending stiffness is constant along the flagellum, but the steps to obtain the additional terms arising from a varying stiffness model follow in the same manner.

We consider the expansion of (E.1) term by term. The fourth-order derivative term can be written

$$\left(\boldsymbol{I} + (\gamma - 1)\boldsymbol{X}_s\boldsymbol{X}_s\right) \cdot (-E\boldsymbol{X}_{ssss}) = -E\boldsymbol{X}_{ssss} - E(\gamma - 1)(\boldsymbol{X}_s \cdot \boldsymbol{X}_{ssss})\boldsymbol{X}_s, \quad \text{(E.2)}$$

recalling that the tensor product can be written $\boldsymbol{a}\boldsymbol{a} \cdot \boldsymbol{b} = (\boldsymbol{a} \cdot \boldsymbol{b})\boldsymbol{a}$. Terms involving the

tension expand as

$$\left(\boldsymbol{I} + (\gamma - 1)\boldsymbol{X}_s\boldsymbol{X}_s\right) \cdot (T\boldsymbol{X}_s)_s = \left(\boldsymbol{I} + (\gamma - 1)\boldsymbol{X}_s\boldsymbol{X}_s\right) \cdot (T_s\boldsymbol{X}_s + T\boldsymbol{X}_{ss}), \tag{E.3a}$$

$$= T_s\boldsymbol{X}_s + T\boldsymbol{X}_{ss} + T_s(\gamma - 1)(\boldsymbol{X}_s \cdot \boldsymbol{X}_s)\boldsymbol{X}_s, \tag{E.3b}$$

$$= \gamma T_s\boldsymbol{X}_s + T\boldsymbol{X}_{ss}, \tag{E.3c}$$

noting that $\boldsymbol{X}_s \cdot \boldsymbol{X}_s = 1$ and $\boldsymbol{X}_s \cdot \boldsymbol{X}_{ss} = 0$ as $\boldsymbol{X}_s \perp \boldsymbol{X}_{ss}$. Contributions from the twist terms simplify through

$$\begin{aligned}\left(\boldsymbol{I} + (\gamma - 1)\boldsymbol{X}_s\boldsymbol{X}_s\right) &\cdot C(\kappa_3\boldsymbol{X}_s \wedge \boldsymbol{X}_{ss})_s \\ &= \left(\boldsymbol{I} + (\gamma - 1)\boldsymbol{X}_s\boldsymbol{X}_s\right) \cdot (C\kappa_{3,s}\boldsymbol{X}_s \wedge \boldsymbol{X}_{ss} + C\kappa_3\boldsymbol{X}_s \wedge \boldsymbol{X}_{sss}), \\ &= C\kappa_{3,s}\boldsymbol{X}_s \wedge \boldsymbol{X}_{ss} + C\kappa_3\boldsymbol{X}_s \wedge \boldsymbol{X}_{sss},\end{aligned} \tag{E.4}$$

noting that the terms arising from the dyadic onto the cross products i.e.

$$\boldsymbol{X}_s\boldsymbol{X}_s \cdot (\boldsymbol{X}_s \wedge \boldsymbol{X}_{ss}) = [\boldsymbol{X}_s \cdot (\boldsymbol{X}_s \wedge \boldsymbol{X}_{ss})]\boldsymbol{X}_s = \boldsymbol{0}, \tag{E.5a}$$

$$\boldsymbol{X}_s\boldsymbol{X}_s \cdot (\boldsymbol{X}_s \wedge \boldsymbol{X}_{sss}) = [\boldsymbol{X}_s \cdot (\boldsymbol{X}_s \wedge \boldsymbol{X}_{sss})]\boldsymbol{X}_s = \boldsymbol{0}, \tag{E.5b}$$

are zero by properties of the triple product. The vector product between the active internal moment per unit length $\boldsymbol{m}$ and the tangent $\boldsymbol{X}_s$ contains information only on the active bending contributions since $\boldsymbol{X}_s \wedge \boldsymbol{m} = m_1\mathbf{d}_2 - m_2\mathbf{d}_1$, for m_1, m_2 scalar functions of s describing the rotation of the director frame about the $\mathbf{d}_1$ and $\mathbf{d}_2$ axes respectively.

The final expansion involving the actuation terms is then

$$\begin{aligned}\left(\boldsymbol{I} + (\gamma - 1)\boldsymbol{X}_s\boldsymbol{X}_s\right) \cdot (\boldsymbol{X}_s \wedge \boldsymbol{m})_s \\ &= \left(\boldsymbol{I} + (\gamma - 1)\boldsymbol{X}_s\boldsymbol{X}_s\right) \cdot (\boldsymbol{X}_{ss} \wedge \boldsymbol{m} + \boldsymbol{X}_s \wedge \boldsymbol{m}_s) \\ &= \boldsymbol{X}_{ss} \wedge \boldsymbol{m} + \boldsymbol{X}_s \wedge \boldsymbol{m}_s + (\gamma - 1)\boldsymbol{X}_s\boldsymbol{X}_s \cdot (\boldsymbol{X}_{ss} \wedge \boldsymbol{m}) \quad \text{(E.6)}\end{aligned}$$

Combining expressions (E.2), (E.3), (E.4) and (E.6) yields the final elastohydrodynamic equation as written in (4.17).

As discussed in section 4.2.2, the auxiliary equation for the line tension is obtained by substituting the expression for the centreline velocity from equation (4.17) into the inextensibility constraint

$$(\boldsymbol{X}_t)_s \cdot \boldsymbol{X}_s = \lambda(1 - \boldsymbol{X}_s \cdot \boldsymbol{X}_s), \quad \text{(E.7)}$$

where $\lambda \in \mathbb{R}$ is a damping parameter, analogous to a spring stiffness coefficient working to converse unit arclength. Expressing the elastohydrodynamic equation (4.17) as $\xi_\perp \boldsymbol{X}_t = \text{RHS} + \xi_\perp \boldsymbol{V}$, equation (E.7) becomes

$$\xi_\perp \lambda(1 - \boldsymbol{X}_s \cdot \boldsymbol{X}_s) - \xi_\perp \boldsymbol{V}_s \cdot \boldsymbol{X}_s = (\text{RHS})_s \cdot \boldsymbol{X}_s. \quad \text{(E.8)}$$

The right hand side of equation (E.8), substituting for the right hand side terms from equation (4.17), is

$$\begin{aligned}[-E\boldsymbol{X}_{ssss} - E(\gamma - 1)(\boldsymbol{X}_s \cdot \boldsymbol{X}_{ssss})\boldsymbol{X}_s + \gamma T_s \boldsymbol{X}_s + T\boldsymbol{X}_{ss} + \boldsymbol{X}_{ss} \wedge \boldsymbol{m} + \boldsymbol{X}_s \wedge \boldsymbol{m}_s \\ + C(\kappa_{3,s}\boldsymbol{X}_s \wedge \boldsymbol{X}_{ss} + \kappa_3 \boldsymbol{X}_s \wedge \boldsymbol{X}_{sss}) + (\gamma - 1)\boldsymbol{X}_s\boldsymbol{X}_s \cdot (\boldsymbol{X}_{ss} \wedge \boldsymbol{m})]_s \cdot \boldsymbol{X}_s. \quad \text{(E.9)}\end{aligned}$$

Terms in this expansion are reduced using differential identities deriving from succes-

sive differentiation of $\boldsymbol{X}_s \cdot \boldsymbol{X}_s = 1$. These identities are

$$\boldsymbol{X}_s \cdot \boldsymbol{X}_s = 1, \tag{ID1}$$

$$\boldsymbol{X}_s \cdot \boldsymbol{X}_{ss} = 0, \tag{ID2}$$

$$\boldsymbol{X}_s \cdot \boldsymbol{X}_{sss} + \boldsymbol{X}_{ss} \cdot \boldsymbol{X}_{ss} = 0, \tag{ID3}$$

$$\boldsymbol{X}_s \cdot \boldsymbol{X}_{ssss} + 3\boldsymbol{X}_{ss} \cdot \boldsymbol{X}_{sss} = 0, \tag{ID4}$$

$$\boldsymbol{X}_s \cdot \boldsymbol{X}_{sssss} + 4\boldsymbol{X}_{ss} \cdot \boldsymbol{X}_{ssss} + 3\boldsymbol{X}_{sss} \cdot \boldsymbol{X}_{sss} = 0. \tag{ID5}$$

We examine this expansion in stages, and begin by considering the first term

$$(-E\boldsymbol{X}_{ssss})_s \cdot \boldsymbol{X}_s = -E\boldsymbol{X}_{sssss} \cdot \boldsymbol{X}_s = 4E\boldsymbol{X}_{ss} \cdot \boldsymbol{X}_{ssss} + 3E\boldsymbol{X}_{sss} \cdot \boldsymbol{X}_{sss}, \tag{E.10}$$

where the fifth derivative is reduced by (ID5). The nonlinear bending term becomes

$$(-E(\gamma - 1)(\boldsymbol{X}_s \cdot \boldsymbol{X}_{ssss})\boldsymbol{X}_s)_s \cdot \boldsymbol{X}_s = -E(\gamma - 1)(\boldsymbol{X}_s \cdot \boldsymbol{X}_{ssss})_s, \tag{E.11a}$$

$$= -E(\gamma - 1)(\boldsymbol{X}_{ss} \cdot \boldsymbol{X}_{ssss} + \boldsymbol{X}_s \cdot \boldsymbol{X}_{sssss}), \tag{E.11b}$$

$$= E(\gamma - 1)(3\boldsymbol{X}_{ss} \cdot \boldsymbol{X}_{ssss} + 3\boldsymbol{X}_{sss} \cdot \boldsymbol{X}_{sss}), \tag{E.11c}$$

utilising (ID1), (ID2) and (ID5). Combining these terms (E.10) + (E.11c), we have

$$(-E\boldsymbol{X}_{ssss} - E(\gamma - 1)(\boldsymbol{X}_s \cdot \boldsymbol{X}_{ssss})_s)_s \cdot \boldsymbol{X}_s = E(1 + 3\gamma)\boldsymbol{X}_{ss} \cdot \boldsymbol{X}_{ssss} + 3E\gamma\boldsymbol{X}_{sss} \cdot \boldsymbol{X}_{sss}. \tag{E.12}$$

Terms involving the tension expand as

$$(\gamma T_s \boldsymbol{X}_s + T\boldsymbol{X}_{ss})_s \cdot \boldsymbol{X}_s = \gamma T_{ss}\boldsymbol{X}_s \cdot \boldsymbol{X}_s + (\gamma + 1)T_s \boldsymbol{X}_{ss} \cdot \boldsymbol{X}_s + T\boldsymbol{X}_{sss} \cdot \boldsymbol{X}_s, \tag{E.13a}$$

$$= \gamma T_{ss} - T(\boldsymbol{X}_{ss} \cdot \boldsymbol{X}_{ss}), \tag{E.13b}$$

employing (ID2) and (ID3). The first twist term,

$$C(\kappa_{3,s}\boldsymbol{X}_s \wedge \boldsymbol{X}_{ss})_s \cdot \boldsymbol{X}_s = C\kappa_{3,ss}(\boldsymbol{X}_s \wedge \boldsymbol{X}_{ss}) \cdot \boldsymbol{X}_s + C\kappa_{3,s}(\boldsymbol{X}_s \wedge \boldsymbol{X}_{sss}) \cdot \boldsymbol{X}_s = 0, \tag{E.14}$$

by triple product identities. The second twist term simplifies similarly as

$$C(\kappa_{3,s}\boldsymbol{X}_s \wedge \boldsymbol{X}_{sss})_s \cdot \boldsymbol{X}_s = C\kappa_{3,s}(\boldsymbol{X}_{ss} \wedge \boldsymbol{X}_{sss}) \cdot \boldsymbol{X}_s, \tag{E.15a}$$

$$\equiv C\kappa_{3,s}(\boldsymbol{X}_s \wedge \boldsymbol{X}_{ss}) \cdot \boldsymbol{X}_{sss}, \tag{E.15b}$$

with the final circular shift performed for numerical reasons, allowing the higher-order third derivative to be more easily treated as the unknown in the subsequent iterative linear system. The terms involving the active moment per unit length $\boldsymbol{m}$ are

$$\begin{aligned}(\boldsymbol{X}_{ss} \wedge \boldsymbol{m} + \boldsymbol{X}_s \wedge \boldsymbol{m}_s)_s \cdot \boldsymbol{X}_s \\ = (\boldsymbol{X}_{sss} \wedge \boldsymbol{m} + \boldsymbol{X}_{ss} \wedge \boldsymbol{m}_s) \cdot \boldsymbol{X}_s + (\boldsymbol{X}_{ss} \wedge \boldsymbol{m}_s + \boldsymbol{X}_s \wedge \boldsymbol{m}_{ss}) \cdot \boldsymbol{X}_s \\ = (\boldsymbol{X}_{sss} \wedge \boldsymbol{m}) \cdot \boldsymbol{X}_s + 2(\boldsymbol{X}_{ss} \wedge \boldsymbol{m}_s) \cdot \boldsymbol{X}_s.\end{aligned} \tag{E.16}$$

The active moment term including the tangent dyadic is

$$(\gamma - 1)[(\boldsymbol{X}_s \cdot (\boldsymbol{X}_{ss} \wedge \boldsymbol{m}))\boldsymbol{X}_s]_s \cdot \boldsymbol{X}_s = (\gamma - 1)\boldsymbol{X}_s \cdot (\boldsymbol{X}_{sss} \wedge \boldsymbol{m} + \boldsymbol{X}_{ss} \wedge \boldsymbol{m}_s), \tag{E.17}$$

after repeated application of the triple mixed product identity. Combining the right hand side expressions from equations (E.16) and (E.17) yields the active moment contribution to the tension equation

$$\gamma(\boldsymbol{X}_{sss} \wedge \boldsymbol{m}) \cdot \boldsymbol{X}_s + (\gamma + 1)(\boldsymbol{X}_{ss} \wedge \boldsymbol{m}_s) \cdot \boldsymbol{X}_s. \tag{E.18}$$

Combining the expressions in equations (E.12–E.18) yields the auxiliary equation as presented in (4.19).

Appendix F

Surface integral operators onto unknown forces

In the SPX method (chapter 4), we formulate the mathematical model describing an internally actuated motile sperm cell. The boundary conditions for the proximal flagellum balance the elastohydrodynamic motion of the flagellum against the force and moment of the rigid body cell head, in equations of the form

$$\iint_{\partial B} \boldsymbol{\varphi}(\boldsymbol{Y})\, dS_Y = \ldots \tag{F.1a}$$

$$\left(\iint_{\partial B} (\boldsymbol{Y} - \boldsymbol{X}_0) \wedge \boldsymbol{\varphi}(\boldsymbol{Y})\, dS_Y \right) \wedge \boldsymbol{X}_s(0) = \ldots \tag{F.1b}$$

$$\left(\iint_{\partial B} (\boldsymbol{Y} - \boldsymbol{X}_0) \wedge \boldsymbol{\varphi}(\boldsymbol{Y})\, dS_Y \right) \cdot \boldsymbol{X}_s(0) = \ldots \tag{F.1c}$$

for the force, bending moment, and twist moment respectively, with ellipses representing terms describing the proximal motion of the flagellum.

After spatial discretisation using the nearest-neighbour regularised stokeslet method, an operator onto the body forces from the force boundary condition (equation (F.1a)) is readily obtainable. However, reorganising the moment boundary conditions

as operators multiplying onto the forces is not trivial. Here, we consider an analytical expansion of the expression on the left hand side of (F.1b) so that the required numerical method is more readily apparent. A similar (and simpler) expansion is obtainable for equation (F.1c), but is not considered here.

We desire to compute

$$\left(\iint_{\partial B} (\boldsymbol{Y} - \boldsymbol{X}_0) \wedge \boldsymbol{\varphi} \, dS_Y \right) \wedge \boldsymbol{X}_0. \tag{F.2}$$

Rewriting the above in index notation, we have the equivalent problem, using the Levi-Civita symbol

$$\epsilon_{ijk} M_j^B t_k = -\epsilon_{ijk} t_j M_k^B = -\epsilon_{ijk} t_j \left(\iint_{dB} \epsilon_{klm} \Delta Y_l \varphi_m dS \right), \tag{F.3}$$

summing over the repeated indices j, k, l, m, and for $i = 1, 2, 3$, where M_i^B are the components of the surface integral over the cell body. The substitutions $\Delta Y_i = Y_i - X_i(0)$, $t_i = X_{i,s}(0)$, and $dS = dS_Y$ are made for notational convenience and clarity. By way of example, we consider the first ($i = 1$) component, which is

$$-\epsilon_{1jk} t_j M_k^B = -\epsilon_{123} t_2 M_3 - \epsilon_{132} t_3 M_2 = -t_2 M_3 + t_3 M_2 \tag{F.4a}$$

$$= -t_2 \left(\iint_{\partial B} \epsilon_{3lm} \Delta Y_l \varphi_m dS \right) + t_3 \left(\iint_{\partial B} \epsilon_{2lm} \Delta Y_l \varphi_m dS \right) \tag{F.4b}$$

$$= -t_2 \iint_{\partial B} (\Delta Y_1 \varphi_2 - \Delta Y_2 \varphi_1) dS + t_3 \iint_{\partial B} (\Delta Y_3 \varphi_1 - \Delta Y_1 \varphi_3) dS. \tag{F.4c}$$

The second and third components can be computed similarly as

$$-\epsilon_{2jk} t_j M_k^B = t_1 \iint_{\partial B} (\Delta Y_1 \varphi_2 - \Delta Y_2 \varphi_1) dS - t_3 \iint_{\partial B} (\Delta Y_2 \varphi_3 - \Delta Y_3 \varphi_2) dS, \tag{F.5}$$

$$-\epsilon_{3jk} t_j M_k^B = -t_1 \iint_{\partial B} (\Delta Y_3 \varphi_1 - \Delta Y_1 \varphi_3) dS + t_2 \iint_{\partial B} (\Delta Y_2 \varphi_3 - \Delta Y_3 \varphi_2) dS. \tag{F.6}$$

The component expressions in equations (F.4c)–(F.6), after spatial discretisation, more readily lend themselves as linear operators onto the unknown force components $\varphi_i[1], \dots, \varphi_i[N]$, forming the left hand side of the proximal bending moment boundary conditions (equation (4.54c)) for the elastohydrodynamic model. Component expressions for the components of the proximal twist moment boundary condition (equation (4.54d)) can be derived through a similar procedure as described above.

List of References

D. J. Acheson. *Elementary fluid dynamics.* Clarendon Press Oxford, 1991.

B. Afzelius. Electron microscopy of the sperm tail results obtained with a new fixative. *J. Exp. Biol.*, 5(2):269–278, 1959.

J. Ainley, S. Durkin, R. Embid, P. Boindala, & R. Cortez. The method of images for regularized Stokeslets. *J. Comput. Phys.*, 227(9):4600–4616, 2008.

B. Audoly & Y. Pomeau. *Elasticity and geometry: from hair curls to the non-linear response of shells.* Oxford University Press, 2010.

A. G. Bailey, C. P. Lowe, & A. P. Sutton. Efficient constraint dynamics using MILC SHAKE. *J. Comput. Phys.*, 227(20):8949–8959, 2008.

E. Ballowitz. Untersuchungen über die Struktur der Spermatozoën, zugleich ein Beitrag zur Lehre vom feineren Bau der contraktilen Elemente (*Investigations into the structure of the spermatozoa, and a contribution to the theory of the finer structure of the contractile elements*). *Arch. Mikrosk. Anat.*, 32(1):401–473, 1888.

P. V. Bayly & K. S Wilson. Analysis of unstable modes distinguishes mathematical models of flagellar motion. *J. R. Soc. Interface*, 12(106):20150124, 2015.

L. E. Becker & M. J. Shelley. Instability of elastic filaments in shear flow yields first-normal-stress differences. *Phys. Rev. Lett.*, 87(19):198301, 2001.

T. C. Bishop, R. Cortez, & O. O. Zhmudsky. Investigation of bend and shear waves in a geometrically exact elastic rod model. *J. Comput. Phys.*, 193(2):642–665, 2004.

J. R. Blake. A note on the image system for a stokeslet in a no-slip boundary. *Math. Proc. Camb. Philos. Soc.*, 70(2):303–310, 1971. doi: 10.1017/S0305004100049902.

J. R. Blake & A. T. Chwang. Fundamental singularities of viscous flow. *J. Eng. Math.*, 8 (1):23–29, 1974.

E. L. Bouzarth, A. T. Layton, & Y-N. Young. Modeling a semi-flexible filament in cellular Stokes flow using regularized Stokeslets. *Int. J. Numer. Meth. Bio.*, 27(12):2021–2034, 2011.

A. F. Bower. *Applied mechanics of solids.* CRC press, 2009.

C. J. Brokaw. Bending moments in free-swimming flagella. *J. Exp. Biol.*, 53(2):445–464, 1970.

C. J. Brokaw. Bend propagation by a sliding filament model for flagella. *J. Exp. Biol.*, 55(2):289–304, 1971.

C. J. Brokaw. Computer simulation of flagellar movement: I. Demonstration of stable bend propagation and bend initiation by the Sliding Filament Model. *Biophys. J.*, 12 (5):564–586, 1972.

C. J. Brokaw. Automated methods for estimation of sperm flagellar bending parameters. *Cell Motil.*, 4(6):417–430, 1984.

C. J. Brokaw. Computer simulation of flagellar movement: VI. simple curvature-controlled models are incompletely specified. *Biophys. J.*, 48(4):633–642, 1985.

C. J. Brokaw. Microtubule sliding in swimming sperm flagella: direct and indirect measurements on sea urchin and tunicate spermatozoa. *J. Cell Biol.*, 114(6):1201–1215, 1991.

C. J. Brokaw. Control of flagellar bending: a new agenda based on dynein diversity. *Cell Motil. Cytoskelet.*, 28(3):199–204, 1994.

C. J. Brokaw. Computer simulation of flagellar movement: VII. Conventional but functionally different cross-bridge models for inner and outer arm dyneins can explain the effects of outer arm dynein removal. *Cell Motil. Cytoskelet.*, 42(2):134–148, 1999.

C. J. Brokaw. Simulating the effects of fluid viscosity on the behaviour of sperm flagella. *Math. Method Appl. Sci.*, 24(17-18):1351–1365, 2001.

C. J. Brokaw. Computer simulation of flagellar movement: VIII. Coordination of dynein by local curvature control can generate helical bending waves. *Cell Motil. Cytoskelet.*, 53(2):103–124, 2002.

C. J. Brokaw. Simulation of cyclic dynein-driven sliding, splitting, and reassociation in an outer doublet pair. *Biophys. J.*, 97(11):2939–2947, 2009.

S. Camalet & F. Jülicher. Generic aspects of axonemal beating. *New J. Phys.*, 2(1):24, 2000.

S. Camalet, F. Jülicher, & J. Prost. Self-organized beating and swimming of internally driven filaments. *Phys. Rev. Lett.*, 82(7):1590, 1999.

L. Carichino & S. D. Olson. Emergent three-dimensional sperm motility: coupling calcium dynamics and preferred curvature in a Kirchhoff rod model. *Math. Med. Biol.*, 36(4):439–469, 2019.

N. Coq, O. du Roure, M. Fermigier, & D. Bartolo. Helical beating of an actuated elastic filament. *J. Phys. Condens. Matter*, 21(20):204109, 2009.

R. Cortez. The method of regularized Stokeslets. *SIAM J. Sci. Comput.*, 23(4):1204–1225, 2001.

R. Cortez. Regularized stokeslet segments. *J. Comput. Phys.*, 375:783–796, 2018.

R. Cortez & D. Varela. A general system of images for regularized Stokeslets and other elements near a plane wall. *J. Comput. Phys.*, 285:41–54, 2015.

R. Cortez, L. Fauci, & A. Medovikov. The method of regularized Stokeslets in three dimensions: analysis, validation, and application to helical swimming. *Phys. Fluids*, 17(3):031504, 2005.

M. Cosentino Lagomarsino, I. Pagonabarraga, & C. P. Lowe. Hydrodynamic Induced Deformation and Orientation of a Microscopic Elastic Filament. *Phys. Rev. Lett.*, 94: 148104, 2005.

R. G. Cox. The motion of long slender bodies in a viscous fluid. Part 1. General theory. *J. Fluid Mech.*, 44(4):791–810, 1970.

R. Coy & H. Gadêlha. The counterbend dynamics of cross-linked filament bundles and flagella. *J. R. Soc. Interface*, 14(130):20170065, 2017.

J. M. Cummins & P. F. Woodall. On mammalian sperm dimensions. *Reproduction*, 75 (1):153–175, 1985.

A. H. D. M. Dam, I. Feenstra, J. R. Westphal, L. Ramos, R. J. T. Van Golde, & J. A. M. Kremer. Globozoospermia revisited. *Hum. Reprod. Update*, 13(1):63–75, 2007.

B. Delmotte, E. Climent, & F. Plouraboué. A general formulation of bead models applied to flexible fibers and active filaments at low Reynolds number. *J. Comput. Phys.*, 286: 14–37, 2015a.

B. Delmotte, E. E. Keaveny, F. Plouraboué, & E. Climent. Large-scale simulation of steady and time-dependent active suspensions with the force-coupling method. *J. Comput. Phys.*, 302:524–547, 2015b.

R. Dillon, L. Fauci, & C. Omoto. Mathematical modeling of axoneme mechanics and fluid dynamics in ciliary and sperm motility. *Dyn. Contin. Discrete Impuls. Syst. A: Math. Anal.*, 10:745–758, 2003.

R. H. Dillon & L. J. Fauci. An integrative model of internal axoneme mechanics and external fluid dynamics in ciliary beating. *J. Theor. Biol.*, 207(3):415–430, 2000.

R. H. Dillon, L. J. Fauci, C. Omoto, & X. Yang. Fluid dynamic models of flagellar and ciliary beating. *Ann. N. Y. Acad. Sci.*, 1101(1):494–505, 2007.

R. D. Dresdner & D. F. Katz. Relationships of mammalian sperm motility and morphology to hydrodynamic aspects of cell function. *Biol. Reprod.*, 25(5):920–930, 1981.

T. A. Driscoll, N. Hale, & L. N. Trefethen. *Chebfun guide*. Pafnuty Publications, Oxford, 2014.

G. J. Elfring & E. Lauga. Theory of locomotion through complex fluids. In *Complex fluids in biological systems*, pages 283–317. Springer, 2015.

L. J. Fauci & R. Dillon. Biofluidmechanics of reproduction. *Annu. Rev. Fluid Mech.*, 38: 371–394, 2006.

L. J. Fauci & A. McDonald. Sperm motility in the presence of boundaries. *Bull. Math. Bio.*, 57(5):679–699, 1995.

D. W. Fawcett. The study of epithelial cilia and sperm flagella with the electron microscope. *Laryngoscope*, 64(7):557–567, 1954.

B. M. Friedrich, I. H. Riedel-Kruse, J. Howard, & F. Jülicher. High-precision tracking of sperm swimming fine structure provides strong test of resistive force theory. *J. Exp. Biol.*, 213(8):1226–1234, 2010.

H. Gadelha. The filament-bundle elastica. *IMA J. Appl. Math.*, 83(4):634–654, 2018.

H. Gadêlha, E. A. Gaffney, D. J. Smith, & J. C. Kirkman-Brown. Nonlinear instability in flagellar dynamics: a novel modulation mechanism in sperm migration? *J. R. Soc. Interface*, 7(53):1689–1697, 2010.

H. Gadêlha, E. A. Gaffney, & A. Goriely. The counterbend phenomenon in flagellar axonemes and cross-linked filament bundles. *Proc. Natl. Acad. Sci.*, 110(30):12180–12185, 2013.

E. A. Gaffney, H. Gadêlha, D. J. Smith, J. R. Blake, & J. C. Kirkman-Brown. Mammalian sperm motility: observation and theory. *Annu. Rev. Fluid Mech.*, 43:501–528, 2011.

M. T. Gallagher & D. J. Smith. Meshfree and efficient modeling of swimming cells. *Phys. Rev. Fluids*, 3(5):053101, 2018.

M. T. Gallagher & D. J. Smith. Passively parallel regularized stokeslets. *Philos. Trans. R. Soc. A*, 378(2179):20190528, 2020.

M. T. Gallagher & D. J. Smith. The art of coarse stokes: Richardson extrapolation improves the accuracy and efficiency of the method of regularized stokeslets. *Roy. Soc. Open Sci.*, 8(5):210108, 2021.

M. T. Gallagher, D. J. Smith, & J. C. Kirkman-Brown. CASA: tracking the past and plotting the future. *Reproduction Fertil. Dev.*, 2018.

M. T. Gallagher, G. Cupples, E. H. Ooi, J. C. Kirkman-Brown, & D. J. Smith. Rapid sperm capture: high-throughput flagellar waveform analysis. *Human Reprod.*, 34(7):1173–1185, 2019.

M. T. Gallagher, T. D. Montenegro-Johnson, & D. J. Smith. Simulations of particle tracking in the oligociliated mouse node and implications for left–right symmetry-breaking mechanics. *Philos. Trans. R. Soc. B*, 375(1792):20190161, 2020.

Y. Gao, M. A. Hulsen, T. G. Kang, & J. M. J. Den Toonder. Numerical and experimental study of a rotating magnetic particle chain in a viscous fluid. *Phys. Rev. E*, 86(4): 041503, 2012.

I. R. Gibbons. Cilia and flagella of eukaryotes. *J. Cell Biol.*, 91(3):107s–124s, 1981.

E. A. Gillies, R. M. Cannon, R. B. Green, & A. A. Pacey. Hydrodynamic propulsion of human sperm. *J. Fluid Mech.*, 625:445–474, 2009.

R. E. Goldstein & S. A. Langer. Nonlinear dynamics of stiff polymers. *Phys. Rev. Lett.*, 75(6):1094, 1995.

R. E. Goldstein, T. R. Powers, & C. H. Wiggins. Viscous nonlinear dynamics of twist and writhe. *Phys. Rev. Lett.*, 80(23):5232, 1998.

A. Goriely & M. Tabor. The nonlinear dynamics of filaments. *Nonlinear Dynam*, 21(1): 101–133, 2000.

J. C. Gower. Generalized procrustes analysis. *Psychometrika*, 40(1):33–51, 1975.

G. Goyal. *Drag and thrust effects of Viscoelastic fluids.* PhD thesis, University of British Columbia, 2016.

J. Gray & G. J. Hancock. The propulsion of sea-urchin spermatozoa. *J Exp Biol*, 32(4): 802–814, 1955.

S. Gueron & K. Levit-Gurevich. Computation of the internal forces in cilia: application to ciliary motion, the effects of viscosity, and cilia interactions. *Biophys. J.*, 74(4): 1658–1676, 1998.

S. Gueron & K. Levit-Gurevich. The three-dimensional motion of slender filaments. *Math. Method Appl. Sci.*, 24(17-18):1577–1603, 2001a.

S. Gueron & K. Levit-Gurevich. A three–dimensional model for ciliary motion based on the internal 9+2 structure. *P Roy Soc Lond B Bio*, 268(1467):599–607, 2001b.

S. Gueron & N. Liron. Ciliary motion modeling, and dynamic multicilia interactions. *Biophys. J.*, 63(4):1045–1058, 1992.

S. Gueron & N. Liron. Simulations of three-dimensional ciliary beats and cilia interactions. *Biophys. J.*, 65(1):499, 1993.

A. L. Hall-McNair. MATLAB code supporting Hall-McNair (2019). `https://gitlab.com/atticushm/eif`, 2019.

A. L. Hall-McNair. MATLAB code for the SPX method. https://gitlab.com/atticushm/sperm-x, 2021.

A. L. Hall-McNair, T. D. Montenegro-Johnson, H. Gadêlha, D. J. Smith, & M. T. Gallagher. Efficient implementation of elastohydrodynamics via integral operators. *Phys. Rev. Fluids*, 4(11):113101, 2019.

J. J. L. Higdon. A hydrodynamic analysis of flagellar propulsion. *J. Fluid Mech.*, 90(4): 685–711, 1979a.

J. J. L. Higdon. The hydrodynamics of flagellar propulsion: helical waves. *J. Fluid Mech.*, 94(2):331–351, 1979b.

M. Hines & J. J. Blum. Bend propagation in flagella. I. Derivation of equations of motion and their simulation. *Biophys. J.*, 23(1):41–57, 1978.

M. Hines & J. J. Blum. Three-dimensional mechanics of eukaryotic flagella. *Biophys. J.*, 41(1):67–79, 1983.

J. Huang, L. Carichino, & S. D. Olson. Hydrodynamic interactions of actuated elastic filaments near a planar wall with applications to sperm motility. *J. Coupled Syst. Multiscale Dyn.*, 6(3):163–175, 2018.

Human Fertilisation and Embryology Authority. Fertility treatment in 2010: trends and figures, 2014. URL https://www.hfea.gov.uk/media/1783/fertility-treatment-2014-trends-and-figures.pdf.

K. Ishimoto & E. A. Gaffney. Fluid flow and sperm guidance: a simulation study of hydrodynamic sperm rheotaxis. *J. R. Soc. Interface*, 12(106):20150172, 2015.

G. Jayaraman, S. Ramachandran, S. Ghose, A. Laskar, M. S. Bhamla, P. B. S. Kumar, & R. Adhikari. Autonomous motility of active filaments due to spontaneous flow-symmetry breaking. *Phys. Rev. Lett.*, 109(15):158302, 2012.

G. B. Jeffery. The motion of ellipsoidal particles immersed in a viscous fluid. *P. R. Soc. Lond. A*, 102(715):161–179, 1922.

R. M. Jendrejack, M. D. Graham, & J. J. de Pablo. Hydrodynamic interactions in long chain polymers: Application of the Chebyshev polynomial approximation in stochastic simulations. *J. Chem. Phys.*, 113(7):2894–2900, 2000.

R. M. Jendrejack, Juan J. de P., & M. D. Graham. Stochastic simulations of DNA in flow: Dynamics and the effects of hydrodynamic interactions. *J. Chem. Phys.*, 116(17): 7752–7759, 2002.

H. Jian, A. V. Vologodskii, & T. Schlick. A combined wormlike-chain and bead model for dynamic simulations of long linear DNA. *J. Comput. Phys.*, 136(1):168–179, 1997.

R. E. Johnson & C. J. Brokaw. Flagellar hydrodynamics. a comparison between resistive-force theory and slender-body theory. *Biophys. J.*, 25(1):113–127, 1979.

V. Kantsler, J. Dunkel, M. Blayney, & R. E. Goldstein. Rheotaxis facilitates upstream navigation of mammalian sperm cells. *eLife*, 3:e02403, 2014.

P. Katsamba, S. Michelin, & T. D. Montenegro-Johnson. Slender phoretic theory of chemically active filaments. *J. Fluid Mech.*, 898:A24, 2020.

D. F. Katz & D. M. Phillips. The response of rhesus monkey sperm motility to cervical mucus and solid surfaces. *Gamete Res.*, 13(3):231–239, 1986.

D. F. Katz, J. R. Blake, & S. L. Paveri-Fontana. On the movement of slender bodies near plane boundaries at low Reynolds number. *J. Fluid Mech.*, 72(3):529–540, 1975.

S. Kim & S. J. Karrila. *Microhydrodynamics: principles and selected applications*. Courier Corporation, 2013.

I. Klapper. Biological applications of the dynamics of twisted elastic rods. *J. Comput. Phys.*, 125(2):325–337, 1996.

I. Klapper & M. Tabor. A new twist in the kinematics and elastic dynamics of thin filaments and ribbons. *J. Phys. A–Math. Gen.*, 27(14):4919, 1994.

L. D. Landau & E. M. Lifshitz. *Theory of Elasticity*. Nauka, 1965.

J. Lighthill. *Mathematical biofluiddynamics*. SIAM, 1975.

J. Lighthill. Flagellar hydrodynamics. *SIAM Rev. Soc. Ind. Appl. Math.*, 18(2):161–230, 1976.

S. Lim. Dynamics of an open elastic rod with intrinsic curvature and twist in a viscous fluid. *Phys. Fluids*, 22(2):024104, 2010.

S. Lim, A. Ferent, X. S. Wang, & C. S. Peskin. Dynamics of a closed rod with twist and bend in fluid. *SIAM J. Sci. Comput.*, 31(1):273–302, 2008.

C. B. Lindemann. A "geometric clutch" hypothesis to explain oscillations of the axoneme of cilia and flagella. *J. Theor. Biol.*, 168(2):175–189, 1994a.

C. B. Lindemann. A model of flagellar and ciliary functioning which uses the forces transverse to the axoneme as the regulator of dynein activation. *Cytoskeleton*, 29(2): 141–154, 1994b.

C. B. Lindemann. Functional significance of the outer dense fibers of mammalian sperm examined by computer simulations with the geometric clutch model. *Cell Motil. Cytoskelet.*, 34(4):258–270, 1996.

C. B. Lindemann. Geometric clutch model version 3: The role of the inner and outer arm dyneins in the ciliary beat. *Cell Motil. Cytoskelet.*, 52(4):242–254, 2002.

C. B. Lindemann. Testing the geometric clutch hypothesis. *Biol. Cell*, 96(9):681–690, 2004.

C. B. Lindemann. Heart of the beat (the flagellar beat, that is). *Biophys. J.*, 97(11):2865, 2009.

Y. Liu, B. Chakrabarti, D. Saintillan, A. Lindner, & O. du Roure. Morphological transitions of elastic filaments in shear flow. *Proc. Natl. Acad. Sci. U.S.A*, 115(38):9438–9443, 2018.

C. P. Lowe. Dynamics of filaments: modelling the dynamics of driven microfilaments. *Philos. Trans. R. Soc. B*, 358(1437):1543–1550, 2003.

K. E. Machin. Wave propagation along flagella. *J. Exp. Biol.*, 35(4):796–806, 1958.

I. Manton & B. Clarke. An Electron Microscope Study of the Spermatozoid of *Sphagnum*. *J. Exp. Bot.*, 3(9):265–275, 1952.

B. Marchetti, V. Raspa, A. Lindner, O. Du Roure, L. Bergougnoux, E. Guazzelli, & C. Duprat. Deformation of a flexible fiber settling in a quiescent viscous fluid. *Phys. Rev. Fluids*, 3(10):104102, 2018.

O. Maxian, A. Mogilner, & A. Donev. Integral-based spectral method for inextensible slender fibers in Stokes flow. *Phys. Rev. Fluids*, 6(1):014102, 2021.

A. Meunier. Friction coefficient of rod-like chains of spheres at very low Reynolds numbers. II. Numerical simulations. *J. Phys. II*, 4(4):561–566, 1994.

K. Miki & D. E. Clapham. Rheotaxis guides mammalian sperm. *Curr. Biol.*, 23(6):443–452, 2013.

T. D. Montenegro-Johnson, A. A. Smith, D. J. Smith, D. Loghin, & J. R. Blake. Modelling the fluid mechanics of cilia and flagella in reproduction and development. *Eur. Phys. J. E*, 35(10):111, 2012.

T. D. Montenegro-Johnson, H. Gadêlha, & D. J. Smith. Spermatozoa scattering by a microchannel feature: an elastohydrodynamic model. *Roy. Soc. Open Sci.*, 2(3):140475, 2015.

C. Moreau, L. Giraldi, & H. Gadêlha. The asymptotic coarse-graining formulation of slender-rods, bio-filaments and flagella. *J. R. Soc. Interface*, 15(144):20180235, 2018.

A. N. Morozov & W. van Saarloos. An introductory essay on subcritical instabilities and the transition to turbulence in visco-elastic parallel shear flows. *Phys. Rep.*, 447: 112–143, 2007.

G. P. Muldowney & J. J. L. Higdon. A spectral boundary element approach to three-dimensional Stokes flow. *J. Fluid Mech.*, 298:167–192, 1995.

C. V. Neal, A. L. Hall-McNair, J. Kirkman-Brown, D. J. Smith, & M. T. Gallagher. Doing more with less: The flagellar end piece enhances the propulsive effectiveness of human spermatozoa. *Phys. Rev. Fluids*, 5(7):073101, 2020.

H-N. Nguyen & R. Cortez. Reduction of the regularization error of the method of reg-

ularized Stokeslets for a rigid object immersed in a three-dimensional Stokes flow. *Commun. Comput. Phys.*, 15(1):126–152, 2014.

R. Nosrati, A. Driouchi, C. M. Yip, & D. Sinton. Two-dimensional slither swimming of sperm within a micrometre of a surface. *Nat. Commun.*, 6(1):1–9, 2015.

E. J. Nyström. Über die praktische Auflösung von Integralgleichungen mit Anwendungen auf Randwertaufgaben. *Acta Math.*, 54:185–204, 1930.

University of Birmingham. University of Birmingham BlueBEAR HPC service. `http://www.birmingham.ac.uk/bear`, 2021.

S. D. Olson & L. J. Fauci. Hydrodynamic interactions of sheets vs filaments: Synchronization, attraction, and alignment. *Phys. Fluids*, 27(12):121901, 2015.

S. D. Olson & K. Leiderman. Effect of fluid resistance on symmetric and asymmetric flagellar waveforms. *J. Aero Aqua Biomech.*, 4(1):12–17, 2015.

S. D. Olson, S. S. Suarez, & L. J. Fauci. Coupling biochemistry and hydrodynamics captures hyperactivated sperm motility in a simple flagellar model. *J. Theor. Biol.*, 283 (1):203–216, 2011.

S. D. Olson, S. Lim, & R. Cortez. Modeling the dynamics of an elastic rod with intrinsic curvature and twist using a regularized Stokes formulation. *J. Comput. Phys.*, 238: 169–187, 2013.

C. K. Omoto & C. J. Brokaw. Structure and behaviour of the sperm terminal filament. *J. Cell Sci.*, 58(1):385–409, 1982.

J. Oprea. *Differential geometry and its applications*, volume 59. American Mathematical Soc., 2019.

C. Pozrikidis. *Boundary integral and singularity methods for linearized viscous flow.* Cambridge University Press, 1992.

C. Pozrikidis. Shear flow past slender elastic rods attached to a plane. *Int. J. Solids Struct.*, 48(1):137–143, 2011.

D. Qi. Direct simulations of flexible cylindrical fiber suspensions in finite Reynolds number flows. *J. Chem. Phys.*, 125(11):114901, 2006.

I. H. Riedel-Kruse, A. Hilfinger, J. Howard, & F. Jülicher. How molecular motors shape the flagellar beat. *HFSP Journal*, 1(3):192–208, 2007.

L. Rothschild. Non-random distribution of bull spermatozoa in a drop of sperm suspension. *Nature*, 198(488):1221, 1963.

P. Sartori, V. F. Geyer, J. Howard, & F. Jülicher. Curvature regulation of the ciliary beat through axonemal twist. *Phys. Rev. E*, 94(4):042426, 2016a.

P. Sartori, V. F. Geyer, A. Scholich, F. Jülicher, & J. Howard. Dynamic curvature regulation accounts for the symmetric and asymmetric beats of *Chlamydomonas* flagella. *Elife*, 5:e13258, 2016b.

P. Satir. Studies on cilia: II. Examination of the distal region of the ciliary shaft and the role of the filaments in motility. *J. Cell Biol.*, 26(3):805–834, 1965.

P. Satir. Studies on cilia: III. Further studies on the cilium tip and a “sliding filament" model of ciliary motility. *J. Cell Biol.*, 39(1):77–94, 1968.

X. Schlagberger & R. R. Netz. Orientation of elastic rods in homogeneous Stokes flow. *Europhys. Lett.*, 70(1):129, 2005.

C. F. Schmid, L. H. Switzer, & D. J. Klingenberg. Simulations of fiber flocculation: Effects of fiber properties and interfiber friction. *J. Rheol.*, 44(4):781–809, 2000.

S. F. Schoeller, A. K. Townsend, T. A. Westwood, & E. E. Keaveny. Methods for suspensions of passive and active filaments. *J. Comput. Phys.*, 424:109846, 2021.

C. M. Schroeder, E. S. G. Shaqfeh, & S. Chu. Effect of hydrodynamic interactions on DNA dynamics in extensional flow: Simulation and single molecule experiment. *Macromolecules*, 37(24):9242–9256, 2004.

L. F. Shampine & M. W. Reichelt. The MATLAB ODE suite. *SIAM J. Sci. Comput.*, 18 (1):1–22, 1997.

P. Sharan, C. Maslen, B. Altunkeyik, I. Rehor, J. Simmchen, & T. Montenegro-Johnson. Fundamental Modes of Swimming Correspond to Fundamental Modes of Shape: Engineering I-, U-, and S-Shaped Swimmers. *Adv. Intell. Syst. Comput.*, 3:2100068, 07 2021.

J. Simons & A. Rosenberger. Flagellar Cooperativity and Collective Motion in Sperm. *Fluids*, 6(10), 2021.

J. Simons, S. Olson, R. Cortez, & L. Fauci. The dynamics of sperm detachment from epithelium in a coupled fluid-biochemical model of hyperactivated motility. *J. Theor. Biol.*, 354:81–94, 2014.

J. Simons, L. Fauci, & R. Cortez. A fully three-dimensional model of the interaction of driven elastic filaments in a Stokes flow with applications to sperm motility. *J. Biomech.*, 48(9):1639–1651, 2015.

J. E. Simons & S. D. Olson. Sperm Motility: Models for Dynamic Behavior in Complex Environments. In *Cell Movement: Modeling and Applications*, pages 169–209. Springer International Publishing, 2018.

P. Skjetne, R. F. Ross, & D. J. Klingenberg. Simulation of single fiber dynamics. *J. Chem. Phys.*, 107(6):2108–2121, 1997.

D. J. Smith. A boundary element regularized Stokeslet method applied to cilia-and flagella-driven flow. *P. Roy. Soc. A–Math. Phy.*, 465(2112):3605–3626, 2009.

D. J. Smith. A nearest-neighbour discretisation of the regularized stokeslet boundary integral equation. *J. Comput. Phys.*, 358:88–102, 2018.

D. J. Smith, E. A. Gaffney, J. R. Blake, & J. C. Kirkman-Brown. Human sperm accumulation near surfaces: a simulation study. *J. Fluid Mech.*, 621, 2009a.

D. J. Smith, E. A. Gaffney, H. Gadêlha, N. Kapur, & J. C. Kirkman-Brown. Bend propagation in the flagella of migrating human sperm, and its modulation by viscosity. *Cell. Motil. Cytoskel.*, 66(4):220–236, 2009b.

D. J. Smith, M. T. Gallagher, R. Schuech, & T. D. Montenegro-Johnson. The Role of the Double-Layer Potential in Regularised Stokeslet Models of Self-Propulsion. *Fluids*, 6(11), 2021.

S. E. Spagnolie & E. Lauga. Hydrodynamics of self-propulsion near a boundary: predictions and accuracy of far-field approximations. *J. Fluid Mech.*, 700:105–147, 2012.

P. Sunanda, B. Panda, C. Dash, R. N. Padhy, & P. Routray. An illustration of human sperm morphology and their functional ability among different group of subfertile males. *Andrology*, 6(5):680–689, 2018.

S. Timoshenko. *History of strength of materials: with a brief account of the history of theory of elasticity and theory of structures*. Courier Corporation, 1983.

A-K. Tornberg & M. J. Shelley. Simulating the dynamics and interactions of flexible fibers in Stokes flows. *J. Comput. Phys.*, 196(1):8–40, 2004.

S. Vogel. *Life in Moving Fluids: The Physical Biology of Flow-Revised and Expanded Second Edition*. Princeton University Press, 2020.

E. Wajnryb, K. A. Mizerski, P. J. Zuk, & P. Szymczak. Generalization of the Rotne–Prager–Yamakawa mobility and shear disturbance tensors. *J. Fluid Mech.*, 731, 2013.

B. J. Walker & E. A. Gaffney. Regularised non-uniform segments and efficient no-slip elastohydrodynamics. *J. Fluid Mech.*, 915, 2021a.

B. J. Walker & E. A. Gaffney. Regularised non-uniform segments and efficient no-slip elastohydrodynamics. *J. Fluid Mech.*, 915, 2021b.

B. J. Walker, K. Ishimoto, H. Gadêlha, & E. A. Gaffney. Filament mechanics in a half-space via regularised Stokeslet segments. *J. Fluid Mech.*, 879:808–833, 2019.

B. J. Walker, K. Ishimoto, & E. A. Gaffney. Efficient simulation of filament elastohydrodynamics in three dimensions. *Phys. Rev. Fluids*, 5(12):123103, 2020.

A. Walton. Flow orientation as a possible explanation of 'wave-motion'and 'rheotaxis' of spermatozoa. *J. Exp. Biol.*, 29(4):520–531, 1952.

L. Wang, S. Tlupova, & R. Krasny. A Treecode Algorithm for 3D Stokeslets and Stresslets. *Adv. Appl. Math. Mech.*, 11(4):737–756, 2019.

C. H. Wiggins & R. E. Goldstein. Flexive and propulsive dynamics of elastica at low Reynolds number. *Phys. Rev. Lett.*, 80(17):3879, 1998.

C. W. Wolgemuth, T. R. Powers, & R. E. Goldstein. Twirling and whirling: Viscous dynamics of rotating elastic filaments. *Phys. Rev. Lett.*, 84(7):1623, 2000.

C. W. Wolgemuth, R. E. Goldstein, & T. R. Powers. Dynamic supercoiling bifurcations of growing elastic filaments. *Physica D*, 190(3-4):266–289, 2004.

D. M. Woolley. Motility of spermatozoa at surfaces. *Reproduction*, 126(2):259–270, 2003.

D. M. Woolley & I. W. Osborn. Three-dimensional geometry of motile hamster spermatozoa. *J. Cell Sci.*, 67(1):159–170, 04 1984.

World Health Organisation. *WHO laboratory manual for the Examination and processing of human semen, 5th edition.* Cambridge University Press, 2010.

H. Yamakawa. Transport properties of polymer chains in dilute solution: hydrodynamic interaction. *J. Chem. Phys.*, 53(1):436–443, 1970.

S. Yamamoto & T. Matsuoka. A method for dynamic simulation of rigid and flexible fibers in a flow field. *J. Chem. Phys.*, 98(1):644–650, 1993.

M. Yamanoi, J. Maia, & T-S. Kwak. Analysis of rheological properties of fibre suspensions in a Newtonian fluid by direct fibre simulation. Part 2: Flexible fibre suspensions. *J. Non-Newton. Fluid*, 165(19-20):1064–1071, 2010.

Y. Yang, J. Elgeti, & G. Gompper. Cooperation of sperm in two dimensions: synchronization, attraction, and aggregation through hydrodynamic interactions. *Phys. Rev. E*, 78(6):061903, 2008.

C-H. Yeung & D. M. Woolley. Three-dimensional bend propagation in hamster sperm models and the direction of roll in free-swimming cells. *Cell Motil.*, 4(3):215–226, 1984.

Y. N. Young. Hydrodynamic interactions between two semiflexible inextensible filaments in Stokes flow. *Phys. Rev. E*, 79(4):046317, 2009.

D. Zabeo, J. T. Croft, & J. L. Höög. Axonemal doublet microtubules can split into two complete singlets in human sperm flagellum tips. *FEBS Lett.*, 593(9):892–902, 2019.

B. Zhao & L. Koens. Regularized Stokeslets Lines Suitable for Slender Bodies in Viscous Flow. *Fluids*, 6(9), 2021.

B. Zhao, E. Lauga, & L. Koens. Method of regularized stokeslets: Flow analysis and improvement of convergence. *Phys. Rev. Fluids*, 4(8):084104, 2019.

L. Zhu & C. S. Peskin. Simulation of a flapping flexible filament in a flowing soap film by the immersed boundary method. *J. Comput. Phys.*, 179(2):452–468, 2002.

L. Zhu & C. S. Peskin. Drag of a flexible fiber in a 2D moving viscous fluid. *Comput. Fluids*, 36(2):398–406, 2007.

P. J. Zuk, A. M. Słowicka, M. L. Ekiel-Jeżewska, & H. A. Stone. Universal features of the shape of elastic fibres in shear flow. *J. Fluid Mech.*, 914, 2021.